

# **Crystallization of Polyethylene as Detected via RheoNMR**

zur Erlangung des akademischen Grades einer

DOKTORIN DER INGENIEURWISSENSCHAFTEN (DR.-ING.)

von der KIT-Fakultät für Chemieingenieurwesen und Verfahrenstechnik des

Karlsruher Instituts für Technologie (KIT)

genehmigte

DISSERTATION

von

M. Sc. Mürüvvet Begüm Özen

aus

Ankara, Türkei

Tag der mündlichen Prüfung: 23.07.2020

Erstgutachter: Prof. Dr. Manfred Wilhelm

Zweitgutachter: Prof. Dr. Norbert Willenbacher



Ich versichere, dass die hier vorliegende Dissertation mit dem eingereichten und genehmigten Prüfungsexemplar der Doktorarbeit übereinstimmt.

Mürüvvet Begüm Özen

Karlsruhe, den 24 August 2020

*“Our true mentor in life is science.”*

*Mustafa Kemal Atatürk*

## Acknowledgement

It is a pleasure to thank many people who made possible this Ph.D. thesis.

I earned a scholarship in 2011 as a result of the high scores I got in the exams. This was a turning point in my life. During my studies abroad, I gained serious knowledge and had unforgettable experiences. This international education scholarship program started in 1929 with the support of Mustafa Kemal Atatürk to realize the science and technology transfer that our country needs in especially in higher education institutions. Therefore, I would like to thank the **Ministry of National Education of the Republic of Turkey** for financial support during my Ph.D. study.

Gratefully thanks to my supervisor **Prof. Dr. Manfred Wilhelm** for giving me the opportunity to work with the bests in the rheology field, encouraging my interest in polymer science with the precious teachings, advice, and criticisms to finish this work with success. Many thanks to my co-supervisor **Prof. Dr. rer. nat. Norbert Willenbacher** for scientific discussions, all his valuable support, and understanding. I want to thank **Prof. Dr. Michael A. R. Meier** for scientific discussions and fruitful cooperation. I would like to thank my committee members, **Prof. Dr. Gisela Guthausen** and **Prof. Dr. rer. nat. Sabine Enders** for agreeing to be on my committee and for their time.

I want to thank **Dr. Karl-Friedrich Ratzsch** particularly for his developments of the unique instrument RheoNMR and also scientific discussions. Thanks to **Dr. Iakovos Vittorias** for PE samples and GPC analysis; **Milliken** for providing HPN-20E; **Dr. Darin L. Dotson** for scientific discussion on HPN-20E; **Dr. Peter Weidler** for the XRD analysis and scientific discussion; **Volker Zibat** for SEM analysis; **Dr. Krassimir Garbev** for high-temperature XRD measurement; **Dr. Gülperi Cavusoglu** and **Dr. Ceylan Yildiz** for XRD measurements, **Dr. Erich Müller** for scientific discussions on the imageJ; **Dr. Alexander Welle** for TOF SIMS analysis; **Dr. Pavleta Tzvetkova** for high-field NMR measurements; **Sebastian** and **Selim** for assistance in the lab; **Dr. Philip Scholten**, **Dr. Patrick Dannecker**, **Nehir Kavak** and **Carmen Spottog** for our cooperation that teaches me so much.

I am especially grateful to **Canan**, **Nonkululeko**, **Miriam**, **Jonas**, **Matthias**, **Kamran**, **Karl**, **Volker**, **Christoph**, **Pavleta**, **Hatice**, **Emmerich**, **Burcu**, **Hasan**, **Uğur Can**, **Ahmet**, **Selime** and **Zafer** for their proofreading of my thesis. Many thanks to **Sabine Weiland** for her support on administration and guidance for bureaucratic work. Additionally, her advice is lightening

my future. Thanks a lot to **Daniel Zimmerman** for valuable friendship, and he was always supportive whenever there was a problem related to the instrument or computer. I am grateful to **Helena Hörig** for teaching on DSCs; being a precious colleague and also friend with her positive spirit. Many thanks to all actual and former members of the group for their support on my research, and the successful production of several movies.

Imagine powerful souls surrounding yourself and they make you feel at home, they clear out negative energies, leaving you feeling happy and refreshed for the next day. **Dr. Hatice Mutlu** and **Dr. Emmerich Tempfli** have been these powerful free souls for me. Many thanks to them my life has been very much easier and happier at work and outside of the work in Germany. Additionally, I have learned a lot about chemistry and including how to do science with a passionate way from **Dr. Hatice Mutlu**. Our Il Caminetto dinners are valuable to me! Many thanks to **Dr. Pavleta Tzvetkova** for being a precious friend and always finding time to listen to me. She makes me calm and stronger. Her advice helps me to see the reality behind the fog! She encourages me to take the steps to tackle the issues efficiently. I love NMR thanks to her. Our Sunday walks and golden coffee breaks are priceless! Many thanks to **Dr. Canan Karakaya** for her supports in my studies since 2007! Her supports and friendship for me the great and important in the milestones in my life. She is my role model. Thanks to my dear friend **Burcu**, I feel the world is small. She always finds time and a way to reach me wherever I am!

Special thanks for **Hatice-Emmerich, Pavleta, Canan, Dilara, Burcu, Helena-Micheal, Christina, Azadeh-Kamran, Eren, Nüzhet, Selime-Zafer, Nurhayat-Mehmet Memis**, and **Müge-Kamil Sönmez** who have been precious friends helping me during my difficult times and sharing with me all the happy, joyful moments with wonderful gatherings. Thanks to my two **blue beads**, worldwide unique **Rahime** and the rebellious wise young lady **Beril** for accompanying me on this road.

Last but certainly not least, I would like to thank especially my parents **Berrin** and **Tolunay** and my brother **Kutay**, for their absolute confidence, support in me all the time! They have been ready to give all they have to protect my health and happiness. I feel blessed to have them. Their love is always my power to live in happiness and health!

## Abstract

Crystallization of semicrystalline materials, e.g., polyolefines or fats, is a quite important topic not only from a scientific point of view but also from an industrial outlook. The comprehensive interactions during crystallization have not been not fully understood, such as the interaction between the material structures, the additives, the processing conditions which are leading to the final properties of the product. The novel developed RheoNMR is a combined technique in the group of Prof. Dr. Manfred Wilhelm with a combination of rotational rheology and low-field  $^1\text{H-NMR}$ . It provides the correlation of the viscoelastic behavior and local mobility of the crystallizing material under identical shear and thermal conditions.

In this thesis, the effects of the critical parameters such as the crystallization temperature, applied steady shear, and large strain amplitude on the isothermal crystallization mechanism of neat HDPE, HDPE/nucleating agent (NA) blends and coconut fat were investigated via the RheoNMR method. The final degree of crystallinity for HDPE/NA blends under quiescent crystallization was found to be equivalent to the crystallinity values observed via DSC, and thus, the accuracy of the RheoNMR technique is confirmed. A direct correlation between the time of gelation  $t_{\text{gel}}$  from rheology (where the dynamic moduli  $G' = G''$ ) and the required time to reach 20% crystallinity  $t_{0.2}$  measured by NMR, showed a strong relationship of crystallization mechanisms with the crystallization temperature, the NA content within the HDPE sample and the applied large deformation during crystallization. The  $t_{0.2}$  and  $t_{\text{gel}}$  values reduced almost 50% by a 0.5 °C decreased in crystallization temperature in the used temperature range. Additionally, the increasing NA content up to 3 weight % in the HDPE sample accelerated the crystallization with consequence a decreased the  $t_{\text{gel}}$  to half and reduced the  $t_{0.2}$  value to almost one-third compared to the  $t_{0.2}$  and  $t_{\text{gel}}$  values of the neat HDPE sample. This result indicated both enhanced nucleation and crystal growth stage. Besides, steady shear, conducted at the beginning of the experiment, also accelerated the crystallization by an increased number of nuclei, and hence, shortened  $t_{\text{gel}}$  and the  $t_{0.1}$  (required time for 10% crystallinity). However, a delay in  $t_{\text{gel}}$  and shortened the  $t_{0.2}$  were observed when the large strain amplitude ( $\gamma_0 = 30\%$ ) was applied during the complete crystallization process. This could be stated that the nucleation stage of the crystallization was delayed by possibly destroying nuclei via deformation. However, continuously applied deformation effectively enhanced the crystal growth stage by the oriented crystal structure, and thus, reduced the  $t_{0.2}$ .

Morphologies of HDPE/NA blends were investigated by SEM analysis after RheoNMR experiments. Analysis of lamellae orientation was studied by using fast Fourier transforms (FFT) based on the conversion of the SEM image into frequency spacing. The symmetrical circular shape of FFT image indicated randomly distributed lamellae for samples crystallized under quiescent conditions. The elliptical shape of FFT images for the samples crystallized under applied large deformation showed the oriented lamellar structure.

Additionally, the analysis of the isothermal hardening behavior of coconut fat was investigated via RheoNMR under quiescent and applied deformation conditions. While the crystallization temperature significantly influenced the final degree of the crystallinity, the applied deformation caused a slight decrease in the fractal dimensions at the early stage of the crystallization.

Demonstrated herein are the robustness, reproducibility, and convenience of RheoNMR analysis for investigation of the crystallization process of PE and coconut fat under the specified conditions. Analyzing empirical crystallization data by using classical suspension models or by developing semi-empirical equations for kinetic analysis can help to develop the simulation programs for solidification processes. Additionally, the RheoNMR method can be useful for valuable quality control analysis i.e., in the food industry using different qualities of fat since confectionery products contain a significant amount of fat. The RheoNMR method opens up the possibility to learn required deformation or shear rate for intentional application to the commercial processing which allows a better controlling physical property of the fat product.

Within this Ph.D. work, the dispersion of the cellulose with plant-oil based compatibilizers into the LDPE matrix was studied by using the shear rheology for investigating the material flow properties. The cellulose dispersion within the polymer matrix was improved. Modified amylose showed a higher capacity to compatibilize the cellulose compare to the modified starch within the LDPE matrix.

Lastly, the investigation of the melt rheological properties of the novel, renewable long-chain spaced aliphatic polyether mimic samples was studied via using shear rheology. Importantly, the polymers were with unique structures due to the fact that they were synthesized via non-conventional polymerization methodologies e.g. acyclic diene metathesis and thiol-ene polymerization, respectively. According to the results, samples based on acyclic diene metathesis polymerization can find an application as an impact modifier for some polymers,

mainly due to their inherent biodegradability and the calculated low flow activation energies of them.

## Zusammenfassung

Die Kristallisation von teilkristallinen Materialien wie z.B. Polyolefinen und Fetten ist nicht nur aus wissenschaftlicher, sondern auch aus industrieller Sicht von großer Bedeutung, da die vielfältigen Wechselwirkungen während der Kristallisation noch nicht vollständig verstanden sind, wie z.B. die Wechselwirkung zwischen den Materialstrukturen, den Additiven, den Verarbeitungsbedingungen, welche zu den endgültigen Eigenschaften des Produktes führen. Eine, im Arbeitskreis von Prof. Dr. Manfred Wilhelm, neu entwickelte kombinierte Methode aus Rotationsrheologie und Niederfeld- $^1\text{H-NMR}$ , die sogenannte RheoNMR, erlaubt die Korrelation des viskoelastischen Verhaltens mit der lokalen Mobilität des kristallisierenden Materials unter identisch Scher- und thermischen Bedingungen.

In dieser Arbeit werden die Auswirkungen der kritischen Parameter, wie der Kristallisationstemperatur, der groß Scheramplituden und der angewandten stetigen Scherrate, auf den isothermen Kristallisationsmechanismus von reinen HDPE und HDPE/ Keimbildner NA-Mischungen, sowie Kokosnussfett mittels RheoNMR untersucht. Es wurde festgestellt, dass der finale Kristallinitätsgrad für HDPE/NA-Mischungen für Kristallisation im Ruhezustand im RheoNMR Gerät, mit den mittels DSC beobachteten Kristallinitätswerten übereinstimmt, und somit wird die Genauigkeit der RheoNMR-Technik bestätigt. Eine direkte Korrelation zwischen der Zeit der Gelierung  $t_{\text{gel}}$  aus der Rheologie (wobei die dynamischen Module  $G' = G''$ ) und der erforderlichen Zeit zum Erreichen einer 20%igen Kristallinität  $t_{0,2}$  gemessen mittels NMR, zeigte eine starke Abhängigkeit des Kristallisationsmechanismus von der Kristallisationstemperatur, dem NA-Gehalt in den HDPE-Proben und der angewandten Deformation während der Kristallisation. Die  $t_{\text{gel}}$  und  $t_{0,2}$  Werte nehmen um fast 50% ab mit 0.5 °C verringerter Kristallisationstemperatur im verwendeten Temperaturbereich. Die Erhöhung des NA-Gehalts auf 3 Gew.-% in der HDPE-Probe beschleunigte die Kristallisation mit der Folge, dass die  $t_{\text{gel}}$  auf die Hälfte, und die  $t_{0,2}$  auf fast ein Drittel reduziert wurde, verglichen zu den  $t_{0,2}$ - und  $t_{\text{gel}}$ -Werten der reinen HDPE-Probe. Dieses Ergebnis zeigte sowohl eine verbesserte Keimbildung als auch ein Kristallwachstumsstadium an. Zusätzlich beschleunigte die zu Beginn des Experiments durchgeführte stetige Scherung die Kristallisation um eine erhöhte Anzahl von Kernen und verkürzte daher  $t_{\text{gel}}$  und  $t_{0,1}$  (Zeit zum Erreichen einer 10%igen Kristallinität). Eine Verzögerung in  $t_{\text{gel}}$  und eine Verkürzung von  $t_{0,2}$  wurden jedoch beobachtet, wenn die große Dehnungsamplitude ( $\gamma_0 = 30\%$ ) während des vollständigen

Kristallisationsprozesses angewendet wurde. Es kann davon ausgegangen werden, dass hierdurch die Keimbildungsstufe der Kristallisation verzögert wurde, indem möglicherweise Kerne durch Verformung zerstört wurden. Eine kontinuierlich angewendete große Scherdeformation verbesserte jedoch effektiv die Wachstumsstufe der Kristallisation durch die orientierte Kristallstruktur und reduzierte somit die  $t_{0,2}$ . Die Morphologien der HDPE/NA-Proben wurden mittels REM-Analyse untersucht. Die Morphologien der Proben wurden mittels REM-Analyse im Anschluss an die RheoNMR-Experimente untersucht. Die Analyse der Lamellenorientierung wurde unter Verwendung der schnellen Fourier-Transformationen (FFT) untersucht, die auf der Umwandlung des REM-Bildes in Frequenzabstände basierten. Die symmetrische Kreisform des FFT-Bildes zeigte zufällig verteilte Lamellen für Proben an, die im Gleichgewichtszustand kristallisierten. Die elliptische Form der FFT-Bilder zeigte die orientierte Lamellenstruktur für Proben an, welche unter Anwendung großer Dehnungsamplituden kristallisierten. Während bei Proben, welche im Gleichgewichtszustand kristallisierten, zufällig verteilte Lamellen beobachtet wurden, führte eine angewendete Deformation zu ausgerichteten Lamellenstrukturen.

Zusätzlich wurde die Analyse des isothermen Aushärtungsverhaltens von Kokosfett mittels RheoNMR im Gleichgewichtszustand und bei angewandter Deformation durchgeführt. Während die Kristallisationstemperatur den finalen Kristallinitätsgrad signifikant beeinflusst hat, führte die angewandte Deformation zu einer leichten Abnahme der fraktalen Dimensionen im frühen Stadium der Kristallisation.

Hierbei wurden die Robustheit, Reproduzierbarkeit und Einfachheit der RheoNMR-Analyse zur Untersuchung des Kristallisationsprozesses von PE und Kokosfett unter den gegebenen Bedingungen demonstriert. Die Analyse empirischer Kristallisationsdaten unter Verwendung klassischer Suspensionsmodelle oder durch die Entwicklung semi-empirischer Gleichungen für die kinetische Analyse kann zur Entwicklung von die Simulationsprogramme für Erstarrungsprozesse beitragen. Zusätzlich kann das RheoNMR-Verfahren eine wertvolle Qualitätskontrollanalyse sein, z.B. in der Lebensmittelindustrie unter Verwendung unterschiedlicher Fettqualitäten, da Süßwaren häufig eine signifikante Menge an Fett enthalten. Das RheoNMR-Verfahren eröffnet die Möglichkeit, die erforderliche Scherdeformations- oder Schergeschwindigkeit für die gezielte Anwendung auf die kommerzielle Verarbeitung zu ermitteln, was eine bessere Kontrolle der physikalischen Eigenschaften des Fettprodukts ermöglicht.

In dieser Doktorarbeit wurde die Dispersion von Cellulose mit, auf Pflanzenölen basierenden Vermittlern in einer LDPE-Matrix mittels Scherrheologie zur Analyse der Materialflusseigenschaften untersucht. Die Cellulosedispersion innerhalb der Polymermatrix wurde verbessert. So zeigte modifizierte Amylose eine höhere Fähigkeit zur Kompatibilisierung von Cellulose im Vergleich zu modifizierter Stärke innerhalb der LDPE-Matrix.

Abschließend wurden die schmelzrheologischen Eigenschaften einer neuartigen, erneuerbaren Polyetherprobe mit langkettigen, aliphatischen Segmenten mittels Scherrheologie untersucht. Wichtig war, dass die Polymere einzigartige Strukturen aufwiesen, da sie mittels unkonventioneller Polymerisationsmethoden, z.B. azyklische Dien-Metathese bzw. Thiol-En-Polymerisation, synthetisiert wurden. Den Ergebnissen zufolge können Proben, die auf der azyklischen Dien-Metathese-Polymerisation basieren, eine Anwendung als Schlagzähmodifikator für einige Polymere finden, hauptsächlich aufgrund ihrer inhärenten biologischen Abbaubarkeit und ihrer berechneten niedrigen Fließaktivierungsenergien.

## Özet

Yarı kristallin malzemelerin (örneğin poliolefinler veya yağlar) kristalizasyonu, sadece bilimsel açıdan değil, aynı zamanda endüstriyel açıdan da oldukça önemli bir konudur. Kristalizasyon sırasındaki kapsamlı etkileşimler, örneğin ürünün nihai özelliklerini etkileyen malzeme yapıları, katkı maddeleri ve malzeme işleme koşulları arasındaki etkileşim, tam olarak anlaşılmamıştır. Prof. Dr. Manfred Wilhelm'in grubunda yeni geliştirilen Rheo-NMR metodu, rotasyonel reoloji ve düşük alanlı  $^1\text{H-NMR}$  ile birlikte kombine bir tekniktir. Bu metot, aynı deformasyon ve termal koşullar altında kristalleşen malzemenin viskoelastik davranışı ve yerel hareketliliğinin korelasyonunu sağlar.

Bu tezde, kristalizasyon sıcaklığı, uygulanan sabit kayma ve büyük gerinim genliği gibi kritik parametrelerin saf HDPE, HDPE/çekirdeklenme maddesi (NA) karışımları ve hindistancevizi yağının izotermal kristalizasyon mekanizması üzerindeki etkileri RheoNMR yöntemi kullanılarak araştırılmıştır. Sonuçta, durgun kristalleşme koşulunda elde edilen HDPE/NA karışımları için kristalinite değerleri, DSC aracılığıyla gözlemlenen kristalinite değerlerine eşdeğer bulunmuştur ve bu RheoNMR tekniğinin doğruluğunu teyit etmektedir. Reolojiden gelen jelleşme süresi  $t_{\text{gel}}$  ile NMR ile ölçülen %20 kristalinite değerine ulaşmak için gerekli süre  $t_{0.2}$  arasında yapılan doğrudan bir korelasyon, kristalizasyon mekanizmaları ile kristalizasyon sıcaklığı, HDPE numunesi içindeki NA içeriği ve kristalizasyon sırasında uygulanan büyük deformasyon arasında güçlü bir ilişki olduğunu göstermiştir. Elde edilen  $t_{\text{gel}}$  ve  $t_{0.2}$  değerleri, kullanılan sıcaklık aralığında kristalizasyon sıcaklığındaki  $0.5\text{ }^\circ\text{C}$ 'lik bir düşüş ile neredeyse %50 azalmıştır. Bundan başka, HDPE numunesine eklenen NA içeriğinin ağırlıkça %3'e kadar artırılması kristalleşmeyi hızlandırmıştır. Bunun sonucunda, saf HDPE örneği için elde edilen  $t_{\text{gel}}$  ve  $t_{0.2}$  değerlerine kıyasla  $t_{\text{gel}}$  yarıya düşerken ve  $t_{0.2}$  değeri ise neredeyse üçte birine düşmüştür. Bu sonuç, eklenen NA ile artırılmış çekirdeklenme ve geliştirilmiş kristal büyüme aşamasını göstermektedir. Ayrıca, deneyin başlangıcında uygulanan sabit kesme oranı da çekirdeklenmeyi artırarak kristalleşmeyi hızlandırmıştır ve dolayısıyla  $t_{\text{gel}}$  ve  $t_{0.1}$  (%10 kristalleşme için gerekli süre) değerleri azalmıştır. Bununla birlikte, kristalizasyon işlemi sırasında uygulanan büyük gerinim genliği ( $\gamma_0 = 30\%$ ) sonucunda  $t_{\text{gel}}$ 'de gecikme ve  $t_{0.2}$ 'de ise azalma gözlenmiştir. Bu  $t_{\text{gel}}$ 'deki gecikmenin kristalleşmenin çekirdeklenme aşamasının, uygulanan büyük deformasyonun muhtemelen bir süreliğine oluşan çekirdekleri yok etmesinden kaynaklandığı söylenebilir. Çekirdeklenme aşamasındaki gecikmeye rağmen sürekli olarak uygulanan büyük deformasyon kristallerin

büyüme aşamasında kristal yapılarını yönlendirerek kristalizasyon hızını etkili bir şekilde arttırmıştır ve böylece  $t_{0.2}$  değerini düşürmüştür. HDPE/NA örneklerinin morfolojileri, RheoNMR deneylerinden sonra SEM analizi ile incelenmiştir. Lamel oryantasyonunun analizi, SEM görüntüsünün hızlı Fourier dönüşümü (FFT) tekniği kullanılarak frekans aralığına dönüştürülmesiyle incelenmiştir. FFT görüntüsünün simetrik dairesel şekli, durgun koşullar altında kristalize edilen numunelerin rastgele dağılmış lamellere sahip olduğunu göstermiştir. Uygulanan büyük deformasyon altında kristalize edilen numunelerden elde edilen FFT görüntülerinin eliptik şekli ise örneklerin yönlendirilmiş lamel yapısına sahip olduklarını ortaya çıkarmıştır.

Ek olarak, hindistancevizi yağının izotermal kristallenme davranışının durgun halde ve uygulanan deformasyon koşulları altında RheoNMR metodu ile incelenmiştir. Kristalizasyon sıcaklığı elde edilen son kristalinite değerini önemli ölçüde etkilerken; uygulanan deformasyon ise kristalizasyonun erken aşamasındaki fraktal boyutlarda hafif bir azalmaya neden olmuştur.

Burada gösterilenler, belirtilen koşullar altında PE örneklerinin ve hindistancevizi yağının kristalizasyon sürecinin araştırılması için RheoNMR analizinin uygun, tekrarlanabilir ve etkin olduğunu ortaya koymuştur. Klasik süspansiyon modellerini kullanarak veya kinetik analiz için yarı-ampirik denklemler geliştirerek deneysel kristalizasyon verilerini analiz etmek, katılma süreçleri için simülasyon programlarının geliştirilmesine yardımcı olabilir. Ayrıca, RheoNMR yöntemi yüksek standartlarda kalite kontrol analizleri için örneğin şekerleme ürünleri önemli miktarda farklı kalitede yağ içerdiğinden gıda endüstrisinde yararlı olabileceği açıktır. RheoNMR yöntemi, ticari proseslerde uygulanması için gerekli deformasyon veya kayma oranını öğrenme imkânı sağlar; ve bu da yağ ürününün fiziksel özelliğinin daha iyi kontrol edilmesini sağlayabilecektir.

Bu doktora çalışmasında, selülozun bitkisel yağ bazlı bağdaştırıcılarla LDPE matrisine dağılımı, malzeme akış özelliklerinin araştırılması için kesme reolojisi kullanılarak incelenmiştir. Polimer matris içindeki selüloz dispersiyonu iyileştirilmiştir. Modifiye edilmiş amiloz, LDPE matrisi içindeki modifiye nişastaya kıyasla selülozu uyumlu hale getirmek için daha yüksek bir kapasite göstermiştir.

Son olarak, yeni sentezlenmiş yenilenebilir uzun zincirli, aralıklı alifatik polieter mimik numunelerinin eriyik reolojik özelliklerinin araştırılması kesme reolojisi kullanılarak incelenmiştir. Daha da önemlisi, bu polimerler, asiklik dien metatez ve tiyol-en polimerizasyonu gibi geleneksel olmayan polimerizasyon metodolojileriyle sentezlendikleri

için benzersiz yapılara sahiptir. Bu sonuçlar, asiklik dien metatez polimerizasyonuna dayalı numunelerin temel olarak doğal biyolojik bozunurlukları ve hesaplanan düşük akış aktivasyon enerjileri nedeniyle bazı polimerler için bir darbe modifiye edici olarak uygulama bulabileceğini göstermiştir

# Contents

Acknowledgement.....	v
Abstract .....	vii
Zusammenfassung.....	x
Özet .....	xiii
Abbreviations .....	xix
Nomenclatures.....	xxi
1 Introduction.....	1
1.1 Outline .....	4
2 Polyethylene.....	8
2.1 Types of polyethylene (PE) .....	9
2.1.1 Low-density polyethylene (LDPE) .....	9
2.1.2 High-density polyethylene (HDPE) .....	11
2.1.3 Linear low-density polyethylene (LLDPE).....	12
3 Polymer Crystallization .....	14
3.1 Thermodynamics of Polymer Crystallization.....	18
3.2 Quiescent crystallization.....	21
3.2.1 Nucleation theory .....	22
3.2.2 Crystal growth mechanism.....	24
3.2.3 Crystallization kinetics .....	30
3.3 Factors Affecting Crystallization.....	33
4 Characterization Techniques Principles.....	40
4.1 Rheology.....	40
4.1.1 The concept of shear rheology .....	40
4.1.2 Phenomenological models.....	42
4.1.3 Linear viscoelasticity.....	45
4.1.4 Nonlinear viscoelasticity .....	48
4.2 Nuclear magnetic resonance (NMR) .....	50
4.2.1 Nuclear spins and magnetization.....	51
4.2.2 NMR interactions .....	54
4.2.3 Nuclear relaxation .....	55
4.2.4 NMR applications .....	59

4.3	Differential scanning calorimetry (DSC).....	63
4.4	X-ray diffraction (XRD).....	65
4.5	Scanning electron microscopy (SEM).....	67
5	RheoNMR Setup and Improvements .....	68
5.1	Setup details and experimental protocol.....	69
5.2	Improvements .....	75
5.3	Reproducibility of the results .....	81
6	In situ Correlation of Viscoelastic Behavior and Local Mobility of Neat and Nucleated HDPE Crystallization via RheoNMR .....	83
6.1	Introduction .....	83
6.2	Samples and their preparations.....	85
6.3	Quiescent crystallization.....	87
6.3.1	Thermal behavior of the commercial HDPE.....	87
6.3.2	Thermal behavior of the synthesized HDPE .....	98
6.3.3	Thermal behavior of the neat HDPE and HDPE/NA blends .....	102
6.4	Shear-induced crystallization.....	112
6.4.1	Steady shear effect on isothermal crystallization of neat HDPE.....	112
6.4.2	Short-term applied high deformation effect on HDPE/NA blend.....	117
6.4.3	Long-term applied high deformation effect on HDPE/NA blends.....	120
6.5	Microstructure, crystallinity and morphology analyses.....	129
6.6	Concluding remarks.....	141
7	Fat Crystallization Kinetics-Coconut Oil.....	144
7.1	Isothermal crystallization of coconut fat via RheoNMR.....	146
7.1.1	Kinetic analysis of isothermal coconut fat crystallization.....	148
7.1.2	Analyses of the fractal dimension .....	153
7.2	Concluding remarks.....	158
8	Rheological Properties of Cellulose/LDPE Composites Combined with Sustainable Plant-Based Compatibiliser .....	159
8.1	Introduction .....	159
8.2	Samples and their preparation .....	161
8.3	Melt shear rheology analysis of composites.....	162
8.4	Concluding remarks.....	170
9	Rheological Behavior of Renewable Based Long Chain Spaced Polyether Derivatives	171
9.1	Introduction .....	171

9.2	Sample synthesis.....	172
9.3	Melt rheology analysis.....	176
9.4	Concluding remarks.....	180
10	General Conclusion and Future Work .....	182
A	Appendix .....	188
	List of Figures .....	190
	List of Tables.....	206
	References .....	207

## Abbreviations

BPP	Bloembergen-Purcell-Pound
BVT	Bruker Variable Temperature
CERM	Center for Education and Research on Macromolecules
CPMG	Carr-Purcell-Meiboom-Gill pulse sequence
CoD	Coefficient of determination
DSC	Differential scanning calorimetry
EVA	Ethylene-vinyl acetate copolymer
F	Fluorine
FIC	Flow induced crystallization
FID	Free induction decay
FFT	Fast Fourier transforms
FT	Fourier-Transform
HDPE	High density polyethylene
ICI	Imperial Chemical Industries
IOC	Institute of Organic Chemistry
ITCP	Institute for Chemical Technology and Polymer Chemistry
iPP	Isotactic polypropylene
KIT	Karlsruhe Institute of Technology
LAOS	Large amplitude oscillatory shear
LCB	Long chain branching
LDPE	Low density polyethylene
LH	Lauritzen-Hoffman
LLDPE	Linear low density polyethylene
MDPE	Medium density polyethylene
NA	Nucleating agent
NMR	Nuclear magnetic resonance
MHz	Megahertz
MSE	Magic-sandwich echo
PA	Polyacrylate
PE	Polyethylene

PET	Polyethylene terephthalate
PP	Polypropylene
PS	Polystyrene
PUR	Polyurethane
PVC	Polyvinyl chloride
RF	Radio frequency
ROMP	Ring opening metathesis polymerization
SAOS	Small amplitude oscillatory shear
SCB	Short chain branching
SFC	Solid fat concentration
SEM	Scanning electron microscopy
SG	Sadler-Gilmer
T	Tesla
TGA	Thermogravimetric analysis
TTS	Time-Temperature-Superposition
UHMWPE	Ultra-high-molecular-weight polyethylene
ULMWPE	Ultra-low-molecular-weight polyethylene
VLDPE	Very-low-density polyethylene
WLF	William-Landel-Ferry
XRD	X-ray diffraction

## Nomenclatures

$\beta$	Integral breadth
$\gamma$	Deformation
$\gamma$	Gyromagnetic ratio
$\dot{\gamma}$	Shear rate
$\gamma_0$	Deformation amplitude
$\varepsilon$	Interaction energy
$\eta$	Viscosity
$\eta^*$	Complex viscosity
$\theta$	Angle of the incident beam
$\theta$	Spin pair vector
$\phi$	Filler weight fraction
$\lambda$	Wavelength
$\lambda$	Relaxation time
$\mu$	Magnetic moment
$\psi$	Constant
$\Psi$	Wave function
$\nu$	Foubert model rate parameter
$\nu_c$	Represents the volume fraction of spherulites
$\nu_L$	Larmor frequency
$\rho_a$	Density of melt
$\rho_c$	Density of the crystalline region
$\sigma$	Stress
$\sigma_i$	Specific surface free energies
$\tau$	Relaxation time
$\tau_c$	Correlation time
$\omega_1$	Angular frequency
$\phi_{\max}$	Maximum filler weight (wt) fraction
$\varphi_c$	Volume related relative crystallinity
$\nu_c$	Volume crystallinity
$\text{\AA}$	Angstrom

$A_i$	Area
$B_{loc}$	Local field
$\vec{B}_0$	External magnetic field
$C_{1,2}$	Constant
$C_C$	Constant
$C'$	Related with self-organization of growing crystals $D'$ and $\psi$
$D'$	The dynamic range of $G'$
$d_{hkl}$	Interplanar distance between $(hkl)$ reflecting planes
$\mathcal{D}$	The molecular weight distribution
$E$	Energies
$e$	Elemental charge
$F$	Correlation function
$F$	Force
$G$	Gibbs free energy
$G$	Growth rate radially
$g$	Lateral spreading rate
$g$	The volume concentration of the nuclei
$G$	Shear modulus
$G'$	Storage modulus
$G''$	Loss modulus
$g^0$	Specific melting free energy
$G_N^0$	Plateau modulus
$G'_{norm}$	Normalization of $G'$
$G'_{\infty}$	The dynamic moduli reached a maximum stable value
$H$	Enthalpy
$\hat{H}$	Hamiltonians
$h$	Plank`s constant
$h$	Distance
$h^0$	Per unit enthalpy
$H_{f,m}$	Enthalpy of fusion
$I$	Intensity

$I$	Spin
$I$	Nucleation rate
$I_0$	Prefactor
$I_A$	Integrated amorphous area
$I_T$	Integrated total area
$J$	Spectral density
$K$	Boltzmann`s constant
$K$	Avrami model rate parameter
$k$	Scherrer constant
$L$	Volume average of the thickness of the crystallites
$l$	Length
$l$	The nucleation density
$L_c$	Crystal thickness
$L_c^*$	New formed crystal with thickness
$L_p$	Lamellae width
$m$	Foubert model exponent
$m$	The number of neighboring sides
$M_e$	Entanglement molecular weight
$M_w$	The weight average molecular weight
$\vec{M}_0$	The bulk magnetization at the thermal equilibrium
$n$	Avrami model exponent
$n$	Integer number
$P$	Arbitrarily chosen point
$p$	Chemical length exponent depends on the fractal dimension
$R$	Universal gas constant
$r^*$	Radius
$\dot{r}$	Constant rate
$S$	Average number of the spherulite fronts
$T$	Absolute temperature
$t$	Time
$T_C$	Crystallization temperature
$T_C^0$	Equilibrium crystallization temperature

$T_{C,max}$	Maximum crystallization at which a crystal grows with a maximum rate
$T_g$	Glass transition temperature
$t_{gel}$	The gel time
$t_{indx}$	Induction time
$T_m^0$	Equilibrium melting temperature
$T_1$	Spin-lattice relaxation
$T_2$	Spin-spin relaxation
$\tan\delta$	Dissipation factor
$S$	Entropy
$V$	Volume
$V$	Local electric field gradient tensor
$Q^\infty$	Equilibrium triple point
$x$	Fronts of growing crystals
$X_C$	Mass crystallinity

# 1 Introduction

Polyethylene (PE) is one of the most consumed semi-crystalline polymers in the world. It constitutes the largest segment (32%) of the worldwide plastic production (Plastic Europe report 2016). The global demand for PE is expected to rise owing to its wide-ranging versatility, easy processability, and low cost (Roger 2014). Different PE types find an enormously broad range of applications in many aspects due to diverse mechanical, chemical, thermal, electrical and optical properties of them.

Polyethylene can be classified based on its density. The main PE types regarding the sold volumes are; high-density polyethylene (HDPE), low-density polyethylene (LDPE) and linear low-density polyethylene (LLDPE). Other common varieties include ultra-high-molecular-weight polyethylene (UHMWPE), ultra-low-molecular-weight polyethylene (ULMWPE), medium density polyethylene (MDPE) and very-low-density polyethylene (VLDPE). The mechanical properties of PE significantly change by the extent and type of branching, the weight average molecular weight ( $M_w$ ), the molecular weight distribution ( $D$ ) and the crystal structure. The rigid property with a highly crystalline structure of HDPE makes it suitable to use as milk jugs, detergent bottles, butter tubs, garbage containers, chemical storage tanks, water pipes and toys (Peacock 2000). Beside HDPE, UHMWPE has outstandingly tough mechanical properties and high chemical resistance with a molecular weight numbering in the millions. Hence, it is possible to see UHMWPE as a chute, hopper, truck bed liners, machinery parts, fibers of bulletproof vests and even as hip, knee as well as shoulder implants (Kurtz 2004). Conversely, LDPE is a flexible product with low crystallinity, which results in applications such as films for commercial and retail packaging, bags, squeeze bottles and food storage containers (Peacock 2000).

These physical and mechanical characteristics of PE types can be improved for specific applications by composites and also copolymerization of ethylene with different monomers. For instance, copolymerization of vinyl acetate with ethylene results in ethylene-vinyl acetate copolymer (EVA) which is commonly used in athletic shoe sole foams (Verdejo and Mills 2002). Composites of PE are widely used in many applications

i.e. textile, carpets, packing, electrical, thermal energy storage, automotive applications, biomedical and space applications (Khanam and AlMaadeed 2015; van Dam 2008). Designed PE composites can be categorized into two groups regarding reinforcing material as fiber-reinforced PE and particle-reinforced PE composites. Particles and fibers are used to increase the modulus. While the addition of fibers into the PE polymer matrix is used to obtain higher strength, added particles decrease the ductility of the polymer matrix (Khanam and AlMaadeed 2015). Beside improved properties, the addition of them reduces the cost of composites. In the last decades, environmental benefits have been critically considered due to heavy plastic pollution worldwide, and thus bio-based, degradable, natural materials are preferred for developments on PE composites (van Dam 2008). For instance, the most commonly used fibers are natural cellulosic fibers i.e. sisal, cotton and protein-based fibers i.e., wool, silk (van Dam 2008). In addition to bio-based PE composites, the further modification of PE properties can be done by the use of newly developed bio-based plastics as an impact modifier.

The crucial task at this point is to investigate the processability of the produced PE composites, newly synthesized renewable polymer or modified PE with additives such as nucleating agents before the potential large-scale manufacturing. Despite the investigation of the bulk properties, crystallization kinetic of PE materials is considerably important. Thus, processing conditions are seriously and inevitably tailor the final material properties due to changing crystallization kinetics, the crystal morphology, and ultimate crystallinity.

### ***Fabrication process and processing conditions effects on PE properties***

The most common techniques in PE processing are injection molding, blow molding and extrusion. Fabrication processes convert the pellet or powder PE material into a final consumer product by manipulating the material in the molten state. During processing, molten PE is shaped into its final form and cooled down below the melting temperature to keep its form. Crystallization of the polymers mostly starts during the cooling that depends on the degree of supercooling. Crystallization in polymers is quite important and comprehensive topic in the field of polymer research. Challenging questions are especially the vigorous interactions ongoing during crystallization between the molecular

characteristic i.e. chemical composition and molecular topology (branching) (Pasch and Malik 2014) and the fabrication conditions, such as applied thermal mechanism (e.g., cooling rate and crystallization temperature  $T_C$ ), flow type (e.g., shear, elongation or both) and the duration of the high deformation (Zuidema 2000). Therefore, research on crystallization kinetics of PE and controlling of the nucleation process have a great interest not only from a scientific point of view but also from an industrial one to understand their influence on material properties and the efficiency of the PE production. Here, the possibility to influence the crystal morphology by the addition of a nucleating agent (NA) into PE is of particular interest. Previous research showed that an addition of an effective NA, i.e. HPN-20E, into HDPE enabled a significant reduction in a cycle time of ~10% in injection molding and an increased performance in the production with more stable and consistent neck ovality ratio (Seven *et al.* 2016).

The fundamentals of the nucleation theory and crystal growth and their relation on the temperature difference between the equilibrium melting temperature  $T_m^0$  and crystallization temperature  $T_C$  were explained by Lauritzen and Hoffman (1960); Sadler (1987). The mesomorphic layer transition reported by Strobl (2007). Temperature and pressure effect on PE phases were described by Wunderlich and Melillo (1968); Keller *et al.* (1994). Flow-induced crystallization was studied by many scientists Kawai *et al.* (1968); Mackley *et al.* (1975); Lagasse and Maxwell (1976); Eder and Janeschitz-Kriegl (1988). These studies revealed the orientation of polymer chains to the applied flow direction and promoted nucleation by the applied shear flow. Despite the researches that have been carried out for decades, the comprehensive relationship between the polymer structures, the processing conditions and the final properties of the product have not been fully understood due to a large number of variable parameters. Besides, the evolution over complex polymer structures, e.g., PE composites, blends with other polymers or additives, as well as improved processing techniques demonstrates the necessity of deeper investigations on the correlation of viscoelastic behavior and the local mobility via characterization techniques.

Commonly used characterization techniques for semi-crystalline polymers, such as PE, include differential scanning calorimetry (DSC) for thermal and physical properties; diffraction and scattering (X-ray, light) for microstructures determination; nuclear

magnetic resonance (NMR) for investigation of structure, chain relaxation as well as crystallinity; microscopies (optical, electron) for morphology analyses and rheology for mechanical testing (Piorkowska and Rutledge 2013). For the investigation of the crystallization process in polymers in situ via a combination of different characterization techniques under thermally and mechanically, identical conditions enable a deepened understanding by a direct association of material properties, such as the viscoelastic behavior, to its crystallinity, while avoiding problems, like e.g., not comparable homogeneous cooling rates for different methods. For instance, novel developed a combined technique with a combination of rheology and low-field  $^1\text{H-NMR}$ , RheoNMR (Ratzsch, *et al.* 2017; Özen *et al.* 2015, 2016; Rätzsch *et al.* 2019) enables the correlation of the viscoelastic behavior and local mobility, measured by the proton relaxation, under oscillatory shear at identical temperature conditions. Low-field RheoNMR is a powerful technique for precise investigation of temperature-sensitive processes such as PE crystallization.

## 1.1 Outline

The present thesis is divided into ten chapters. In details, the thesis is organized as follows:

*Chapter 1* introduces a literature review of the production and classification of PE. The chapter provides a summary of the crystallization behavior of PE during processing with the parameters such as cooling rate, applied deformation, and chosen crystallization temperature. Additionally, commonly used characterization techniques for analyzing PE crystallization and mechanical properties of it are briefly introduced.

Polyethylene along with its copolymers is used in a wide variety of consumer products owing to its semicrystalline structures. A more detailed description and the types of PE are mentioned in *Chapter 2*.

During thermoplastic processing, the orientation of PE chains due to flow under supercooling causes shear-induced crystallization which affects the final crystallinity. The crystallization is a highly sensitive process depending on the processing conditions such as temperature, cooling rate, and applied deformation. Therefore, crystallization has

been an attractive topic in scientific and industrial aspects. In *Chapter 3*, the fundamentals of crystallization theories and parameters affecting crystallization kinetics are explained.

The processability of the polymeric materials can be investigated by using rheology. Low-field (time-domain) NMR is a useful tool to quantitatively investigate and monitor the molecular dynamics in the phases of a crystallizing polymer. Other commonly used characterization techniques, DSC, XRD, and scanning electron microscopy (SEM) are presented in *Chapter 4*.

The crystallization of polymers is a highly temperature-dependent process. The difficulties of thermal history effects for different characterization techniques are experimentally challenging especially for samples with fast crystallization kinetics, e.g., high-density polyethylene (HDPE). Thus, the recently introduced novel method, RheoNMR, enables the correlation of macroscopic material properties and microscopic molecular dynamics with a single experimental run, under identical temperature, cooling rate, and shear conditions. The details of the RheoNMR method, the developments on the method to obtain a sensitive and accurate measurement for fast crystallize bulk samples are announced in *Chapter 5*.

Nucleation of HDPE has a great interest in both the industrial and scientific points of the view to alter the physical properties of HDPE, e.g., the cycle time in extrusion. An organic salt based on *cis*-1,2-cyclohexanedicarboxylic acid calcium salt (Hyperform HPN-20E) has been found as an effective nucleating agent (NA) for PE and polypropylene (PP) (Seven *et al.* 2016; Jiang *et al.* 2012). Nevertheless, a detailed examination of the effects of the concentration of NA on PE crystallization under flow conditions has not been available in the literature. The newly developed RheoNMR method was used to investigate the influence of deformation, temperature, and addition of NA on crystallization kinetics, final crystallinity and viscoelastic behavior of HDPE. In *Chapter 6*, the resulting information was used for a potential new direction to correlate the macroscopic mechanical properties (gelation point) with microscopic properties as the rate of crystallization and half time of the crystallization process. The practical importance of the fundamental questions was used as a motivation for this chapter:

-How does temperature under quiescent condition effects crystallization kinetics of the HDPE sample?

-How does the existence of a NA in the HDPE sample change the gelation point (crossover of the moduli), crystallization kinetics?

-How does the applied shear flow type and duration of it impact the gel point, crystallization kinetics, and crystallinity of neat and nucleated HDPE?

-How are the microstructures, e.g., the unit cell of crystal, alignment of the lamellae, and resulting morphology of NA/HDPE blends after RheoNMR experiments?

-How are the resulting crystallinity, crystallization kinetic parameters of NA/HDPE blend under quiescent conditions with similar cooling rate experiments performed with different characterizations techniques such as DSC, XRD?

Different models were used to obtain a deeper understanding of all results which were also compared with previous studies in *Chapter 6*.

Knowledge of the flow properties and crystallization under-identified conditions of fat is important to control processing, and thus obtain target product characteristics i.e. firmness, texture, and stability at a certain temperature. Coconut oil was used as a model substance for a fat crystallization kinetic study in *Chapter 7*. Coconut oil finds several applications to be used in the food industry and the kinetic study of its crystallization has rarely been reported. Therefore, the low-field RheoNMR technique was used to investigate the effects of oscillatory shear on fat crystallization kinetics and the final crystallinity.

One of the most attractive reinforcing filler material is cellulose due to its a biodegradable, non-toxic, low cost, lightweight material structure. Synthesized amylose and starch-based compatibilizers with reinforcing filler material cellulose were added into low-density polyethylene (LDPE) in various weight ratios. In *Chapter 8*, the melt shear rheological properties of composites were investigated by using commercial rheometers for the understanding of processability, thermal stability, and critically the state of filler dispersion in the matrix.

In *Chapter 9*, shear rheology was used to analyze the melt material properties of novel synthesized renewable-based polyether derivatives. Resulting properties and possible industrial applications were discussed.

A summary of all studied topics mentioned previous chapters is given and the main contributions are discussed. Additionally, future research directions based on determined results are suggested in the final *Chapter 10*.

## 2 Polyethylene

Polyethylene (PE) is a semi-crystalline thermoplastic. It has a wide range of physical properties such as elasticity, and resistance towards water weather, chemical, etc. These final physical properties of PE products depend on the crystallinity, molecular weight, molecular weight distribution, branching characteristics. The global demand for PE has been on the rise due to its versatility, easy processability, low cost, chemical inertness, and recyclability. Polyethylene represents the largest segment (32%) of the total plastic demand in worldwide plastic production as seen in Figure 2.1 (Plastic Europe report 2016). The demand for PE was expected to expand by 4% per year to reach 99.6 million metric tons in 2018 (Roger 2014).

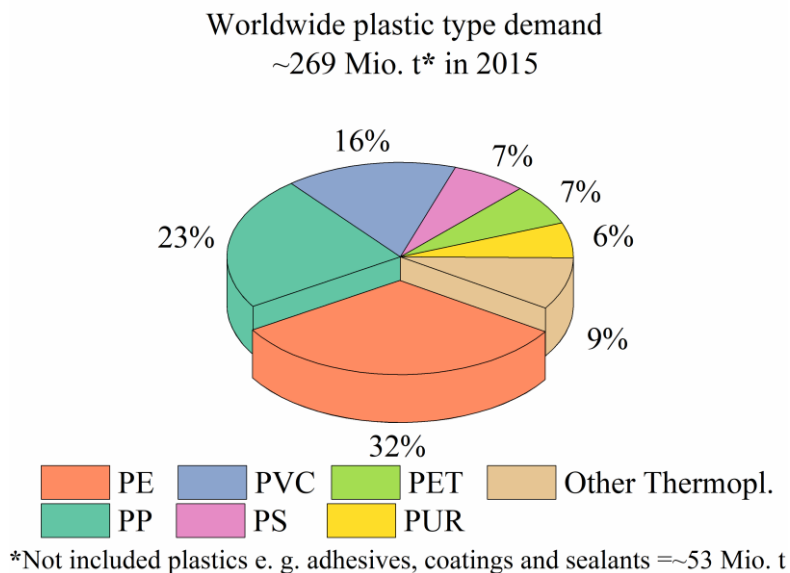


**Figure 2.1:** The worldwide plastic-type demand in 2015. PE: polyethylene, PP: polypropylene, PVC: polyvinyl chloride, PET: polyethylene terephthalate, PS: polystyrene, PUR: polyurethane, PA: polyacrylate. Data was taken from the Plastic Europe Report (2016).

Polyethylene can be classified, depending on its density and sold volume, into three important types which are high-density polyethylene (HDPE), low-density polyethylene (LDPE) and linear low-density polyethylene (LLDPE). The first synthesized polyethylene was LDPE discovered by Micheal Perrin using free-radical initiators in the 1930s (Peacock 2000). In 1936 the British company Imperial Chemical Industries (ICI) started the manufacturing of LDPE (Peacock 2000). The production of HDPE started in the 1950s by the discovery of the Ziegler-Natta catalyst (Ziegler *et al.* 1955; Natta 1956;

Peacock 2000). In 1960, the first commercial LLDPE was produced by DuPont using copolymers of ethylene with  $\alpha$ -olefins via gas-phase polymerization (Peacock 2000). The different types of PE can vary depending on the synthesis method, used comonomer type and amount.

## 2.1 Types of polyethylene (PE)

Polyethylene ((C<sub>2</sub>H<sub>4</sub>)<sub>n</sub>) is a large molecule consists of repeating structural units (C<sub>2</sub>H<sub>4</sub>), known as monomers, which are covalently bonded.

### 2.1.1 Low-density polyethylene (LDPE)

Low-density polyethylene (LDPE) was the first synthesized and commercially produced PE in the 1930s. High pressure (~1100 to 2000 bar) and high temperatures (100-300 °C) are used during the free radical polymerization of ethylene to produce LDPE (Luft *et al.* 1982; Peacock 2000). The most common types of initiators for the polymerization process are listed in Table 2.1.

**Table 2.1:** The most common types of initiators (Peacock 2000).

Initiator	Reaction
Hydroperoxide	ROOH $\rightarrow$ RO• + HO•
Dialkyl peroxide	ROOR' $\rightarrow$ RO• + R'O•
Tertiary perester	RCOOCOCR' <sub>3</sub> $\rightarrow$ RCO• + R' <sub>3</sub> COCO•
Azodialkyl	RNNR' $\rightarrow$ RN• + R'N•

R and R'=an alkyl or aryl group or various other organic moieties.

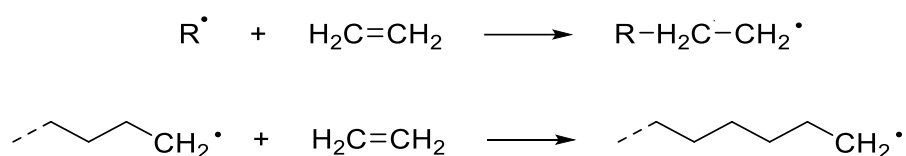


**Figure 2.2:** The growth of polyethylene chains via free radical polymerization (Peacock 2000).

After decomposition of the initiator, polyethylene chains grow by attachment of an ethylene molecule to the free radical species via a carbon-carbon covalent bond, and the unpaired electron is transposed to the new chain end, as shown in Figure 2.2. The chain branching occurs via intramolecular and intermolecular radical transfer that results in

short chain branching (SCB) and long-chain branching (LCB) respectively as seen in Figure 2.3.

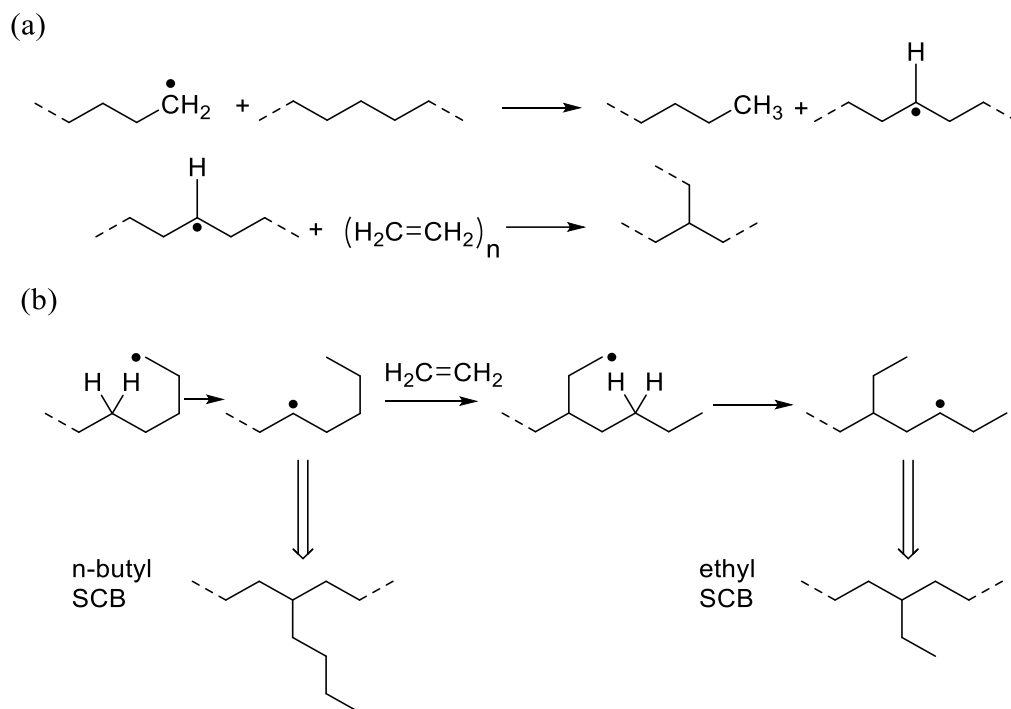


**Figure 2.3:** The (a) intermolecular and (b) intramolecular radical transfer during the free radical polymerization of ethylene used for LDPE production (Peacock 2000).

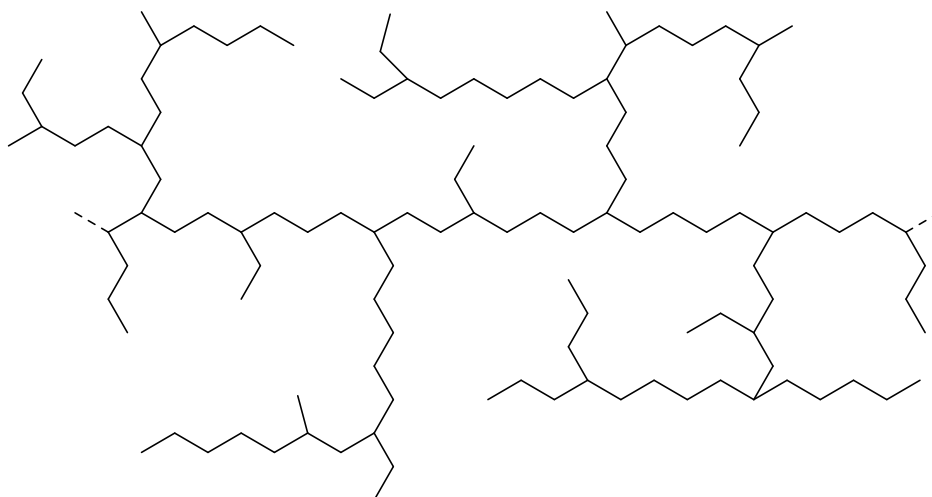


**Figure 2.4:** Illustration of the chemical structure of low-density polyethylene (LDPE).

Low-density polyethylene has a molecular structure as illustrated in Figure 2.4 that can be altered mainly by controlling the polymerization conditions. The increase in the reaction pressure increases the resulting molecular weight of LDPE. The systematically

altered reactor pressure causes a broad molecular weight distribution. By raising the polymerization temperature, the branching level of LDPE increases which leads to a decrease in the degree of crystallinity. The melting point of LDPE is around 100 °C which limits its use, for example in contact with hot water (Kricheldorf *et al.* 2005).

### **2.1.2 High-density polyethylene (HDPE)**

The Ziegler-Natta catalyst discovered in 1950 and enabled the important progress in ethylene polymerization by means of the production of high-density polyethylene HDPE (Ziegler *et al.* 1955; Natta 1956; Peacock 2000). High-density polyethylene is a semicrystalline polymer that consists of a linear polymer chain with very few or no branches as illustrated in Figure 2.5 (Kricheldorf *et al.* 2005). In contrast to LDPE, a combination of the catalyst type and polymerization condition affect the molecular structure of HDPE. There are three groups of catalysts used in this polymerization process (Kricheldorf *et al.* 2005):

1. Titanium or zirconium halogenides or hydrides based catalysts (Ziegler catalysts) e.g., titanium tetrachloride (TiCl<sub>4</sub>)
2. Chromium compounds based catalysts (Phillips catalysts)
3. Metallocenes based catalysts and also other single-site catalysts such as nickel ylid, nickel diimine, palladium, iron or cobalt complexes

Using a catalyst in the polymerization process makes the production possible at the low-pressure condition in three different ways, namely as a slurry (suspension) process, a gas phase process, and a solvent process (Kricheldorf *et al.* 2005).

1. Slurry process: Hydrocarbons e.g., isobutane, hexane, n-alkane are used to dissolve the monomers and the catalysts in the temperature range from 70 to 90 °C, with pressure varying in between 0.7 and 3 MPa. The polymerization takes 1 to 3 hours with the efficiency ranges 95 to 98%. Polyethylene precipitates due to the polymerization temperatures being kept below the melting point range of HDPE (125-143 °C). While the molecular weight distribution can be controlled by the type of catalysts or by stepwise performed polymerization processes, the molecular weight of HDPE depends on the hydrogen amount.

2. Gas-phase polymerization: In this process, the catalysts are supported on an inert substrate (e.g., silica or alumina). The monomer and the catalysts are brought in contact in a fluidized bed which is stirred at 2 to 2.5 MPa the pressure and temperature between 85 and 100 °C (Kricheldorf *et al.* 2005). The produced polymer can be removed from the reactor regularly.

3. Solvent polymerization: Polymerization is performed in cyclohexane or another appropriate solvent with the addition of catalysts at 140-150 °C, and the under the pressure of 0.7-7 MPa (Kricheldorf *et al.* 2005). Although this process takes 1 to 5 min with a conversion of 95%, the achieved maximum molecular weight of HDPE is restricted by increased viscosity of the solution.

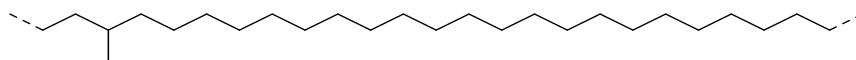


*Figure 2.5: Illustration of the chemical structure of high-density polyethylene (HDPE).*

Additionally, a class of HDPE is known as an ultra-high molecular weight polyethylene (UHMWPE) with a molecular weight of over 1,000,000 g/mol. The physical and mechanical properties of UHMWPE are outstanding such as high abrasion resistance, high impact toughness, good chemical resistance. Therefore, UHMWPE has a wide range of industrial applications including pickers for textiles machinery, bumpers and siding for ships, runners for bottling production, bullet-proof vests and also in orthopedics as an artificial joint owing to (Kurtz 2004).

### **2.1.3 Linear low-density polyethylene (LLDPE)**

In 1960, the first commercial LLDPE was produced by DuPont with gas-phase polymerization (Peacock 2000). In this polymerization, the copolymerization of ethene with  $\alpha$ -olefins is done by using the Ziegler catalysts in commercial production or single site catalysts based on metallocene/MAO on a laboratory scale. The commonly used  $\alpha$ -olefins are 1-butene, 1-hexene, and 1-octene (Kricheldorf *et al.* 2005; Peacock 2000). In contrast to LDPE, LLDPE has much higher tensile strength due to SCB molecular characteristics. The chemical structure of an LLDPE can be seen in Figure 2.6. This SCB structure reduces the degree of crystallinity, the melting point and the density of LLDPE compare to HDPE (Kricheldorf *et al.* 2005; Peacock 2000). These properties make

LLDPE more flexible; and consequently, favorable material for packaging films and sealing layers in multilayer films.

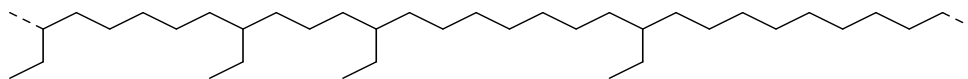


**Figure 2.6:** Illustration of the chemical structure of a linear low-density polyethylene (LLDPE).

The incorporation of substantially high levels of comonomer content i.e., octane content between 3.3-14.6 mol%, leads to a reduction in the density below the density of LDPE (Wypych 2016). These products are named ultra-low density or very low-density polyethylene (ULDPE and VLDPE, respectively). The ULDPE has the potential to be used neat or blended into other polymers as impact strength and clarity modifier due to its flexible, transparent, and elastomeric structure (Peacock 2000).

All the above mentioned different types of polyethylene have a diverse range of densities, the degree of crystallinities and the range of melting temperature is also in a varying range as described in Table 2.2.

**Table 2.2:** Properties of different types of polyethylene (Peacock 2000).

Property	HDPE	LDPE	LLDPE	VLDPE
Density (g/cm <sup>3</sup> )	0.94-0.97	0.91-0.94	0.90-0.94	0.86-0.90
Degree of crystallinity (%)	62-82	42-62	34-62	4-34
Melting temperature (°C)	125 -140	98-115	100-125	60-100

### 3 Polymer Crystallization

Polymer crystallization has been extensively studied in recent decades, and it still attracts significant interest. This is mainly because of the commercial interest and importance of semi-crystalline polymers for the polymer industry. The physical properties of the commercial semi-crystalline product can be tailored by controlling crystal size, shape, orientation and final crystallinity. In this chapter, general important aspects of the polymer crystallization theory are explained with reference to polyethylene which is the most popular globally demanded semi-crystalline polymer.

Many stereoregular polymers (polyethylene, isotactic or syndiotactic polypropylene, poly(ethylene oxide), etc.) crystallize due to the packing of individual polymer chains into a regular array (Hiemenz and Lodge 2007). The ordered region of the semi-crystalline polymer consists of crystallites that are surrounded by disordered chains comprising a partially ordered layer adjacent to the crystallites as shown schematically in Figure 3.1. The noncrystalline phase consisted of tie chains, loops, and cilia as a type of chain configurations that depends on the molecular weight, branching, and crystallization conditions of the PE sample (Peacock 2000).

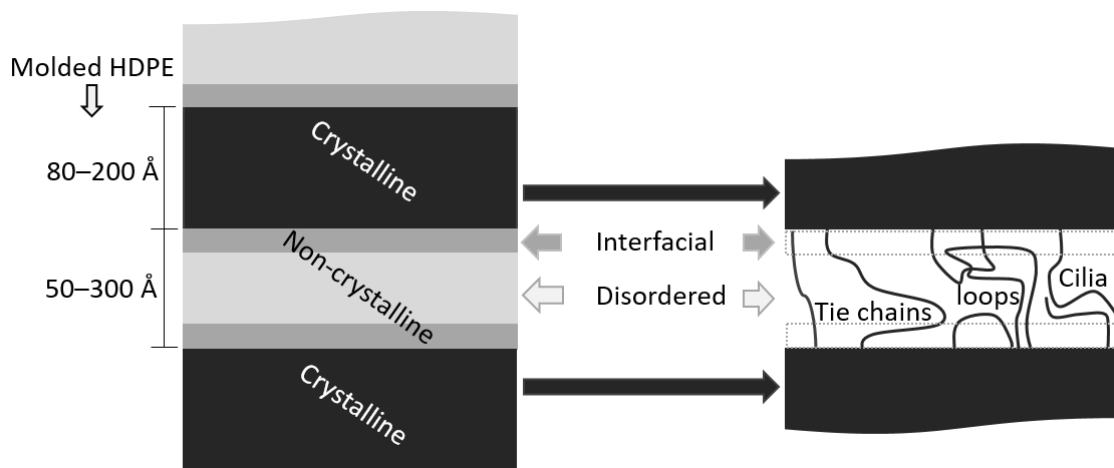


**Figure 3.1:** A simple illustration of the three-phase morphology in solid polyethylene and tie chains, loops, and cilia in the non-crystalline phases of polyethylene (Peacock 2000). A specification is given for high-density polyethylene (HDPE) as a thickness range of approximately 80-200 Å with several micrometers lateral dimension for crystallites and the range of non-crystalline phase approximately 50-300 Å (Peacock 2000).

Molded HDPE samples typically comprise of crystallites, which have a thickness in the range of 80–200 Å with lateral dimensions of several micrometers, and the non-crystalline region size varies between 50 Å and 300 Å (Peacock 2000). Crystallites are thinner and smaller for LDPE and LLDPE samples compare to HDPE.

Additionally, the crystalline part of a polymer is composed of multiscale structures. The smallest entity is the unit cell. Polyethylene shows three different types of unit cells as orthorhombic, monoclinic and hexagonal. Unit cell types are defined according to the different constraints on values of unit cell sides (axes = a, b, c) and unit cell axial angles ( $\alpha$ ,  $\beta$ ,  $\gamma$ ) (Gedde 1995; Hiemenz and Lodge 2007; Strobl 2007; Peacock 2000). The orthorhombic is the most common and stable unit cell type of PE. In contrast, the monoclinic is a metastable phase formed under elongation condition during PE crystallization, and the hexagonal can be produced at extremely high pressure in laboratory crystallization conditions (Peacock 2000; Gedde 1995; Hiemenz and Lodge 2007). Therefore, the orthorhombic unit cell can be considered the only unit cell type in commercial samples. Figure 3.2 shows an illustration of the orthorhombic unit cell. The dimension of the orthorhombic unit cell is known as to be  $a = 7.42$ ,  $b = 4.95$ ,  $c = 2.55$  Å with angles  $\alpha = \beta = \gamma = 90^\circ$  which are reported for HDPE at room temperature (Bunn 1939). The density of the HDPE orthorhombic unit cell is accepted as  $1.00 \text{ g/cm}^3$ . The a and b axes of the orthorhombic unit cell are larger for LDPE and LLDPE compare to the orthorhombic unit cell of HDPE, while the length of the c axis remains constant for all type of PE. Additionally, the monoclinic unit cell dimensions are  $a = 8.09$ ,  $b = 4.79$  and  $c = 2.55$  Å with angles  $\alpha = \beta = 90^\circ$ ,  $\gamma = 107.9^\circ$ , and the hexagonal unit cell has  $a = 8.42$ ,  $b = 4.56$ ,  $c < 2.55$  Å with angles  $\alpha = \beta = 90^\circ$ ,  $\gamma = 120^\circ$  (Peacock 2000). Another entity in multi-scale structures of the crystalline part is a single crystal that is constructed by repeating unit cells. The concept was first described by Storks in 1938 as a “fringed micelle model” as illustrated in Figure 3.3a. In the fringed micelle model, “micelles” were the crystalline region in which polymer chains are aligned parallel, and “fringed” was a representation of the part in which non-crystalline (disordered) chains were assumed to be attached to the crystallites as partially ordered (Peacock 2000).

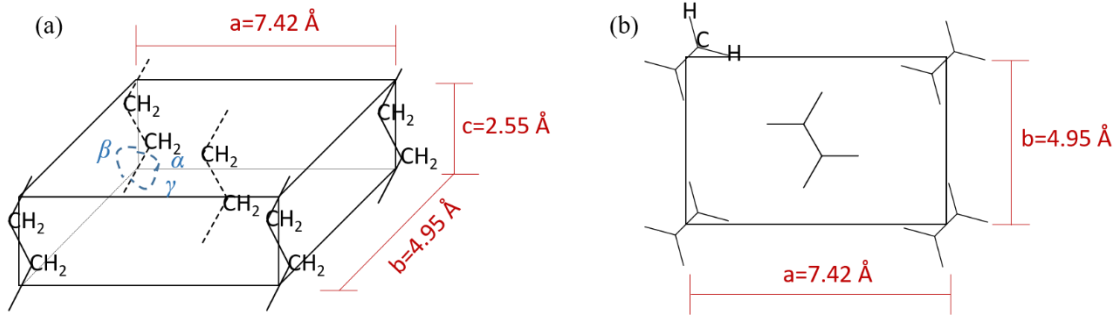


**Figure 3.2:** Polyethylene orthorhombic crystal (a) orthogonal view and (b) a view along the  $c$  axis (Peacock 2000).

In 1957, a single crystal was independently reported by Keller. The reported a lozenge-shaped single crystal was obtained from a very dilute solution with a thickness of 10 nm and lateral dimensions varying from a few micrometers up to more than 100  $\mu\text{m}$  as seen in Figure 3.3b.

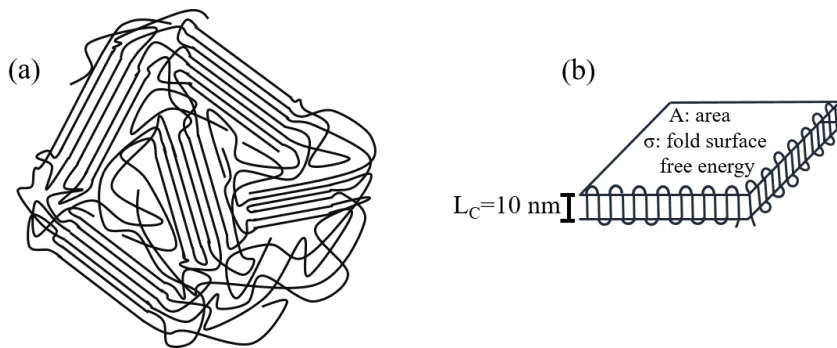


**Figure 3.3:** Simple illustration of two central concepts: (a) fringed micelle model (Keller 1968), (b) a lozenge-shaped single crystal with perfect (regular) chain folding (Gedde and Hedenqvist 2019).

Later developments on the technology for imaging and different etching protocols of polymer surface made it possible to imagine a lamellae and spherulite morphologies that can be seen in Figure 3.4. During the growth of stacked lamellar morphologies, lamellae can be bent, splayed or branched which causing the formation of a spherulite structure. The spherulite consists of bundles of lamellae growth radially from a nucleus with an amorphous phase in between the lamellae. The spherulites grow until the impingement with the neighboring spherulites. The spherulites in thin films of HDPE appear as “Maltese crosses” under an optical microscope. The size of the spherulites can be within a wide range depending on the molecular structure of the polymer and density of the

nucleation. In the case of a high concentration of nucleation, spherulites can not grow due to the limited space. Therefore, a multitude of lamellar bundles is generated under this circumstance. These bundles are called sheaves due to their similarity to wheat sheaves. Another entity is a stack of lamellae which takes place when higher molecular weight PE chains align parallel to each other due to oriented melt by application of the high shear rate during crystallization. Such a stack of lamellae is also known as row-nucleated structures or cylindrites. While stacked lamellar morphologies are major growth patterns of polyethylene samples, the isotactic polypropylene sample shows mostly spherulites type morphology. Under the application of elongation stress during crystallization, a shish kebab supermolecular morphology can be generated. The core of the shish kebab structure is consisted of fully extended long PE chains, cylindrites, and kebab part lamellae grow perpendicular to the shish part.

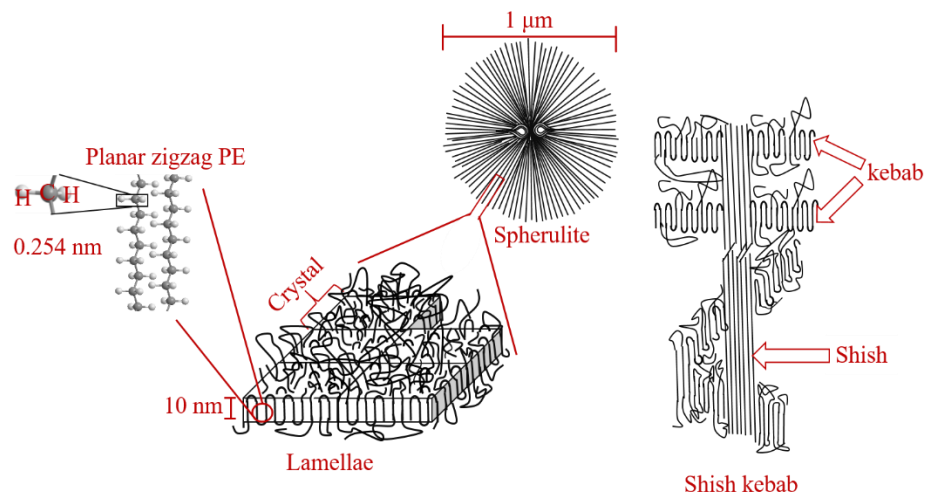


**Figure 3.4:** Multi-scale crystalline structures for polyethylene. Chain folded lamellae stack is constituted by packed crystals as a plate shape. Spherulites are formed as results of the lamellae splays, bends, and branches (Hiemenz and Lodge 2007). Shish kebab morphology consists of extended chains called shish, which act as nuclei and lamellae called kebab part grow on shish. Shish kebab morphology can be generated by conducted elongation flow during crystallization.

The crystallization process can be explained by thermodynamics, which is the subject of the next section. In the next section, the theory of the relation between the microscopic structure to the macroscopic parameters is explained.

### 3.1 Thermodynamics of Polymer Crystallization

In this section, theoretical concepts on polymer crystallization are explained by using the following sources: Keller (1968); Gedde (1995); Peacock (2000); Bower (2002); Muthukumar (2004); Hiemenz and Lodge (2007); Piorkowska and Rutledge (2013).

Thermodynamic fundamental principles enable the possibility to compare theoretical predictions with experiments, e.g., the change of lamellar thickness with supercooling. Crystallization of polymers is the process where the molten disordered state changes to the ordered stable crystalline state. During crystallization, the system tries to adopt a state of minimum free energy. At constant pressure, the crystallization process is described thermodynamically by the following equation:

$$\Delta G = \Delta H - T\Delta S \quad (3.1)$$

where  $\Delta G$  is the change of Gibbs free energy,  $\Delta H$  is the change of enthalpy (changes in the internal heat energy),  $T$  indicates the absolute temperature and  $\Delta S$  is the change of entropy. The transformation process from melt state to crystalline states by decreased temperature causes an internal heat release which is larger than the loss of entropy multiplied by the absolute temperature. On the one hand, lowering temperature is the driving force of crystallization thermodynamically. On the other hand, from the kinetic point of the view, it leads to an increase in viscosity, and hence the crystallization process slows down. Therefore, the phase transition mechanism can be described by the equilibrium of both thermodynamic and kinetic factors.

The nature of the crystallization mechanism is based fundamentally on the knowledge of the equilibrium melting temperature  $T_m^0$ , which is extrapolated theoretical temperature for the melting of perfect infinitely thick crystal. This thermodynamic quantity is very important. It gives information about the conformational character of the polymer chain. Additionally, morphological and structural information can be predicted by comparison of the experimentally observed melting temperature and the  $T_m^0$ . Moreover, it is crucial to determine the temperature dependence of the crystal growth rate. At the  $T_m^0$ , the change in the Gibbs free energy  $\Delta G$  per unit mass is zero. Thus, the  $T_m^0$  is given by:

$$T_m^0 = \Delta H / \Delta S \quad (3.2)$$

Combination of Equation 3.1 and Equation 3.2 provides the following,

$$\Delta G = \Delta H(1 - T/T_m^0) \quad (3.3)$$

The change in Gibbs free energy with a temperature drop below  $T_m^0$  to a crystallization temperature  $T_C$  initiates the crystallization. This temperature change is represented as the supercooling  $\Delta T = T_m^0 - T_C$  in the following equation:

$$\Delta G = \Delta H(\Delta T)/T_m^0 \quad (3.4)$$

After being cooled polymer melt to below  $T_m^0$ , polymer chains fold upon themselves to generate a crystal. The dimension of the stable cuboid shape crystal (see Figure 3.5) can be calculated with respecting the minimum specific free energy  $\Delta g^0$  at given volume  $V = L_1L_2L_3$  and the specific surface free energies  $\sigma_i$  with a surface  $i$ :

$$\Delta G = V\Delta g^0 + 2L_1L_2\sigma_3 + 2L_1L_3\sigma_2 + 2L_2L_3\sigma_1 \quad (3.5)$$

$$V = L_1L_2L_3 \rightarrow L_2 = V/L_1L_3 \quad (3.6)$$

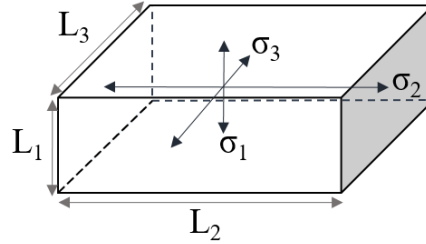


**Figure 3.5:** Equilibrium cuboid shape of crystal with three different surfaces ( $i = 1, 2, 3$ ) with specific surface free energies  $\sigma_i$  (Gedde 1995).

Equation 3.6 is inserted to Equation 3.5:

$$\Delta G = V\Delta g^0 + \frac{2V}{L_3}\sigma_3 + 2L_1L_3\sigma_2 + \frac{2V}{L_1}\sigma_1 \quad (3.7)$$

The derivatives of  $\Delta G$  with respect to  $L_1$  and  $L_3$  is set to zero:

$$\frac{\partial(\Delta G)}{\partial L_1} = L_3\sigma_2 - \frac{V}{L_1^2}\sigma_1 = 0 \rightarrow \frac{L_1}{\sigma_1} = \frac{L_2}{\sigma_2} \quad (3.8)$$

$$\frac{\partial(\Delta G)}{\partial L_3} = L_1\sigma_2 - \frac{V}{L_3^2}\sigma_3 = 0 \rightarrow \frac{L_2}{\sigma_2} = \frac{L_3}{\sigma_3} \quad (3.9)$$

And the combination of Equation 3.8 and Equation 3.9 gives:

$$\frac{L_1}{\sigma_1} = \frac{L_2}{\sigma_2} = \frac{L_3}{\sigma_3} \quad (3.10)$$

Equation 3.10 shows the existence of the proportion between the dimension and the surface free energies. For instance, the equilibrium proportion of the specific surface energy of the fold surface to the specific energy of the lateral surface is close to seven for polyethylene (Gedde 1995). Additionally, the thickness of the formed crystal  $L_c$  related with the fold surface energy  $\sigma_e$  and the supercooling  $\Delta T$ . This important relation is explained by the Thompson-Gibbs equation. The change in free energy is equal to zero at the equilibrium melting point as following:

$$\Delta G = \Delta G^* + \sum_{i=1}^n A_i \sigma_i = 0 \rightarrow \Delta G^* = -\sum_{i=1}^n A_i \sigma_i \quad (3.11)$$

where  $\Delta G^*$  is the surface-independent change in free energy with an area of the formed crystal surface  $A_i$ . The two-fold surface of the lamellae shaped polymer crystal as shown in Figure 3.3 constitutes almost the total surface energy due to the need for high energy for folding chains. Thus, the surface energy per unit area is much higher compared to lateral surface energies:

$$\sum_{i=1}^n A_i \sigma_i \approx 2A\sigma \quad (3.12)$$

The surface-independent term is equal to:

$$\Delta G^* = \Delta g^0 A L_c \rho_c \quad (3.13)$$

where  $\rho_c$  is the density of the crystalline region. The specific bulk free energy change  $\Delta g^0$  could be expressed similarly Equation 3.4 based on specific  $\Delta h^0$  and  $\Delta s^0$  per unit mass:

$$\Delta g^0 = \Delta h^0 - T_m \Delta s^0 = \Delta h^0 \left( \frac{T_m^0 - T_m}{T_m^0} \right) \quad (3.14)$$

The insertion of Equation 3.14 into Equation 3.13 gives the following equation:

$$\Delta G^* = \Delta h^0 (T_m^0 - T_m) \frac{A L_c \rho_c}{T_m^0} \quad (3.15)$$

Consequently, Equation 3.15 and Equation 3.12 is inserted into Equation 3.11 as follows:

$$\Delta h^0 (T_m^0 - T_m) \frac{A L_c \rho_c}{T_m^0} = 2A\sigma T_m^0 \quad (3.16)$$

$$T_m^0 - T_m = \frac{2\sigma T_m^0}{L_c \rho_c \Delta h^0} \quad (3.17)$$

The resulting simplified Equation 3.18 is known as Thompson-Gibbs equation:

$$T_m = T_m^0 \left( 1 - \frac{2\sigma}{L_c \rho_c \Delta h^0} \right) \quad (3.18)$$

where the nominal melting point  $T_m$  for the crystal is solely depends on the crystal thickness  $L_c$ . There is a strong relationship between the thickness ( $L_c^*$ ) of the first formed crystal and the degree of supercooling that can be explained as:

$$L_c^* = \frac{C_1}{\Delta T} + C_2 \quad (3.19)$$

where  $C_1$  and  $C_2$  are constants. Thus, the thickness of the first crystal is controlled only by supercooling, and the thickening rate depends on the absolute crystallization temperature  $T_C$ . The dependence of the growth rate of a crystal at chosen  $T_C$  can be predicted by developed models explained in the next section.

## 3.2 Quiescent crystallization

The nucleation and the growth processes depend strongly on the temperature difference between the  $T_m^0$  and  $T_C$ . The maximum crystallization  $T_{C,max}$  is a temperature at which a crystal grows with a maximum rate. Another characteristic temperature is the glass transition temperature  $T_g$ . Empirical rules exist between these characteristic temperatures of polymer samples (Okui 1990). For instance, the proportion of  $T_m^0/T_g$  (in  $K$ ) known as Boyer-Beaman rule was found as an average value about 1.5 for all polymers (van Krevelen and te Nijenhuis 2009). This proportion for linear PE was reported as 2.18 (van Krevelen and te Nijenhuis 2009). Additionally, a similar relationship was found for  $T_{C,max}/T_g = 1.25-1.33$  (Okui 1990). Based on the aforementioned empirical relationship between  $T_m^0$ ,  $T_{C,max}$ , and  $T_g$ , the  $T_{C,max}$  arises in the middle of the  $T_m^0$  and the  $T_g$ , and hence  $T_{C,max} \sim (T_m^0 + T_g) / 2$  (Okui 1990).

Crystallization process starts when the isotropic polymer melt cooled below the  $T_m^0$ . Then, crystallization involves two stages, which are called the primary and secondary crystallization. Primary crystallization includes the initial, rapid and dominated crystallization stage. Nuclei form and start growing radially during the primary crystallization stage. When the spherulites impinge on each other, the crystallization rate decreases. Hereby, secondary crystallization is the slower stage of the polymer crystallization. It involves the crystal thickening of the already formed crystals behind the crystal front and the formation of the subsidiary crystal. These stages should not be confused with the primary and the secondary nucleation steps which are mentioned in the next section (see Section 3.2.1).

In the following sections, the fundamentals of the nucleation theory and crystal growth theories are explained. The mentioned theories of nucleation and crystal growth mechanisms are assumed under ambient pressure conditions. Additionally, the Avrami model is presented as a method for the kinetic analysis of isothermal crystallization.

### **3.2.1 Nucleation theory**

In the nucleation the stage, a new independent crystal (nuclei) forms. This stage is also known specifically as primary nucleation. Further secondary and tertiary nucleation steps lead to crystallite growth (see Section 3.2.2) by the addition of the chain stems to the surface of the nuclei or growing crystal.

In the primary nucleation stage, a crystalline nucleus forms by compilation of unit cells in a cooled polymer melt below the equilibrium melting point. Primary nucleation is classified into three categories as homogenous, heterogeneous and self-nucleation. Spontaneous formation of the nuclei is called homogeneous nucleation. Homogeneous nucleation occurs under large supercooling conditions. It is also possible to observe homogeneous nucleation when the sample is a thin film by fast quenching, or droplets too small to contain the heterogeneities. Alternatively, nuclei can appear on the surface of some heterogeneities (impurities or nucleating agents), within the disordered phase of polymer. This type of nucleation is termed heterogeneous nucleation. In the heterogeneous nucleation process, heterogeneities act as preexisting nuclei. If this preexisting nucleus is a polymer crystal, that was not completely molten under heated

condition, the type of nucleation is called self-nucleation. Heterogeneous nucleation is the most common nucleation process during polymer crystallization from the bulk melt. This is mainly because the commercial polymers contain additives, and it is also hard to prevent the presence of foreign contaminating particles in polymer melts.

Nucleation and diffusion occur in crystallization simultaneously. Molecules, which are close to the critical size boundary of a new lattice, are diffused to form a stable nucleus. While diffusion is faster for short-range at higher temperatures, there is no dominant diffusion below the glass transition. The nucleation rate  $I$  to obtain a stable nucleus can be explained by Arrhenius type dependency towards  $T_C$  (Fisher *et al.* 1948; Piorkowska and Rutledge 2013; Frenkel 1946):

$$I = I_0 \exp\left(-\frac{\Delta G^*}{kT_C}\right) \quad (3.20)$$

where  $I_0$  is the prefactor,  $\Delta G^*$  is activation free energy required for a stable nucleus generation,  $k$  is Boltzmann's constant. The prefactor  $I_0$  is described by the following with the contribution of the temperature dependence of particle transport;

$$I_0 = N \left(\frac{kT_C}{h}\right) \exp\left(-\frac{E_D}{kT_C}\right) \quad (3.21)$$

where  $N$  is the number of stems,  $h$  is Planck's constant, and  $E_D$  is the activation free energy for the short-range diffusion of molecules. Combination of Equation 3.20 and Equation 3.21 gives the following:

$$I = \left(\frac{NkT_C}{h}\right) \exp\left(-\frac{(E_D + \Delta G^*)}{kT_C}\right) \quad (3.22)$$

For cuboid shape crystal, the free energy barrier  $\Delta G^*$  was already provided by Equation 3.7 based on the surface to volume ratio of the growing crystal. The following equations describe the free energy barrier formation of spherical and cylinder-shaped nuclei:

$$\text{Spheres: } \Delta G^* = \frac{4\pi(r^*)^3}{3} \Delta g^0 + 4\pi(r^*)^2 \sigma \quad (3.23)$$

$$\text{Cylinder: } \Delta G^* = \pi(r^*)^2 l \Delta g^0 + 2\pi r^* l \sigma_s + 2\pi(r^*)^2 \sigma_e \quad (3.24)$$

where  $\sigma_i$  is the specific surface free energy of surface  $i$  with the radius  $r^*$  and the length  $l$ , and the  $\Delta g^0$  is the specific Gibbs free energy difference. The expression of  $\Delta G^*$  can also be expressed as a function supercooling  $\Delta T$  (Yi *et al.* 2013; Gedde 1995):

$$\text{Spheres: } \Delta G^* = \frac{16\pi\sigma^3(T_m^0)^2}{3(\Delta h^0)^2(\Delta T)^2} \quad (3.25)$$

$$\text{Cylinders: } \Delta G^* = \frac{8\pi\sigma_s^2\sigma_e(T_m^0)^2}{(\Delta h^0)^2(\Delta T)^2} \quad (3.26)$$

$$\text{Cuboids: } \Delta G^* = \frac{32\sigma_s^2\sigma_e(T_m^0)^2}{(\Delta h^0)^2(\Delta T)^2} \quad (3.27)$$

Equation 3.27 describes  $\Delta G^*$  for homogeneous nucleation. The activation free energy barrier  $\Delta G^*$  decreases with an increased supercooling  $\Delta T$  due to the inverse relationship:  $\Delta G^* \sim \frac{1}{(\Delta T)^2}$ . Consequently, the thermodynamic driving force is stronger at the lower  $T_C$  that leads to more nuclei with smaller critical nucleus sizes. When nuclei reach their critical size, they become stable and can grow.

### 3.2.2 Crystal growth mechanism

The temperature dependence of the growth rate of newly formed crystals of thickness  $L_c^*$  can be explained by the kinetic theories of crystal growth. The kinetics theories of crystal growth are divided into two types as enthalpic nucleation and entropic nucleation theories. An early theory for the growth of polymer crystals was introduced by Lauritzen and Hoffman in 1960. They assumed the required free energy of nuclei formation and the number of formed new nuclei have an enthalpic origin. In the Lauritzen-Hoffman (LH) theory, lamellae have a thickness as  $L_c^*$  and width as  $L_p$  as seen in Figure 3.6a. The lamellae grow as a function of the degree of supercooling  $\Delta T$  with a constant growth rate radially  $G$ , and lateral spreading rate  $g$  (Gedde 1995; Reiter and Strobl 2007; Bower 2002). A single stem with a thickness  $b$  along the radial growth direction attaches to the lamellae with chain folding to form secondary nuclei. For the attachment of the new stem, the necessary free energy barrier  $\Delta G^*$  must be crossed for the addition of a single stem, which adds surface to the lamellae. The crystal growth with formed nuclei (attached and detached stems) on the preexisting surface (secondary nucleation) is illustrated in Figure

3.7a. The free energy change with formed nuclei (stems) amount is shown as a chart in the same figure.

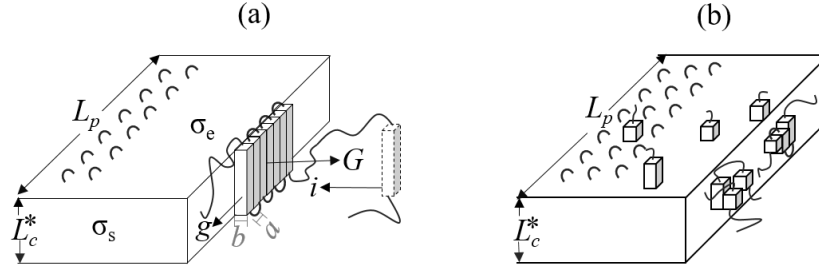


**Figure 3.6:** Illustration of a lamellae growth with thickness as  $L_c^*$  and width as  $L_p$  based on (a) the Lauritzen-Hoffman (LH) theory. The LH theory describes the crystal growth with a growth rate radially  $G$ , lateral spreading rate  $g$ , and nucleation rate  $i$  by attachment of a single stem has a thickness  $b$  and a width  $a$ . (b) Schematic a lamellae growth instantaneously with varying lengths based on the Sadler-Gilmer (SG) theory. Figures are replotted from references: Piorkowska and Rutledge (2013) and Bower (2002).

The LH theory explains the crystallization kinetics of polymers in three regimes depending on the degree of supercooling  $\Delta T$  as depicted in Figure 3.7b. The radial growth rate  $G$  can be expressed based on surface nucleation rate  $i$ , the spreading rate of surface nuclei  $g$  and lamellae width  $L_p$  for different regimes:

$$\text{Regime I: } g \gg i \rightarrow G_I = biL_p \quad (3.28)$$

$$\text{Regime II: } g \approx i \rightarrow G_{II} = b\sqrt{ig} \quad (3.29)$$

$$\text{Regime III: } g \ll i \rightarrow G_{III} = biL_p \quad (3.30)$$

For regime I, the new layer is completed by formed nuclei resulting from the small degree of supercooling  $\Delta T$ . In this instance of  $g \gg i$ , monolayers are formed one at a time, and hence, the radial growth rate  $G_I$  can be described through Equation 3.28. In regime II, multiple nucleations occur, and cause secondary or more layers before the initial layer has been covered under the relatively larger degree of  $\Delta T$  to compare to regime I. In regime II, the lateral growth rate is closer or equal to the nucleation rate  $g \approx i$ . This allows the radial growth rate  $G_{II}$  to be expressed by Equation 3.29. In the case of regime III, many layers consist of prolific multiple nucleations before the layers are fully covered. For this regime,  $\Delta T$  is even larger than the regime II. This means the radial growth rate

$G_{III}$  can be modeled by Equation 3.30 which is the same equation as Regime I. Additionally, the LH theory describes the radial growth rate  $G$  is the inverse function of supercooling:

$$G \approx G_0 \exp\left(-\frac{K_g}{T_c \Delta T}\right) \quad (3.31)$$

where  $K_g$  represents the nucleation constant which depends on the polymer, and  $G_0$  is a pre-exponential factor depending on the segmental flexibility of polymers. Equations for different regimes are derived from Equation 3.31. The radial growth rate  $G$  of the crystal for regime I ( $G_I$ ) can be expressed with a diffusion activation energy  $E_D$  e.g., 24 kJ/mol of  $-\text{CH}_2-$  groups for PE with  $M_{nw} = 70.3$  K (Sperling 2006), as following:

$$G_I = G_{0(I)} \exp\left(-\frac{E_D}{kT_c}\right) \exp\left(-\frac{K_{g(I)}}{T_c \Delta T}\right) \quad (3.32)$$

The regime II and regime III can be explained with similar Equation 3.32:

$$G_{II} = G_{0(II)} \exp\left(-\frac{E_D}{kT_c}\right) \exp\left(-\frac{K_{g(II)}}{T_c \Delta T}\right) \quad (3.33)$$

$$G_{III} = G_{0(III)} \exp\left(-\frac{E_D}{kT_c}\right) \exp\left(-\frac{K_{g(III)}}{T_c \Delta T}\right) \quad (3.34)$$

These three regimes can be identified with a different slope as  $K_{g(I)} = K_{g(III)} = 2K_{g(II)}$  from the plot of  $(\log G)/G_0$  as a function of  $1/(T_c \Delta T)$  (see Figure 3.7b). The nucleation constants can be determined as a function of surface energy terms  $\sigma$  as following:

$$K_{g(I)} = \frac{4b\sigma_e\sigma_s T_m^0}{\Delta h^0 k} = K_{g(III)}, \text{ and } K_{g(II)} = \frac{2b\sigma_e\sigma_s T_m^0}{\Delta h^0 k} \quad (3.35)$$

For instance, the transition points for three regimes were reported as  $\Delta T_{I-II} = 23.8$  °C and  $\Delta T_{II-III} = 15.8$  °C and  $K_{g(II)} = 0.94 \times 10^5$  for PE with  $M_{nw} = 70.3$  K,  $T_m = 144.7$  °C (Sperling 2006).

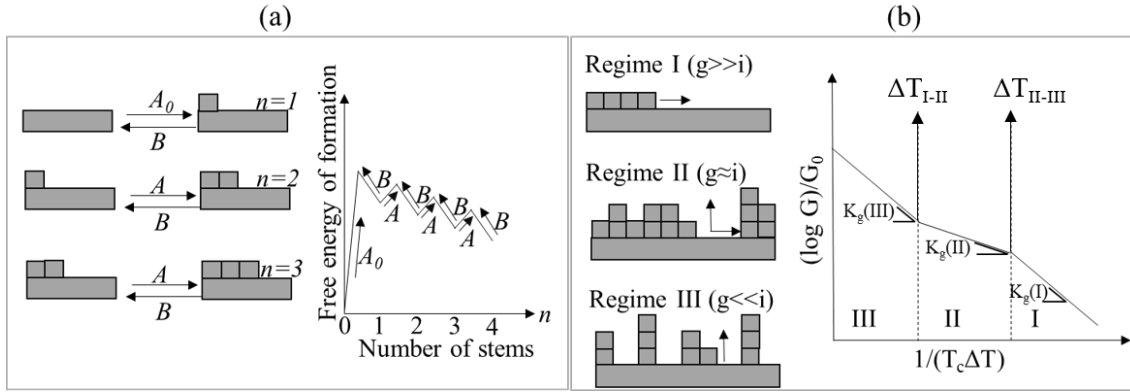


**Figure 3.7:** (a) Illustration of crystal growth with formation nuclei (attached and detached stems) on the preexisting surface (secondary nucleation) and the chart shows the free energy change with formed nuclei (stems) amount. The  $A_0$  is the required free energy for the generation of the first stem. The next steps in the crystal growths with the detachment and attachment of the stem have a lower free energy barrier. (b) Schematic representation of three regimes in LH theory. The growth rate of the complete crystal (lamella) is determined by using the lateral growth rate  $g$  and the surface nucleation rate  $i$  as a function of  $\Delta T$ . These three regimes can be identified with a different slope as  $K_{g(I)} = K_{g(III)} = 2K_{g(II)}$  from the plot of  $(\log G)/G_0$  according to as  $1/(T_c \Delta T)$ . Figures are replotted from reference: Gedde (1995).

An entropic nucleation theory was introduced by Sadler and Gilmer (Sadler 1987; Sadler and Gilmer 1988). In 1983 Sadler revealed the inconsistent nucleation on the crystal surface at low supercooling caused macroscopically rounded and microscopically rough crystal shapes according to the low entropy free energy barrier. Nucleation on the lamellae is instantaneous with existing even incomplete layers, and stems have a varying length that may even be smaller than stable stem length as seen in Figure 3.6b. The Sadler-Gilmer (SG) theory based on basic phenomenological laws as Equation 3.31 and Equation 3.19 as respectively  $G \propto \exp\left(-\frac{K_g}{T_c \Delta T}\right)$  and  $L_c^* = \frac{C_1}{\Delta T} + C_2$ . The concept of crystal growth can be defined in various forms as stem attachment, pinning and/or detachment. Pinning occurs when the crystal growth is obstructed due to the way of chain folds and loops (non-viable chain conformation). The crystal growth continues by the detachment of non-viable chain conformation. In the SG model, the pinning and detachment parts mainly control the crystal growth instead of the free energy barrier to stem attached to the pre-existing surface in LH theory. This forward (attachment)  $k_+$  and backward (detachment)  $k_-$  reactions ratio can be expressed as:

$$\frac{k_-}{k_+} = \exp\left(\frac{2\varepsilon}{kT_m^0} - \frac{m\varepsilon}{kT_C}\right) \quad (3.36)$$

where  $\varepsilon$  is the interaction energy, the number of neighboring sides referred with  $m$ . Monte Carlo computer simulation was used by Sadler and Gilmer to generate the kinetic expression (Sadler and Gilmer 1988; Sadler 1987).

Recently, the mesomorphic layer transition (multistage model) concept was addressed by Strobl to describe the process of growth lamellae as seen in Figure 3.8 (Reiter and Strobl 2007; Strobl 2000, 2009). According to this model, a mesomorphic thin layer forms in the melt. The mesomorphic thin layer thickens spontaneously due to high inner mobility and creates granular crystal. As a final step, granular crystals merge to reduce the excess energy of the folded surface to stabilize, and hence, lamellae crystals form. The thermodynamic based development of the multistage model relies on Ostwald's rule of stages. Ostwald's rule of stages states that the nanometer size crystals form into the mesomorphic phase. These nano-crystals are stable, but also energetically close to the disordered state. The system evolves with crystal growth and causes the differences in the surface free energy on macroscopically stable lamellae (Strobl 2006; Keller *et al.* 1994).

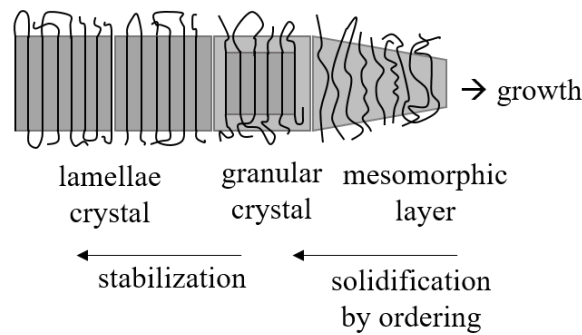


**Figure 3.8:** Multistage crystal growth model (Strobl 2006; Strobl 2009, 2000). The polymer chains are formed into a thin layer called a mesomorphic layer. The thickening of the mesomorphic layer spontaneously causes the solidification and generates the granular crystal structure. The stabilization occurs with the merging of granular crystal blocks to reduce the excess energy of the folded surface. Figure is replotted from references: Strobl 2000; 2006; 2009.

Based on the multi-stage polymer crystal growth, a thermodynamic scheme is constructed as seen in Figure 3.9a to describe crystallization, recrystallization and melting line. Crystallization and melting are controlled by different laws, which means they are not reverse processes. The equilibrium crystallization temperature  $T_C^0$  and the equilibrium

melting temperature  $T_m^0$  are determined by linear extrapolation of the straight melting and crystallization lines to  $1/L_c = 0$ . The relation between temperature and thickness of crystal can simply be explained by the crystallization line in Figure 3.9a, and as given by:

$$L_c = \frac{C_c}{T_c^0 - T} \quad (3.37)$$

where  $C_c$  is constant. The  $T_c^0$  is higher than  $T_m^0$ . Therefore, the existence of a transient mesomorphic phase is indicated by the difference between  $T_c^0$  and  $T_m^0$ .

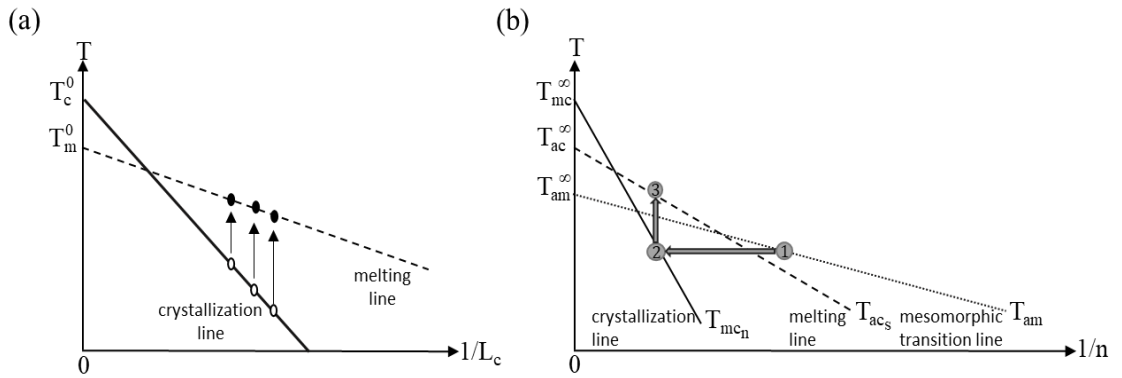


**Figure 3.9:** (a) The linear dependencies in between temperature and the inverse crystal thickness for crystallization and melting line in a multi-stage crystallization model. Here, the equilibrium crystallization temperature  $T_c^0$  is higher than the equilibrium melting temperature  $T_m^0$ , and this difference shows existence of a transient mesomorphic phase. (b) Relationship between the temperature ( $T$ ) and the inverse of the number of structural units in stem ( $1/n$ ) in multi-stage crystallization model in which labels are as following: (a) amorphous melt, mesomorphic ( $m$ ), native crystals ( $c_n$ ), and stable crystals ( $c_s$ ) for multistage crystallization model. The three lines indicate the limits as following: melting line ( $T_{ac_s}^\infty = T_m^0$ ), the crystallization line ( $T_{mc}^\infty = T_c^0$ ), the mesomorphic structure line ( $T_{am}^\infty = T_{zg}$ ). For instance, of isothermal crystallization, the route is numbered starting from one and end at number three and direction showed with a grey color arrow lines. The charts are replotted from references: Strobl 2006; 2009.

Additionally, the temperature dependence of inverse of the number of structural units in the stem,  $n = L_c / \Delta z$  with  $\Delta z$  the length per structure unit diagram can be seen in Figure 3.9b. This diagram based on four different phases: the melt, mesomorphic layer, native crystals (labeled  $c_n$ ) and stabilized crystals (labeled  $c_s$ ). This model lies on three lines, melting line ( $T_{ac_s}^\infty = T_m^0$ ) is named as  $T_{ac_s}^\infty$ , the crystallization line ( $T_{mc}^\infty = T_c^0$ ) is represented by  $T_{mc_n}^\infty$ , and mesomorphic structure is limited by the line called  $T_{am}^\infty$ . The mesomorphic phase does not exist above the mesomorphic phase line. There is zero-

growth at the exact temperature  $T_{am}^\infty$  which is also called as  $T_{zg}$ , ( $T_{am}^\infty = T_{zg}$ ). The ordering of the limiting temperatures as following:

$$T_{am}^\infty = T_{zg} < T_{acs}^\infty = T_m^0 < T_{mc}^\infty = T_C^0 \quad (3.38)$$

These transition temperatures are thermodynamically related as follows:

$$\frac{\Delta h_{ma}}{\Delta h_{ca}} = \frac{\Delta s_{ma} T_{am}^\infty}{\Delta s_{ca} T_{ac}^\infty} \approx \frac{(T_{mc}^\infty - T_{ac}^\infty) T_{am}^\infty}{(T_{mc}^\infty - T_{am}^\infty) T_{ac}^\infty} \quad (3.39)$$

where the entropy changes during melting of the mesomorphic  $\Delta s_{ma} = s_a - s_m$  and crystalline phase  $\Delta s_{ca} = s_a - s_c$  (Strobl 2009; Strobl and Cho 2007; Strobl 2006). According to the study of Strobl and Cho (2007) extrapolated temperature values for linear PE was found as  $T_{am}^\infty = 132.5$  °C,  $T_{acs}^\infty = 144$  °C,  $T_{mc}^\infty = 154$  °C.

### 3.2.3 Crystallization kinetics

The Avrami model describes the crystallinity as a function of time under isothermal condition. This model is commonly used to analyze the crystallization kinetics for any type of solidification (crystallization) process (Strobl 2006, 2007; Banks and Sharples 1963; Avrami 1939, 1940; Hiemenz and Lodge 2007; Gedde 1999) under heterogeneous nucleation with some assumptions. The assumptions are (1) spherical growth in three dimensions, (2) the beginning of the nucleation is simultaneous and positioning of the crystals are random, and (3) radially crystal growth with a constant velocity. The illustration of the fundamental idea of the Avrami model can be seen in Figure 3.10. This illustration is based on the idea of falling raindrops in a puddle creates circles of waves that expand and intersect, covering the whole surface. The probability of the expanding waves to touch arbitrarily chosen point  $P$  is derived as an equation by Poisson. The points of the impact of the raindrops are implied the nuclei, and growing spherules are indicated as waves in this model. All nuclei are distributed randomly and grow radially. The probability  $p_x$  that a point  $P$  intersect by  $x$  fronts of growing crystals (spherulites) can be explained by Poisson distribution (Gedde 1995; Hiemenz and Lodge 2007; Gedde and Hedenqvist 2019):

$$p(x) = \frac{\exp(-S) S^x}{x!} \quad (3.40)$$

where  $S$  is the average number of the spherulite fronts passing the point  $P$ . The probability of the no fronts crosses the point  $P$  when the polymer is still molten can be given by:

$$p(0) = \exp(-S) = 1 - \left(\frac{v_c}{v_{c\infty}}\right) \quad (3.41)$$

where  $v_c$  represents the volume fraction of spherulites and the final reached volume crystallinity  $v_{c\infty}$ . The spherulites are growing radially with a constant rate  $\dot{r}$  during time  $t$ . The average number of the fronts crossing  $P$  is given by:

$$S(t) = \frac{4}{3}\pi(\dot{r}t)^3g \quad (3.42)$$

where  $g$  is the volume concentration of the nuclei. The combination of Equation 3.41 and 3.42 is given as:

$$1 - \left(\frac{v_c}{v_{c\infty}}\right) = \exp\left(\frac{4}{3}\pi(\dot{r}t)^3g\right) \quad (3.43)$$

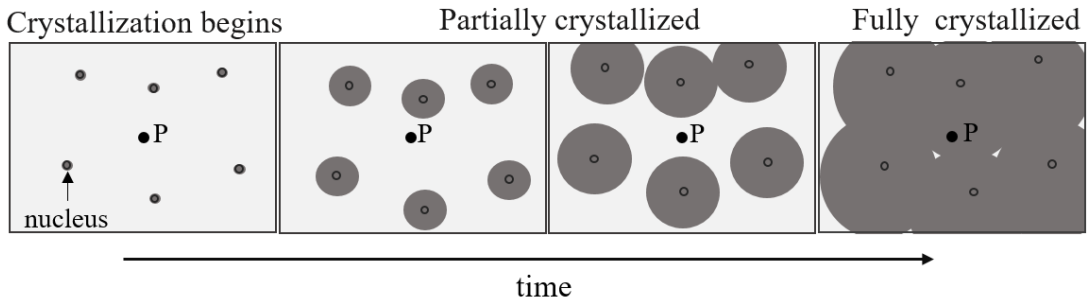


**Figure 3.10:** Snapshots illustrating the circular crystal growth in case of heterogeneous nucleation to describe the fundamental idea of the Avrami model (Gedde and Hedenqvist 2019).

The description of the homogeneous nucleation is slightly more complex. Here, several nuclei appear at a constant rate both in space and time. Under the assumption of three-dimensional growth of the number of spherulites ( $dS$ ) within the spherical shape confined between the radii  $r$  and  $r + dr$  crosses the point  $P$  is described by:

$$d(S) = 4\pi r^2 \left(t - \frac{r}{\dot{r}}\right) l dr \quad (3.44)$$

where  $l$  is the nucleation density. Integration of  $dS$  between 0 and  $\dot{r}t$  gives the total number of spherulites which cross the point  $P$ :

$$S = \int_0^{\dot{r}t} 4\pi r^2 l \left( t - \frac{r}{\dot{r}} \right) dr = \frac{\pi \dot{r}^3 l}{3} t^4 \quad (3.45)$$

Insertion of Equation 3.45 into Equation 3.41 gives:

$$1 - \left( \frac{v_c}{v_{c\infty}} \right) = \exp\left(-\frac{\pi \dot{r}^3 l}{3} t^4\right) \quad (3.46)$$

The volume-related relative crystallinity can be express as  $\varphi_c = v_c / v_{c\infty}$ . Equation 3.43 and 3.46, which are based on different nucleation mode, can be generalized in the same form as the Avrami equation:

$$\varphi_c(t) = 1 - \exp(-(K(t - t_i))^n) = 1 - \exp(-k(t - t_i)^n) \quad (3.47)$$

Where  $\varphi_c(t)$  is the relative crystallinity at the time  $t$ ,  $t_i$  indicates the induction time (required time to observe nuclei),  $K$  (time)<sup>-1</sup> and  $n$  (-) are the Avrami constant and exponent, respectively (Strobl 2006, 2007; Banks and Sharples 1963; Avrami 1939, 1940; Hiemenz and Lodge 2007; Gedde 1999). Crystallinity can be determined by some characterization techniques such as DSC, NMR, and dilatometry as a mass crystallinity  $X_c(t)$  evaluation as a function of time  $t$ , and the achieved final mass crystallinity  $X_c^\infty$ . The relative mass crystallinity  $\frac{X_c}{X_c^\infty}$  can also be described by Equation 3.47 as  $\left(\frac{X_c}{X_c^\infty}\right) = 1 - \exp(-(K(t - t_i))^n)$  which is the general expression of the Avrami model. Additionally, the mass crystallinity can be converted to volume fraction with related the density of crystal  $\rho_c$  and the density of melt  $\rho_a$  ( $\rho_{c,PE} = 1.00$  g/cm<sup>3</sup> for orthorhombic stable form (Silvestre *et al.* 2000),  $\rho_{a,PE} = 0.85$  g/cm<sup>3</sup> (Sperling 2006; Schonhorn and Ryan 1966) as follows:

$$\varphi_c = \frac{X_c}{X_c + \frac{\rho_c}{\rho_a}(1 - X_c)} \quad (3.48)$$

The exponent  $n$  reflects both the dimensionality of the growth and the nucleation mode as tabulated in Table 3.1 under the assumption of constant nucleation rate of heterogeneous ( $n$ ) and homogeneous ( $n + 1$ ) (Sperling 2006). The Avrami approach provides a good fit up to 50% of the final crystallinity that is assumed to be the period of primary crystallization (Piorkowska and Rutledge 2013). The rate of crystallization, the morphology of the sample and overall degree of crystallinity of polymer sample is

affected by many factors such as molecular characteristics of the polymer, temperature, orientation, and additives.

**Table 3.1:** The relation between  $n$  and nucleation mode/crystal growth shape (Sperling 2006).

Crystal growth shape	Nucleation mechanism	Avrami exponent $n$
Rod	Heterogeneous	1
	Homogeneous	2
Disc	Heterogeneous	2
	Homogeneous	3
Sphere	Heterogeneous	3
	Homogeneous	4

### 3.3 Factors Affecting Crystallization

#### *Temperature effect*

Crystallization occurs between glass transition temperature ( $T_g$ ) and the  $T_m^0$  as displayed in Figure 3.11.

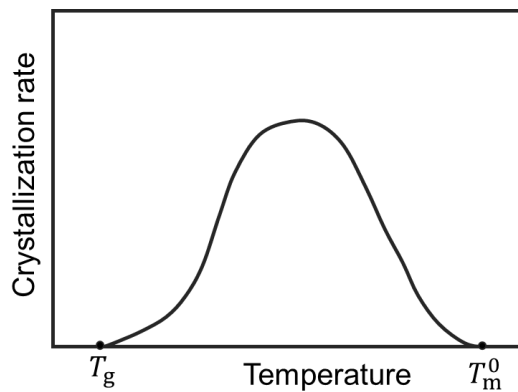


**Figure 3.11:** General curve of crystallization rate as a function of temperature (Gedde 1995).

If a polymer is crystallized by heating above its  $T_g$ , this phenomenon is defined as cold crystallization. In case of a temperature drop below its  $T_m^0$ , it is called crystallization or melt crystallization. A decrease in temperature causes an increase in the viscosity, which inhibits the diffusion of the polymer chain, and hence crystallization is slower. On the other hand, a temperature drop lowers the energy barrier to the formation of stable nuclei.

Thus, the energetic factors accelerate the crystallization process while kinetic factors slower the crystallization with a temperature drop below the melting point of the polymer.

### ***Molecular characteristics and interlamellar connection effects***

The characteristics of the molecules are important to obtain sufficient freedom of movement of the polymer chains for crystallization. Therefore, while the linear segments of PE with sufficient chain length and freedom could crystallize, entanglements and branches are specifically compact in the interlamellar regions or at the interfaces between spherulites. Increasing molecular weight increases the number of entanglement, causing higher viscosity, and thus overall crystallization is slower. Additionally, the PE chain length distribution is also important. The presence of very short non-crystallizable polymer chains increases free volume and the mobility of longer chains in their environs. In the case of applied flow on crystallizing HDPE sample with a broad molecular weight distribution ( $\mathcal{D}$ ), higher molecular weight chains align more than shorter chains (Peacock 2000). Therefore, increasing  $M_w$  with broader  $\mathcal{D}$  makes the PE crystallization process more sensitive to applied flow. Additionally, the broad  $\mathcal{D}$  could cause diverse population lamellae with different thicknesses (Peacock 2000). The broad molecular weight distribution is commercially widespread in the high molecular weight PE due to the easier synthesis and the needs in the industrial applications. The molecular weight effect on the crystallization of PE is smaller than the branching effect. For example, an increase in the average molecular weight ( $M_w$ ) of PE from 60,000 to 3,000,000 caused a dropped at crystallinity from 78% to 52% (Mandelkern 1985; Peacock and Mandelkern 1990). The crystallinity can be decreased even further to less than 50% by the addition of about 1.9 ethyl branches per 100 carbon atoms to the backbone of PE with  $M_w = 104,000$  (Mandelkern 1985; Peacock and Mandelkern 1990).

Another important effect on crystallinity is interlamellar connections between neighboring crystallites. All PE types have covalent links. Covalent interlamellar connections are known as two types: tie chains and entangled loose loops (see Figure 3.1). The interlamellar connection cannot be directly displayed. The general assumption for polymers is the tie chain type connection. The interlamellar connections convey the force between crystallites, hence influencing the mechanical properties of the product such as

ductility, toughness, and the modulus. As a case in the absence of interlamellar connections, PE would be a brittle material with low physical strength.

### ***Orientation effect-Flow induce crystallization (FIC)***

Despite the quiescent crystallization is not being completely understood, crystallization induced by flow or shear (flow-induced crystallization FIC) has been an important subject of research for decades. Interest in flow-induced crystallization comes from orientation, temperature, and pressure, which are common phenomenon within polymer processing technology (injection molding, extrusion, blow molding, etc.). These processing conditions affect the rate of crystallization, the final degree of crystallinity and also the morphology, and consequently final material properties. However, despite a decade of research, the relation between polymer structures, processing conditions and the ultimate properties of the product are not fully understood. This is mainly because the FIC process cannot be simply divided into stages. There are severe interactions between the type of applied flow (e.g., shear, elongation or both), thermal history (e.g., cooling rate and  $T_C$ ), chain relaxation dynamics, nucleation and the growth of polymer crystals.

Previous researches on FIC (Kawai *et al.* 1968; Keller and MacKley 1974; Mackley 1975; Mackley *et al.* 1975; Lagasse and Maxwell 1976; Yeh 1976; Eder and Janeschitz-Kriegl 1988; Eder *et al.* 1990; Eder *et al.* 1992) revealed that the applied shear causes a localized orientation of the polymer chains in the direction of the shear. This localized orientation of chains reduces the energy barrier, and thus the nucleus formation is promoted. Even an applied small shear at higher isothermal crystallization temperature can instantly induce crystallization because of the high mobility of the polymer chain. For instance, Lagasse and Maxwell (1976) mentioned that the ultrahigh molecular weight polyethylene could be crystallized very fast by the application of a small shear at the temperature near the equilibrium melting point. They observed also that the critical shear rate, above which shear flow accelerated crystallization, decreased with either an increase in molecular weight of the sample or a drop in flow temperature as a result of molecular relaxation dynamics of polymeric melt (Lagasse and Maxwell 1976). The important role of the high molecular weight chain in the polymer was emphasized also by the study of Kumaraswamy (2005). Kumaraswamy (2005) reported that a sample with even a very

small fraction of an increased high molecular weight chain showed accelerated crystallization by the applied flow.

The morphology is also affected by the applied flow type and duration. Hill and Keller (1969) showed that the applied stress level on thin PE film influenced the morphology. In their study, the twisted lamellae in spherulitic disks shape were attained under the quiescent crystallization condition (Hill and Keller 1969). Additionally, they noted that high stress enhanced nucleation, and promoted the formation of chain extended PE fibrils (Hill and Keller 1969). Odell *et al.* (1978) and Bashir *et al.* (1986) reported that melt extrusion of PE through a capillary caused an elongational flow-induced high degree of chain orientation along the flow direction. This generated extremely high modulus chain extension (fibrils) with interlocking shish kebab morphology. Furthermore, in the study of Monasse (1995), applied shear under isothermal crystallization conditions accelerated PE crystallization, and promoted anisotropic row nucleation. The polyethylene samples essentially show the stacked lamellar morphologies. It is very common to see the shish kebab morphologies for isotactic polypropylene (iPP) crystallization under shear.

Moreover, the nature of flow is important for understanding the dynamics of polymer molecules under applied flow such as the possible amount of chain orientation. The simple shear flow can be defined with a combination of elongational flow and rotational flow. The explanatory pictures for shear flow were proposed by Smith *et al.* (1999). In this representation, while the pure rotational flow causes only rotation with no deformation, the pure elongational flow with strain rate can be determined as large deformation without any rotation. Thus, it is expected that rotational and elongational components in simple shear flow are equal. Under these conditions, while the extensional flow orient and/or stretch polymer chain state, the rotational flow creates a fluctuation in the extension due to end-over-end tumbling (coiled) of the chain. Therefore, the shear flow is accepted as a weak flow for orientation or stretching compare to elongation.

Thermodynamically, the chain extension is the reason for the drop in polymeric melt entropy which leads to a rise in crystallization temperature and hence causes faster crystallization kinetics. At the  $T_m^0$  is given as  $T_m^0 = \Delta H / \Delta S$  in Equation 3.2. This equation can be represented as the following:

$$T_{m(\text{flow})} = \frac{\Delta H^{\circ}}{\Delta H^{\circ} - T_m^{\circ} \Delta S_{(\text{flow})}} T_m^{\circ} \quad (3.49)$$

where  $^{\circ}$  represents the quiescent condition,  $\Delta H$  is the change of enthalpy (assumed no change underflow) and  $\Delta S_{(\text{flow})}$  is the change in the melting entropy due to flow (Pantani *et al.* 2005). The meaning of Equation 3.49 is that applied flow causes a decrease in entropy which increases the melting temperature for the oriented polymer melt (Flory 1947; Pantani *et al.* 2005). The enhancement of nucleation with the applied flow was described by Kosher and Fulchiron (2002). Kosher and Fulchiron (2002) expressed the total number of nuclei  $N$  as the sum of the observed nuclei in quiescent condition  $N_q$ , and flow-induced nuclei  $N_s$  as following:

$$N = N_q + N_s \quad (3.50)$$

The flow-induced nuclei  $N_s$  were created at a rate proportional to the first normal stress difference  $N_1$  which is a measure of elasticity in the molten phase:

$$\dot{N}_s = C N_1 \quad (3.51)$$

where  $C$  is the constant. Furthermore, Zuidema *et al.* created an advanced model based on the modification of the Eder rate equation (Eder *et al.* 1990) to predict the dynamic of flow-induced nucleation, the amount of oriented structure and morphology changes. Consequently, Zuidema *et al.* (2001) observed applied higher shear rates than the critical shear rate accelerated the nucleation rate, increased rheological relaxation time and caused stronger shish growth for iPP.

In this study, the kinetic model to describe the FIC under isothermal condition was established with a modified Avrami theory equation (Equation 3.47) assuming that the hypothesis of the theory is still valid after shear treatment.

### ***Additive effect-nucleating agent (NA)***

Nucleating agents (NAs) are one of the most used additives in the polymer industry. The NAs are used to controlling the nucleation process during crystallization. The addition of an NA provides the sites and surfaces on which lamellae can grow epitaxially (Binsbergen 1977; Okada *et al.* 2007; Piorkowska and Rutledge 2013; Wittmann and Lotz 1981;

Mercier 1990; Beck 1967). The presence of a foreign surface reduces the free energy of the formation of a critical nucleus, and hence, the crystallization rate is increased (Hoffman *et al.* 2001). The enhancement of the rate of crystallization increases the crystallization temperature  $T_C$  as 20 °C or more for PP, and only 2-5 °C for PE (Tolinski 2015). The NA is considered more effective for iPP compared to PE because of effectively increased  $T_C$ . The nucleation of HDPE has also a great interest in both the industrial and scientific points of the view to modify the physical properties of HDPE. The HPN-20E has a wide range of used commercialized organic NA for PP and HDPE (Dotson 2007; Jiang *et al.* 2012; Tolinski 2015). The used HPN-20E in HDPE has led to improvements in productivity, optimizing barrier and clarity properties, cycle time reduction (Seven *et al.* 2016). It has a non-harmful structure, and hence, possible to use it also in the food PE package market (Seven *et al.* 2016; Jiang *et al.* 2012; Sherman 2014; Tolinski 2015). The HPN-20E is an organic salt based on *cis*-1,2-cyclohexanedicarboxylic acid calcium salt. This commercial NA is sold as a blend that contains one-third of zinc stearate, which has a melting temperature at  $T_m = 120$  °C. The added zinc stearate increases the bulk density of the pure NA and makes the product easier to handle commercially. While the zinc stearate is fully soluble in HDPE, the calcium salt-based part of the NA remains solid in the molten HDPE. A chemical structure and SEM image of the organic salt part of the HPN-20E can be seen in Figure 3.12. It is composed of two parts that are polar and nonpolar. The nonpolar part has close contact with the polymer melt, and it aligns parallel to the layered polymer chains during crystallization (Wittmann and Lotz 1981; Mercier 1990; Seven *et al.* 2016). A polar group increases the cohesion of the salt crystal and makes the NA insoluble in the melt (Wittmann and Lotz 1981; Mercier 1990). For instance, the benzene ring surface of NA interacts with the CH<sub>2</sub> backbone of PE while PE crystallizes through with this interaction (Khanna 1993). Additionally, a rod shape (ruler-like) of the HPN-20E particle allows the polymer crystals to align owing to the process flow dynamics. It has an average particle width of 2.8 μm (Seven *et al.* 2016). The geometrical form, optimum particle size and amount of NA have a strong influence on its effectiveness (Seven *et al.* 2016; Mercier 1990; Beck 1967). The concentration of NA in PE has typically ranged from 0.5 to 5 wt% (Seven *et al.* 2016). The well-dispersed NA-PE blend can be achieved by using a masterbatch blend with using a co-rotating twin-screw extruder.

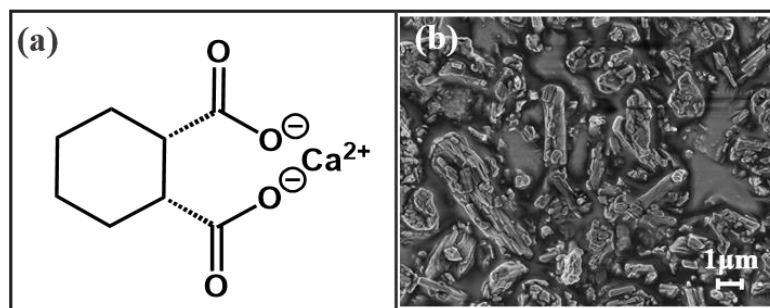


**Figure 3.12:** (a) Structure of calcium salt part of the HPN-20E (*cis*-1,2-cyclohexanedicarboxylic acid) nucleating agent (NA). (b) SEM images of commercially available powder like HPN-20E material.

### ***Nucleating agents (NAs) effect on flow-induced crystallization (FIC)***

Lagasse and Maxwell (1976) showed that the presence of the nucleating agent in the polymer (carbon black-iPP blend and carbon black-ethylene-propylene copolymer) did not significantly affect the shear-induced crystallization kinetics. However, Jerschow and Janeschitz-Kriegl (1997) reported that the addition of NA enhanced the effect of shear on crystallization, and caused the formation of highly oriented (not randomly aligned) surface layers in iPP. Huo *et al.* (2004) observed that a low content of the NA ( $\beta$ -phase) (less than 0.1 wt%) in the iPP increases the formation of the  $\beta$ -phase crystals under applied shear rate  $20 \text{ s}^{-1}$ . But, increased concentrations of NA decreased the  $\beta$ -phase crystallinity with the application of shear. Thus, they considered that the  $\beta$ -phase crystallinity is more dependent on the shear rate.

## 4 Characterization Techniques Principles

### 4.1 Rheology

Rheology is the science of how materials flow and deform as a result of an applied force (Goodwin and Hughes 2000; Osswald and Rudolph 2015). The field of rheology comprehends by the behavior of ideal viscous liquid (Newtonian fluid) and perfectly elastic solid (Hookean solid). Most materials (e.g., polymers) possess both elastic and viscous behavior under deformation and are therefore referred to as viscoelastic. The rheological characterization provides important information about the structure and performance of the materials. In this section, the basic principles of shear rheology are introduced based on the following sources Goodwin and Hughes 2000; Osswald and Rudolph 2015; Rosato and Rosato 2003; Schramm 2000; Dealy and Larson 2006; Shaw 2012; Macosko 1994.

#### 4.1.1 The concept of shear rheology

The concept of simple shear rheology can be explained as in Figure 4.1 by a two-plate model with a material placed between two parallel plates of a distance  $h$ . The upper plate, having an area  $A$ , is moved in one direction by an applied force  $F$  over a distance  $x$ .

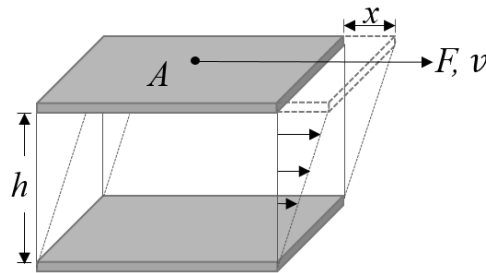


**Figure 4.1:** Two-plate model for the shear experiment. Material is located between two plates in a distance  $h$ . The upper plate with the area  $A$  is moved by the force  $F$  over a distance  $x$ .

The resulting stress (or shear stress)  $\sigma$  is defined as the shear force  $F$  divided by the shear area  $A$  of the plate:

$$\sigma [Pa] = F [N]/A [m^2] \quad (4.1)$$

The applied stress to the material causes a deformation  $\gamma$  (strain) as given by the following equation.

$$\gamma = x [m]/h [m] \quad (4.2)$$

The velocity gradient  $v$ , synonymously the rate of strain or shear rate  $\dot{\gamma}$ , drops at the bottom plate to  $v_{min} = 0$  and it is defined as a time-derivative of the strain  $\gamma$ .

$$\dot{\gamma}[s^{-1}] = d\gamma/dt = v [\frac{m}{s}]/h [m] \quad (4.3)$$

The force  $F$  and the displacement  $x$  can be affected by the type and dimensions of geometry used for the measurements, such as cone-plate, plate-plate or Couette geometry (see Figure 4.2).

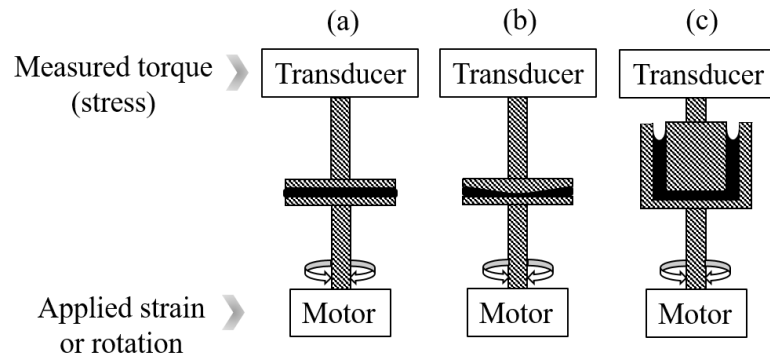


**Figure 4.2:** Schematic illustration of (a) parallel-plate, (b) cone-plate and (c) Couette geometry in a strain-control rheometer. The motor is located at the bottom and applies defined deformation to the sample (the black part in between geometries) via the lower geometry. The torque transducer measures the resulting mechanical response and it is connected to the upper geometry.

There are two instrument set-ups commonly used for shear rheology measurements which are stress-controlled and strain-controlled. In the stress-control instrument, the torque is applied to one plate and the mechanical response is measured as a deformation. The schematic illustration in Figure 4.2 shows a strain-control rheometer design in which the deformation rate is set and the corresponding torque, or stress respectively, is recorded. The cone-plate geometry with a set truncation gap is used to produce a uniform shear rate throughout the sample. The parallel-plate geometry has an adjustable gap height, but it produces an uneven velocity field. The highest shear rate is on the rim and zero at the center. While the cone-plate geometry is a popular tool for investigating non-linear

properties, the parallel-plate geometry is commonly used for measuring the linear properties of the material and for testing boundary effects like a slip. The Couette geometry has a small gap between two cylinders, and the shear rate is constant overall points within the gap. Additionally, it has a higher sensitivity for low-viscosity fluids due to the bigger contact area with samples.

#### 4.1.2 Phenomenological models

The term “viscoelastic” corresponds to a material partially viscous (fluid-like) and partially elastic (solid-like). The viscoelastic behavior of a material can be understood by the introduction of two simple linear constitutive models which are Hooke’s law (see Equation 4.4) for ideal elastic materials and Newton’s law (see Equation 4.7) for viscous materials under a specific case of shear flow.

Ideal elastic behavior can be explained by Hooke’s law as seen in Figure 4.3a. In this model, the stress  $\sigma$  and the strain  $\gamma$  are proportional with a material-dependent proportionality constant  $G$  (shear modulus) as seen in the following equation.

$$\text{Ideal elastic materials: } \sigma = G\gamma \quad (4.4)$$

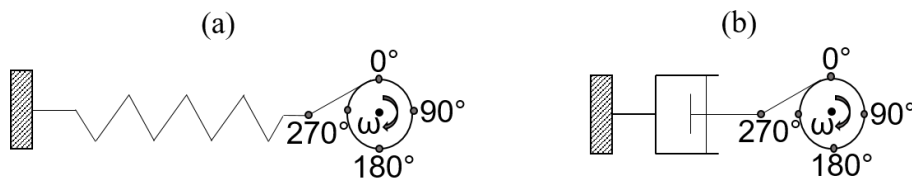


**Figure 4.3:** (a) Hooke’s spring for ideal elastic materials and (b) dash-pot for ideal viscous materials at a constant temperature. A sinusoidal deformation is applied with a rotational movement at a constant angular frequency.

The applied deformation  $\gamma$  is sinusoidal over time  $t$  and the deformation amplitude  $\gamma_0$  and angular frequency  $\omega_1 = 2\pi\nu$  with  $\nu$  being the frequency of strain oscillation:

$$\gamma(t) = \gamma_0 \sin(\omega_1 t) \quad (4.5)$$

Combining Equation 4.4 and Equation 4.5 show the time-dependent stress  $\sigma(t)$ .

$$\sigma(t) = G\gamma_0 \sin(\omega_1 t) \quad (4.6)$$

The ideal viscous material follows Newton's linear dash-pot model (see Figure 4.3b) with proportionality between the stress  $\sigma$  and the shear rate  $\dot{\gamma}$ . The constant of proportionality is the viscosity  $\eta$  as shown in Equation 4.7.

$$\text{Ideal viscous materials: } \sigma = \eta \dot{\gamma} \quad (4.7)$$

The time-dependent shear rate  $\dot{\gamma}$  under oscillatory shear is as follows:

$$\dot{\gamma}(t) = d\gamma/dt = \gamma_0 \omega_1 \cos(\omega_1 t) \quad (4.8)$$

The time-dependent shear stress  $\sigma(t)$  is determined with a combination of Equation 4.7 and Equation 4.8.

$$\sigma(t) = \eta \gamma_0 \omega_1 \cos(\omega_1 t) \quad (4.9)$$

$$\sigma(t) = \eta \gamma_0 \omega_1 \sin(\omega_1 t + \delta), \delta = 90^\circ \quad (4.10)$$

The physical meaning of the Hookean spring is that the applied force is stored as energy in the spring. It returns to its initial state when the mechanical force is removed. On the other hand, the given energy is dissipated in the Newtonian damper, and the damper movements are irreversible.

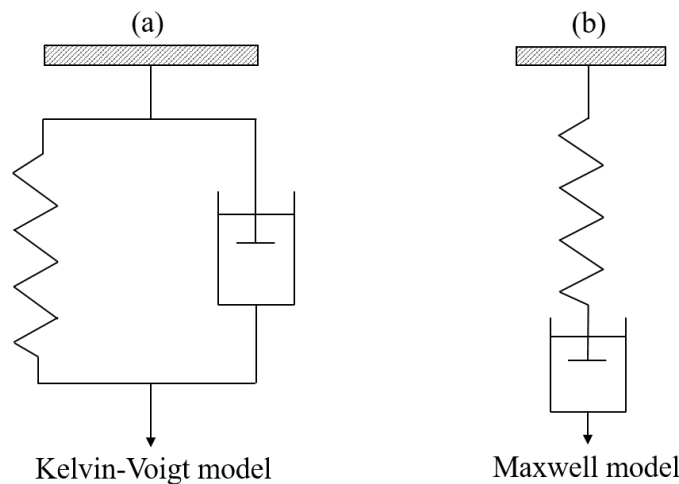


**Figure 4.4:** (a) Kelvin-Voigt model for elastic solids with some viscous part. (b) Maxwell model for viscous liquids with some elastic part.

The aforementioned models are combined in series or parallel to explain viscoelastic behavior most simply. A Kelvin-Voigt model (see Figure 4.4a) is the parallel connection

of the spring and the damper to describe an elastic solid with some viscous part. A Maxwell model (Figure 4.4b) combines the spring and the damper in series to explain viscous liquids with some elastic part.

Linear addition of stress with the Hooke`s law for the elastic part and Newton`s law for the viscous part expresses the total stress of the Kelvin-Voigt model:

$$\sigma = G\gamma + \eta\dot{\gamma} \quad (4.11)$$

However, the stress is equally distributed over all parts of the Maxwell model. Thus, the shear rates are linearly added. Under the assumption of oscillatory shear as follows:

$$\dot{\gamma}(t) = (\dot{\sigma}/G) + (\sigma/\eta) = \gamma_0 \omega_1 \cos(\omega_1 t) \quad (4.12)$$

The relaxation time  $\lambda = \eta/G$  is used to calculate the oscillatory shear stress of the Maxwell model.

$$\sigma(t) = \gamma_0 \left( G \frac{(\omega_1 \lambda)^2}{1 + (\omega_1 \lambda)^2} \sin(\omega_1 t) + G \frac{\omega_1 \lambda}{1 + (\omega_1 \lambda)^2} \cos(\omega_1 t) \right) \quad (4.13)$$

$$\sigma(t) = \gamma_0 (G' \sin(\omega_1 t) + G'' \cos(\omega_1 t)) \quad (4.14)$$

Here, a storage modulus  $G'$  represents the reversible deformation energy (elastic contribution), and a loss modulus  $G''$  measures dissipating deformation energy (viscous contribution). The dissipation factor (loss tangent,  $\tan\delta$ ) is determined by the proportion of the two moduli:

$$\tan\delta = G''/G' \quad (4.15)$$

When the material flows (fluid-like behavior) the loss tangent ( $\tan\delta > 1$ ) is bigger than one. If the loss tangent is smaller than one ( $\tan\delta < 1$ ), the material shows elastic (solid-like) behavior. While in the ideal elastic response the loss tangent is zero ( $\tan\delta = 0$ ), it is equal to infinite for the ideal viscous response ( $\tan\delta = \infty$ ).

Together  $G'$  and  $G''$  results in a complex modulus  $G^*$  which has an imaginary and a real part:

$$G^* = G' + iG'' \quad (4.16)$$

$$|G^*| = \sqrt{(G')^2 + (G'')^2} \quad (4.17)$$

The complex modulus and complex viscosity are related as follows:

$$\eta^* = G^*/i\omega \quad (4.18)$$

The Maxwell model can be extended via parallel connections of many Maxwell elements to explain a material that has a broader distribution of relaxation times. The extended Maxwell model is called as a multiple Maxwell mode in which the storage and the loss moduli can be expressed as follows:

$$G'(\omega) = \sum_{i=1}^n \left[ G_i \frac{(\omega_1 \lambda_i)^2}{1 + (\omega_1 \lambda_i)^2} \right] \quad (4.19)$$

$$G''(\omega) = \sum_{i=1}^n \left[ G_i \frac{\omega_1 \lambda_i}{1 + (\omega_1 \lambda_i)^2} \right] \quad (4.20)$$

### 4.1.3 Linear viscoelasticity

The introduced Maxwell model is used for the characterization of the viscoelastic materials with the dynamic oscillatory shear measurements. The oscillatory shear measurements describe to the material under periodic sinusoidal deformation with a strain amplitude  $\gamma_0$  at an angular frequency  $\omega_1$  as  $\gamma(t) = \gamma_0 \sin(\omega_1 t)$ . The materials response is an oscillating function of stress  $\sigma(t) = \sigma_0 \sin(\omega_1 t + \delta)$  with the amplitude  $\sigma_0$  and a phase angle  $\delta$ . The Maxwell model (see Equation 4.14) is valid only in the linear viscoelastic regime for small-amplitude oscillatory shear (SAOS) flow, where the modulus  $G$  is independent of the applied deformation  $\gamma_0$ . The linear and non-linear viscoelastic behavior regions of the material can be distinguished by a measurement with a set frequency  $\omega_1$  and a varying strain amplitude  $\gamma_0(t)$ . Illustration of the strain dependency test result can be seen in Figure 4.5.

Viscoelastic materials such as polymers have properties that are strongly influenced by the temperature. The temperature dependence of the viscoelastic properties can be

determined in the linear viscoelastic regime by using the William-Landel-Ferry (WLF) equation and the Time-Temperature-Superposition principle (TTS). The TTS principle is used to create a master curve at a reference temperature ( $T_{ref}$ ) in a substantially increased range of times or angular frequency  $\omega_1$ . Shear rheometers could be limited in the angular frequency range for especially higher angular frequencies ( $\omega_1 \geq 100$  rad/s). Hence, the TTS principle provides more information about the molecular structure of the material at a certain reference temperature. This principle depends on the phenomena that the relaxation mechanisms involved in the modulus  $G(t)$  have an equal temperature dependency. The molecular relaxation is accelerated by increasing temperature and this corresponds to a decrease in the time scale of the measurement. The experimental advantages are that time is saved at low frequencies and accessibility to the information at high frequency is obtained. Furthermore, the frequency-dependent measurements are conducted for the same frequency range at different temperatures with the set strain amplitude  $\gamma_0$ , which is chosen in the linear viscoelastic region. This also is of advantage towards material degradation at higher temperatures and temperature-dependent material phases changes like crystallization and the glass transition.

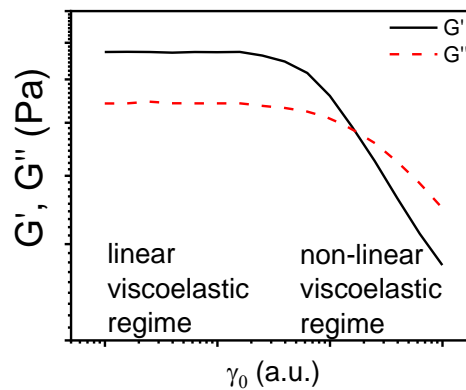


**Figure 4.5:** A strain dependency test of a predominantly elastic material ( $G' > G''$ ). In the linear viscoelastic regime, moduli are independent of applied strain. After the critical strain  $\gamma_0$ , the module  $G$  is dependent to applied strain  $\gamma_0$ , and this regime is called as the non-linear viscoelastic regime.

The master curve is designated by shifting the data horizontally with using a shift factor  $a_T$ . The dependence of the shift factor on the temperature is described by the William-Landel-Ferry (WLF) equation (Williams *et al.* 1955):

$$\log a_T = \frac{-C_1(T-T_{\text{ref}})}{C_2+T-T_{\text{ref}}} \quad (4.21)$$

where  $T$  and  $T_{\text{ref}}$  are the temperatures and the reference temperature respectively,  $C_1$  and  $C_2$  are empirical constants. Empirical constants are similar for dynamically similar materials. The reference  $T_{\text{ref}}$  should be chosen to be in between  $T_g$  (glass transition temperature) and  $T_g + 100$  K.

In Figure 4.6 the shifting process is represented for linear polystyrene ( $M_w = 105$  kg/mol). The reference temperature was chosen as  $T_{\text{ref}} = 160$  °C, and  $a_T = 1$  for the master curve at the  $T_{\text{ref}}$ . The vertical shift  $b_T$  may also be necessary to obtain a smooth master curve. The vertical shift factor depends weakly on temperature and is to set  $b_T = 1$  at the  $T_{\text{ref}}$ . The phenomenon explaining this vertical shift factor is that the relaxation modulus is proportional to the temperature-dependent material density  $\rho$ .

$$G_i(T) = G_i(T_0)T\rho/T_0\rho_0 \quad (4.22)$$

$$b_T = \frac{T_0\rho_0}{T\rho} \quad (4.23)$$

The TTS principle is valid for thermorheologically simple materials. The master curve (see Figure 4.6) shows the characteristic behavior of an entangled, linear, monodisperse polymer (polystyrene). The moduli have the proportionality as  $G' \propto \omega^2$  and  $G'' \propto \omega^1$  that is based on the Maxwell model (see Equation 4.13). The loss modulus ( $G'' \geq G'$ ) is dominant at the low-frequency region, thus this region is called the “flow region”. In the flow region, where  $\omega \ll 1/\lambda_d$ , the complex viscosity  $|\eta^*|$  is independent on the  $\omega$  due to the linear relation between  $G''$  and  $\omega$ . The longest relaxation time ( $\lambda_d = \frac{1}{\omega}$ ) can be calculated by the inverse of  $\omega$  at the crossover of the moduli ( $G' = G''$ ) for monodisperse polymers. The crossover of the moduli provides an indication of the weight average molecular weight ( $M_w$ ) and the dispersity ( $D$ ) of the polymers. The crossover of the moduli is shifted horizontally to the left by increasing  $M_w$  and could be changed vertically to up by narrowing  $D$ . In the range of higher frequencies ( $\omega > 1/\lambda_d$ ), polymer chains can not slip past one another, and the entanglement points act as fixed network connections. As a result, the ability of this temporary polymer network to temporarily

store the applied energy increases that causes a crossover of the moduli. Thus, elastic solid behavior ( $G' \geq G''$ ) is dominant above the crossover frequency of the modulus, hence this regime is called “rubbery plateau”.

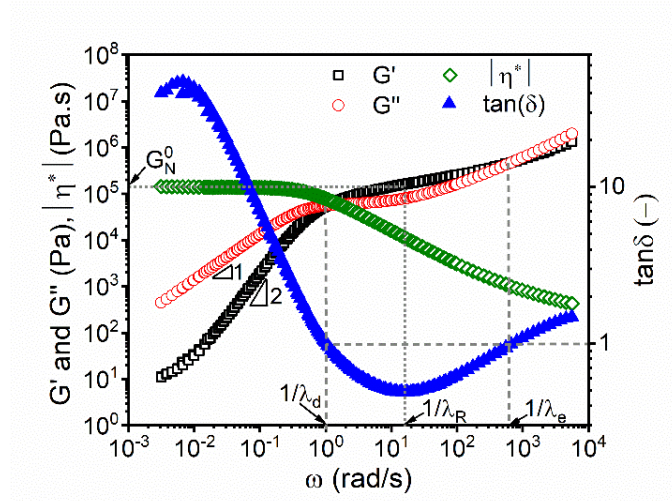


**Figure 4.6:** Master curve, designated via TTS, shows the frequency dependency of the storage ( $G'$ ), loss modulus ( $G''$ ), complex viscosity  $|\eta^*|$  and  $\tan\delta$  (linear polystyrene with  $M_w = 105$  kg/mol,  $T_{ref} = 160$  °C).

The plateau modulus  $G_N^0$  can be extracted from the value of the  $G'(\omega)$  where  $\tan\delta$  has the minimum value. The entanglement molecular weight  $M_e$  can be derived from the  $G_N^0$  with using the universal gas constant  $R$  as follows (Ferry 1980):

$$M_e = \frac{\rho RT}{G_N^0} \quad (4.24)$$

The defined time  $\lambda_R$  in this regime is called as Rouse time, where relaxation along the polymer chain before entanglements come into effect (Rouse-like movements) (Fetters *et al.* 1994). The extension of the plateau region is  $M_w$  dependent. The second moduli crossover at the higher frequencies (or reduced temperatures) is observed at  $\omega = 1 / \lambda_e$ , where  $\lambda_e$  is the entanglement time. This region is called the transition zone and it describes the relaxation process of the chain segments.

#### 4.1.4 Nonlinear viscoelasticity

Previously explained (see Section 4.1.3) the linear viscoelastic behavior is observed under small amplitude oscillatory shear (SAOS) conditions. While the material response is directly proportional to the amplitude of applied deformation in the linear regime, this

simple proportionality is lost in the nonlinear regime. Most of the processing (e.g., blow or injection molding, extrusion) methods imply high deformation or shear rate on the materials and cause a non-linear material response of the material. Therefore, the non-linear rheology is of great interest in both industry and academia. Well-known examples of the nonlinear rheological behavior of material are shear thinning (e.g., pseudoplastic) is a case where the material viscosity decreases with increasing shear strain, and shear-thickening (dilatant fluids), which is simply the opposite of the shear thinning.

The method of Fourier-Transform (FT) has been used (Wilhelm 2002, 1998) for the prediction of nonlinear rheological response of the material under large amplitude oscillatory shear (LAOS). The aperiodic frequency domain material stress response can be quantified by the intensities of the odd harmonics via Fourier transform. The complex function of the Fourier transform is defined as a frequency-dependent signal  $F(\omega_1)$  or time-dependent signal  $f(t)$ , which is reversibly transformed into the frequency dependent signal in the following way:

$$f(t) = \frac{1}{2\pi} \int_{-\infty}^{\infty} F(\omega) e^{i\omega t} d\omega \quad (4.25)$$

$$F(\omega_1) = \int_{-\infty}^{\infty} f(t) e^{-i\omega t} dt \quad (4.26)$$

After the FT analysis, the resulting frequency spectrum consists of monotonically decaying odd harmonics  $I_n$  ( $n = 1, 3, ..$ ). The intensity of the third harmonic  $I_3$  is normalized to the stress response  $I_1$  at the excitation frequency  $\omega_1$  and the corresponding property  $I_{3/1}(\gamma_0, \omega_1)$  is a sensitive quantity towards the mechanical non-linearity of the material (Wilhelm 2002; Cziep *et al.* 2016; Dötsch *et al.* 2003; Hyun *et al.* 2011). This concept can be explained by following mathematical derivation of the equations. As previously mentioned, a Newtonian fluid under a constant shear rate follows Equation 4.7 as  $\sigma = \eta\dot{\gamma}$ . However, when the material is non-Newtonian, the viscosity  $\eta$  is a function of shear rate  $\eta(|\dot{\gamma}|)$  independently in the direction of shear. Therefore, the viscosity can be determined as a polynomial with respect to the absolute shear rate for small shear rates via a Taylor expansion.

$$\eta(|\dot{\gamma}|) = \eta_0 + a_1|\dot{\gamma}| + a_2|\dot{\gamma}|^2 + \dots \quad (4.27)$$

where  $\eta_0, a_1, a_2$  might be complex in oscillatory shear. Alternatively, considering the independence of the shear rate is independent of the applied direction of shear, it is possible to express Equation 4.27 as follows:

$$\eta(\dot{\gamma}) = \eta_0 + a_2 \dot{\gamma}^2 + a_4 \dot{\gamma}^4 + \dots \quad (4.28)$$

The oscillatory strain  $\gamma$  and strain rate  $\dot{\gamma}$  are defined in a simplified notation:

$$\gamma(t) = \gamma_0 e^{i\omega_1 t} \quad (4.29)$$

$$\dot{\gamma}(t) = \gamma_0 \omega_1 i e^{i\omega_1 t} \quad (4.30)$$

The shear stress  $\sigma$  is derived by the insertion of Equation 4.28 in Equation 4.7:

$$\sigma(\dot{\gamma}) = (\eta_0 + a_2 \dot{\gamma}^2 + a_4 \dot{\gamma}^4 + \dots) \dot{\gamma} \quad (4.31)$$

Substitution of the strain rate Equation 4.30 into Equation 4.31 results the shear stress as a function of time:

$$\sigma(t) = (\eta_0 + a_2 \gamma_0^2 \omega_1^2 i^2 e^{i2\omega_1 t} + a_4 \gamma_0^4 \omega_1^4 i^4 e^{i4\omega_1 t} + \dots) \gamma_0 \omega_1 i e^{i\omega_1 t} \quad (4.32)$$

$$\sigma(t) = \underbrace{\eta_0 \gamma_0 \omega_1 i e^{i\omega_1 t}}_{I_1 \alpha \gamma_0 \omega_1} + \underbrace{a_2 \gamma_0^3 \omega_1^3 i^3 e^{i3\omega_1 t}}_{I_3 \alpha \gamma_0^3 \omega_1^3} + \underbrace{a_4 \gamma_0^5 \omega_1^5 i^5 e^{i5\omega_1 t} + \dots}_{I_5 \alpha \gamma_0^5 \omega_1^5} \quad (4.33)$$

The resulting property  $I_{3/1} \propto \gamma_0^2$  shows a quadratic scaling law at low strain amplitudes.

## 4.2 Nuclear magnetic resonance (NMR)

Nuclear magnetic resonance is a powerful characterization technique that is used to observe local magnetic fields around atomic nuclei by excitation of the nuclei of the sample with radio frequency waves in a magnetic field. Rabi *et al.* in 1939 detected nuclear magnetic moments using magnetic resonance absorption of molecular beams, and developments were continued by Bloch *et al.* (Bloch 1946; Bloch *et al.* 1946) and independently by Purcell *et al.* (1946). Today, the versatility of the NMR methods provide profound access to the structure and dynamics of complex molecules in many scientific

fields. In this chapter, the basic NMR interactions and relaxation phenomena are introduced based on the following sources Schmidt-Rohr and Spiess (1994), Bovey and Mirau (1996), Keeler (2010), Haris (1986).

#### 4.2.1 Nuclear spins and magnetization

The atom nucleus consists of a core with protons and neutrons which is positively charged. The nucleus is surrounded by a cloud of electrons which leads to the neutrally charged atom. The nucleus has magnetic properties known as a spin angular momentum or a spin  $I$  when both atomic number and the atomic mass are odd or one of them is odd. The spin properties are defined by using both the atomic number (the number of protons) and the atomic mass (the sum of the protons and neutrons). The spin quantum number  $I$  is zero (no spin and magnetic properties) when the nucleus has even numbers of both protons and neutrons in the nuclei such as carbon  $^{12}\text{C}$  and oxygen  $^{16}\text{O}$ , which cannot be observed via NMR. The typical  $I$  and other NMR properties for some common nuclei are given in Table 4.1. The most common nuclei used in NMR are hydrogen  $^1\text{H}$  and  $^{13}\text{C}$ , which can be found generally in organic molecules. They have a spin of  $\frac{1}{2}$  (i.e.  $I = \frac{1}{2}$ ). If  $I$  of a respective nucleus is not  $\frac{1}{2}$ , the possible different alignments in the presence of the  $\vec{B}_0$  is  $2I + 1$  nuclear spin energy levels e.g.,  $^2\text{H}$  have a spin of 1. In case a nucleus has a  $I > \frac{1}{2}$ , it is called a quadrupolar nucleus. The different energy levels are given by the magnetic nuclear spin quantum number  $\hat{I}_z = m = -I, -I + 1, \dots + I$ .

The charged nucleus rotates about its axis, which generates a magnetic field. Thus, there is a magnetic moment  $\mu$  associated with this angular momentum. The magnetic moment is a vector with both magnitude and direction. The magnitude of the nuclear magnetic moment  $\mu$  is defined by the magnetogyric ratio  $\gamma$  (gyromagnetic ratio) or the ratio of magnetic moment and angular momentum as following:

$$\mu = \gamma \hbar I \quad (4.34)$$

where  $\hbar$  is reduced Planck constant in which  $\hbar$  equals to Planck constant  $h$  divided by  $2\pi$ , and the gyromagnetic ratio  $\gamma$  is characteristic of the nucleus. In absence of an external magnetic field, the distribution of the magnetic moments of all nuclei has an isotropic orientation, and hence, no magnetization.

**Table 4.1:** The NMR properties of some nuclei (Bovey and Mirau 1996).

Nucleus	Abundance (%)	Spin	Relative sensitivity	Gyromagnetic ratio ( $10^7$ rad/Ts)
$^1\text{H}$	99.98	1/2	1.0	26.752
$^{19}\text{F}$	100	1/2	0.83	25.167
$^{29}\text{Si}$	4.7	1/2	0.078	-5.316
$^{13}\text{C}$	1.1	1/2	0.0159	6.726
$^2\text{H}$	0.015	1	0.00964	4.107
$^{15}\text{N}$	0.365	1/2	0.0010	-2.711

**H:** Hydrogen, **F:** Fluorine, **Si:** Silicon, **C:** Carbon, **N:** Nitrogen

When an external magnetic field  $\vec{B}_0$  is applied, the energies of the nuclei are altered which causes the magnetic moment to move in a circular fashion. This motion is called precession and is depicted in Figure 4.8a on an example of a nucleus with a spin of  $\frac{1}{2}$ . The combination of the magnetic field  $\vec{B}_0$  and the magnetic moment  $\vec{\mu}$  generate a force  $\vec{F}$  orthogonal to  $\vec{B}_0$  (y-direction in Figure 4.7). The force  $\vec{F}$  is defined as;

$$\vec{F} = \vec{\mu} \times \vec{B}_0 \quad (4.35)$$

The force is related to the spin via the time derivative, which causes the spin vector to turn in the direction of  $\vec{F}$  as defined by the following equation:

$$\vec{F} = \frac{d}{dt} \vec{I} \quad (4.36)$$

Thus, resulting in precession with magnetization is around  $\vec{B}_0$  direction. This precession occurs with an angular frequency called Larmor frequency  $\omega_L$  (rad/s) which is given by,

$$\omega_L = \gamma \vec{B}_0 \quad (4.37)$$

Two spin states are designated for a spin  $\frac{1}{2}$  nucleus as seen in Figure 4.7a-b. The magnetic moment of the element depends on  $\hat{I}_z$  as here:

$$\mu_z = \gamma \hbar \hat{I}_z \quad (4.38)$$

Thus, resulting in individual energies  $E$  can be calculated by:

$$E_m = -\hat{I}_z \gamma \hbar \vec{B}_0 \quad (4.39)$$

For nuclei with  $I = \frac{1}{2}$ , the energy difference  $\Delta E$  between the spin states (see Figure 4.7b) is a function of the  $\vec{B}_0$  field, called Zeeman interaction, as follows:

$$\Delta E = \gamma \hbar B_0 \quad (4.40)$$

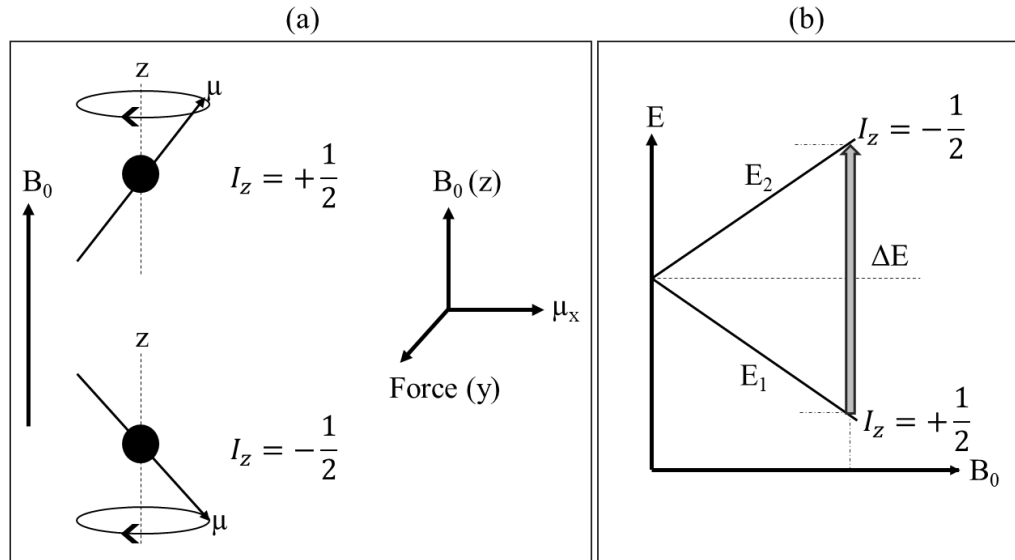


**Figure 4.7:** (a) Interaction between a spinning nucleus and an external magnetic field  $\vec{B}_0$  and precession of nuclear magnetic moments  $\mu$ . The axis set shows xyz-planes (Keeler 2010). (b) The energy splitting as a function of an external magnetic field  $\vec{B}_0$  for nucleus with the magnetic nuclear spin quantum number  $\hat{I}_z = \frac{1}{2}$  (Keeler 2010). This interaction is called Zeeman interaction.

The population of spin states with nuclei  $n$  in  $+z$  direction in the applied magnetic field  $B_0$  is given by Boltzmann's law:

$$\frac{n(+\frac{1}{2})}{n(-\frac{1}{2})} = \exp\left(\frac{-\Delta E}{kT}\right) \quad (4.41)$$

in which  $k$  represent Boltzmann's constant,  $T$  is the absolute temperature in Kelvin ( $K$ ).

The transition between energy levels is related to the Larmor frequency ( $\omega_L = 2\pi\nu_L$ ) by the formula:

$$\Delta E = \hbar\omega_L = \gamma \hbar B_0 = \hbar\nu_L \quad (4.42)$$

where  $\nu_L$  represents the Larmor frequency that is in the megahertz (MHz) range. For instance, a proton in a magnetic field  $B_0$  of 7.05 tesla (T) has a Larmor frequency of  $\nu_L \approx 300$  MHz and the energy difference  $\Delta E$  between the spin states is 0.120 J/mol.

#### 4.2.2 NMR interactions

In this section, the important interactions between the NMR frequencies and molecular parameters with the evolution of the system in time are introduced by the spin Hamiltonians  $\hat{H}$ . The quantum state of a nucleus is characterized by a wave function  $\Psi$ , that contains information about the position, velocity, and spin of a nucleus. The time  $t$  dependence of the wave function is described by the Schrödinger equation:

$$i\hbar \frac{d\Psi(t)}{dt} = \hat{H}\Psi(t) \quad (4.43)$$

where  $\hat{H}$  describes all interactions during the time evolution. The Hamiltonians  $\hat{H}_r$  of a nuclear spin system in a given environment  $r$  can be written:

$$\hat{H}_r = \hat{H}_r^Z + \hat{H}_r^{CS} + \hat{H}_r^D + \hat{H}_r^{RF} + \hat{H}_r^J \quad (4.44)$$

The direct magnetic interaction of a static external magnetic field and nuclear spins is represented as  $\hat{H}_r^Z$ . It is known as Zeeman interaction as in Figure 4.7 schematically demonstrated in for nucleus with a spin of  $\frac{1}{2}$  and resulting from the nucleus resonance at Larmor frequency  $\omega_L$ .

$$\hat{H}_r^Z = -\mu_z B_0 = -\hat{I}_z \gamma \hbar B_0 \quad (4.45)$$

The Hamiltonian  $\hat{H}_r^{CS}$  describes the chemical shift (CS) interaction. The electrons surrounding the nucleus are creating a counter field and it is shielding the nucleus from the static external magnetic field. Thus, the effect of the external magnetic field on the nucleus is changed and a shift relative to the resonance Larmor frequency  $\omega_L$ . The chemical shielding is generally anisotropic due to the sensitivity towards type and geometry of chemical bonds, and hence it is described by the chemical shielding tensor  $\sigma$  such that:

$$\hat{H}_r^{CS} = \gamma \hat{I} \sigma \vec{B}_0 \quad (4.46)$$

The dipole-dipole interaction or more concisely the dipolar coupling is described by the term  $\hat{H}_r^D$ . Each nucleus can be considered as a dipole. Therefore, when more than one nucleus is presented in the system, dipole-dipole interactions can be observed. In the NMR signal, this interaction causes two spectral lines and/or line broadening.

$$\hat{H}_r^D = -\frac{\mu_0 \hbar \gamma_1 \gamma_2}{4\pi r^3} \frac{1}{2} (3 \cos^2 \theta - 1) \{3 \hat{I}_{1z} \hat{I}_{2z} - \hat{I}_1 \hat{I}_2\} \quad (4.47)$$

The gyromagnetic ratios of the two spins are  $\gamma_1$  and  $\gamma_2$ ,  $r$  is the distance between spins, the orientation angle between the spin pair vector is  $\theta$  and the vacuum permeability is represented as  $\mu_0$ .

The direct magnetic interaction of the applied transverse oscillating magnetic field  $B_1$  and nuclear spins is represented in Equation 4.48 as  $\hat{H}_r^{RF}$ . This is also known as radio frequency (RF). Applied RF effects the Larmor precession of nuclei into different angles depending on the strength of the  $B_1$ .

$$\hat{H}_r^{RF} = \omega_1 \hat{I}_{x/y} = -\gamma B_1 \hat{I}_{x/y} \quad (4.48)$$

The indirect magnetic interaction between two nuclear spins, through the involvement of electrons, is known as  $\hat{H}_r^J$ , which is called  $J$ -coupling.

$$\hat{H}_r^J = -2\pi J \hat{I}_1 \hat{I}_2 \quad (4.49)$$

The coupling constant  $J$  is a measure of the interaction between a pair of nuclei.

### 4.2.3 Nuclear relaxation

The application of the radio frequency (RF) pulse flips the nuclei between their energy states via absorption and stimulated emission. This process is called resonance. The application of a static magnetic field  $\vec{B}_0$  changes the magnetic moment. The individual magnetic moments are not able to align with the direction of the applied magnetic field due to the random thermal motion of the molecules. The average alignment of all of the individual magnetic moments is called bulk magnetization. The vector of the bulk magnetization at the thermal equilibrium is of size  $\vec{M}_0$ . This vector precesses about the  $z$ -

axis at an angular frequency  $\omega_L$  and at time  $t$ . The rotation of the vector has an angle as  $\omega_L t$ . The bulk magnetization returns to its thermal equilibrium position with time via a process called relaxation. The bulk magnetization vector along  $z$ -axis and  $xy$ -plane is described by the Bloch equation (Bloch 1946) at  $\omega_L$ :

$$M_x(t) = M_0 \cos(\omega_L t) \exp\left(-\frac{t}{T_2}\right) \quad (4.50)$$

$$M_y(t) = M_0 \sin(\omega_L t) \exp\left(-\frac{t}{T_2}\right) \quad (4.51)$$

$$M_z(t) = M_0 \left[1 - \exp\left(-\frac{t}{T_1}\right)\right] \quad (4.52)$$

where the relaxation along the  $z$ -axis at a rate constant  $1/T_1$ . In the  $xy$ -plane, the relaxation rate constant is  $1/T_2$ . This means that in the  $xy$ -plane decays by spin-spin relaxation ( $T_2$ ), while the  $z$ -axis magnetization reappears by spin-lattice relaxation ( $T_1$ ). Magnetization in both directions, the  $z$ -axis and  $xy$ -plane, decay exponentially in time.

The term lattice describes the atoms in the environment of an ensemble of a nucleus, e.g., solution, which acts as a reservoir of energy in the form of molecular motion. In the spin-lattice also called longitudinal relaxation the excited proton (spin nuclei) transfer the energy to the surrounding lattice by the time constant  $T_1$ . The magnitude of  $T_1$  varies from  $10^{-2}$ - $10^2$  seconds (s) for liquids, much larger values can be observed in solids depending on the nucleus and its environment. The magnetization to return to the equilibrium takes almost  $5 \times T_1$ , which can be calculated from Equation 4.52 e.g.,  $\frac{M_z}{M_0} = 100[1 - \exp(-5)] = 99.3\%$ .

Spin-spin also called transverse relaxation ( $T_2$ ) occurs by exchange of magnetization between the nuclei when the nuclei are precessing at Larmor frequency. If external magnetic field inhomogeneity exists, the relaxation depends on the location of the molecule in the magnet. The corresponding apparent transverse relaxation  $T_2^*$  is consist of contributions of external influences  $T_2^\Delta$ , and of the internal energy transfers (intrinsic transverse relaxation time)  $T_2$  as following;

$$\frac{1}{T_2^*} = \frac{1}{T_2^\Delta} + \frac{1}{T_2} \quad (4.53)$$

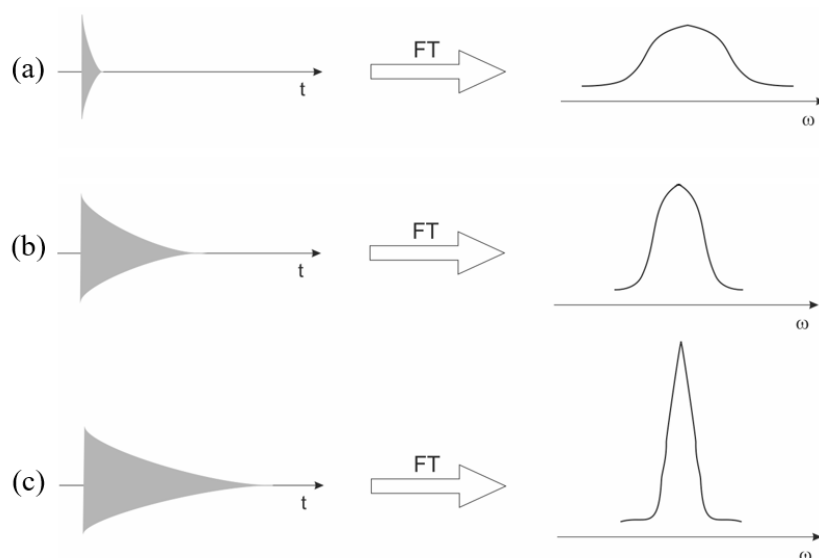


**Figure 4.8:** Illustration of (a) a rapidly dephasing signal as a result of short  $T_2^*$ . Fourier transform (FT) of this spectrum gives a broad frequency-domain signal. (b) The dephasing speed is slower than the example in Figure 4.8a due to longer  $T_2^*$  and hence, result in a narrower frequency-domain peak. (c) The slowly dephasing signal with long  $T_2^*$  and sharp frequency-domain signal.

The transverse relaxation determines the width of the lines in spectra (see Figure 4.8). The field inhomogeneity contribution is dominant for the  $T_2^*$  relaxation of highly mobile samples. The magnetization rapidly dephasing due to the short  $T_2^*$  causes a broadening of the frequency domain peak shape signal. However, the slowly dephasing magnetization because of longer  $T_2^*$  results in a narrower frequency-domain signal. Therefore, observed frequency domain signal has a full-width at half-maximum (FWHM) with inversely proportional to the  $T_2^*$ , i.e.  $\text{FWHM} = 1 / (\pi T_2^*)$ .

Each spin has its magnetic moment and a spin interacts with the applied magnetic field and also with magnetic fields of nearby spins, called the local field  $B_{\text{loc}}$ . The local field changes in magnitude and orientation due to the thermal motion of the molecules, which acts also as a reservoir of the energy. The local fluctuation in the magnetic field due to molecular motion is a source of both relaxations. Thus,  $T_1$  can be identical with  $T_2$  only for rapidly tumbling molecules but other than this  $T_1$  is always longer than  $T_2$ . This molecular motion can be quantified by a rotational correlation time  $\tau_c$  which is the average time for a molecule needed to achieve an orientation one radian away from its

starting point. The time dependence of the random molecular motion can be characterized by the correlation function  $F(\tau)$ .

$$F(\tau) = \exp\left(-\frac{\tau}{\tau_c}\right) \quad (4.54)$$

The Fourier transform of the correlation function gives the spectral density  $J(\omega)$ .

$$F(\tau) \xrightarrow{FT} J(\omega) \quad (4.55)$$

$$J(\omega, \tau_c) = \frac{2\tau_c}{1+\omega^2\tau_c^2} \quad (4.56)$$

The theory of Bloembergen-Purcel-Pound (BPP) shows the proportional relation between the spectral density  $J(\omega)$  and the relaxation rate at Larmor frequency as following (Bloembergen *et al.* 1948):

$$\frac{1}{T_1} \cong (\gamma B_{loc})^2 J(\omega_L) \quad (4.57)$$

The temperature dependence of the correlation time  $\tau_c$  can be obtained through the Arrhenius` theory with the assumption of no phase transition:

$$\tau_c = \tau_0 \exp(-E_a/kT) \quad (4.58)$$

where  $\tau_0$  represents the frequency factor.

The dependence of  $T_1$  and  $T_2$  on  $\tau_c$  is expressed by the BPP model as following:

$$\frac{1}{T_1} = \left(\frac{\mu_0 \hbar}{4\pi}\right)^2 \frac{\gamma^4}{5r^6} I(I+1) [J(\omega_L, \tau_c) + 4J(2\omega_L, \tau_c)] \quad (4.59)$$

$$\frac{1}{T_2} = \left(\frac{\mu_0 \hbar}{4\pi}\right)^2 \frac{\gamma^4}{10r^6} I(I+1) [3J(\Delta\omega, \tau_c) + 5J(\omega_L, \tau_c) + 2J(2\omega_L, \tau_c)] \quad (4.60)$$

where  $\Delta\omega$  represents the interaction angular frequencies and  $r$  is the internuclear distance. Based on this theory,  $T_1$  relaxation is dominant compare to  $T_2$  for magnetic dipolar relaxation.

#### 4.2.4 NMR applications

The pulse sequences in NMR have central importance for the characterization of molecular dynamics and structures of materials. Proton NMR is a commonly used effective technique for the investigation of phase composition in semi-crystalline polymers because the proton spectral information is directly linked to the molecular mobility. Densely packed polymer chains in the crystalline or glassy domain of polymers have limited orientation changes of the proton spin interconnection on the NMR time scale, which causes a strong dipole-dipole interaction. When the semicrystalline polymer has an isotropic structure above the melting temperature, the proton NMR signal is narrow due to slower relaxation times. In contrast, a reduction of the mobile fraction during crystallization leads to shorter relaxation time, and hence broadens the peaks in the NMR spectrum. Since the late 1950s, the crystalline fraction could be estimated by the line shapes of NMR spectral (Fuschillo *et al.* 1957; Slichter and McCall 1957; Wilson and Pake 1953). Later development on pulse sequences such as the free induction decay (FID) (Bridges *et al.* 1979; Kristiansen *et al.* 1999; Kristiansen *et al.* 2001), the magic sandwich echo (MSE) (Rhim *et al.* 1971; Pines *et al.* 1972; Takegoshi and McDowell 1985; Hafner *et al.* 1996) and the Carr-Purcell-Meiboom-Gill pulse sequence (CPMG) (Carr and Purcell 1954; Meiboom and Gill 1958) for obtaining relaxation times, provide information about the degree of crystallinity and enable the analyses of crystallization kinetics. Commonly used pulse excitation experiments to determine  $T_1$  and  $T_2$  relaxations and thus investigate the mobility fractions of semi-crystalline polymers are presented in this section.

##### ***Transverse relaxation $T_2$ experiments***

The free induction decay (FID) (see Figure 4.9a) is a simple and direct way to monitor the  $T_2^*$  relaxation decay following a single  $90^\circ$  or  $\frac{\pi}{2}$  pulse. The bulk magnetization  $\vec{M}_0$  turns from the  $z$ -axis into the  $xy$ -plane with a  $90^\circ$  pulse. The spins begin to relax at unequal rates in the  $xy$ -plane and the signal decays with a time constant  $T_2^*$ . Hahn (1950) proposed a spin-echo method, known also as Hahn echo (see Figure 4.9b), for measuring the  $T_2^*$  relaxation. In this method, an applied  $90^\circ$  pulse is followed by a  $180^\circ$  pulse after a time  $\tau$ , and hence the magnetization flips into the  $y'$ -direction. This  $90_x^\circ - \tau - 180_x^\circ$  sequence is

repeated several times with altering  $\tau$  and  $T_2^*$  is acquired from the observed decay of the intensity of echo. In this method for decaying echo is not only a result of the  $T_2^*$  relaxation but also from a slightly different diffusive flow of magnetization. Therefore, the main disadvantage of this method becomes that a large number of scan is required due to the low sensitivity to obtain good signal-to-noise ratios in the NMR spectra.

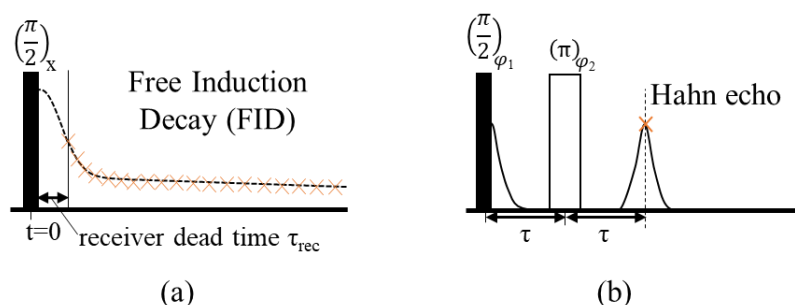


**Figure 4.9:** (a) Representation of a  $90^\circ$  pulse and the resulting free induction decay (FID). (b) The Hahn echo is depicted for measuring the  $T_2^*$  relaxation via variation of  $\tau$ .

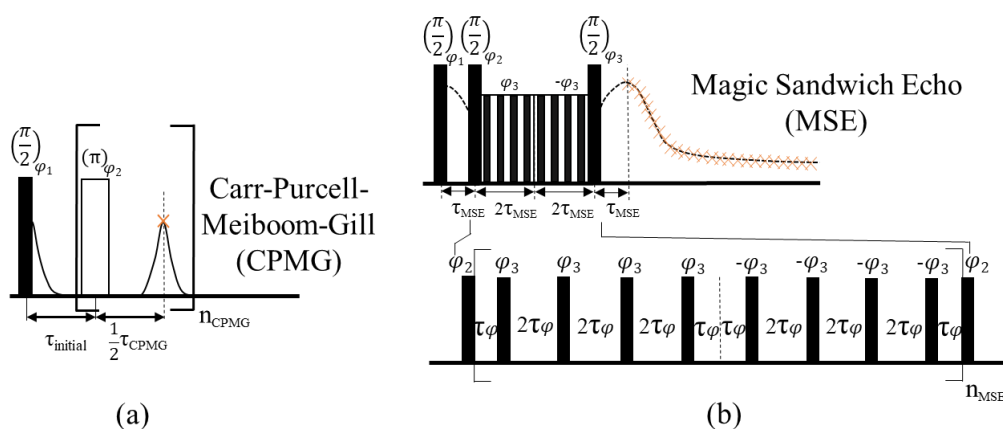


**Figure 4.10:** (a) Illustration of Carr-Purcell-Meiboom-Gill (CPMG) pulse sequence that is used to derive the full  $T_2^*$  relaxation in shorter experimental time compare to Hahn echo. (b) The magic-sandwich echo (MSE) pulse sequence is represented. That provides fast refocusing on decaying signals for solid materials.

Later, the CPMG experiment was developed by Carr and Purcell (1954); Meiboom and Gill (1958) to reduce the effect of diffusion and derived the full  $T_2^*$  relaxation in a shorter experimental time. The CPMG pulse sequence is shown in Figure 4.10a in which a series of  $180^\circ$  pulse is applied with varying  $\tau$  spacing following the  $90^\circ$  pulse. The amplitudes of the CPMG spin-echo train decay exponentially which corresponds to the full  $T_2^*$  relaxation. The full  $T_2^*$  relaxation is analyzed by the height of the each echo signal.

Gullion *et al.* (1990) propounded the idea of removing the chemical shift effect with phase cycles such as MLEV-4, XY-16.

A variety of different techniques tackled the refocused coherences and chemical shift anisotropy problems in the multi-spin system. The magic-sandwich echo (MSE) pulse sequence (Rhim *et al.* 1971) provides fast refocusing on decaying signals for solid materials via strong multiple dipolar coupling, which is done by reversing the dipolar dephasing (Hafner *et al.* 1996). An illustration of the MSE pulse sequence is shown in Figure 4.10b. A main advantage of the MSE over the FID is the overcoming of the signal loss problem at the receiver dead time (Maus *et al.* 2006; Schäler *et al.* 2015). This modified pulse is called mixed MSE which is a combination of the MSE and Hahn echo to refocus the dephasing of the  $T_2^*$  relaxation (Matsui 1991; Fechete *et al.* 2003; Sturniolo and Saalwächter 2011). In this mixed MSE combination sequence, the Hahn echo can be replaced by the CPMG sequence (Ratzsch *et al.* 2017). In this case, while the MSE is used to refocus of the initial transverse magnetization, the purpose of the CPMG sequences is to refocus only the magnetization of the more mobile phase of the sample.

### ***Longitudinal relaxation $T_1$ experiments***

The longitudinal relaxation is commonly measured by the inversion recovery or the saturation recovery. The pulse sequences are depicted in Figure 4.11 and resulting signal intensity as a function of delay time  $\tau$  shown in Figure 4.12. In the inverse recovery method, the magnetization is inverted with the application of a  $180^\circ$  pulse that flips the magnetization to the  $-z$ -axis and the magnetization is allowed to return to the  $+z$ -axis due to the longitudinal relaxation  $T_1$  for a time period  $\tau$ . Then, after a variable time  $\tau$ , a  $90^\circ$  pulse is applied for the detection of the signal into  $xy$ -plane before the magnetization reaches the equilibrium. By varying the  $\tau$ , the magnetization into the  $xy$ -plane is changing, and it allows the monitoring of the return of the magnetization into the  $z$ -axis. Here, long recycle delay time  $\tau_{rd}$  is required, i.e.  $\tau_{rd} > 5 \times T_1$ , for the spins reaching equilibrium, this causes the need for long measurements. Waiting for the spins to recover to equilibrium causes the determination of the wrong  $T_1$  times.

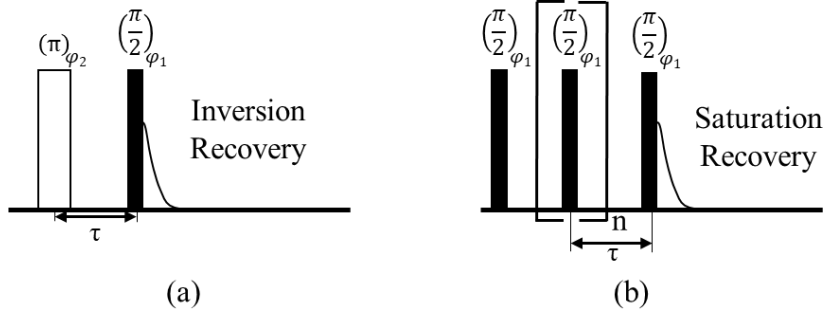


**Figure 4.11:** (a) The inverse recovery pulse sequences and (b) the saturation recovery sequence for measuring the longitudinal relaxation.

The saturation recovery sequence consists of a series of  $90^\circ$  pulses that are rapidly applied. The result in a disintegrated magnetization and after a variable delay  $\tau$  another  $90^\circ$  pulse is applied (McDonald and Leigh 1973). This method is faster than the inversion recovery due to the eliminated length of the long recycle delays.

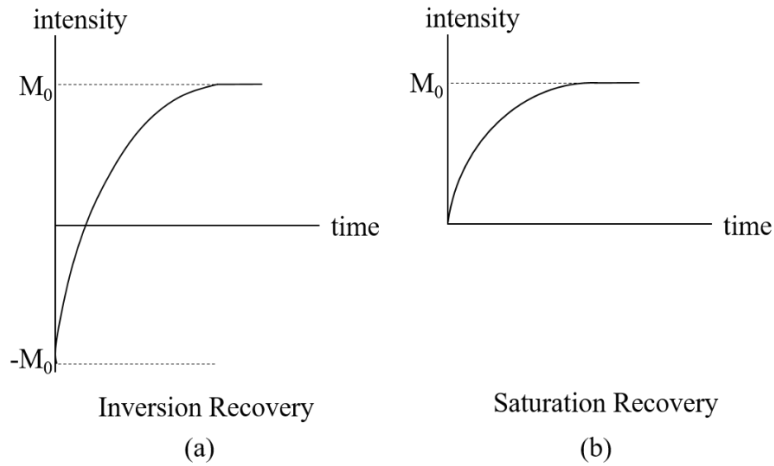


**Figure 4.12:** Illustration plots of signal intensity as a function of delay time  $\tau$  (a) for the inverse recovery pulse sequences and (b) for the saturation recovery sequence for measuring the longitudinal relaxation.

At the end of the inversion recovery experiment, resulting signal intensity is plotted as a function of the  $\tau$ . The resulting curve is fitted to following exponential function to obtain  $T_1$ .

$$M_z(t) = M_0 - 2M_0 e^{-\tau/T_1} \quad (4.61)$$

For the saturation recovery experiment, the dependence of the obtained signals at recovery time  $\tau$  can be described by:

$$M_z(t) = M_0 - M_0 e^{-\tau/T_1} \quad (4.62)$$

Further improvement on the methods has been made by minimizing the experimental uncertainties such as the progressive saturation (Freeman and Hill 1971) and the fast inversion recovery (Canet *et al.* 1975).

### 4.3 Differential scanning calorimetry (DSC)

Differential scanning calorimetry (DSC) is an effective thermal analysis technique for the characterization of the physical properties of a polymer. This technique enables the determination of melting, glass transition, crystallization, and mesomorphic transition temperatures and the corresponding enthalpy (Piorkowska and Rutledge 2013; Wunderlich 1990). A heat flow rate into the sample is monitored as a function of time or temperature with a subtraction of the heat gains and losses of an empty reference pan from the data of the sample. The calibration of the instrument is necessary for the measurement of the heat flow rate and the temperature. Typical standard used materials for calibration are the benzoic acid, indium, anthracene.

A typical DSC thermogram is represented in Figure 4.13 to determine the  $T_C$  and the  $T_m$  of HDPE and enthalpy of fusion of the heating curve. The sample is heated up to 180 °C from 25 °C with a 10 °C/min heating rate. As a result of heating, an endothermic phase transition from solid to molten phase (liquid-like) is observed as a peak. The melting peak maximum shows the  $T_m$ . When the cooling protocol applied to 25 °C with a 10 °C /min cooling rate, an exothermic crystallization peak is observed due to crystallization. This crystallization peak maximum is used to determine  $T_C$ . The measured heat of fusion of the PE sample ( $H_{f,m}$ ) is calculated by the integrated area beneath the melting peak. Then, the mass crystallinity ( $X_C$ ) in percent is calculated by dividing the peak area by the theoretical the heat of fusion of the 100% perfect crystalline PE as  $H_{f,100} = 293$  J/g (Wunderlich 1990) as follows:

$$X_C [\%] = (H_{f,m}/H_{f,100}) * 100 \quad (4.63)$$

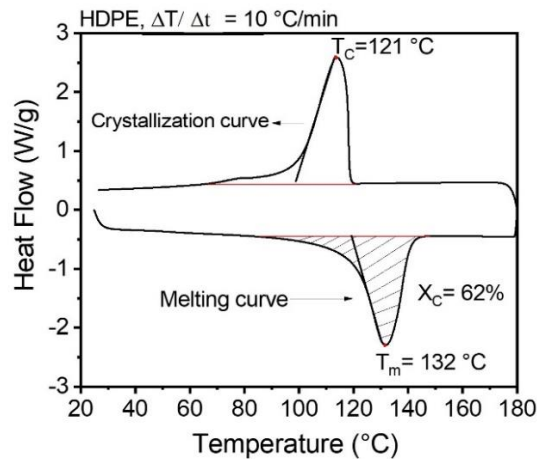


**Figure 4.13:** A typical DSC thermogram of an HDPE sample shows the heat flow rate as a function of the temperature to determine the  $T_C$ , the  $T_m$  of HDPE. The enthalpy of fusion is calculated by the integration of the melting peak, and it is used to calculate the crystallinity of the HDPE sample. The heat of fusion of the 100% perfect crystalline PE is  $H_{f,100} = 293 \text{ J/g}$  (Wunderlich 1990).

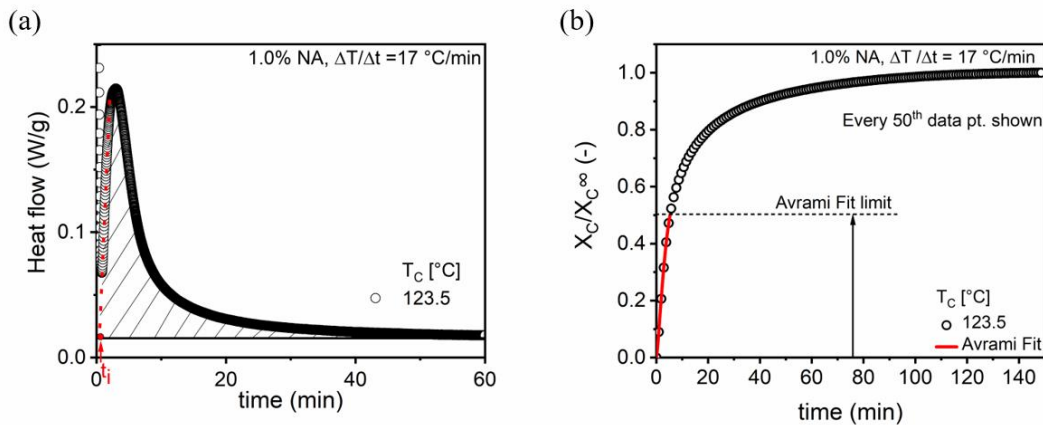


**Figure 4.14:** (a) DSC thermogram of an isothermal crystallization experiment of HDPE with 1 wt% NA content (1.0% NA) at  $T_C = 123 \text{ °C}$  (circle sign) after cooling from  $180 \text{ °C}$  with a cooling rate of  $17 \text{ °C/min}$ . The red-colored dotted line is the extrapolated line of the crystallization beginning. The solid line is the baseline of the peak. The crossover point of the baseline and red-colored dotted line indicates the crystallization induction time  $t_i$ . This approach was used by Choupin et al. 2017. (b) The relative mass crystallinity as a function of time at  $T_C = 123 \text{ °C}$  for sample called 1.0% NA. The Avrami model (see Equation 3.47) is fitted up to half of the final crystallinity.

A typical isothermal crystallization thermogram is shown in Figure 4.14a. The thermal history of the sample is erased before the crystallization process by keeping sample temperature  $40 \text{ °C}$  above the  $T_m^0$  of the sample ( $\sim 141.4 \text{ °C}$  for PE). Next, the sample is cooled down to the  $T_C$  with a constant cooling rate ( $\Delta T/\Delta t = 17 \text{ °C/min}$ ). During

crystallization, a measurable amount of heat is evolved and corresponds to an exothermic peak in the DSC curve. The time  $t$ , temperature  $T$  and cooling rate  $\Delta T/\Delta t$  dependency of the crystallization kinetics are directly related to the shape of this exothermic crystallization peak. The relative mass fraction of  $\frac{X_C}{X_C^\infty}$  (see Figure 4.14b) is calculated by normalization of an integrated of the overall area below the crystallization peak at time  $t$ . If the polymer starts crystallizing during cooling, the induction time  $t_i$ , the required time for crystallization begins, must be defined by a crossover of the extrapolated line of the beginning of the crystallization peak with the baseline as displayed in Figure 4.14a.

#### 4.4 X-ray diffraction (XRD)

The phenomena of XRD based on the Bragg equation:

$$n\lambda = 2d_{hkl} \sin \theta \quad (4.64)$$

where the  $n$ : integer determined by the order of diffraction,  $\lambda$ : wavelength of incident x-ray, the  $d_{hkl}$ : the interplanar distance between  $(hkl)$  reflecting planes and  $\theta$ : angle of the incident beam (see Figure 4.15) (Weidenthaler 2011).

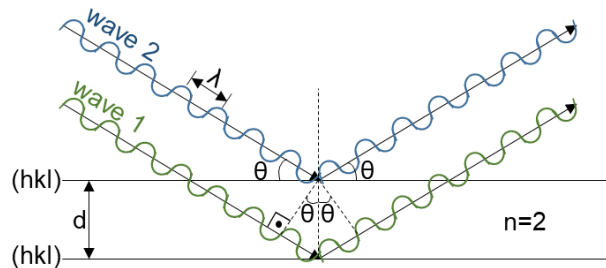


**Figure 4.15:** Schematic representation of the diffraction of incident X-rays by regularly spaced atomic planes (Weidenthaler 2011).

The XRD enables us to examine the degree of crystallinity, unit cell, and crystallite size. Semicrystalline polymers are composed of crystals and amorphous. The degree of crystallinity ( $X_C$ ) is calculated (see Figure 4.16b) by the proportion of integrated amorphous area ( $I_A$ ) with the integrated total area underneath the crystalline peaks ( $I_T$ ) as following;

$$X_C = \frac{I_T - I_A}{I_T} * 100 \quad (4.65)$$

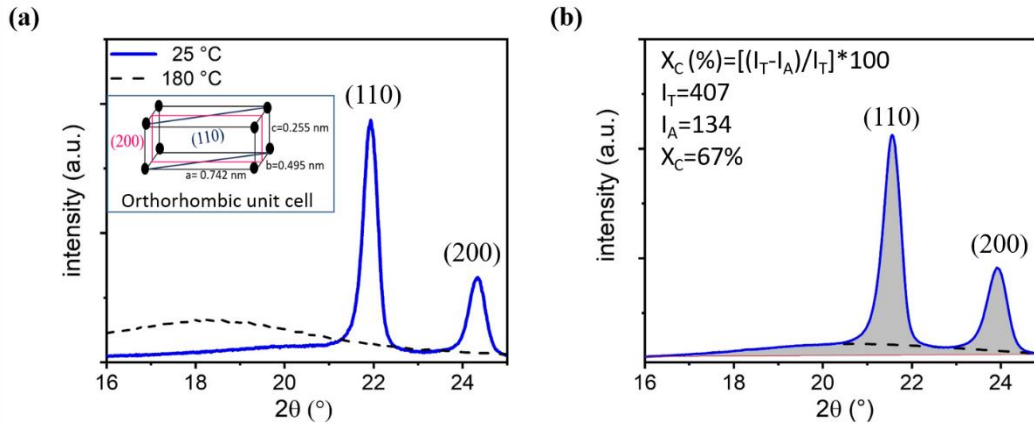


**Figure 4.16:** (a) The XRD patterns of the HDPE sample at 25 and 180 °C. The two distinct reflection peaks (blue line) indicate (110) and (200) planes related to the orthorhombic crystal structure of PE at 25 °C. The broad peak (dash black line) shows the fully molten structure of PE. (b) The XRD diffractogram of the HDPE sample at 25 °C and the calculation of the  $X_C$  (%) by the proportion of the integrated total area ( $I_T$ ) and the integrated amorphous area ( $I_A$ ), which is the area below (dash black line) broad peak.

The polymer sample is composed of different size and shape crystal domain that affects widths and shapes of all diffraction line profile (Scardi *et al.* 2004). Thus, the calculation of the apparent crystallite size is difficult. Integral breadth method can be applied to determine crystallite size to avoid other influences such as instrument contribution, stress/strain effects (Scardi *et al.* 2004). Scherrer equation can be used to determine the average crystallite size:

$$L_{hkl} = \frac{k\lambda}{\beta \cos\theta} \quad (4.66)$$

with  $L$ : volume average of the thickness of the crystallites,  $k$ : Scherrer constant,  $\lambda$ : wavelength,  $\beta$ : integral breadth, and  $\theta$ : angle of the incident beam (Weidenthaler 2011). The Scherrer constant  $k$  depends on the shape of the crystallite, the size distribution, and the way of  $L$  and  $\beta$  definition. Langford and Wilson (1978) reported a detail discussion on  $k$  values which varies from 0.62 to 2.08. Resulting peak pattern provides information about the type of the crystallite. The XRD patterns of the HDPE sample at 25 and 180 °C are shown in Figure 4.16a. Observed two distinct reflection peaks indicate (110) and (200) planes related to the orthorhombic crystal structure. The broad peak at 180 °C shows the fully molten structure of the PE.

## **4.5 Scanning electron microscopy (SEM)**

Scanning electron microscopy (SEM) is a common technique for investigating the surface topology and morphology, crystalline structure and orientation of the crystals. There are three major components as the electron beam source, the illumination system and the imaging system which constitute electron microscopy. A scanned image of SEM is created by produced signals as a result of the interaction of the electrons in the beam with the sample at high spatial resolution and in a low acceleration voltage area.

## 5 RheoNMR Setup and Improvements

RheoNMR is a combination technique of rheology and NMR, and it has been known for almost 30 years (Nakatani *et al.* 1990). There are two approaches on basis of an NMR part of this combined technique by using the high-field NMR (Callaghan 2007; Callaghan 2002; Brox *et al.* 2016) and the low-field NMR (Hardy *et al.* 2006; Herold *et al.* 2013). High-field RheoNMR includes a flow cell that is put into the magnet by using a drive shaft (Callaghan 2002; Brox *et al.* 2016). However, this method is mainly used to analyze low viscous samples, and it has sensitivity and accuracy problems due to interaction between the large magnetic stray fields with motor and transducer. Herold *et al.* (2013) used the capillary rheological apparatus into a low-field permanent magnet and tested also bulk sample. Recently, Ratzsch *et al.* (2017) have introduced low-field RheoNMR (see Figure 5.4) that consists of a combination of a Halbach designed low-field permanent magnet (see Figure 5.1) ( $\nu_L = 30$  MHz,  $B_0 = 0.7$  T) in a commercial strain-controlled TA ARES (TA Instruments, New Castle, DE, USA) shear rheometer or in and also with stress, -strain-controlled discovery hybrid rheometer-3 (DHR-3). This setup enables a simultaneous measurement of the full rheological shear characterization ( $G'$ ,  $G''$  ( $\omega$ ,  $\gamma_0$ ,  $t$ ), LAOS,  $I_{3/1}$ , FT-Rheology) via rheometer and the quantitative molecular mobility by  $^1\text{H}$  NMR. Preliminary results on the setup were reported in following publications: Rätzsch *et al.* 2015; Özen *et al.* 2015, 2016; Ratzsch *et al.* 2017; Rätzsch *et al.* 2019.

The RheoNMR can find applications in material science and industrial quality control experiments. This combined technique overcomes the different thermal history of the sample resulting from slightly diverged temperature distribution in the sample room, cooling/heating rate and varying sample dimensions for separately used different methods. It is difficult to correlate the monitored experimental results from different methods especially for temperature-sensitive processes such as polymer crystallization (Lamberti *et al.* 2007). Consequently, simultaneous measurements with an attentive mutual instrument calibration (temperature, cooling rate, etc.) provide an investigation of sensitively temperature-dependent processes. Thus, the in-situ measured rheological and NMR parameters can be correlated precisely for investigation of sample crystallization is

under identical conditions (Ratzsch *et al.* 2017; Röntzsch *et al.* 2019). The power of low-field RheoNMR methodology finds a high potential to be used for investigation of molecular dynamics under small or large amplitude oscillatory shear.

The previous study of Röntzsch *et al.* 2019 on isotactic polypropylene (iPP) crystallization showed the applicability of the RheoNMR. High-density polyethylene (HDPE) crystallization shows strong temperature dependence, and thus, faster crystallization compared to the iPP. The used HDPE sample in this study revealed the necessity of the improvements on the RheoNMR method in sensitivity and usability for further experimental work in the area.

The setup described below was originally built and used at the Institute for Chemical Technology and Polymer Chemistry (ITCP) / Karlsruhe Institute of Technology (KIT) as published in Ratzsch *et al.* 2017 and also dissertation of Dr. Karl-Friedrich Ratzsch.

This thesis aimed to provide RheoNMR analysis for the investigation of crystallization kinetics of highly temperature-sensitive bulk samples such as HDPE. To this end, the improvements on the RheoNMR are presented in Chapter 5.2. Modifications on the RheoNMR setup were done by Dr. Karl-Friedrich Ratzsch.

## 5.1 Setup details and experimental protocol

### *Setup details*

The Halbach design permanent magnet (see Figure 5.1) consists of an array of 92 NdFeB ( $\nu_L = 30$  MHz,  $B_0 = 0.7$  T), that is placed into a commercial strain-controlled TA ARES (TA Instruments, New Castle, DE, USA) shear rheometer. The Halbach design allows the building of small magnets with a high field homogeneity ( $\Delta B/B_0 \approx 1\%$ ) and a low stray field. The Bruker minispec (ND series) is used as the console/amplifier for the NMR probe. While the rheometer measures simultaneously the full rheological shear characterization ( $G'$ ,  $G''(\omega, \gamma_0, t)$ , LAOS,  $I_{3/1}$ , FT-Rheology (Hyun *et al.* 2011; Wilhelm 2002; Dötsch *et al.* 2003; Cziep *et al.* 2016) and the quantitative molecular mobility is measured by  $^1\text{H}$  NMR (Röntzsch *et al.* 2015; Özen *et al.* 2016; Röntzsch, Haas, *et al.* 2018; Ratzsch *et al.* 2017).

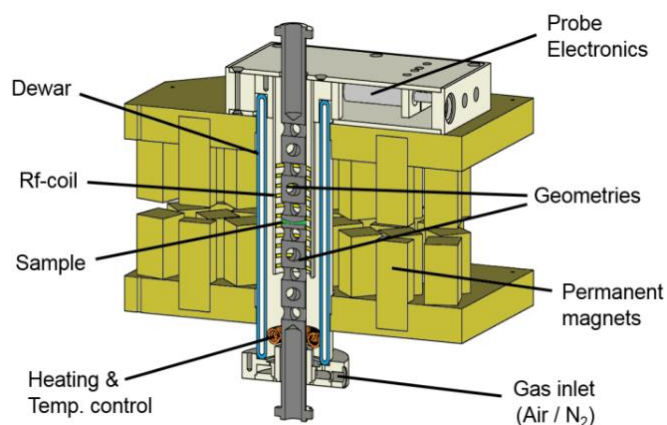


**Figure 5.1:** Schematic overview of used Halbach magnet with the NMR probe of the RheoNMR setup and the rheometry counterparts. Adapted from Ratzsch et al. (2017).

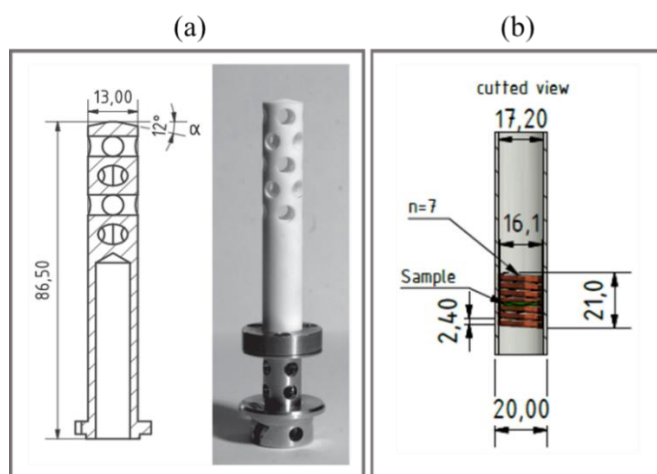


**Figure 5.2 :** (a) Drawing and the photo of the machinable ceramic cone geometry for rheometer which has 13 mm diameter and 86.50 mm length. It has holes for fast thermal stabilization. (b) Illustration of the probe coil (length 21 mm  $N = 7$  turn) is in a glass tube with an inner diameter of 17.2 mm. Adapted from Ratzsch et al. (2017).

Machinable ceramic (Vitronit of Vitron Spezialwerkstoffe GmbH, Germany) was used to make proton-free and non-conducting rheometric tools. Holes were opened on the rheological geometries as shown in Figure 5.2 to provide fast thermal stabilization. A diamagnetic (aluminum) holder is attached to the bottom of the geometries for fitting them to the rheometer. All RheoNMR measurements were performed using a rheological tool with a 13 mm diameter and a cone angle of  $12^\circ$  (0.21 rad) cone-plate geometry to ensure a homogeneous shear rate in the sample during the experiment. The relatively large cone angle is necessary to have enough samples to obtain a sufficient NMR signal. A

convective oven is used for heating of the sample chamber. The lower geometry is surrounded by a heating coil (see Figure 5.3).

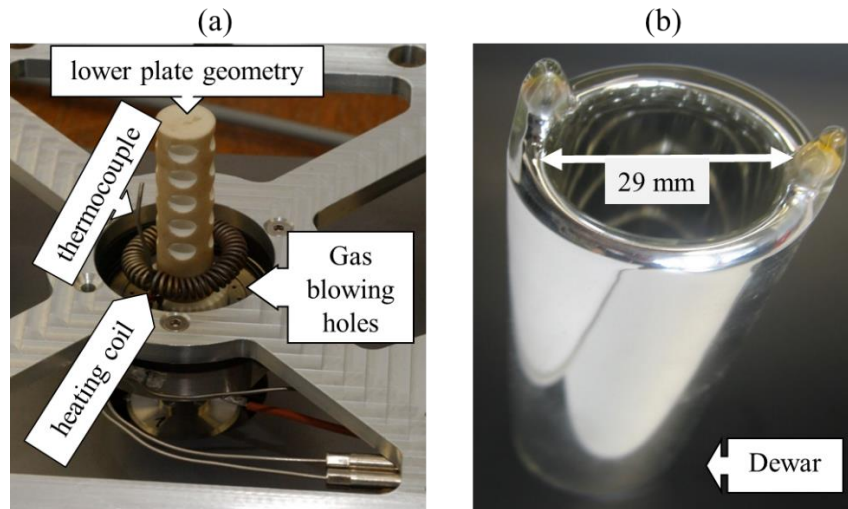


**Figure 5.3:** (a) Photo of the lower geometry, that is surrounded by a heating coil. Nitrogen gas is blown from the bottom holes. The thermocouple measures the temperature of the sample chamber. (b) Dewar is used to insulating the magnet to avoid frequency drifts due to changes in the temperature of the magnet.

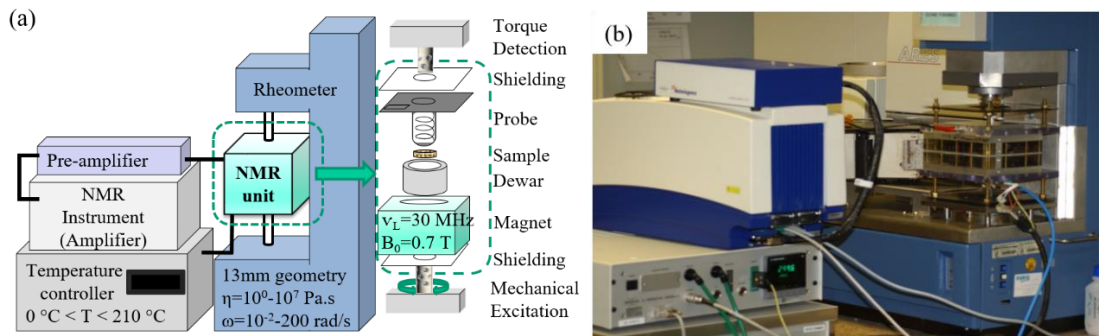


**Figure 5.4:** (a) Illustration and (b) a photograph of the RheoNMR setup taken from Ratzsch et al. 2017. The BVT unit is the temperature controller.

A Bruker Variable Temperature unit (BVT-300) is used to control the temperature. The temperature range for the sample analysis can be controlled between 0 °C and 210 °C by using nitrogen ( $N_2$ ) gas flow, which prevents oxidation. The lower part of the bottom geometry is sealed by a polytetrafluoroethylene ring for insulating the magnet and loss of heated  $N_2$  from the bottom of the setup. A silvered dewar tube (see Figure 5.3) with a diameter of 29 mm and length 115 mm is used for thermal insulation of the magnet. The dewar silvering is paused with a thin stripe of clear glass to avoid interaction with the probe coil. The probe coil, that has length 21 mm  $N = 7$  turns, is in a glass tube with an

inner diameter of 17.2 mm. The glass tube is held by the probe housing of the setup which has tune and match capacitor.

### ***Experimental protocol***

High-density polyethylene (HDPE) crystallizes fast due to its stereoregular structure. The glass transition temperature  $T_g$  can be observed in the range of  $-130^\circ$  to  $-100^\circ \text{C}$  for HDPE (Peacock 2000). The reported  $T_m^0$  of HDPE was in between  $141.45^\circ$  and  $144.85^\circ \text{C}$  (Bower 2002; Wunderlich 2003; Patki and Phillips 2008; Androsch *et al.* 2010). The maximum rate of HDPE crystallization can be acquired by  $T_{C,\text{max}} \sim [T_m^0 + (-T_g)]/2$  (Okui 1990). The temperature for HDPE crystallization experiments was chosen around  $T_{C,\text{max}}$  due to limited experiment time. The used commercial HDPE sample in this section has the  $M_w = 182 \text{ kg/mol}$  with  $D = 11.2$  values, and it was provided from manufacturer LyondellBasell.

Firstly, the RheoNMR setup was assembled. Secondly, a temperature calibration should be done using a digital thermometer (RS Components, Mörfelden-Walldorf, Germany) equipped with a type K thermocouple. The thermocouple was placed inside a special upper geometry for this purpose. It is not possible to use this special geometry during the experiment due to the interaction between the probe circuit and metallic thermocouple. After temperature calibration, the cone upper geometry was assembled, and the gap in between rheometric tools was set the zero at  $T_C$ . The thermal shrinkage is of ceramic geometries is  $\sim 2.5 \mu\text{m}/^\circ\text{C}$ , and the nominal cone truncation gap is  $200 \mu\text{m}$  (Ratzsch *et al.* 2017). The gap between geometries, where the sample stands, must be adjusted manually continuously during temperature change. Additionally, it is important to have a constant pressure and flow of  $\text{N}_2$  (4 bar, 1470 l/h) to have comparable results i.e. reproducible  $T_C$ . After the temperature calibration, settled gap and gas parameters, the next step was a sample loading. The upper cone geometry was heated, and an HDPE disc shape sample was stuck to the hot surface of the upper geometry. The upper geometry with the sample was mounted to the rheometer at  $T_C$ . Later, the temperature was increased to approximately  $40^\circ \text{C}$  above the  $T_m^0$  in order to obtain isotropic melt.

The general temperature routine for quiescent crystallization RheoNMR experiments as seen in Figure 5.5 is similar to the routine used by Janeschitz-Kriegl in 1992 (Janeschitz-Kriegl 1992; Alfonso and Ziabicki 1995; Janeschitz-Kriegl *et al.* 1999). The samples were first heated to at least 40 °C above the  $T_m^0$  and kept at this temperature for 20 min to obtain a fully relaxed, isotropic melt. The thermal history was erased before each crystallization experiment. When the temperature changed from  $T_{\text{iso-melt}} = 180$  °C to  $T_C$ , the oscillatory shear experiment was started “ $t_{\text{exp}} = 0$ ” simultaneously with NMR. A storage  $G'$  and loss moduli  $G''$  were used to monitor in rheo part of the setup during the experiment. During the isothermal quiescent crystallization experiment, an angular frequency ( $\omega_1$ ) and strain amplitude ( $\gamma_0$ ) were kept constant respectively as 0.5 rad/s and 1%.

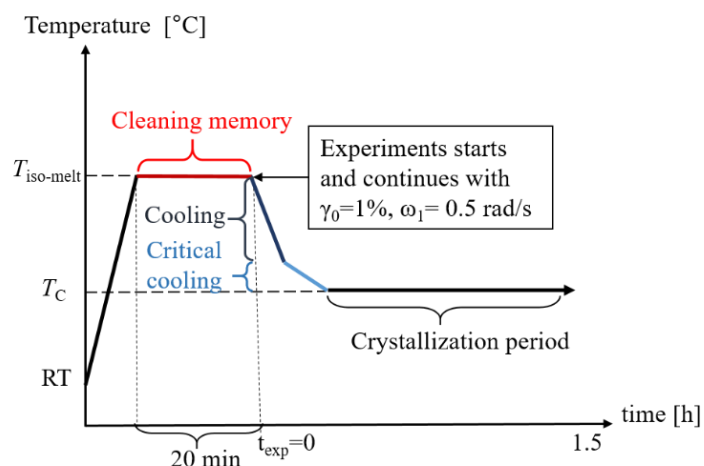


**Figure 5.5:** Schematic illustration of the general temperature protocol that is applied for all RheoNMR and DSC isothermal crystallization experiments. The melt temperature  $T_{\text{iso-melt}}$  was chosen as 180 °C in order to remove the thermal and shear memory. Cooling was divided into two regions as cooling and critical cooling. A similar temperature protocol was also used by Mursalin *et al.* (2016) for fat crystallization.

The combination pulse sequence with MSE and CPMG was used in the NMR method. While the MSE is used to refocus of the initial transverse magnetization, the purpose of the CPMG sequences is to refocus only the magnetization of the more mobile phase of the sample. An apparent mass crystallinity  $X_C$  was determined as a function of time  $t_{\text{exp}}$  via the relative intensity of CPMG echoes (Maus *et al.* 2006; Röntzsch *et al.* 2015; Röntzsch, Haas, *et al.* 2018; Rätzsch *et al.* 2017). The 90° pulse length was 2.4  $\mu\text{s}$ , and the 180° pulse length was 4.8  $\mu\text{s}$ . A recycle delay  $\tau_{\text{rd}}$  of 3.5 s, that was equal to  $5 \times T_1$

for the spins reaching equilibrium, was used with 16 scans and  $\tau = 20 \mu\text{s}$  ( $\tau$ - waiting time) between subsequent  $180^\circ$  pulses for the applied CPMG sequence.

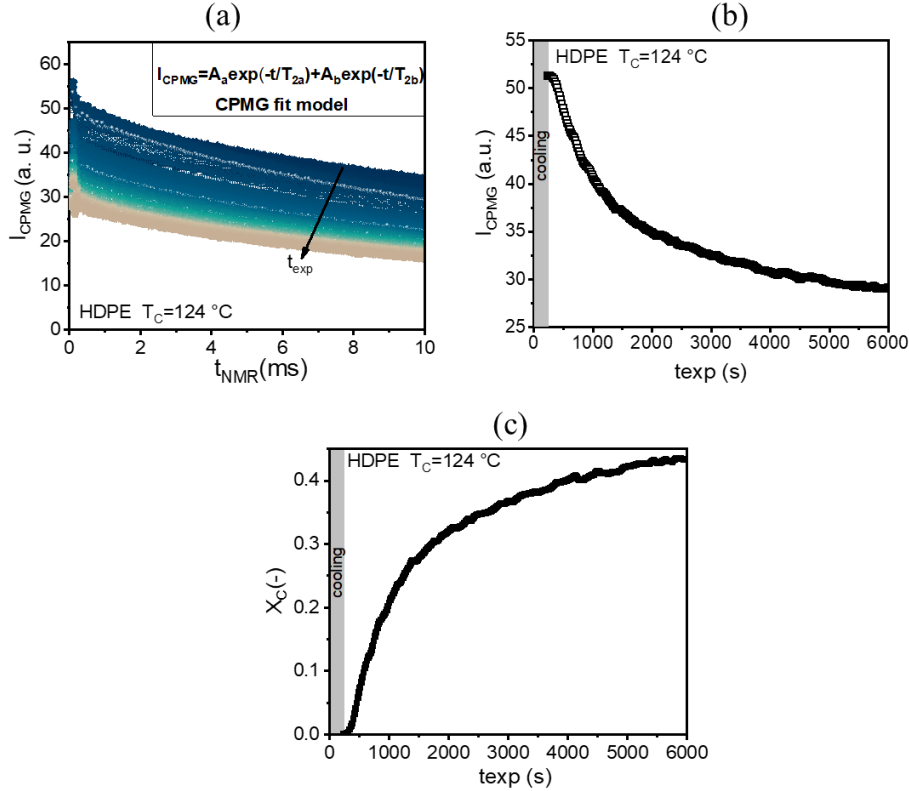


**Figure 5.6:** (a) The  $I_{\text{CPMG}}$  echoes as a function of  $t_{\text{NMR}}$ , (b) the back extrapolated intensity  $I_{\text{CPMG}}$  values at  $t_{\text{NMR}} = 0$  ms as a function of  $t_{\text{exp}}$  and (c) the time evolution of  $X_C$  for an isothermal crystallization of HDPE at  $T_C = 124^\circ\text{C}$ .

The observed CPMG decay curves (see Figure 5.6a) were fitted using a biexponential function as Equation 5.1 with pre-factors  $I_A$  and  $I_B$  which are referred to  $I_{\text{CPMG}} = I_A + I_B$ . Two transverse relaxation times  $T_{2A}$  and  $T_{2B}$  were used to back extrapolate the initial intensity  $I_{\text{CPMG}}$  at  $t_{\text{NMR}} = 0$  ms (Ratzsch *et al.* 2017; Rantzsch *et al.* 2015; Özen *et al.* 2015, 2016).

$$I_{\text{CPMG}} = I_A \exp(-t/T_{2A}) + I_B \exp(-t/T_{2B}) \quad (5.1)$$

Then, the back-extrapolated  $I_{\text{CPMG}}$  as a function of the experiment time  $t_{\text{exp}}$  is shown in Figure 5.6b. Calculated  $I_{\text{CPMG}}(t_{\text{exp}})$  was compared with the  $I_{\text{CPMG}}$  of a supercooled melt close to  $T_C$  for achieving the mass crystallinity  $X_C$  with the following equation;

$$X_C(t_{\text{exp}}) = \left(1 - (I_{\text{CPMG}}(t_{\text{exp}})/I_{\text{CPMG,max}})\right) \quad (5.2)$$

where  $t_{\text{exp}}$  is the experiment time during the crystallization process (Ratzsch *et al.* 2017; Rätzsch, Haas, *et al.* 2018). Resulting  $X_C$  evolution by time can be seen in Figure 5.6c.

## 5.2 Improvements

The strong temperature dependence of the HDPE crystallization showed the limits of RheoNMR and revealed the necessity of improvement in temperature homogeneity in sample volume and reproducible  $T_C$ .

### *Temperature homogeneity across sample volume*

RheoNMR setup consists of portable pieces such as shieldings, probe, dewar as displayed in Figure 5.4a and they should be assembled one by another. Each piece has slight flexibility to move ( $\pm 1$  mm), which changes the nitrogen flow into the sample chamber result in not repeatable crystallization experiment at chosen  $T_C$ . A digital thermometer (RS Components, Mörfelden-Walldorf, Germany) equipped with a type K thermocouple was used to control temperature homogeneity in the sample chamber after the setup was assembled without upper geometry. Upper geometry was not mounted as it prevented the thermometer entrance into the sample chamber. The used geometry has 13 mm diameter and the inner diameter of the glass tube, which holds the probe coil, is 17 mm. This means that there is a 2 mm space in between sample and probe coil. Thus, the positioning of the probe coil depended on the user. After positioning of the probe coil, and it was fixed by tightening screws. The inside view of the RheoNMR setup from the top is illustrated in Figure 5.7a-b. The thermocouple was put into the sample chamber until the position of the sample and moved around it. The temperature was set to 126.3 °C. Then, observed temperatures in the area were displayed in Figure 5.7b. The read temperature values showed  $\Delta T = 126.3 - 123.9 = 2.4$  °C difference in sample chamber which caused the temperature inhomogeneity across sample volume.

To solve emerged temperature inhomogeneity across sample volume, the heating resistor coil was equally spaced. Some of the holes at the bottom for blowing heated N<sub>2</sub> were blocked by dirt. Therefore, they were cleaned via a thin wire. Although this slightly

reduced the temperature difference to  $\sim 1.8$ , this was not enough to be able to investigate isothermal crystallization of HDPE samples that studies are presented in Chapter 6. Another approach to the temperature inhomogeneity problem solving was to design a vortex creator for equilibrating the temperature in the sample chamber with attaining a turbulent gas flow. The vortex creator was designed by Karl-Friedrich Ratzsch as shown in Figure 5.8. The vortex creator was useful to reduce temperature inhomogeneity to  $\Delta T = 0.8$  °C.

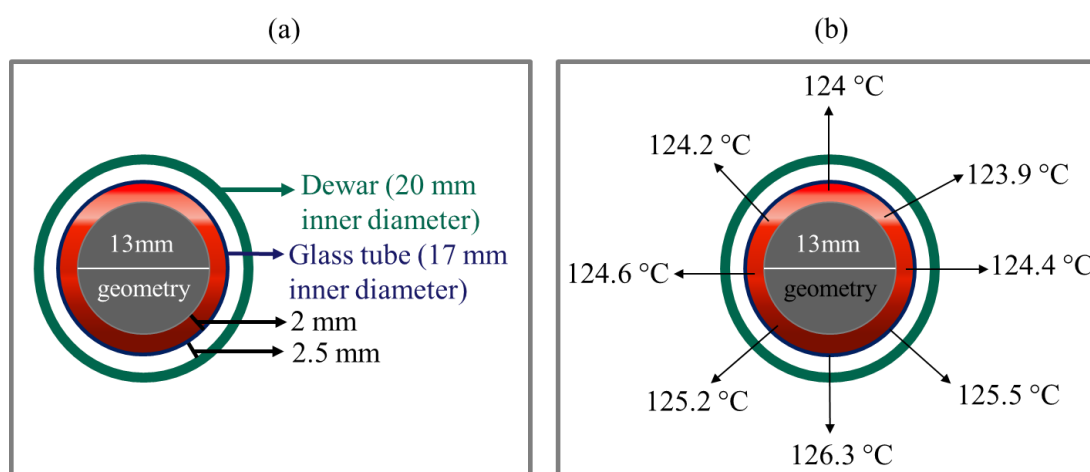


**Figure 5.7:** Illustrated inside view of RheoNMR setup from the top shows that (a) the pieces with inner diameter and distance in between pieces and (b) the measured temperature gradient in the sample chamber which causes temperature inhomogeneity across sample volume.

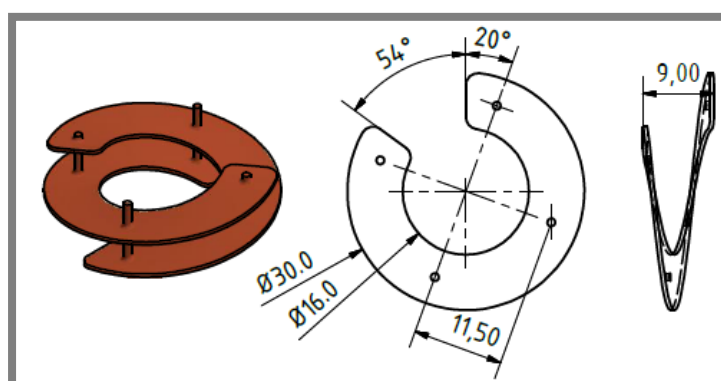


**Figure 5.8:** The designed and plotted vortex creator by Karl-Friedrich Ratzsch. Dimensions are in mm size.

The reproducibility of cooling rate and  $T_C$  was checked using vortex creator by controlling gas flow and gas pressure. A special design upper geometry with a thermocouple placed in the center of the plate surface (see Figure 5.9) was used to learn the absolute

temperature inside of the sample. The special upper geometry with a sample was mounted to the rheometer. This upper geometry with the sample was lowered until the sample covered the lower geometry surface. The temperature was set at 177 °C on the BVT unit which was connected to the thermocouple. This thermocouple was positioned next to the bottom geometry and 2.2 cm away from the sample. The temperature was changed and again set to 177 °C in the BVT unit to see reproducibility for different gas flow and gas pressure conditions. When the temperatures reached the equilibrium in the sample and on the BVT unit screen, achieved values were noted as displayed in Table 5.1. The lowered gas pressure and increased gas flow caused a lower temperature difference between absolute sample temperature and set value on the BVT unit. Better reproducibility for the equilibrium sample temperature was achieved within  $\pm 0.5$  °C when the gas flow and gas pressure were set respectively 1470 l/h, 4 bar.



**Figure 5.9:** Photograph of the special upper geometry with the connected thermocouple.

**Table 5.1:** Thermocouple temperatures of the BVT controller of RheoNMR and thermometer in the center of upper geometry under constant gas flow and gas pressure.

<b>BVT Thermocouple (°C)</b>	<b>Thermometer Thermocouple (°C)</b>	<b>Gas Flow (l/h)</b>	<b>Gas pressure (bar)</b>	<b><math>\Delta T</math> (°C)</b>
177	175.1	1200	6	1.9
177	174.6	1200	5	2.4
177	176	1470	6	1
177	177	1470	5	0
177	176	1470	5	1
177	177.1	1470	4	0.1
177	177.6	1470	4	0.6

A further important parameter for investigating crystallization processes is the reproducibility of the cooling trend. Knowing the absolute temperature in the sample and cooling rate to chosen  $T_C$  in RheoNMR permits to perform the crystallization experiment under comparable conditions within other characterization techniques. However, the RheoNMR setup was not able to record the temperature change during cooling. Therefore, the set temperature on the BVT unit and observed sample temperature on thermometer screen were recorded by a camera during cooling to  $T_C$ . First, the temperature was stabilized at 180 °C. Thereafter, the temperature was decreased to  $T_C$  via BVT controller with a temperature ramp as 50 °C/min, and later on, repeated protocol without temperature ramp. These two different cooling styles was plotted as displayed in Figure 5.10a with using the recorded video. When the BVT unit reached to  $T_C = 127$  °C, the temperature was still decreasing inside of a sample. The final temperature inside of the sample was 2.3 °C higher than the set temperature on the BVT unit under the non-used temperature ramp. Under 50 °C/min temperature ramp conditions, the final temperature was 2.5 °C higher. Additionally, resulting cooling was within ~5 minutes for  $\pm\Delta T = 0.5$  °C to the final temperature with the 50 °C/min temperature ramp. When there was no temperature ramp, cooling took half a minute shorter. Nevertheless, considering the crystallization kinetic of HDPE can be strongly influenced by the cooling rate. The controlled cooling rate with the 50 °C/min temperature ramp was chosen for further crystallization tests. Later on, the setup was reassembled to check the reproducibility of  $T_C$  and  $\Delta T_C$ . The same cooling protocol with the 50 °C/min temperature ramp was repeated for  $T_C = 124$  °, which was shown with the blue circle sign in Figure 5.10b. Plotted results from the recorded video showed that there were 0.6 °C undershoot from the set  $T_C$  at around 3<sup>rd</sup> minute, and then, the sample temperature stabilized a 0.5 °C higher from the set  $T_C$  within ~5 minutes. The cooling test was repeated for  $T_C = 122$  with the 50 °C/min temperature ramp. This result is displayed as a black square sign in Figure 5.10b. This test showed the cooling time to  $T_C$  as ~6 minutes for  $\Delta T = 0.5$  °C without any undershoot temperature. This reveals that the observed undershoot was not the same for each cooling. These results revealed that the chosen varying  $T_C$  the difference was not constant. For instance, the difference in  $T_C$  between 124 and 122 °C is 2 °C. However, the repeated cooling trend as depicted in Figure 5.10b showed that this 2 °C difference

could be even larger in the case of present undershoot from the set  $T_C$ . This could drastically affect the crystallization trend of temperature-sensitive samples and leads to not reproducible results. The variation in the cooling trend for each reassembling was found due to a changed thermocouple position of RheoNMR by reassembling the setup with vortex creator as in Figure 5.11. The vortex creator moved the thermocouple slightly to a different direction for each assembling. Thus, the changed thermocouple position showed a difference in the cooling trend, cooling duration in the sample. This situation revealed the requirement of the set place for thermocouple and the necessity of the temperature calibration at once right after the setup integration.

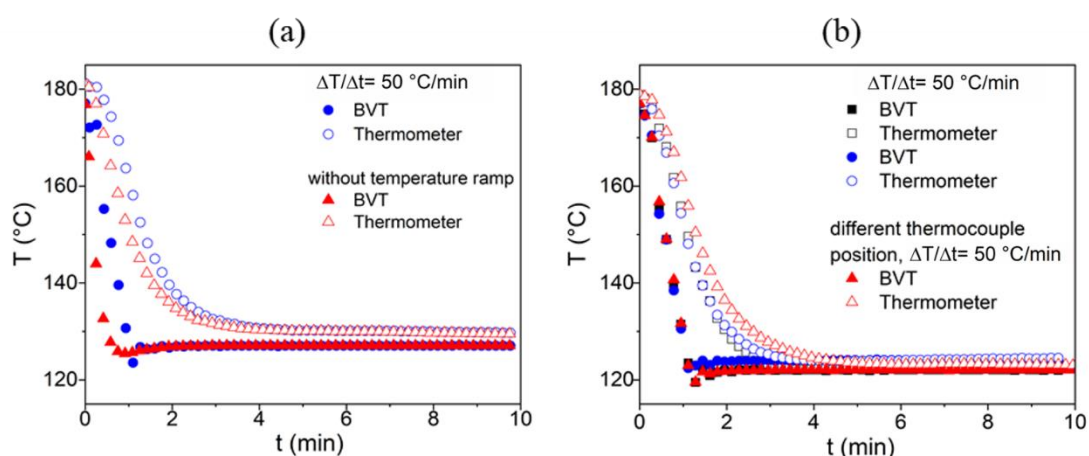


**Figure 5.10:** The recorded temperature change as a function of time during cooling (a) with and without temperature ramp ( $\Delta T/\Delta t$ ) which were set to the BVT unit. (b) The cooling trend for reassembled setup to  $T_C = 124$  °C under a 50 °C/min temperature ramp (blue circle sign), and compared with further cooling test  $T_C = 122$  °C under a 50 °C/min temperature ramp (dark square sign). This difference in the cooling trend was due to the different thermocouple positions (see Figure 5.12).

A further modification was done by fixing the thermocouple to outer to the glass tube which holds the probe coil as demonstrated in Figure 5.12. The cooling trend and cooling duration were checked again with the new thermocouple position with the same protocol as above mentioned. The temperature changed from 180 °C to 125 °C with a 50 °C/min temperature ramp at 1470 l/h  $N_2$  flow at 4 bar. Cooling data was displayed in Figure 5.13. The sample temperature stabilized at 126.1 °C within 6 min and 40 s without any temperature undershoot. The setup was reassembled, and the same temperature protocol with the previous one was repeated to check the repeatability of the cooling trend. The resulting cooling trend plotted with a circular blue sign in Figure 5.13. The cooling trend

was the same for repeated experiments with using upper thermosensor and the observed final  $T_C$  in the sample was the least achieved with  $\pm 0.1$  °C difference.

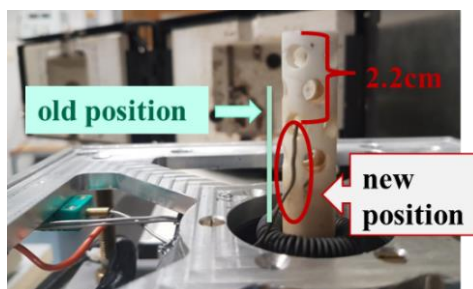


**Figure 5.11:** Photograph of the BVT connected thermocouple which was changed by put vortex creator on the heating resistor.

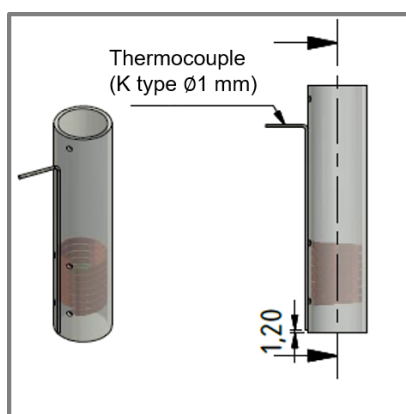


**Figure 5.12:** The designed fixed thermocouple to outer to the glass tube which holds the probe coil. The design and the plot were done by Karl-Friedrich Ratzsch.

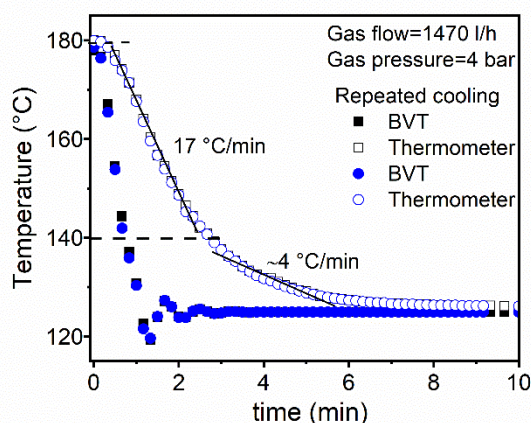


**Figure 5.13:** The temperature change during the time in the BVT unit and the thermometer. The BVT thermocouple was positioned at the outer part of the glass tube which holds probe coils (see Figure 5.12). The thermocouple of the thermometer was placed inside of the special upper geometry as touching the sample from the center. Cooling was divided into two regions with rates of cooling = 17 °C/min and critical cooling = ~4 °C/min.

In addition to optimized reproducible temperature conditions, the surface of the upper geometry was made slightly porous by used sandblaster technique while the bottom geometry was smoothed by sandpaper with a number 2000. This helped to remove the sample from the top of the RheoNMR instrument setup without reassembling which was time-saving and paves the way for more reproducible results. Thus, the morphology analyses were possible on the sample to investigate the applied crystallization condition impacts in the morphology when the sample was taken right after the crystallization experiment from the top of the setup. Furthermore, the probe coil glued to the glass tube using liquid glass. This way provided a stable probe coil with a constant and equal ring distance. These developments have maximized the accuracy and reproducibility of the technique.

### 5.3 Reproducibility of the results

The experimental details like the temperature, cooling trend have been known to play crucial roles in achieving reasonable reproducibility in quantitative analyses. After all developments on the setup, the reproducibility of the results was tested with the use of the same sample under the same experimental conditions with exerted same temperature protocols as depicted in Figure 5.13. For this purpose, the HDPE sample with the addition of 0.1 wt% NA was used to determine the reproducibility. The addition of a nucleating agent in the HDPE sample would be expected to the increase temperature sensitivity of the inherently temperature-sensitive neat HDPE crystallization process. The evolution of dynamic moduli and crystallinity of 0.1% NA sample was determined by Rheo and NMR part of RheoNMR under identical quiescent crystallization conditions. In Figure 5.14a, the overlay of the repeated experiment results is demonstrated. The thermal expansion of the geometer was neglected by the conducted a zero-gap routine at  $T_C$  temperature. Observed results with two consecutively repeated and add one more repeated experiment with a fresh sample were plotted in an error bar as shown in Figure 5.14. Resulting data was achieved within ~90% certainty at the time of gelation  $t_{gel}$  ( $G' = G''$ ) for the moduli and the  $X_{gel}$ , and also at the final value of the moduli  $G'_\infty$  and the final crystallinity  $X_C^\infty$ . Achieved this result indicates the robustness and reproducibility of the analysis.

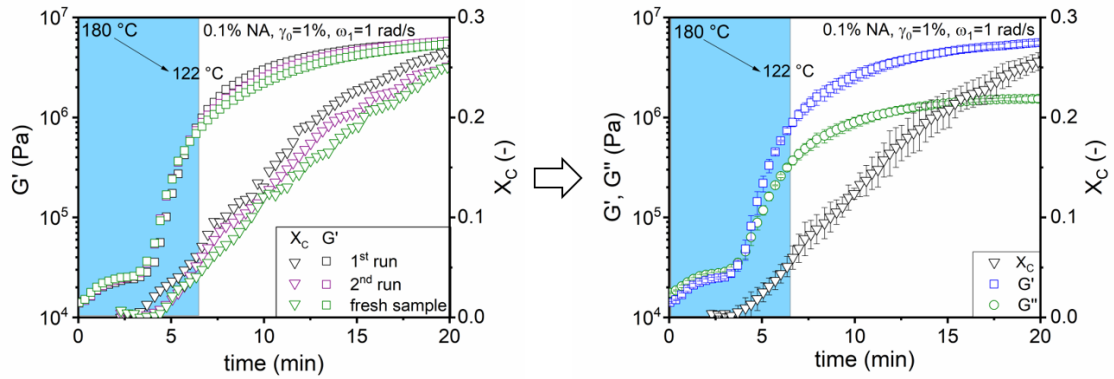


**Figure 5.14:** (a) Consecutively repeated two RheoNMR experiments with an HDPE sample which contents 0.1 wt% NA (0.1% NA) and then, the setup sample was taken out from the top of the setup without disassembling all setup. The experiment was repeated under the same conditions such as  $T_C = 122$  °C,  $\omega_1 = 1$  rad/s,  $\gamma_0 = 1\%$  with loaded fresh sample (0.1% NA). (b) Repeated experiment results in Figure 5.14a displayed with an error bar and ultimately certainty was calculated as  $\sim 90\%$  for the RheoNMR method at the time of gelation  $t_{gel}$  ( $G' = G''$ ) for moduli and  $X_{gel}$ , and also at the final value of the moduli  $G'_\infty$  and crystallinity  $X_C^\infty$  under no disassembled setup conditions.

## **6 In situ Correlation of Viscoelastic Behavior and Local Mobility of Neat and Nucleated HDPE Crystallization via RheoNMR**

In this chapter, crystallization of neat HDPE and addition of varying weight percent (wt%) nucleating agent (NA) into commercial HDPE samples under quiescent and shear/strain-induced crystallization conditions were investigated by using the RheoNMR characterization method. At the end of the quiescent and shear-induced crystallization of HDPE/NA blends, samples were taken out from the RheoNMR instrument for morphology analysis. The morphology analysis was done by scanning electron microscopy (SEM) in collaboration with Volker Zibat from the laboratory for electron microscopy in the Karlsruhe Institute of Technology (KIT). The taken samples from RheoNMR were also evaluated by x-ray diffraction (XRD) with cooperation Dr. Peter G. Weidler from the Institute of Functional Interfaces to see crystallinity and unit cell type. Additionally, Dr. Krassimir Garbev from Institute for Technical Chemistry (ITC) supported the study with the analyses of HDPE melting behavior under XRD observation. Lastly, Dr. Erich Müller from the Laboratory for Electron Microscopy (LEM) introduced the ImageJ software that was used for the conversion of the SEM images to FFT images. Some of the results with the theoretical background in the presented chapter and its subsections were published in the literature Özen *et al.* (2015, 2016).

### **6.1 Introduction**

The nucleation and crystal morphology can be modified by directed processing conditions e.g., cooling rate, and by utilizing a nucleating agent (NA) into a polymer. The addition of NA promotes heterogeneous nucleation by providing a focal center which presents a surface on that the lamellae can grow epitaxially (Binsbergen 1977; Okada *et al.* 2007; Piorkowska and Rutledge 2013; Wittmann and Lotz 1981; Mercier 1990). Hence, the nucleation density and the overall crystallization rate are increased by added NA into the polymer. Nucleating agents are considered more effective for iPP compared to PE due to its inherent slower crystallization. High-density polyethylene crystallizes relatively

faster, owing to its linear structure with no or little branching, compare to other semi-crystalline polymers e.g., iPP. Nevertheless, the nucleation of HDPE has a great interest in both the industrial and scientific points of the view to alter the physical properties of HDPE. For example, applications have shown that HPN-20E as a commercial NA has benefits during processing HDPE products, e.g., improved dimensional stability, cycle time reduction (~10%), productivity improvements (Seven *et al.* 2016; Jiang *et al.* 2012; Dotson 2007). A chemical structure of the calcium salt part of the HPN-20E can be seen in Figure 3.14a. The rod-shape of HPN-20E particles (see Figure 3.14b) allows the polymer crystals to orientate in the direction of flow during crystallization under shear (Seven *et al.* 2016; Dotson 2007). The detailed analysis of the impact of the NA content in HDPE on crystallization kinetics under controlled processing conditions was needed to be investigated due to the practical importance of the fundamental questions.

In light of the requirement of crystallization analysis under controlled processing conditions, the unique low-field Rheo-NMR setup is a suitable method to investigate the time evolution of crystallization under the selected condition. The details of the low-field Rheo-NMR setup was mentioned in Chapter 5. The impact of applied large oscillatory shear or steady shear role on the crystallization kinetics and the final crystallinity of polymers or any bulk material e.g., fat can be investigated by RheoNMR. Moreover, the RheoNMR setup enables the correlation of macroscopic material properties and microscopic molecular dynamics under the same thermal and shear history.

The sensitivity of flow-induced crystallization is increasing for PE samples with large  $D$  and high  $M_w$ . Therefore, a commercial HDPE sample with high  $M_w$  and large  $D$  was used in this study (see Chapter 6.2 for sample details) to investigate the flow-induced crystallization and applicability of the RheoNMR method for fast crystallized samples.

This work aims to investigate the effects of the HPN-20E amount in HDPE, on the crystallization kinetics of HDPE via RheoNMR. The raised several questions of both scientific and technological importance such as how do the crystallization process and the crystallization kinetics of the HDPE/NA blend sample affected by varying NA content and applied large deformation were discussed in this study. In particular, the effects of the critical parameters on the crystallization such as the temperature, steady shear, short

and long term applied large strain amplitude were examined for neat HDPE and HDPE/NA blends via using our unique combined RheoNMR experimental technique. In Chapter 6 all mentioned Rheo data belongs to the Rheo part of the RheoNMR. Similarly, all mentioned NMR results were determined by the NMR part of the RheoNMR. An Avrami model was used for analyzing the HDPE crystallization kinetics. The monitored crystallization data by RheoNMR were used for a potential new direction to correlate the gelation point with the degree of crystallinity, and with the half time of the crystallization process. Additionally, the DSC method was used as a supporting method of this study to investigate the accuracy of this new technique. Moreover, the microstructure analysis of the isothermally crystallized HDPE/NA samples was done by using XRD and SEM.

## 6.2 Samples and their preparations

### *Sample*

A commercial-grade of HDPE was supplied by LyondellBasell Polyolefine GmbH (Frankfurt, Germany). This HDPE was used in Chapter 6.3.1, Chapter 6.4.3 and Chapter 9. This HDPE sample was mixed with NA to create HDPE/NA blends. The neat HDPE was called 0% NA in this study. It has a  $M_w = 182$  kg/mol with  $D = 11.2$ .

Another commercial HDPE with  $M_w = 189$  kg/mol and  $D = 9$  was supplied by LyondellBasell Polyolefine GmbH (Frankfurt, Germany). To analyze the steady shear effect on the isothermal crystallization kinetic experiments this HDPE sample was used as a shown study in Chapter 6.4.1.

Additionally, two HDPE samples were synthesized by using ring-opening metathesis polymerization (ROMP). They were named as PE-1 and PE-2. The sample PE-1 has  $M_w = 100.3$  kg/mol with  $D = 1.52$ , and PE-2 has  $M_w = 71.6$  kg/mol with  $D = 1.57$ . The  $M_w$  of the PE-1 and PE-2 are above the entanglement molecular weight  $M_e = 830$  g/mol of the HDPE. These samples were used in the studies mentioned in Chapter 6.3.2 and Chapter 9. The synthesis of the samples was performed by Patrick-Kurt Dannecker from the group of Prof. Dr. Michael A. R. Meier in the Institute of Organic Chemistry, Karlsruhe Institute of Technology.

A commercial NA, *cis*-1,2-cyclohexane dicarboxylic acid, calcium salt (trade name: Hyperform HPN-20E), was supplied by Milliken Chemical. The chemical structure and SEM image of the organic part in HPN-20E are shown in Figure 3.5. This commercial NA contains one-third of zinc stearate which melts at  $T_m = 120$  °C. While the zinc stearate is fully soluble in HDPE, the calcium salt-based NA remains solid in the molten HDPE.

The  $T_m$  of the used HDPE samples were as  $T_{m,0\%NA} = 132$  °C,  $T_{m,PE-1} = 127$  °C,  $T_{m,PE-2} = 128$  °C via DSC. DSC measurements were done by using a 10 °C/min cooling and heating rate. The second heating run of the DSC measurement for each sample was used to calculate  $T_m$ .

### **Sample Preparation**

*Extruder:* A masterbatch composed of 10 wt% NA and 90 wt% of HDPE was melt-mixed in lab-scale co-rotating twin-screw extruder, the Minilab (Thermo Scientific Haake, Germany) for uniform dispersion of NA. The compounding temperature was 180 °C at 60 rpm screw speed for 10 min processing time. A series of HDPE samples within a varying concentration of NA (see Table 6.1) were melt compounded in the extruder by adding the calculated amounts of HDPE into the prepared masterbatch. The neat HDPE was also extruded under the same conditions to have the same thermal and shear history as nucleated PEs for a reasonable comparison.

**Table 6.1:** Preparation conditions for the HDPE with NA.

PE samples name	Amounts of NA (wt%)
0% NA	0
0.1% NA	0.1
0.3% NA	0.3
0.5% NA	0.5
1% NA	1.0
3% NA	3.0

*Laboratory press:* The samples were press-molded under vacuum at 180 °C and ~20 bar pressure during 15 min in a Weber laboratory press to make 13 mm in diameter disks with ~1 mm thickness.

*Etching protocol for SEM analysis:* The amorphous regions on the surface of PE samples were removed by a prepared etchant which is an acidic solvent with permanganate (Sawyer, Grubb and Meyers 2008). The etchant required 3 wt% solution of  $\text{KMnO}_4$  in a mixture of 10 volumes  $\text{H}_2\text{SO}_4$  (96 wt%), 4 volumes  $\text{H}_3\text{PO}_4$  (85 wt%) and 1 volume water ( $\text{H}_2\text{O}$ ). Samples were kept in this acidic solution for 2 h at room temperature. Afterward, they were washed with distilled water. Then samples were preserved in acetone and ultrasonicated for 30 min to remove etch material.

## 6.3 Quiescent crystallization

### 6.3.1 Thermal behavior of the commercial HDPE

Thermal optimization of polymer processing e.g., injection molding or plasticating extruder is significantly important for energy and time efficiency, and the final product quality (Vera-Sorroche *et al.* 2013). The RheoNMR was used to understand the temperature-dependence of isothermal crystallization of neat commercial HDPE. The sample does not contain a nucleating agent (NA), and thus, it is called as neat or 0% NA. The temperature and experimental protocol as depicted in Figure 5.5 for quiescent crystallization. The maximum  $T_C$  was chosen as 124.5 °C due to experimental time limitation (see Chapter 5.1). The time off-set starts with the temperature change to the  $T_C$ . Figure 6.1 displays the time evolution of the dynamic moduli and crystallinity in commercial HDPE for different  $T_C$ . To avoid flow-induced crystallization with a time-efficient measurement, suitable low deformation and frequency should be taken for quiescent crystallization. All the temperature dependency experiments were carried out with a low strain amplitude  $\gamma_0 = 1\%$  and an angular frequency  $\omega_1 = 0.5$  rad/s. Experimental conditions and the sample name are always mentioned in the graphs. The used NMR condition was always constant for each experiment as described in Chapter 5. The dynamic moduli showed a stepwise increase during cooling due to the temperature dependence of the moduli. Meanwhile, neat HDPE sample started crystallizing which can be seen as an increase of  $X_C$  in Figure 6.1. Additionally, even a 0.5 °C decrease in  $T_C$  caused obvious faster crystallization process with an earlier rise in the dynamic moduli (determined by Rheometer) and in  $X_C$  (determined by NMR). These observations

indicated the high sensitivity of neat HDPE crystallization towards temperature in the selected temperature range. Moreover, the observed crystallization during cooling as seen in Figure 6.1b indicated that the applied maximum available cooling rate for the RheoNMR setup was not high enough to stop crystallization during cooling at chosen  $T_C$ .

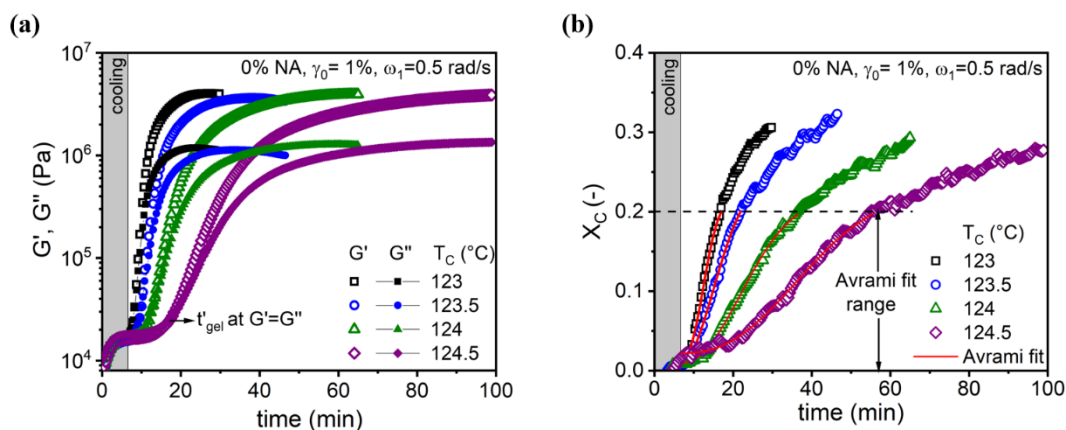


**Figure 6.1:** Simultaneous measurement of low-field RheoNMR data on the isothermal crystallization of 0% NA (neat HDPE) sample. (a) The dynamic moduli ( $G'$  and  $G''$ ), and (b) crystallinity ( $X_C$ ) evolution as a function of time at different crystallization temperatures  $T_C$ .

The temperature drop trend in the sample during cooling was displayed in Chapter 5 see Figure 5.13. The required time to reach the desired crystallization temperature was approximately 6.7 min. Then, a sharp rise observed both in storage modulus  $G'$  and  $X_C$  with solidification. When the dynamic moduli reached a maximum stable value  $G'_\infty$ , final plateau, there was no change anymore on the macroscopic properties. However, the continuous evolution in microstructure was observed by NMR part of RheoNMR with an increase of  $X_C$  which showed an ongoing secondary crystallization process. The crossover point of the dynamic moduli is known as gel point which point depends on the molecular composition of the sample, the existence of additives in the sample, as well as the crystallization condition e.g.,  $T_C$ , deformation history (Schwittay *et al.* 1995; Raghavan *et al.* 1996; Pogodina *et al.* 1999). This transition from a liquid state to solid-state, gelation, is a thermo-reversible process caused by interconnected crystals during crystallization (Schwittay *et al.* 1995; Pogodina *et al.* 1999; Coppola *et al.* 2006). At early stages of the crystallization, crystallites act as physical cross-links that link together several neighboring chains, and thus, causes the physical gelation (Gelfer and Winter 1999). The required time for gelation is called as a “gel time”,  $t_{gel}$  (Ratzsch *et al.* 2017;

Räntzsch 2018). The time  $t_{\text{gel}}$  was used in this study to compare the measurements under different crystallization conditions. Another quantity was the required time of crystallization to obtain  $X_C = 0.2$  which was called as  $t_{0.2}$ . The time  $t_{0.2}$  was assumed as almost equal to half time of the crystallization since the  $X_C$  had approximately achieved half of its ultimate value as measured by NMR and DSC. In order to do the kinetic analysis, the Avrami model was fitted to the data up to  $X_C = 0.2$ . Because of the observed crystallization during cooling, the zero time of the crystallization  $t_0$  was used instead of induction time  $t_i$  in Avrami model (see Equation 3.47). Crystallization of the neat HDPE started during cooling. The  $X_C = \sim 0.8\%$  when the temperature reached at  $T_C$  in  $\sim 400$  s. Isothermal crystallization started with a lower slope than the slope of the crystallization during cooling when the temperature reached the  $T_C$ . This stepwise change in the early crystallization part led to difficulties for the fitting Avrami model. Therefore, the off-set value was used as 0.008. To determine  $t_0$  effect on calculated Avrami parameters, the  $t_0$  was kept as a free parameter for fitting the model to the NMR data. The  $t_0$  value was attained between 400 and 800 s except for  $T_C = 124.5$  °C as displayed in Figure 6.2a. However, the resulting  $t_0$  for  $T_C = 124.5$  °C was a negative value that was obviously a defect. Therefore,  $t_0$  values was decided to be determined as  $400 < t_0 < 800$ . When the  $t_0$  value set as 400 s, and later on, 450 s, the resulting Avrami fit parameters was equivalent as in Figure 6.2b. However, when the  $t_0$  was chosen larger than 500 s, a reduction was observed in fit parameters (see Figure 6.2b) for lower  $T_C$ . Resulting rate parameter  $K$  at 123.5 °C was lower than the calculated rate  $K$  parameter at  $T_C = 124$  °C, and that was meaningless since we can see the faster crystallization for lower  $T_C$ . The reason for this was that missed the initial part of the classical S shape of crystallization curve by chosen larger  $t_0$  due to faster crystallization at lower  $T_C$ . Consequently, the Avrami model was fit to all  $X_C$  data up to  $X_C = 0.2$  with the set offset value as 0.008 and the set the  $t_0 = 400$  s. Each fit to the data was attained with a good value of coefficient of determination (CoD) number as  $\text{CoD} \geq 0.98$ . The coefficient of determination number ranges from 0 to 1, and indicates the better fit with the value close to 1.

For further analysis, the monitored storage modulus  $G'(t)$  was normalized  $G'_{\text{norm}}$ . The Avrami model was fitted up to half of the  $G'_{\text{norm}}$  curves as displayed in Figure 6.3. The shape of the  $G'_{\text{norm}}$  evolution is known as a reflection of the overall crystallization in

consequence of  $T_C$  and deformation  $\gamma$  (Khanna 1993; Pogodina *et al.* 1999; Dötsch *et al.* 2003; Yu *et al.* 2009). Normalization of  $G'$  was done by following equation:

$$G'_{\text{norm}} = \frac{G'(t) - G'_0}{G'_\infty - G'_0} \quad (6.1)$$

where  $G'_0$  is the  $G'$  value just before the sample started crystallizing.

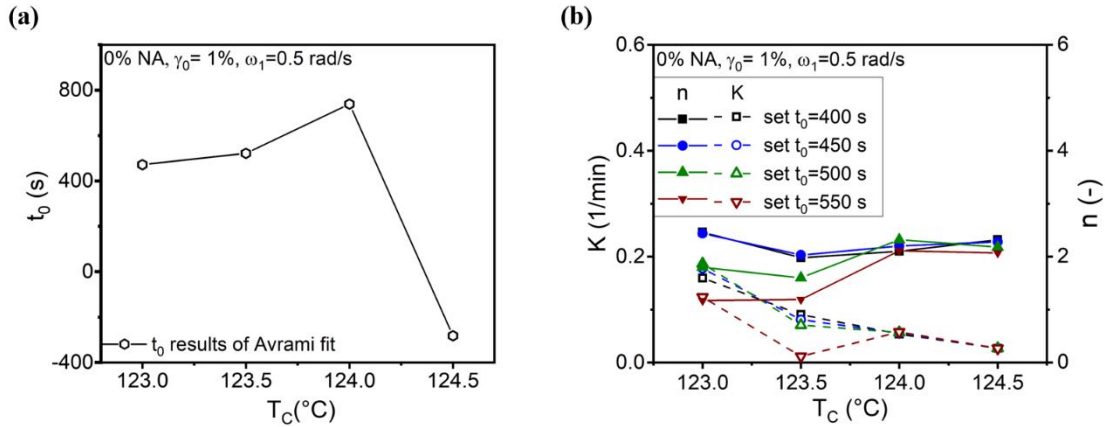


**Figure 6.2:** (a) The time zero  $t_0$ , the time of the beginning of the crystallization, results of in Avrami model as a variable parameter. (b) Chosen  $t_0$  effects on calculated Avrami rate parameter  $K$  and the exponent  $n$ . The resulting  $t_0$  for  $T_C = 124.5$  °C was a negative value that was obviously a defect. Equivalent fit parameters were determined for  $t_0$  to 400 and 450 seconds. The needed time to reach  $T_C$  was 400 seconds in our study regarding  $T_C$  range.

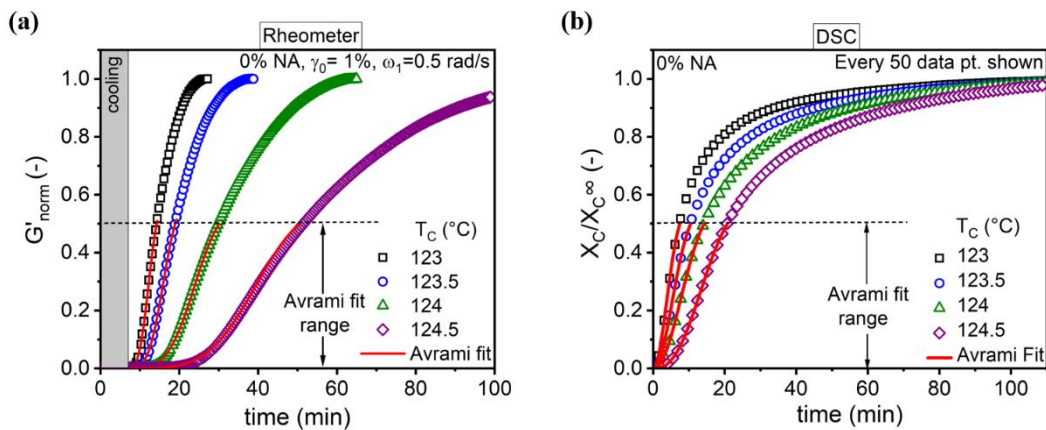


**Figure 6.3:** (a) Normalized  $G'_{\text{norm}}$  determined by the Rheo part of the RheoNMR, and (b) relative crystallinity ( $X_C/X_C^\infty$ ) evolution as a function of time as monitored by the DSC during isothermal crystallization at different crystallization temperatures  $T_C$  for neat HDPE sample called 0% NA.

The isothermal crystallization experiments were also done at the same  $T_C$  via DSC method with a cooling rate  $17$  °C/min that was the same cooling rate observed in RheoNMR measurement as displayed in Chapter 5, Figure 5.13 As mentioned in Chapter 5, the

cooling trend is divided into two regions as cooling and critical. This trend can be observed in almost all characterization techniques, The critical cooling part prevents to undershoot in the temperature from the target  $T_C$ . It is difficult to establish the same critical cooling rate for different analysis techniques. Therefore, the cooling rate was chosen as 17 °C/min for all DSC isothermal crystallization experiments displayed in Chapter 6. The relative crystallinity ( $X_C/X_C^\infty$ ) evolution by time depicted in Figure 6.3b. Calculated Avrami parameters separately from the Rheo and NMR part data of RheoNMR compared with the Avrami fit result of DSC data as seen in Figure 6.4.

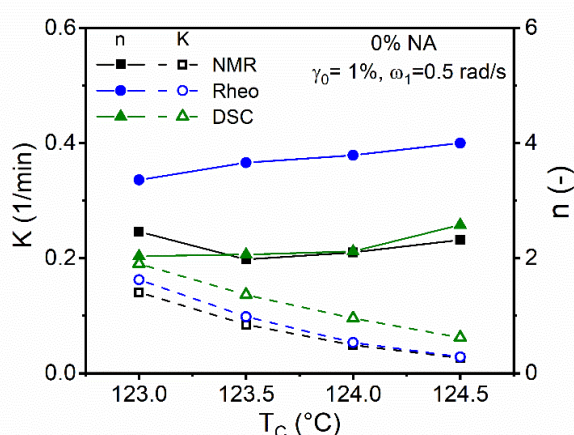


**Figure 6.4:** Comparison of calculated the Avrami rate parameter  $K$  and the exponent  $n$  depending on the  $T_C$  based on the isothermal crystallization data collected by NMR (see Figure 6.1b) and Rheo part (see Figure 6.3a) of RheoNMR and DSC (see Figure 6.3b) for 0% NA.

While Avrami exponent  $n$  reflects crystal growth mechanism e.g., heterogeneous and dimensionality of the crystals, the rate parameter  $K$  related to the nucleation rate, crystal growth rate. The  $K$  is extremely sensitive to  $T_C$  (see Chapter 3.2.3). The extracted  $K$  from the data determined Rheo and NMR part of the RheoNMR decreased a factor of  $\sim 5$  by an increase of  $\Delta T_C = 1.5$  °C. These indicate the high sensitivity of the PE crystallization sample towards  $T_C$  which was presumably as a result of increased nucleation at the early stage of crystallization for lower  $T_C$ . This trend in the  $K$  values determined from DSC data was slightly different, and values were  $\sim 0.04$  min<sup>-1</sup> larger compare to the results of the RheoNMR. The calculated  $K$  value from DSC data decreased to half within an increment of  $\Delta T_C = 1$  °C. In the DSC method sample size was 20 times smaller which eliminates the temperature gradients in the sample, and the critical cooling rate was different than RheoNMR which would affect crystallization kinetic. Moreover, the Avrami exponent  $n$

was found between 2 and 2.5 for NMR and DSC results. The exponent  $n$  value indicated a mixture of one-dimensional (needle shape) and a two dimensional (disc shape) crystal growth under the assumption of heterogeneous nucleation mechanism (Piorkowska and Rutledge 2013; Lorenzo *et al.* 2007). However, the resulted exponent  $n$  value from Rheo data was increasing from 3.3 up to 4 within the increase of  $\Delta T = 1.5$  °C. This  $n \geq 3$  values from Rheo data reflected a spherical crystal growth in the heterogeneous nucleation mechanism. This could be explained by varying the sensitivity scales in a sample for different methods. While the sensitivity of NMR relaxation is in local motion (0.2-2 nm) scale, this scale is macroscopic ( $\approx 1$  mm) in rheological measurement.

In addition to the Avrami model, the Foubert model (see Chapter 7 and Equation 7.5) was used to fit the complete crystallization curves. The Foubert model was developed to describe the temperature dependence of the crystallization parameter of the fat (Foubert *et al.* 2002; 2003). In this study, this model was used to describe HDPE crystallization behavior. Fitted crystallization curves monitored by different characterization techniques are presented in Figure 6.5. Better fitting performance (CoD  $\geq 0.99$ ) was achieved compared to the Avrami model with a quantitative description of complete isothermal crystallization behavior. The rate parameter  $\nu$  of the Foubert model (see Figure 6.5d) showed almost the same values with the rate value  $K$  of the Avrami model for data attained by NMR and Rheometer. However, the extracted rate parameter  $\nu$  from DSC data was almost half of the rate value of  $K$ . It is still possible to say that the trend of rate values achieved quite similar for both models. On the other hand, the exponent  $m$  values were found larger than 4 as seen in Figure 6.5d. Thus, it was not comparable with the exponent  $n$  of the Avrami model. The calculated  $m$  values from the DSC result was in between 28 and 87, which were not shown in Figure 6.5d. The reported  $m$  values were in the range between 3 and 6 for cocoa and milk butter at  $T_C = 20$  °C (Foubert *et al.* 2002). The  $m$  parameter was extracted as  $\sim 6$  for coconut fat at  $T_C = 19$  °C in Chapter 7. Although the missing physical explanation of the parameter of the Foubert model, rate value  $\nu$  was defined as the temperature dependence of the HDPE crystallization process as good as the Avrami rate parameter  $K$ . This study revealed that the Foubert model could be used to determine the rate of the overall polymer crystallization process.

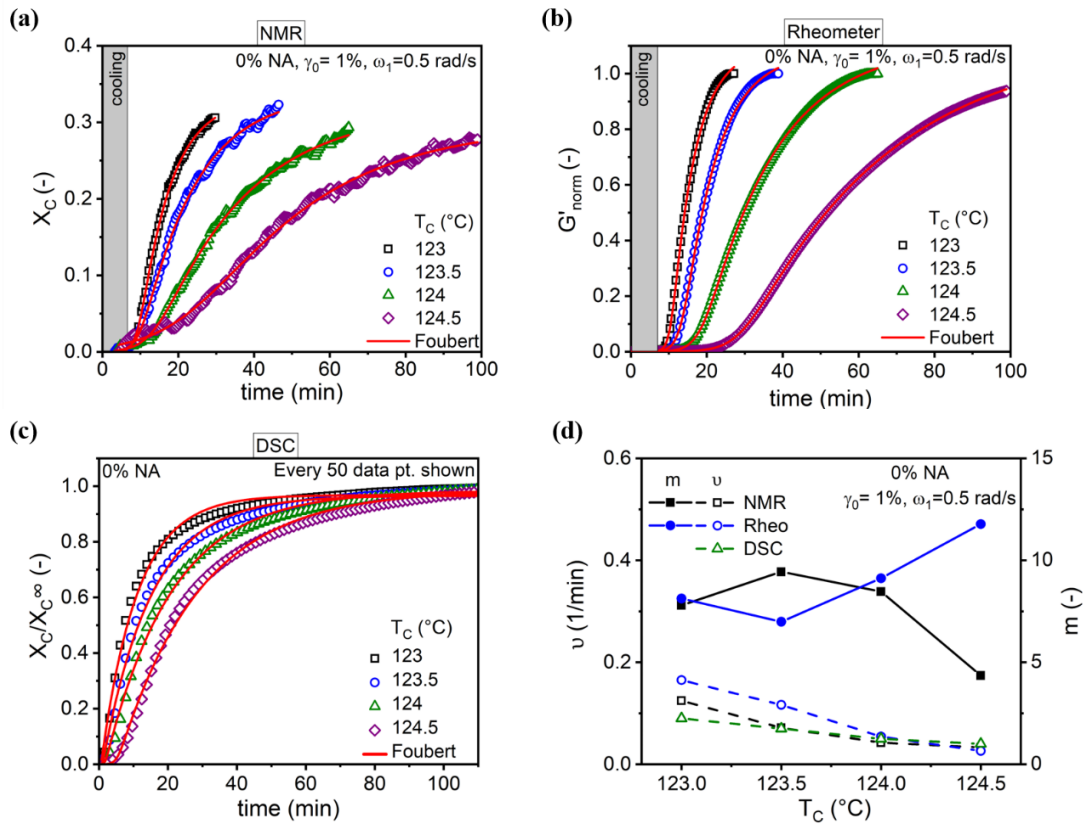


**Figure 6.5:** The Foubert model (see Chapter 7) applied (red line) to complete crystallization curves of 0% NA. (a) The crystallinity  $X_C$  determined by NMR part, and (b) the normalized  $G'_{norm}$  monitored via the Rheo part of the RheoNMR. (c) The relative crystallinity  $X_C/X_C^\infty$  development by time were determined via DSC. (d) Quantified kinetic parameters by the Foubert model. Parameters-  $m$ : exponent and  $v$ : rate constant.

Further analysis was done by the calculation of the activation energy  $E_C$  of segmental transport across to the crystallization site determined by using the Arrhenius approach (Khanna 1993). The activation energy of crystallization  $E_C$  depends on the degree of crystallinity and the  $T_C$  (Alvarez and Perez 2013). The slope of the plot of the rate of crystallization  $\ln K$  versus the reciprocal of temperature should give  $-E_C / R$  (Khanna 1993; Praveen *et al.* 2014). This linear regression of the experimental data based on the deduced Avrami rate parameter was plotted in Figure 6.6. The calculated  $E_C$  values were negative due to the crystallization process from the molten state of the sample (Khanna 1993). The extracted  $E_C$  values from the data of Rheo and NMR part of RheoNMR were -1530 kJ/mol and -1446 kJ/mol respectively. However, the calculated  $E_C$  value using DSC data was -974 kJ/mol. Wang and Zhang (2014) reported the  $E_C = -270$  kJ/mol for the non-isothermal crystallization of HDPE at  $X_C = 10\%$ , and the value increases to -70 kJ/mol at

$X_C = 80\%$ . Beside the commonly studied non-isothermal conditions, there are some studies for isothermal conditions as well. Blaine (2008) reported the  $E_C = -948$  kJ/mol for isothermal crystallization of PP based on the DSC experiment. On the other hand, the  $E_C$  of iPP was determined as  $-317$  kJ/mol by using the reported NMR data of the RheoNMR method in the study of Röntzsch *et al.* (2019). In that study, the  $K$  value of iPP decreased factor of 3 within raised  $\Delta T_C = 4$  °C. On the other hand, the factor of 3 decreased in the  $K$  value of HDPE in this study was observed within increased only of  $\Delta T_C = 1$  °C. In this manner, the difference in  $E_{C,HDPE}$  and  $E_{C,iPP}$  could be related to the high sensitivity of HDPE crystallization toward  $T_C$ .

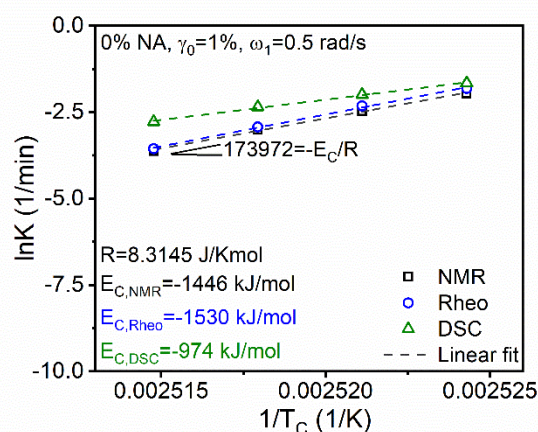


**Figure 6.6:** Comparison of calculated the activation energy of crystallization  $E_C$  values from the linear regression of the Avrami rate parameter  $\ln K$  versus inverse  $T_C$  from the obtained temperature dependency results of 0% NA via Rheo and NMR part of RheoNMR and DSC methods.

Moreover, the gel time  $t_{gel}$  can be taken as a reference state to see the influences of experimental conditions e.g.,  $T_C$  on materials properties (Schwittay *et al.* 1995). Figure 6.7 shows the direct correlation of both the  $t_{0.2}$  and the absolute crystallinity value  $X_{C,gel}$  at the  $t_{gel}$  with  $t_{gel}$  for different  $T_C$  in RheoNMR assay. The correlation between  $t_{0.2}$  and  $t_{gel}$  was achieved in a linearly related as  $t_{0.2} = 4t_{gel}$ . Additionally, the absolute crystallinity value  $X_{C,gel}$  was below 4% at  $t_{gel}$ . The relative crystallinity at gel point was reported for iPP as  $\sim 2\%$  (Pogodina *et al.* 1999). According to a study of Schwittay *et al.* (1995),  $X_{C,gel}$  lies between 6 and 15 % for iPP. A similar range was observed for iPP sample in the study of Pogodina and Winter (1998), and the Ph.D. study of Röntzsch

(2018). The extracted  $X_{C,gel}$  range for HDPE was found slightly lower compared to reported  $X_{C,gel}$  range for the iPP.

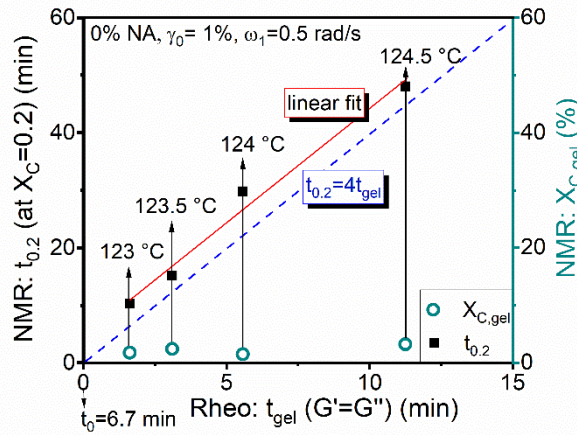


**Figure 6.7:** Direct correlation of the time of crystallization  $t_{0,2}$  at  $X_C = 0.2$  and the absolute crystallinity value  $X_{C,gel}$  at the crossover time  $t_{gel}$  with  $t_{gel}$  for different  $T_C$  assays of 0% NA by RheoNMR. The required time needed to reach  $T_C$  ( $t_0 = 6.7$  min) was removed for plotting Figure 6.6.

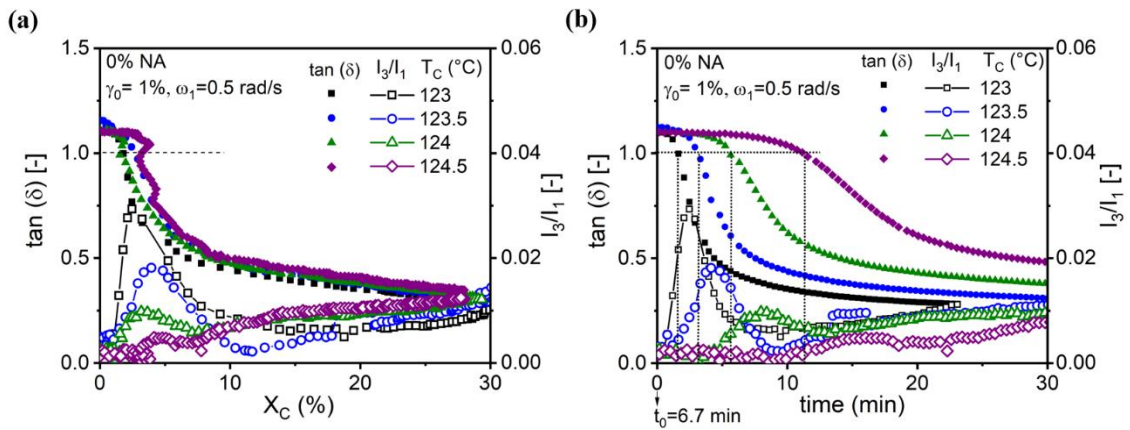


**Figure 6.8:** Loss tangent  $\tan(\delta)$  and relative third harmonic ( $I_3/I_1$ ), reflects nonlinearity, as a function of (a) crystallinity  $X_C$  and (b) time for the different  $T_C$  isothermal crystallization RheoNMR assays of 0% NA. The required time for cooling  $t_0 = 6.7$  min was removed for plotting Figure 6.8b.

Another quantity is the relative intensity of the third harmonic  $I_3/I_1$ . It is sensitive to physical changes during isothermal crystallization (Dötsch *et al.* 2003) and reaches a maximum around the gel point ( $G' = G''$ ). Additionally, the maximum of the  $I_3/I_1$  is also relevant with nonlinear rheological behavior. The relationship between nonlinearity and gel point could be related to the maximum fluctuation in the density (Pogodina *et al.*

1999). Besides, the maximum of  $I_{3/1}$  is related to the  $t_{\text{gel}}$  that can be extracted by the loss tangent  $\tan(\delta) = 1$  (Ratzsch *et al.* 2017; Rantzsch 2018). The  $\tan(\delta)$  and the  $I_{3/1}$  development with  $X_C$  and time during isothermal crystallization of the neat HDPE are visualized in Figure 6.8a-b. The maximum of the  $I_{3/1}$  was attained right after  $t_{\text{gel}}$  which can be approximately determined by the  $\tan(\delta) = 1$ .

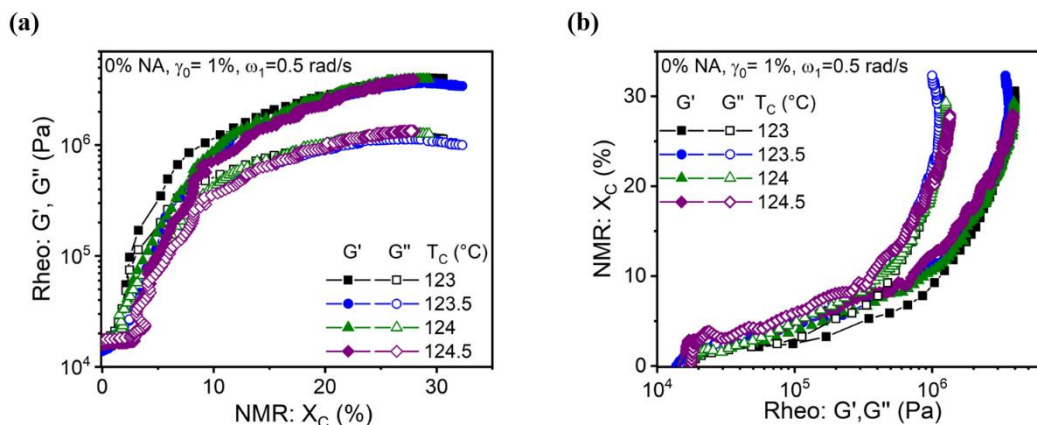


**Figure 6.9:** (a) Correlation of dynamic moduli ( $G'$ ,  $G''$ ) and crystallinity  $X_C$  and (b) vice versa.

Moreover, directly correlated dynamic moduli and crystallinity as a function of time under the same thermal and shear history condition were exhibited temperature dependence as displayed in Figure 6.9. Besides the shown correlations in Figure 6.9, another way of this correlation can be with the relationship between the reduced storage modulus  $\frac{G'}{G'_0}$  and  $X_C$  as depicted in Figure 6.10. Modeling of this directly correlated  $\frac{G'}{G'_0}$  and  $X_C$  can be done by the theories in Table 8.3 (see Chapter 8) based on the similarities between suspension and semi-crystal polymeric systems. In addition to these theories, another suspension model extended Einstein was reported by Rantzsch *et al.* 2019. This model is created by combining the Einstein model (see Table 8.3) and the power-law model (see Equation 7.3). The extended Einstein formula can be expressed as follows:

$$\frac{G'}{G'_0} = 1 + 2.5X_C + D'X_C^{C'} \quad (6.2)$$

where  $G'_0$  is the  $G'$  value at the  $t_0$ , the  $D'$  indicates the dynamic range of  $G'$ ,  $C'$  is related to the self-organization of growing crystals.

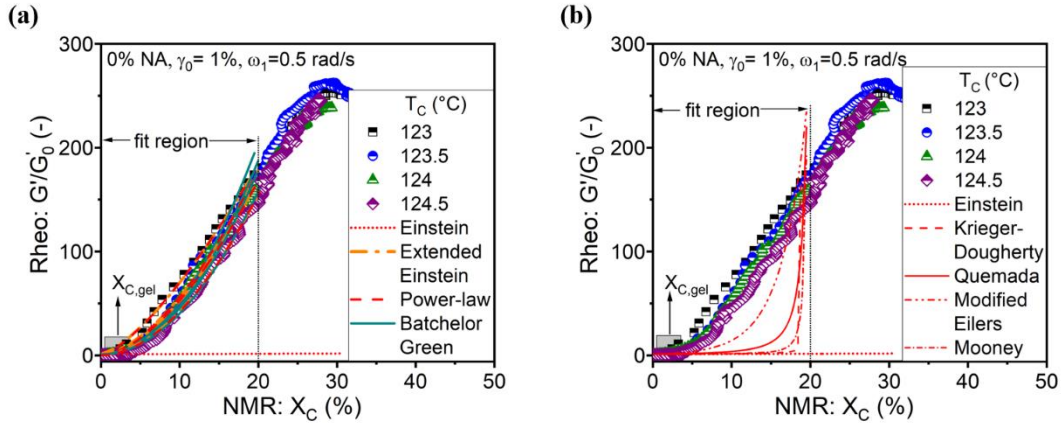


**Figure 6.10:** Correlation among the reduced storage modulus  $\frac{G'}{G'_0}$  and crystallinity  $X_C$  for different  $T_C$ . Suspension models describe the plot up to  $X_C = 20\%$  (a) Einstein, extended Einstein (Equation 6.2), power-law, Batchelor-Green (see Table 6.2). (b) Tried other suspension models that did not describe the correlated plot: Einstein, Krieger-Dougherty, Quemada, Modified Eilers, Money (see Table 8.3).

**Table 6.2:** Results of the fitted models in Figure 6.10a.

Fitted models Experiment Conditions	Extended Einstein (Equation 6.2)		Batchelor-Green $\frac{G'}{G'_0} = 1 + 2.5X_C + k_H\phi^2$	Power-law $\frac{G'}{G'_0} = \psi X_C^p$	
	$D'$	$C'$	$k_H$	$p$	$\psi$
$T_C$					
123	1738	1.4	5086	1.38	1690
123.5	2667	1.68	4660	1.65	2572
124	2637	1.71	4425	1.67	2480
124.5	3401	1.92	3907	1.88	3224

Suspension models were fitted up to  $X_C = 20\%$  (see Figure 6.10). The Einstein model describes the very dilute suspension system (Einstein 1906, 1911). Therefore, Einstein model shows a good fit up to  $X_C = 4.5\%$ . Although the models Mooney, Krieger-Dougherty, Modified Eilers and Quemada were proposed for concentrated suspensions, they did not describe the isothermal crystallization of neat HDPE. Other suspension models such as Batchelor-Green, power-law, extended Einstein models provided good fits until  $X_C = 20\%$ . Table 6.3 shows the extracted fit parameters for different  $T_C$ . The exponents  $C'$  and  $p$  were in a similar trend with increasing values by raised  $T_C$ .

Additionally, the parameter  $D'$  and  $\psi$  also showed similar trends. Values  $D'$  were calculated in the range of 3 to ~5 % larger compared to  $\psi$ . The Batchelor-Green model's parameter  $k_H = \sim 6$  was known value for Brownian motion dominated suspension systems (Mendoza and Santamaría-Holek 2009). The extracted  $k_H > 6$  values may be related to crystal size, the impingement of the crystal particles and high the nucleation density in the crystallizing PE. Experimental results showed that increasing  $T_C$  decreased the  $k_H$  value.

### 6.3.2 Thermal behavior of the synthesized HDPE

The used HDPEs in this section were synthesized by Patrick-Kurt Dannecker (Institute of Organic Chemistry, KIT) with using the ring-opening metathesis polymerization (ROMP) (see Chapter 9), and they are called PE-1 and PE-2. The thermogravimetric (TGA) analysis of PE-1 and PE-2, as displayed in Figure 6.11, was done to know the amount of the metallic based catalyst residual. Results were compared with the commercial neat HDPE (0% NA). All three HDPE samples were found stable up to 400 °C. The remained masses were less than 3 % for all the PE samples at 780 °C.

The RheoNMR isothermal quiescent crystallization experiments were exerted at different  $T_C$  to investigate the temperature dependency of crystallization for the PE-1, PE-2 samples with the same temperature routine as represented in Figure 5.5. The evolution of the dynamic moduli and crystallinity as a function of the time were monitored by the RheoNMR method. Figure 6.12 depicts an isothermal crystallization behavior of the PE-1 and PE-2 samples for the varying  $T_C$  at  $\gamma_0 = 1\%$  and  $\omega_1 = 1$  rad/s. The used experimental condition details in the NMR part was noted in Chapter 5. As a point of the theory that PE with larger  $M_w$  crystallizes slower compare to samples with low  $M_w$  due to less chain mobility (Peacock 2000). The  $X_C$  level remains constant until  $M_n \approx 10^5$ , and then, it decreases with increasing  $M_n$  for the linear PE (Mandelkern 2004b). The results support the theory with the low  $M_w$  sample PE-2 crystallized faster than higher  $M_w$  sample PE-1. While the maximum crystallinity  $X_C^\infty$  was ~84% for PE-2 at  $T_C = 124$  °C, the  $X_C^\infty$  was ~80% for PE-1. In the previous section for the same  $T_C = 124$  °C, the  $X_C^\infty$  was ~35% for the commercial HDPE sample (0% NA).

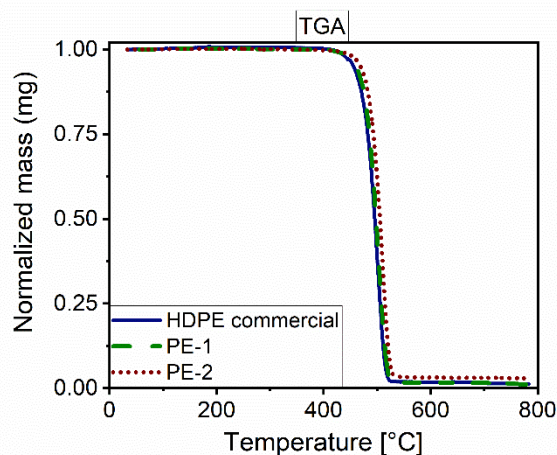


**Figure 6.11:** The results of thermogravimetric analysis (TGA) for commercial HDPE (0% NA), PE-1, and PE-2.

All  $X_C$  and  $G'_{\text{norm}}$  curves were fitted well with the Avrami model up to 50% of the final crystallinity as  $X_C = 0.4$ . Although the crystallization observed during cooling, it was not a stepwise increase in the  $X_C$  until the temperature reached  $T_C$  as it was the behavior in the previous section. Thus, the set  $t_0$  the parameter was not used when the Avrami model was fitted to the data. The Foubert model was also fitted to the same curves for analyzing the overall crystallization rate. It is of interest at this point to compare the derived Avrami and the Foubert model fit parameters as displayed in Figure 6.13. Regarding the extracted  $K$  parameter, (see Figure 6.13a), the PE-2 sample crystallized almost two times faster than PE-1. Lowering the  $T_C$  by 1 °C accelerated the crystallization factor by 2 for PE-1 and by 1.5 for PE-2. Additionally, extracted Foubert rate parameters  $v$  (see Figure 6.13b) from NMR data showed that PE-1 and PE-2 crystallized two times faster crystallization for a 1 °C reduction in the  $\Delta T_C$ . Determined  $v$  parameter from  $G'_{\text{norm}}$  curves indicated that when the  $\Delta T_C$  was reduced 1 °C for both samples, overall crystallization accelerated factor by 1.5. The extracted Avrami index  $n$  values from  $X_C$  curves are shown in Figure 6.13c, and values were remained constant at  $\sim 2.4$  in the used temperature range. These results indicated a disc shape crystal growth under the assumption of a heterogeneous nucleation mechanism. However, extracted  $n$  values from  $G'_{\text{norm}}$  curves increased from 3.5 to 7 for PE -1 and from 2.3 to 4 for PE-2 within 1.5 °C increase in  $\Delta T_C$ . The  $T_C$  effect on the  $n$  values is strong for extracted values from  $G'_{\text{norm}}$ . Since all the  $X_C$  curves reached the final plateau  $X_C^\infty$ , the correlation between the half time  $t_{1/2}$  as a function of  $t_{\text{gel}}$  was possible, and this relationship is shown in Figure 6.14. The correlation between  $t_{1/2}$  and  $t_{\text{gel}}$  was

achieved in a linearly related as  $t_{0.2} = \sim 3t_{\text{gel}}$ . Besides, Figure 6.14b shows that the absolute crystallinity  $X_{C,\text{gel}}$  at  $t_{\text{gel}}$  was stable, and the determined  $X_{C,\text{gel}} < 4\%$  for both samples.

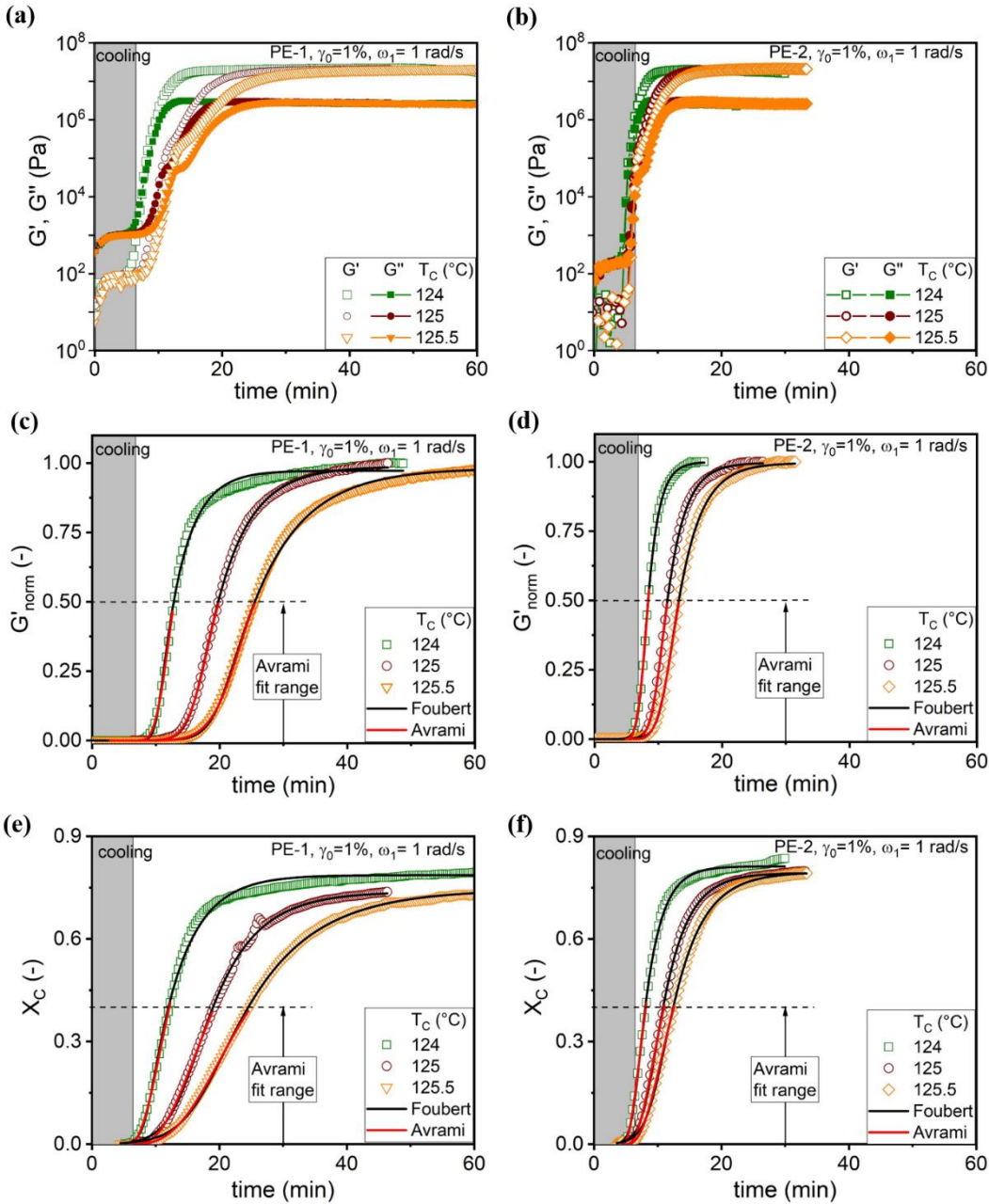


**Figure 6.12:** (a)-(b) The dynamic moduli ( $G'$  and  $G''$ ), and (e)-(f) crystallinity ( $X_C$ ) evolution as a function of time for varying  $T_C$  for PE-1, PE-2. (c)-(d) Normalized  $G'_{\text{norm}}$  (see Equation 6.1) during isothermal crystallization of PE-1 and PE-2. Results were monitored by RheoNMR.

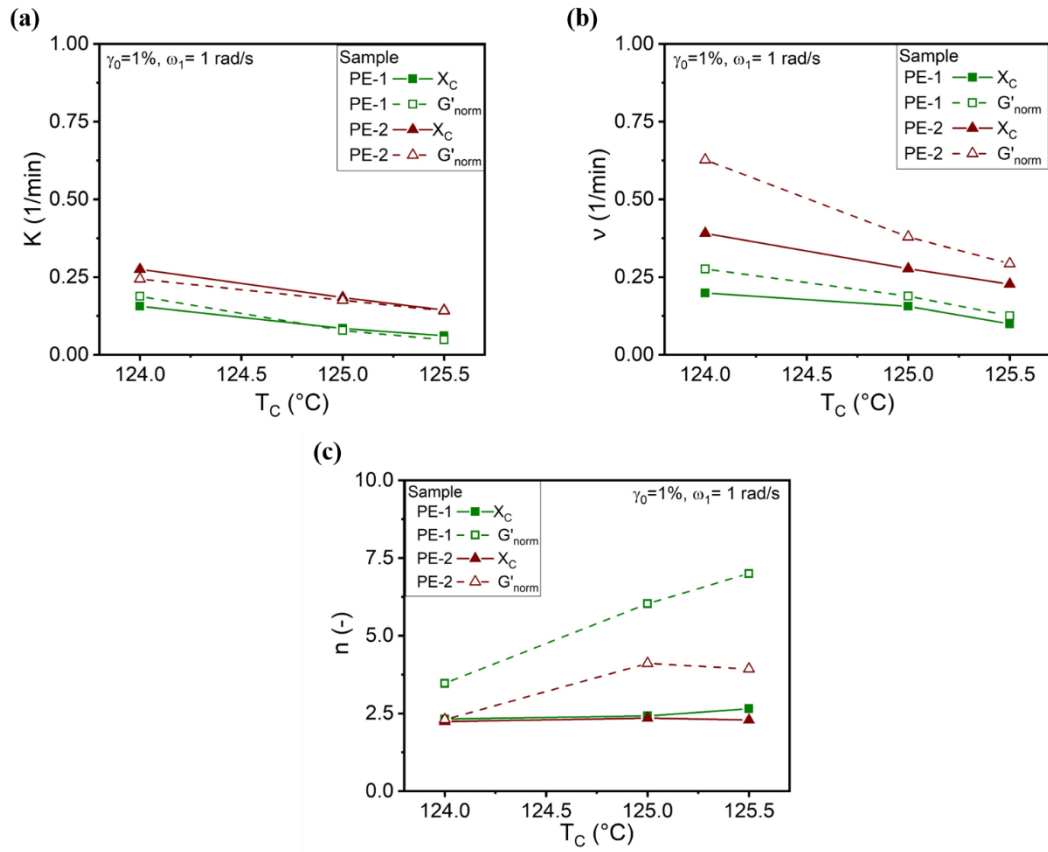


**Figure 6.13:** Comparison of extracted (a) Avrami rate parameter  $K$ , (b) Foubert rate parameter  $v$  and (c) the Avrami exponent  $n$  as a function of the  $T_C$  based on the  $X_C$  data determined by the NMR and the  $G'_{norm}$  monitored by Rheo part of RheoNMR.

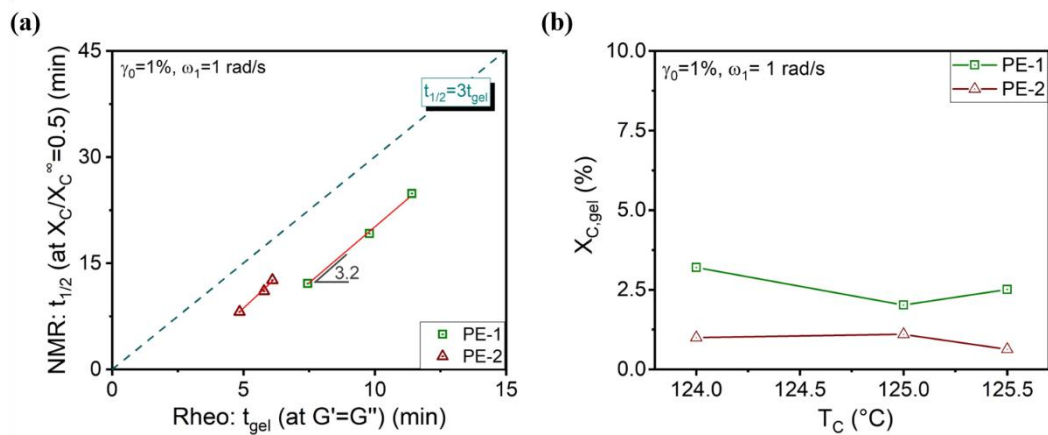


**Figure 6.14:** (a) Direct correlation of half time of crystallization  $t_{1/2}$  and  $t_{gel}$  for varying  $T_C$ . (b) The crystallinity value  $X_{C,gel}$  at the  $t_{gel}$  as a function of the  $T_C$  for the RheoNMR isothermal crystallization of synthesized PE samples.

### 6.3.3 Thermal behavior of the neat HDPE and HDPE/NA blends

Nucleating agents (NAs) are commonly used to raise  $T_C$  and reduce the cycle time in the injection molding process. As a result of NA addition into the polymer, a higher amount of smaller evenly sized crystals occur compare to the neat polymer material. The higher amount of the NA increases the nucleation density; however, it is not in a linear correlation. Commonly used NA concentration range is 0.5 to 5 wt% (Seven *et al.* 2016). Additionally, it was reported that the addition of NA into polymer accelerates the primary crystallization rate, although the secondary crystallization rate stays constant (Mandelkern 2004a).

The temperature dependence of the isothermal crystallization for varying HDPE/NA blends is important to understand the primary crystallization kinetics as a function of the added NA content. Therefore, the RheoNMR isothermal crystallization experiments were carried out under varying  $T_C$ . Thermal and shear history of the sample cleaned every time with keeping the sample for 20 min at 180 °C. When the neat HDPE sample loaded, temperature-dependent and flow-induced crystallization (see Chapter 6.4.3) experiments were all done on the same sample. Then, the sample was taken out from the top of the setup and another sample e.g., 0.1% NA was loaded. Thus, the RheoNMR set up was never disassembled until the end of all the mentioned experiments in Chapter 6.3.3 and Chapter 6.4.3. Therefore, monitored results were comparable with each other. While the monitored dynamic moduli development by the time of neat and HDPE/NA blend samples are shown in Figure 6.15, the simultaneously measured  $X_C$  evolution during crystallization is shown in Figure 6.16. By increasing the NA content to 3wt%, the maximum of the  $G'$  modulus ( $G'_{\infty}$ ) decreased from  $4 \times 10^6$  to almost  $2 \times 10^6$  Pa. When the  $G'$  of 3% NA sample reached maximum  $G'_{\infty}$ , a sharp decrease was observed in the  $G'$ . This is because of the lost contact between the rheometric tool and the sample due to shrinkage of the sample. Thus, the slippage was observed and shown with grey color in Figure 6.15f. For all the HDPE/NA blends although the dynamic moduli reached a maximum stable value  $G'_{\infty}$ , further rising  $X_C$  curves indicated a progressing secondary crystallization. The crystallization of the samples started during cooling in the  $X_C$  results. A stepwise like increase was observed in the  $X_C$  results during cooling as observed similar behavior in Chapter 6.3.1. This made the Avrami model fitting difficult to the data. Thus,

the set value of  $t_0 = 0.008$  parameter was used when the Avrami model was fitted to the  $X_C$  data (see Figure 6.16) up to  $X_C = 0.2$ .

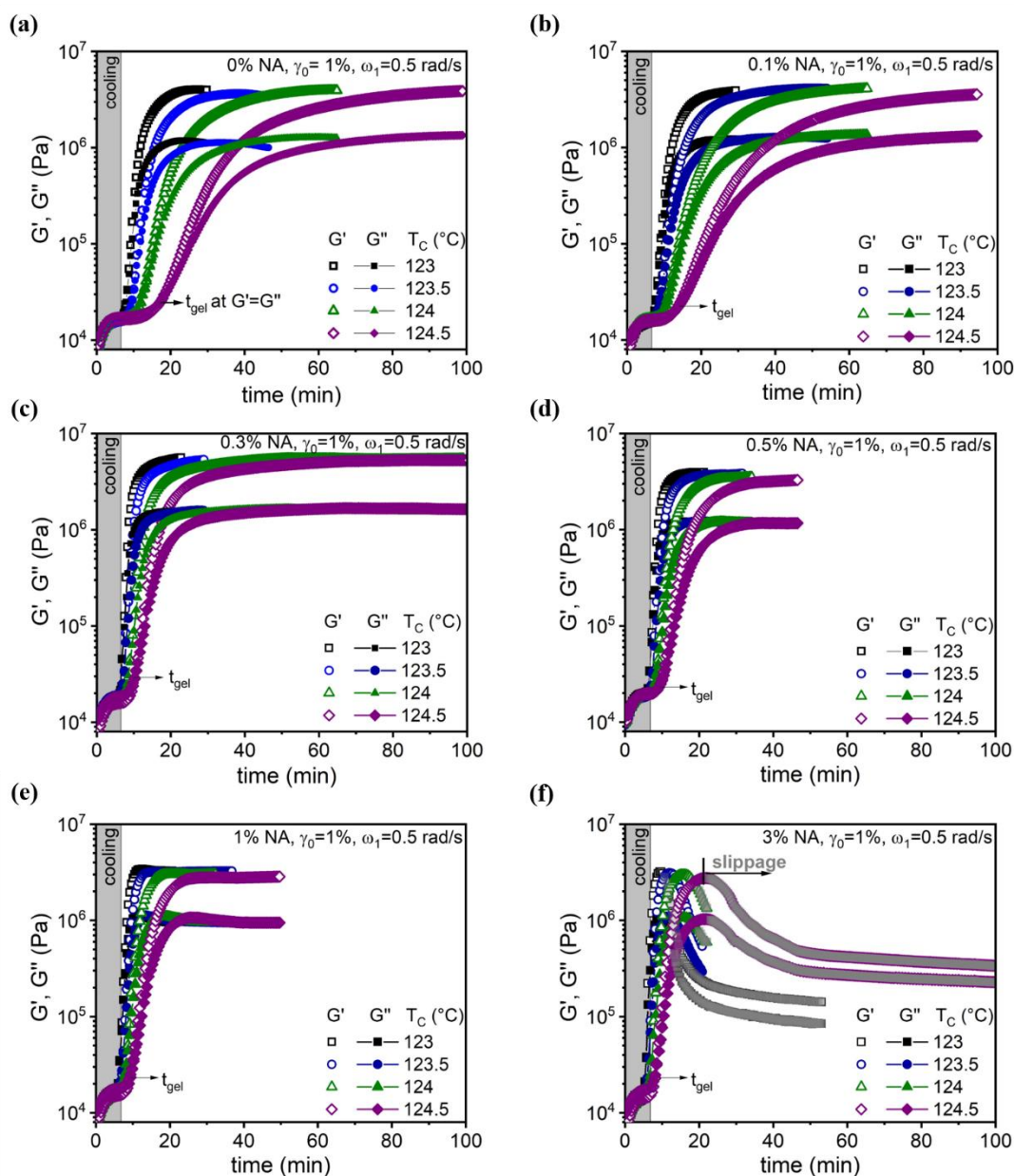


**Figure 6.15:** The dynamic moduli ( $G'$  and  $G''$ ) evolution as a function of time at varying  $T_C$  for (a) 0% NA (neat HDPE) and HDPE/NA blend samples as (b) 0.1% NA, (c) 0.3% NA, (d) 0.5% NA, (e) 1% NA, and (f) 3% NA.

The Avrami model was also fitted to the  $G'_{\text{norm}}$  curves up to half of them as shown in Figure 6.17. Additional to the RheoNMR experiment, the DSC method was used as a supporting characterization technique. The observed cooling rate (17 °C/min) in the

sample for the RheoNMR experiment was used in the DSC experiments. The DSC results for the neat and HDPE/NA blends are shown in Figure 6.18.

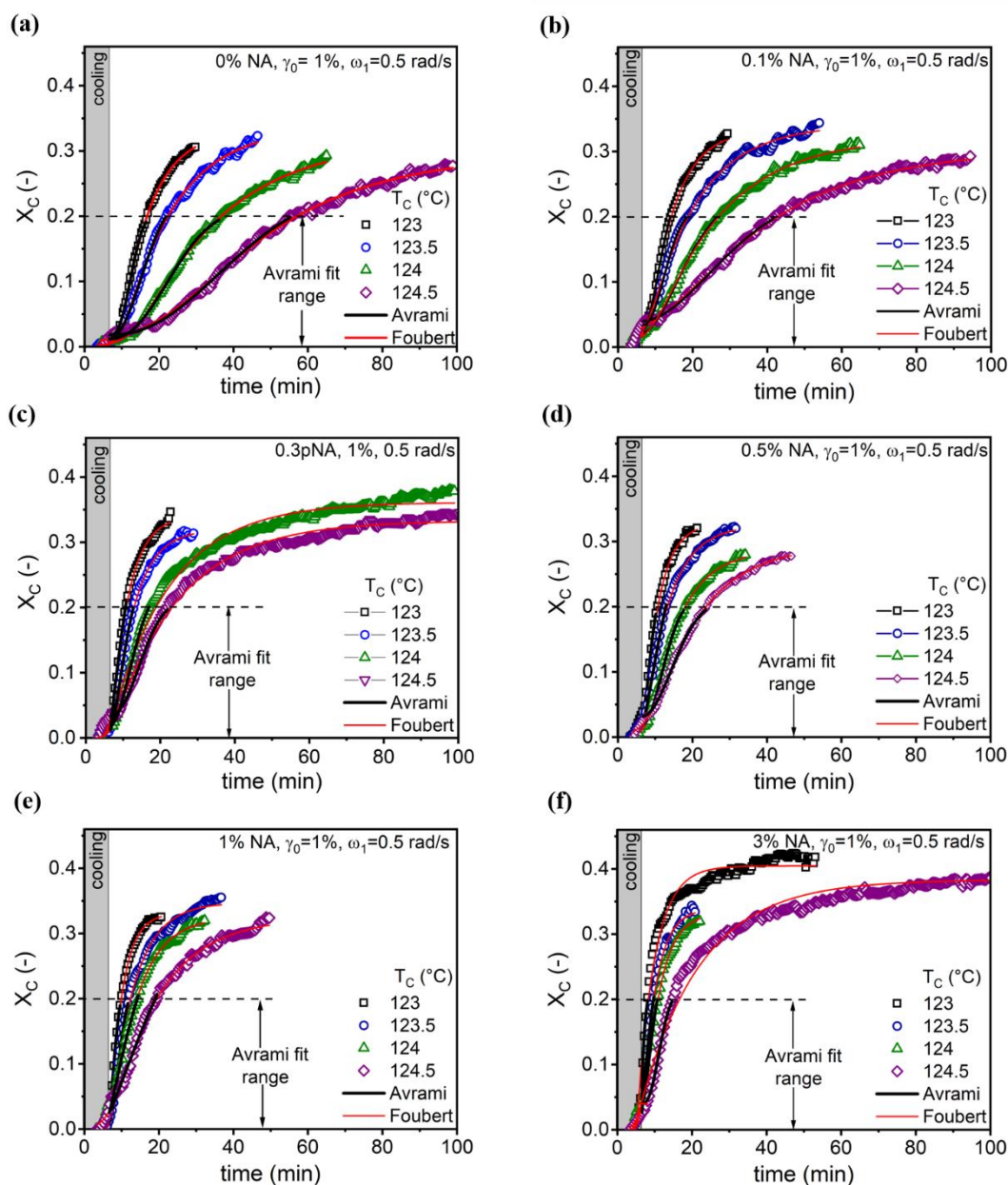


**Figure 6.16:** The crystallinity ( $X_C$ ) evolution as a function of time at different  $T_C$  for (a) 0% NA (neat HDPE) and HDPE/NA blend samples as (b) 0.1% NA, (c) 0.3% NA, (d) 0.5% NA, (e) 1% NA, and (f) 3% NA.

Calculated relative crystallinity  $X_C/X_C^\infty$  was fitted by Avrami model up to  $X_C/X_C^\infty = 0.5$ . Additionally, the Foubert model was fitted to complete crystallization curves shown in Figure 6.16, Figure 6.17 and Figure 6.18 for all samples to determine the overall crystallization rate. The deduced kinetic parameters from DSC results were compared

with the calculated kinetic parameters from  $X_C$  and  $G'_{norm}$  data. The rate parameters are displayed in Figure 6.19.

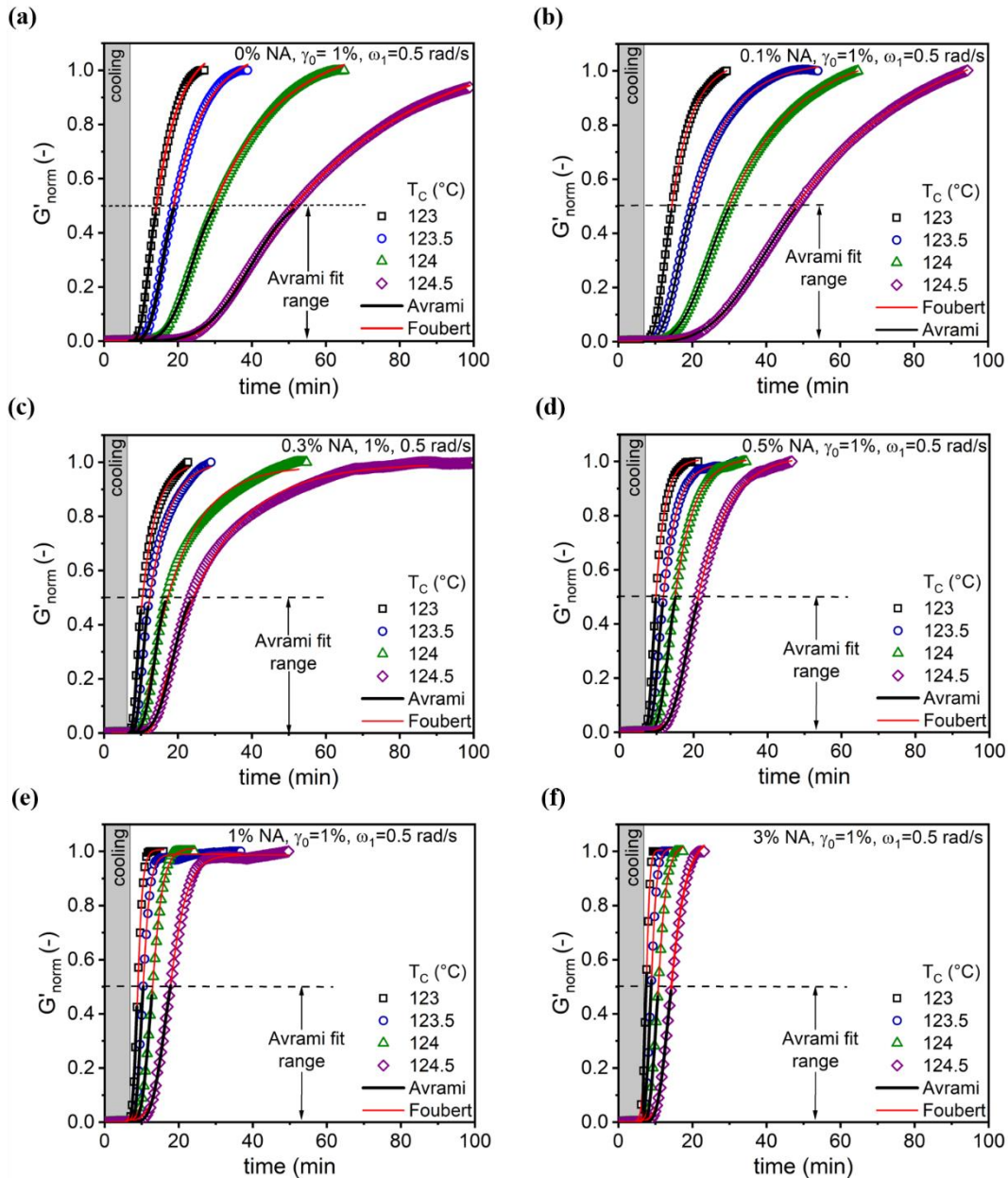


**Figure 6.17:** Normalized storage modulus ( $G'_{norm}$ ) evolution as a function of time at varying  $T_C$  for (a) 0% NA (neat HDPE) and HDPE/NA blend samples as (b) 0.1% NA, (c) 0.3% NA, (d) 0.5% NA, (e) 1% NA, and (f) 3% NA.

In all methods, the rate of crystallization  $K$  was accelerated by increasing NA content in the HDPE sample. This behavior manifested itself as a decrease in  $T_C$  as well. The Avrami and Foubert models could not be precisely fitted up to 50% of the final value in  $X_C$  and

$G'_{\text{norm}}$  data for the sample 3% NA due to the fast crystallization which caused fewer data points. Therefore, the calculated rate parameter was either low or absent (see Figure 6.19a-b-e-f). The calculated rate parameter  $\nu$  by fitting complete curves of Rheo data showed the largest value as  $\sim 2.3$  for 3% NA among the sample set. The Foubert model provided a good description of Rheo data with  $\text{CoD} \geq 0.99$  than NMR and DSC data. The results suggested that the addition of NA possibly promoted the number of nucleation.

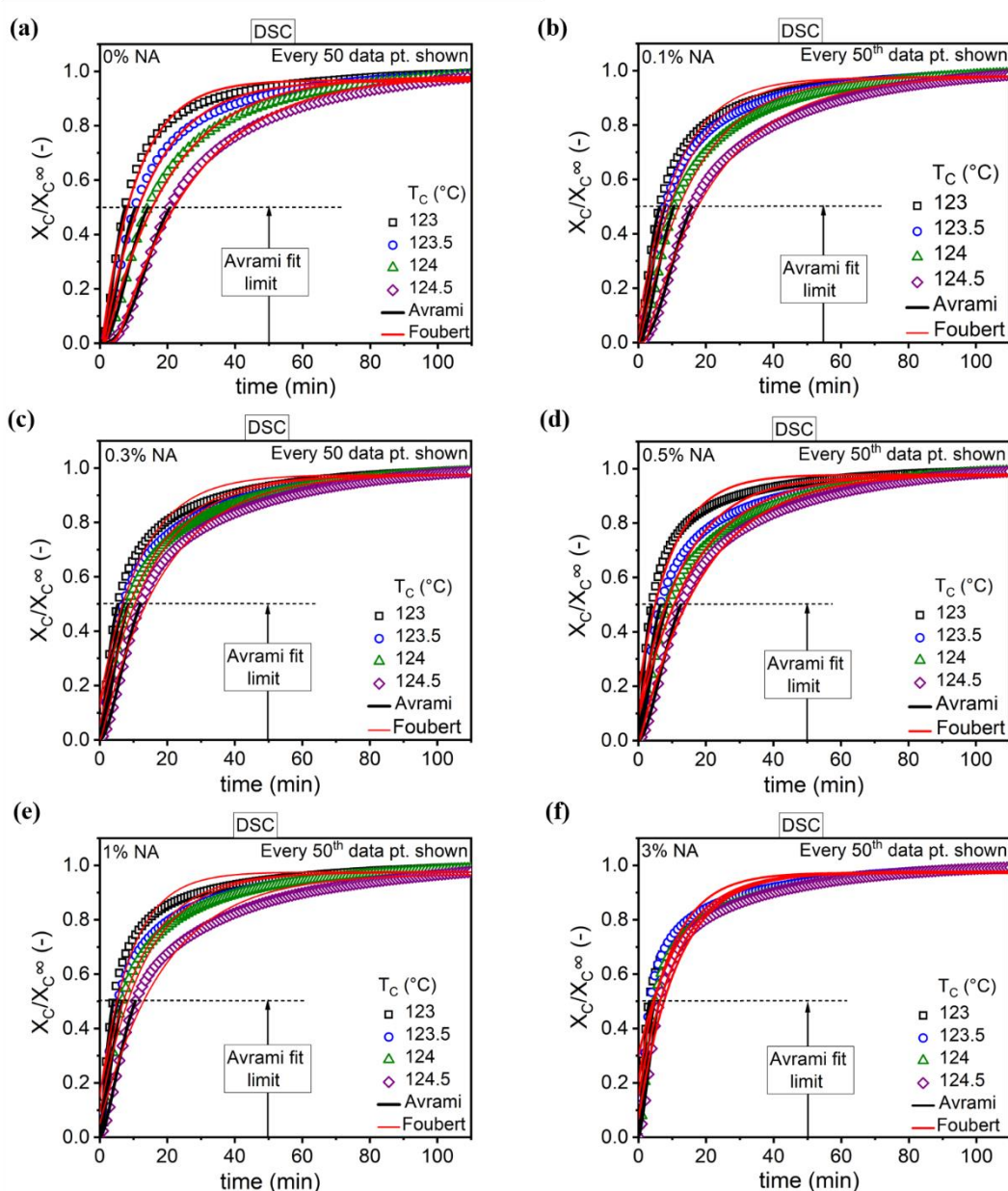


**Figure 6.18:** The relative crystallinity ( $X_C/X_{C^\infty}$ ) development as a function of time determined by the DSC measurement at varying  $T_C$  for (a) 0% HDPE (neat HDPE) and HDPE/NA blend samples as (b) 0.1% NA, (c) 0.3% NA, (d) 0.5% NA, (e) 1% NA, and (f) 3% NA.

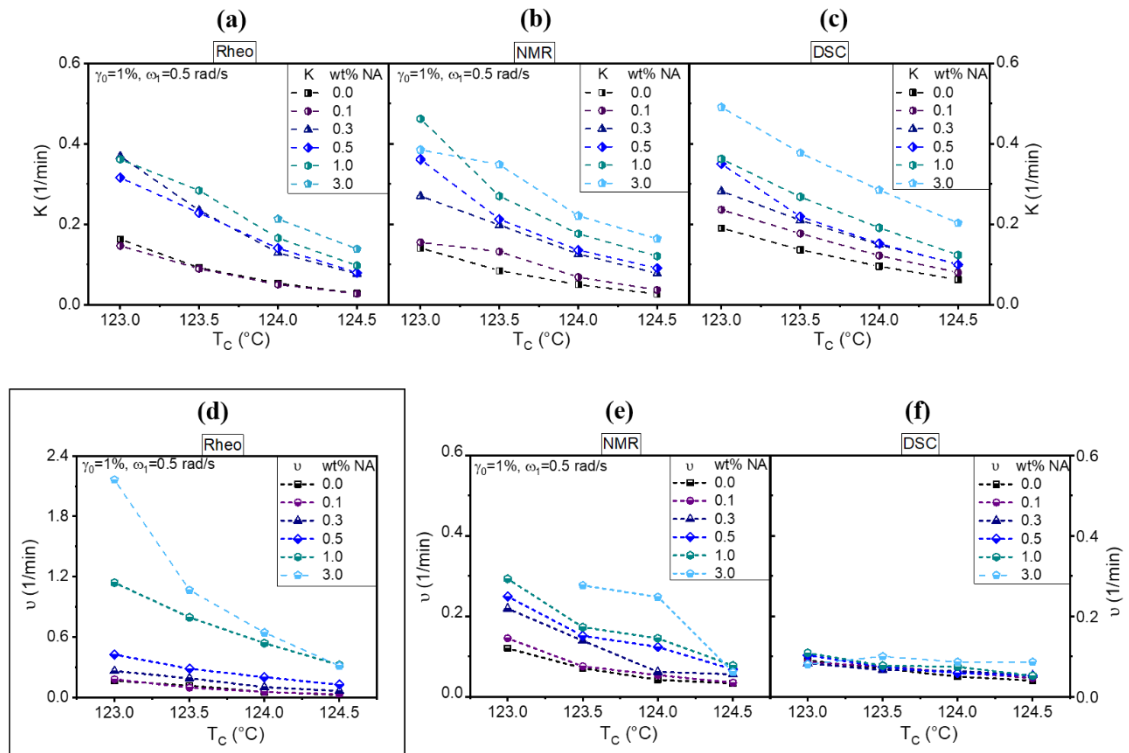


**Figure 6.19:** Rate parameters for neat HDPE and HDPE/NA blends by Avrami model from the data of (a) Rheo and (b) NMR part of RheoNMR method and additionally (c) DSC method. Calculated the overall crystallization rate parameter via the Foubert model fitting to the data of (d) Rheo and (e) NMR part of the RheoNMR and (f) DSC method. The scale of y ax in Figure 6.19d is different than others. Parameters-  $K$ : Avrami rate and  $v$ : Fobert rate constant.

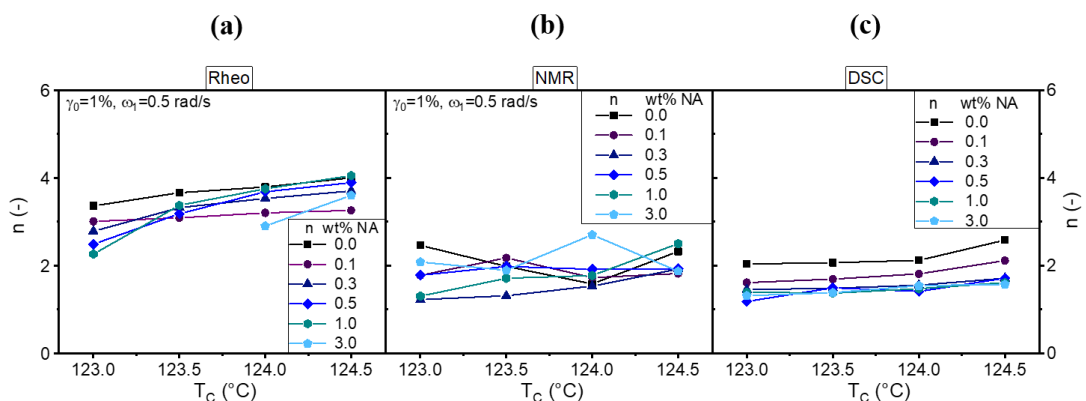


**Figure 6.20:** Comparison of the calculated Avrami exponent  $n$  based on (a) Rheo and (b) NMR part of RheoNMR, and (c) DSC data at varying  $T_c$  for 0%NA and HDPE/NA blends.

It is well known that, when NA is present, the nucleation mechanism becomes heterogeneous (Okada *et al.* 2007; Piorkowska and Rutledge 2013). Depending on its content in the polymer, the presence of NA in the polymer may complicate the crystal growth because it limits normal crystal growth (Lee *et al.* 2008). Figure 6.20 shows a

comparison of the calculated Avrami exponent  $n$  values based on the NMR, Rheo and DSC data. Decreasing  $T_C$  caused a slight reduction in  $n$  values as seen in Figure 6.20a-c. The dimensional  $n$  tended to a decrease by increasing NA content up to the 0.3 wt% and stayed stable for further increased NA content (see Figure 6.20c). While the calculated  $n$  values from Rheo data were larger than 3 at 124.5 °C, the extracted  $n$  values from NMR and DSC results were slightly smaller i.e.,  $\sim 2$ .

Another measure is that the activation energy of crystallization ( $E_C$ ) values of the primary crystallization of the HDPE/NA blend. Previous studies on  $E_C$  values have been commonly reported on the changes by additive content under the non-isothermal crystallization conditions. Wang and Zhang (2014) reported the  $E_C = -250$  kJ/mol for neat HDPE, and this value decreased up to  $-420$  kJ/mol for HDPE/TiO<sub>2</sub> at  $X_C/X_C^\infty = 10\%$  under non-isothermal condition. Huang *et al.* (2008) reported similar behavior as observed decreasing  $E_C$  trend at a given  $X_C/X_C^\infty$  with comparison of neat HDPE and HDPE/CaCO<sub>3</sub> blend under again non-isothermal conditions. Beside the non-isothermal studies, Lee *et al.* (2008) reported the  $E_C$  values under isothermal crystallization of polylactic acid (PLA)/clay nanocomposite and PLA/clay/regenerated cellulose fiber (RCF) composite as  $-57.52$  and  $-108.06$  kJ/mol, respectively. The results suggested that the PLA/clay/RCF hybrid composite was more temperature-dependent, although the observed half time  $t_{0.5}$  of crystallization was shorter at higher  $T_C$  for PLA/clay nanocomposite.

The changes in deduced  $E_C$  values as a function of the NA content are depicted in Figure 6.21. The extracted  $E_C$  from DSC data stayed relatively constant at  $-1000$  kJ/mol within the relative error  $\pm 10\%$ . The calculated  $E_C$  values from RheoNMR data (Rheo and NMR data) increased by rising NA content in the HDPE/NA blend. These results can be interpreted that the temperature dependence of the crystallization for samples 0% NA, 0.1% NA and 0.3% NA was higher than the others. This interpretation can be supported with the following correlation between  $t_{0.2}$  and  $t_{gel}$  for neat HDPE and HDPE/blends as seen in Figure 6.22. In this correlation, the distance between the data of neat HDPE for varying  $T_C$  was the largest. Then, the distance between the data was decreasing by increasing NA content in HDPE/NA blends. This difference in the  $E_C$  for Rheo and the

NMR data of the RheoNMR and DSC method is presumably relevant with the temperature gradient in the larger RheoNMR sample amount.

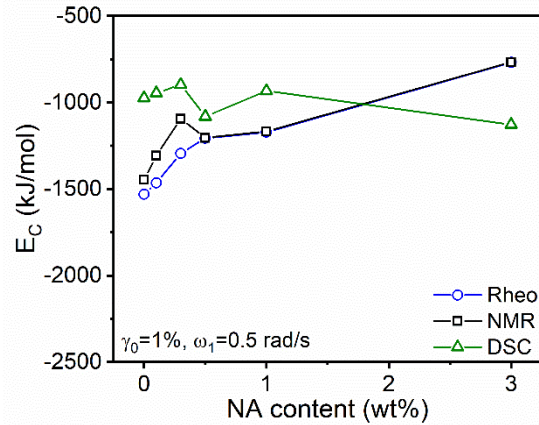


**Figure 6.21:** Comparison of the deduced the activation energy of crystallization ( $E_c$ ) values for the primary crystallization based on the data of Rheo, NMR and DSC method as a function of NA content in HDPE/NA blends.

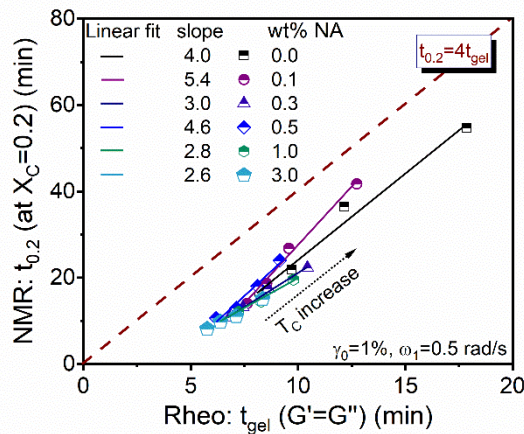


**Figure 6.22:** Direct correlation of the time of crystallization  $t_{0.2}$  at  $X_C = 0.2$  with  $t_{gel}$  for varying  $T_C$  in between 123 and 124.5 °C assays of RheoNMR for 0% NA and HDPE/NA blends.

Additionally, a linear relationship was determined between  $t_{0.2}$  and  $t_{gel}$  for varying  $T_C$  as displayed in Figure 6.22. The slope of the data for each sample was between 5.4 to 2.6. Except for samples 0.1% NA and 0.5% NA, the slope decreased by increasing the NA ratio in HDPE. Addition of 3 wt% NA into HDPE sample decreased  $t_{gel}$  to half and  $t_{0.2}$  to almost one third at constant  $T_C$ . In this correlation, not only a decrease in both  $t_{0.2}$  and  $t_{gel}$  was achieved, but also the time values  $t_{0.2}$  and  $t_{gel}$  became closer to each other for varying  $T_C$  by increasing the NA amount in the HDPE sample.

The analysis was extended to correlate the  $I_{3/1}$  with  $X_C$  as seen in Figure 6.23a. The peak maximum was observed in  $I_{3/1}$  at around the  $t_{\text{gel}}$ , which was equivalent with the time at the loss tangent  $\tan(\delta) = 1$  ( $t_{\tan(\delta)}$ ). Therefore, the peak value of  $I_{3/1}$  and  $t_{\tan(\delta)} = t_{\text{gel}}$  correlation can be shown in Figure 6.23b. Resulting data showed an exponential decay like change that decreasing the peak maximum value of nonlinearity ( $I_{3/1}$ ) and meanwhile increasing the  $t_{\tan(\delta)} = t_{\text{gel}}$  was observed by lowering the NA amount in HDPE and by decreasing  $T_C$ .

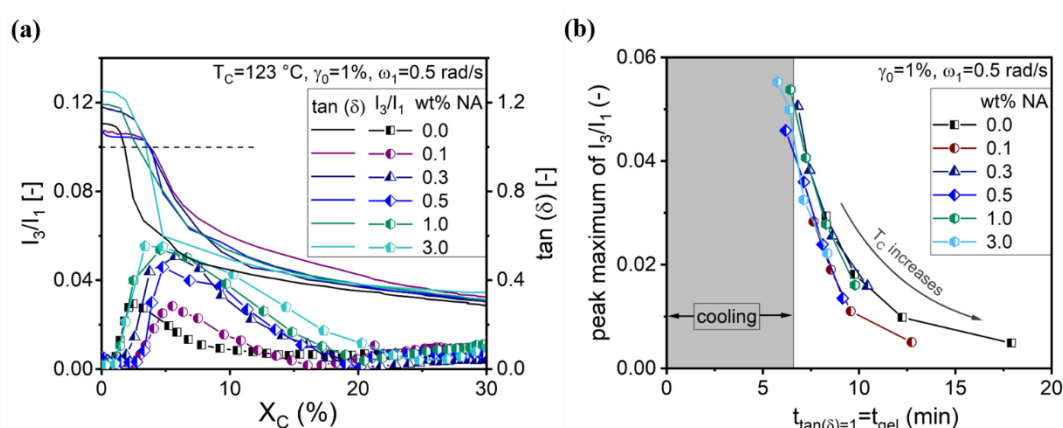


**Figure 6.23:** (a) The relative intensity of third harmonic  $I_{3/1}$  change by  $X_C$  evolution of 0% NA and HDPE/NA blends. (b) The peak maximum of the  $I_{3/1}$  as a function of the  $t_{\tan(\delta)} = t_{\text{gel}}$  for varying  $T_C$  results of 0% NA and HDPE/NA blends.

Another aspect of crystallization dynamic of HDPE/NA blends was the correlation of the reduced storage modulus  $\frac{G'}{G'_0}$  with  $X_C$  which can be described well by fitting some of the suspension models up to  $X_C = 20\%$  as seen in Figure 6.24. Especially the power-law and extended Einstein models showed a better fitting performance to the HDPE/NA blends data with  $\text{CoD} \geq 0.99$  compared to the Batchelor-Green model. Table 6.4 shows the extracted fit parameter from the data of HDPE/NA blends at  $T_C = 123^\circ\text{C}$  shown in Figure 6.24. As mentioned in the previous section 6.3.1, the exponents  $C'$  and  $p$  were the same and the extracted value was almost constant as  $\sim 2.1$  for nucleated HDPE samples. This exponent value was 1.4 for the neat HDPE sample. When the parameter  $D'$  and  $\psi$  compared, they both showed a similar trend with close values.

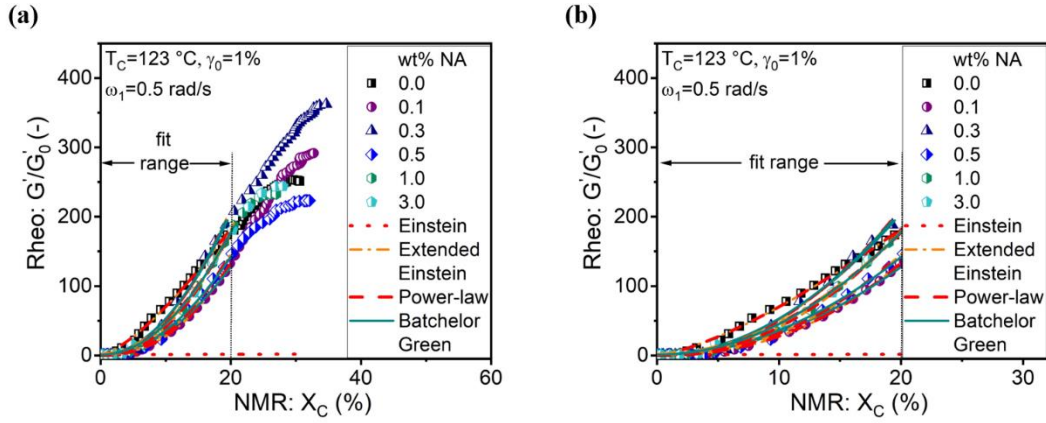


**Figure 6.24:** Correlation among the reduced storage modulus  $\frac{G'}{G'_0}$  and crystallinity  $X_C$  at  $T_C = 123$  °C for neat HDPE and HDPE/NA blends and fitted suspension models up to  $X_C = 20\%$  as follows: Einstein, extended Einstein (Equation 6.2), power-law, Batchelor-Green (see Table 6.2). (b) A closer look of Figure 6.23a.

The Batchelor-Green model described the correlation behavior of  $\frac{G'}{G'_0}$  with  $X_C$  good for HDPE/NA blends sample except for the 5% NA and neat HDPE samples. An increasing  $k_H$  trend was observed within increased NA content in the HDPE/NA blend, except 5% NA and neat HDPE samples. Consequently, the transition from the Einstein model was observed at around  $X_C = 4\%$ .

**Table 6.3:** Results of the fitted models in Figure 6.24a.

Fitted models Experiment Conditions	Extended Einstein (Equation 6.2)		Batchelor-Green $\frac{G'}{G'_0} = 1 + 2.5X_C + k_H\phi^2$	Power-law $\frac{G'}{G'_0} = \psi X_C^p$	
	NA amount (wt%)	$D'$	$C'$	$k_H$	$p$
0.0	1738	1.4	5086	1.4	1690
0.1	5670	2.3	3151	2.3	5194
0.3	5882	2.0	5189	2.0	5621
0.5	5205	2.2	3513	2.2	5283
1.0	6034	2.2	4408	2.2	5760
3.0	4236	1.9	4411	1.9	4037

## 6.4 Shear-induced crystallization

The prediction of the flow effects on crystallization and their relationship is important for both industrial and scientific interests. Stress and strain are well accepted as influencer parameters on crystallization kinetics and crystallinity (Pogodina and Winter 1998; Pogodina *et al.* 1999; Tanner and Qi 2005). While quiescent crystallization experiments typically carried out with low strain 0.01-0.03, the larger strain could induce the crystallization process of the polymers (Pogodina and Winter 1998). This chapter, shearing flow types and duration effects on the isothermal crystallization describes.

### 6.4.1 Steady shear effect on isothermal crystallization of neat HDPE

The steady shear is the most commonly used flow type in polymer crystallization studies. The steady shear is generally applied to the sample after cooling when the temperature reaches to the  $T_C$ . In this study, the application of steady shear was just at the beginning of the experiments when the sample was still molten. Only in one experiment the steady shear  $\dot{\gamma} = 2 \text{ s}^{-1}$ , during a total 11 s was applied 2 min after the experiment started, and this experiment was shown with a “\*” as a top index. After the  $\dot{\gamma}$  was applied, the experiment was continued using the settings of  $\gamma_0 = 1\%$  and  $\omega_1 = 1 \text{ rad/s}$ .

For this study, even the low steady shear was also tried to be applied after cooling. However, the rheometer was overloaded, and hence, the experiment was stopped automatically. Additionally, the application of  $\dot{\gamma} \geq 16 \text{ s}^{-1}$  at the beginning of the experiment was not possible because the sample flowed out from the gap and stacked to the NMR coil. Thus, the experimental limitation was revealed.

In this chapter, all experiments were done by RheoNMR with the commercial neat HDPE. The temperature and the experimental protocol were the same as the previously mentioned protocols (see Chapter 5.2 and Chapter 6.3) except for the existence of the application of steady shear. The RheoNMR set up was not disassembled until the end of all shown experiments in this section. Therefore, the designated results were comparable. The temperature-dependent experiments for HDPE sample were done; and simultaneously measured dynamic moduli, the  $I_{3/1}$ , and the  $X_C$  were represented in Figure 6.25. Faster crystallization was observed with decreased  $T_C$ , and the final crystallinity was

higher  $\Delta X_C^\infty = 0.5$  for each 1 °C decreased in  $T_C$ . The Avrami and the Foubert model were used to determine kinetic parameters. Nonlinearity was indicated with a peak of  $I_{3/1}$  at closer to the  $t_{gel}$ . The peak value of  $I_{3/1}$  was higher for lower  $T_C$ . Avrami model was fitted up to  $X_C = 0.1$  for all  $X_C$  curves which were approximately half of the final crystallinity for the  $T_C = 122$  °C.

Previous studies reported that the application of even small shear rates significantly accelerates the crystallization (Tanner and Qi 2005). According to Vleeshouwers and Meijer (1996), the shorter time shearing with a larger shear rate appeared to be a more effective way of acceleration crystallization. The simultaneously acquired  $G'$ , the  $I_{3/1}$  and the  $X_C$  are shown for the application of steady shear experiments in Figure 6.26. For these experiments,  $I_{3/1}$  showed a sharp rise at the moment when steady shear applied. Application of the steady shear caused faster crystallization and led to reach the  $G'_\infty$  in  $\sim 20$  minutes earlier compared to the quiescent crystallization experiment at the same  $T_C$ . Besides, an increment in  $\Delta X_C^\infty = 0.5$  was found for application of shear rate  $\dot{\gamma} \geq 2$  s<sup>-1</sup>.

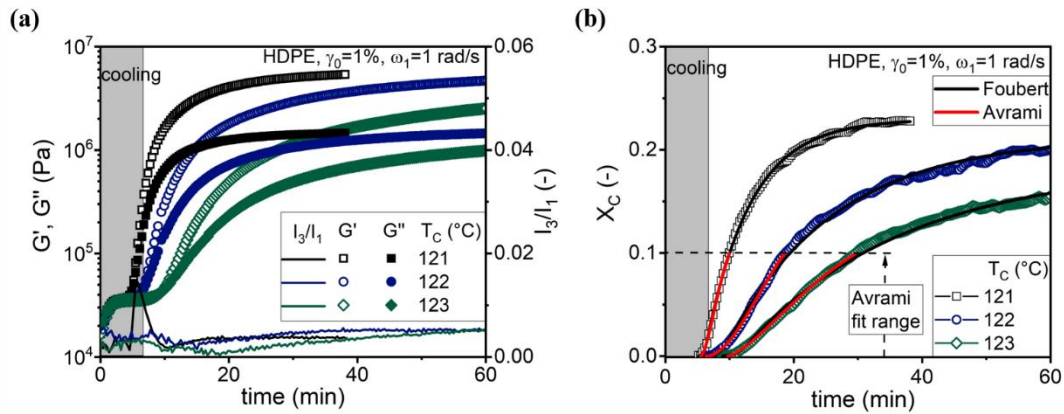


**Figure 6.25:** Temperature-dependent isothermal crystallization experiments of HDPE. Simultaneously monitored (a) dynamic moduli ( $G'$  and  $G''$ ) with the relative intensity of third harmonic  $I_{3/1}$  and (b) the crystallinity  $X_C$  development by time measured by RheoNMR. Kinetic analyses were done by using Avrami and Foubert model represented red and black lines, respectively.

The Avrami and Foubert model was used to fit the  $X_C$  and the  $G'_{norm}$  results, which displayed in Figure 6.27, of steady shear and temperature-dependent experiments. The calculated fitting parameters from  $G'_{norm}$  and  $X_C$  curves are displayed in Figure 6.28. With decreasing 1 °C in  $T_C$  led to 3 times faster crystallization which was indicated by an  $\sim 3$  times the larger  $K$  and  $\nu$  values. The varying  $T_C$  did not result in a change of the  $n = \sim 1.5$

value. The applied  $\dot{\gamma} = 2 \text{ s}^{-1}$  during 11 s accelerated the crystallization and led to an increase in  $K$  and  $\nu$  factor of  $\sim 2.5$ . The calculated  $K$  and  $\nu$  from Rheo data were indicated more pronounced acceleration with a factor of  $\sim 4$  increase by applied  $\dot{\gamma} = 16 \text{ s}^{-1}$ , 11 s and  $2 \text{ s}^{-1}$ , 11 s\*. Although the  $X_C$  and the  $G'_{\text{norm}}$  curves of for the  $2 \text{ s}^{-1}$ , 11 s\* experiment were almost overlapping with the  $\dot{\gamma} = 16 \text{ s}^{-1}$ , 11 s data, the  $K$  parameter was calculated almost half the value of the  $\dot{\gamma} = 16 \text{ s}^{-1}$ , 11 s experiment. This could be due to the monitored less data point in  $X_C$  development because of the fast crystallization.

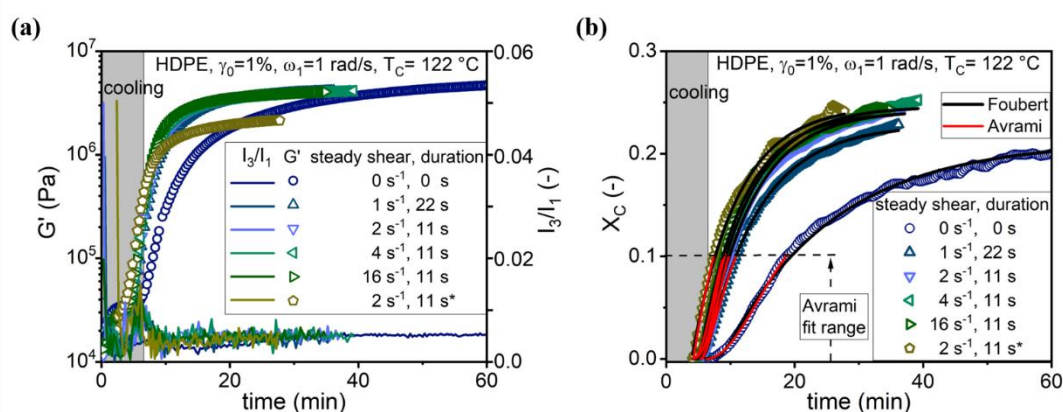


**Figure 6.26:** Applied steady shear effects on (a) the storage modulus  $G'$  with the relative intensity of third harmonic  $I_{3/1}$ , and (b) the crystallinity  $X_C$  of HDPE at  $T_C = 122 \text{ }^\circ\text{C}$ . Kinetic analyses were done by using Avrami and Foubert model represented red and black lines, respectively. The named  $2 \text{ s}^{-1}$ ,  $11 \text{ s}^*$  steady shear experiment was applied during cooling at  $2^{\text{nd}}$  min of the experiment, while the rest of the steady shear was applied at the beginning of the experiment.

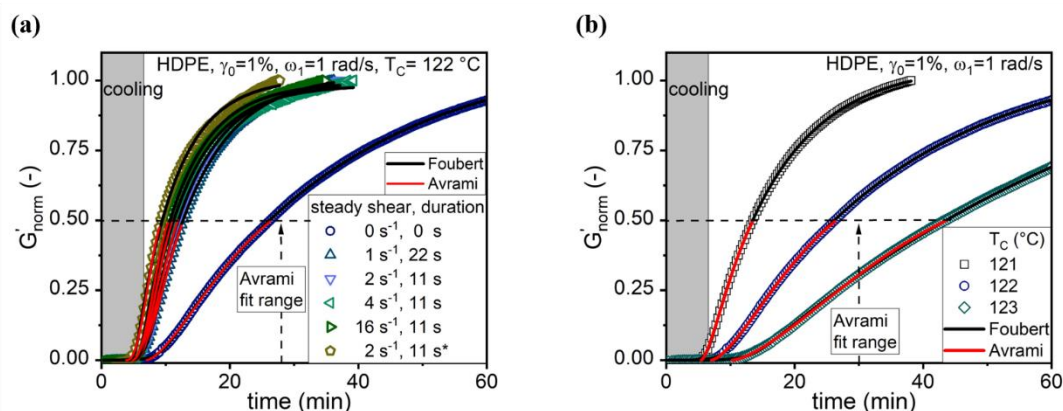


**Figure 6.27:** (a) Applied steady shear effect on the normalized storage modulus  $G'_{\text{norm}}$  at  $122 \text{ }^\circ\text{C}$ . The named  $2 \text{ s}^{-1}$ ,  $11 \text{ s}^*$  steady shear experiment was applied during cooling at  $2^{\text{nd}}$  min of the experiment, while the rest of the steady shear was applied at the beginning of the experiment. (b) The temperature-dependent results of the  $G'_{\text{norm}}$ .

The deduced dimensionality  $n$  from Rheo data showed an increase from 1.5 to 2.5 with the  $\dot{\gamma} = 4 \text{ s}^{-1}$ , 11 s and then stayed stable at around 2.5 for a  $\dot{\gamma} > 4 \text{ s}^{-1}$ . The extracted  $n$  values from NMR data showed a peak for  $\dot{\gamma} = 4 \text{ s}^{-1}$ , 11 s experiment, and then, decreased for a  $\dot{\gamma} > 4 \text{ s}^{-1}$ . This could be related to decreasing dimensionality of the HDPE crystals for applied  $\dot{\gamma} = 16 \text{ s}^{-1}$ , 11 s and the  $\dot{\gamma} = 2 \text{ s}^{-1}$ , 11 s\* experiment. Results indicated that not only the increasing shear rate but also application time in the experiment caused an effect on the crystallization kinetics and the final crystallinity. The fact that the calculated consistent kinetic parameters using the  $X_C$  and the  $G'_{\text{norm}}$  results showed that both databases and the Avrami and Foubert models can be used for kinetic analysis of isothermal crystallization. Foubert model showed a relatively better fit for the crystallization curves determined from Rheo part of the RheoNMR.

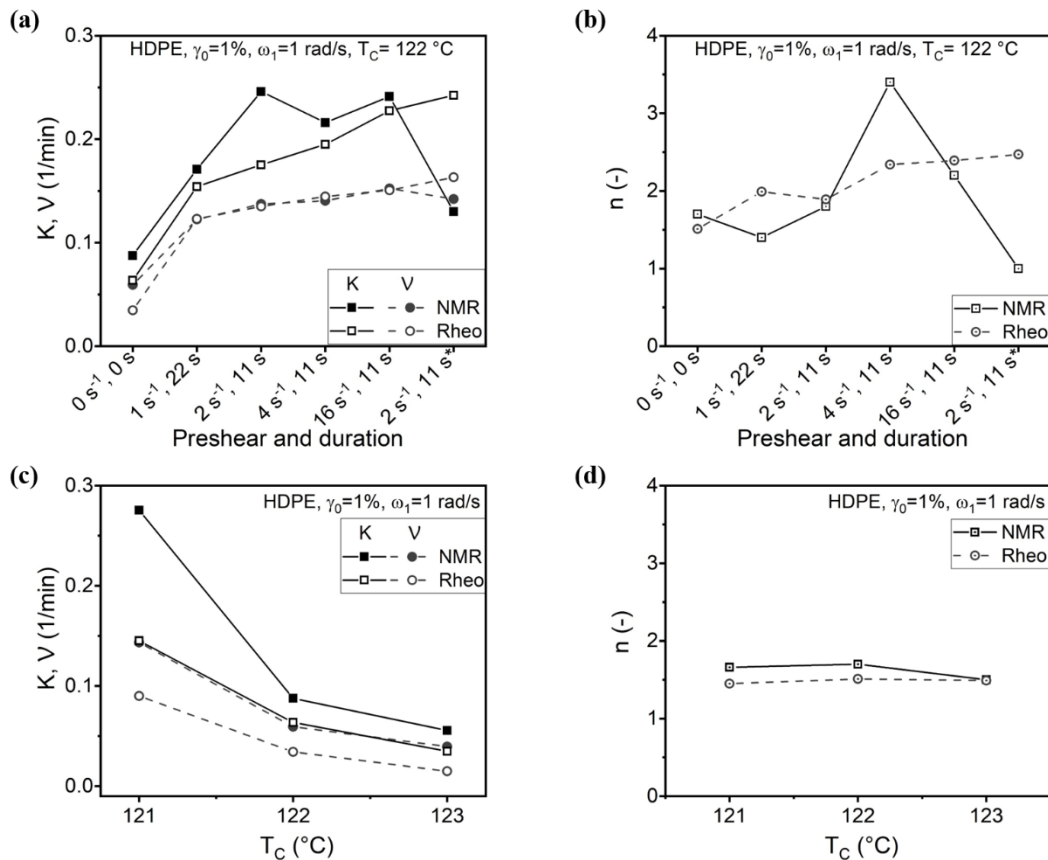


**Figure 6.28:** Fit parameters by using the Avrami and Foubert model to the  $G'_{\text{norm}}$  data determined by rheometer (Rheo) and the  $X_C$  data monitored via NMR (a) rate parameters  $K$  and  $v$ , (b) Avrami exponent  $n$  for applied steady shear; and (c) rate parameters  $K$  and  $v$ , (d) Avrami exponent  $n$  for varying  $T_C$  measurements.

Figure 6.29a shows the correlation between the time of crystallization  $t_{0.1}$  at  $X_C = 0.1$  with  $t_{gel}$  for varying  $T_C$  and applied steady shear assays of HDPE. Varying temperature and the applied steady shear at constant  $T_C$  affected the relationship of  $t_{0.1}$  with  $t_{gel}$  as linearly with a slope of  $\sim 4.3$ . This behavior indicated either a  $1\text{ }^\circ\text{C}$  decrease in  $T_C$  or applied the  $\dot{\gamma} = 2\text{ s}^{-1}$ ,  $11\text{ s}$  had similar effects on the  $t_{0.1}$  and  $t_{gel}$ . Besides, a further increase in the shear rate and the application time of it possibly induced more the crystal nucleation and/or growth mechanism, and led to a much shorter  $t_{0.1}$  and  $t_{gel}$ .

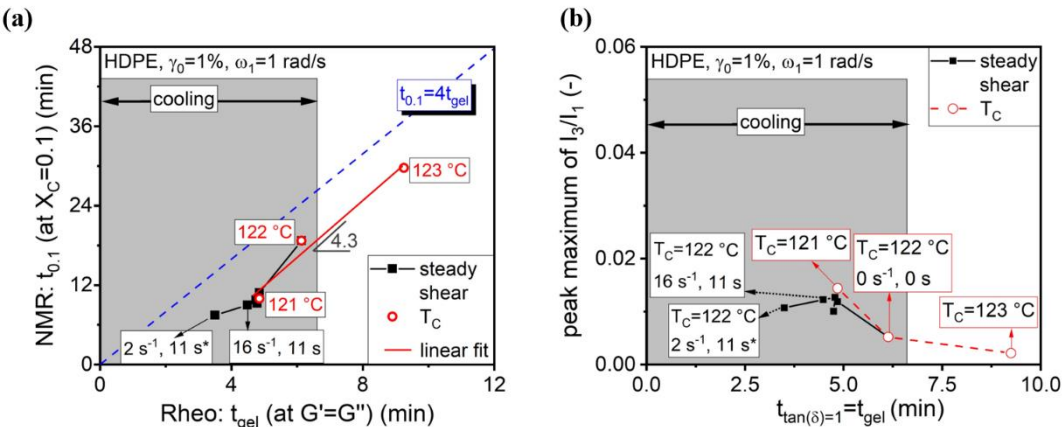


**Figure 6.29:** (a) The relationship between the time of crystallization  $t_{0.1}$  at  $X_C = 0.1$  and  $t_{gel}$  for varying  $T_C$  and applied steady shear at the constant  $T_C$  assays. (b) The peak maximum of the  $I_{3/1}$  as a function of  $t_{tan(\delta)} = t_{gel}$  for varying  $T_C$  and applied steady shear at the constant  $T_C$  experiments.

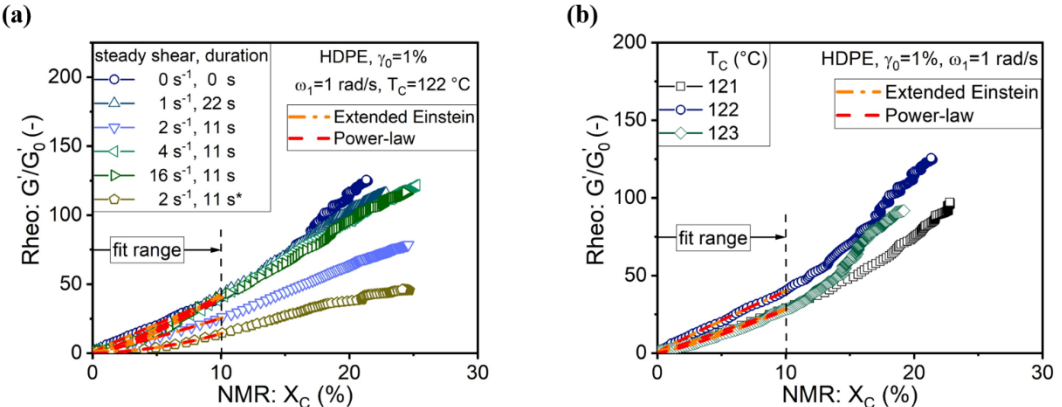


**Figure 6.30:** Correlation between the  $\frac{G'}{G'_0}$  and the  $X_C$  with modelling by using the suspension models up to  $X_C = 10\%$ : extended Einstein (Equation 6.2) and power-law (see Table 6.4) (a) for steady shear experiments at  $T_C = 122\text{ }^\circ\text{C}$ , and (b) for temperature-dependent experiments of HDPE.

To examine the  $T_C$  and the steady shear effects on the nonlinearity, the peak maximum values of the  $I_{3/1}$  as a function of the  $t_{gel}$  correlation is displayed in Figure 6.29b. The nonlinear response from the sample reflects the sensitivity towards the changes in the crystal growth (Dötsch *et al.* 2003). The results showed a factor of 2 higher peak value of the  $I_{3/1}$  by either the 1 °C drop in  $T_C$  or applied steady shear range.

Figure 6.30 shows the correlation among the reduced storage modulus  $\frac{G'}{G'_0}$  and crystallinity  $X_C$  for the steady shear and for varying  $T_C$  experiments. The exerted the  $\dot{\gamma} = 2 \text{ s}^{-1}$ , 11  $\text{s}^*$  reduced the  $\frac{G'}{G'_0}$  value 3 times at  $X_C = 20$ . The extended Einstein and the power-law model were fitted well for all curves in Figure 6.30. The exponents  $C'$  and  $p$  showed a similar trend with increasing values with increasing shear rate and applied the  $\dot{\gamma} = 2 \text{ s}^{-1}$ , 11  $\text{s}^*$ . The parameter  $D'$  and  $\psi$  were close to each other and in an increasing trend with increasing shear rate and applied the  $\dot{\gamma} = 2 \text{ s}^{-1}$ , 11  $\text{s}^*$  except the exerted  $\dot{\gamma} = 2 \text{ s}^{-1}$ , 11  $\text{s}$  assay. The increasing  $T_C$  increased the value of all extracted parameters.

**Table 6.4:** Extracted fit results from the fitted models in Figure 6.30.

Fitted models Experiment Conditions		Extended Einstein (Equation 6.2)		Power-law $\frac{G'}{G'_0} = \psi X_C^p$	
		$D'$	$C'$	$p$	$\psi$
$T_C$ (°C)	Shear rate, duration				
122	0 $\text{s}^{-1}$ , 0 s	360	0.97	0.91	329
	1 $\text{s}^{-1}$ , 22 s	739	1.24	1.22	700
	2 $\text{s}^{-1}$ , 11 s	412	1.22	1.10	321
	4 $\text{s}^{-1}$ , 11 s	738	1.29	1.19	608
	16 $\text{s}^{-1}$ , 11 s	1505	1.56	1.45	1205
	2 $\text{s}^{-1}$ , 11 $\text{s}^*$	1679	2.11	1.74	780
121	0 $\text{s}^{-1}$ , 0 s	336	1.09	0.99	277
123	0 $\text{s}^{-1}$ , 0 s	561	1.31	1.20	441

#### 6.4.2 Short-term applied high deformation effect on HDPE/NA blend

Strain-induced crystallization was studied by an applied large oscillatory strain amplitude e.g.,  $\gamma_0 = 100$  or 200% for a minute or less at the 5<sup>th</sup> min of the experiment. The large

strain was applied close to the end of cooling which stage can be called the early stage of crystallization. After application of short term large strain amplitude, the experiment was continued with a constant  $\gamma_0 = 1\%$  and  $\omega_1 = 1 \text{ rad/s}$  for do not perturb the internal crystallization mechanics during the rest of the crystallization process. Detected  $G'$  and the  $I_{3/1}$  as a function of time via Rheo part of the RheoNMR are shown in Figure 6.31a while simultaneously monitored the  $X_C$  evolution as a function of time by the NMR part of the RheoNMR is presented in Figure 6.31b.

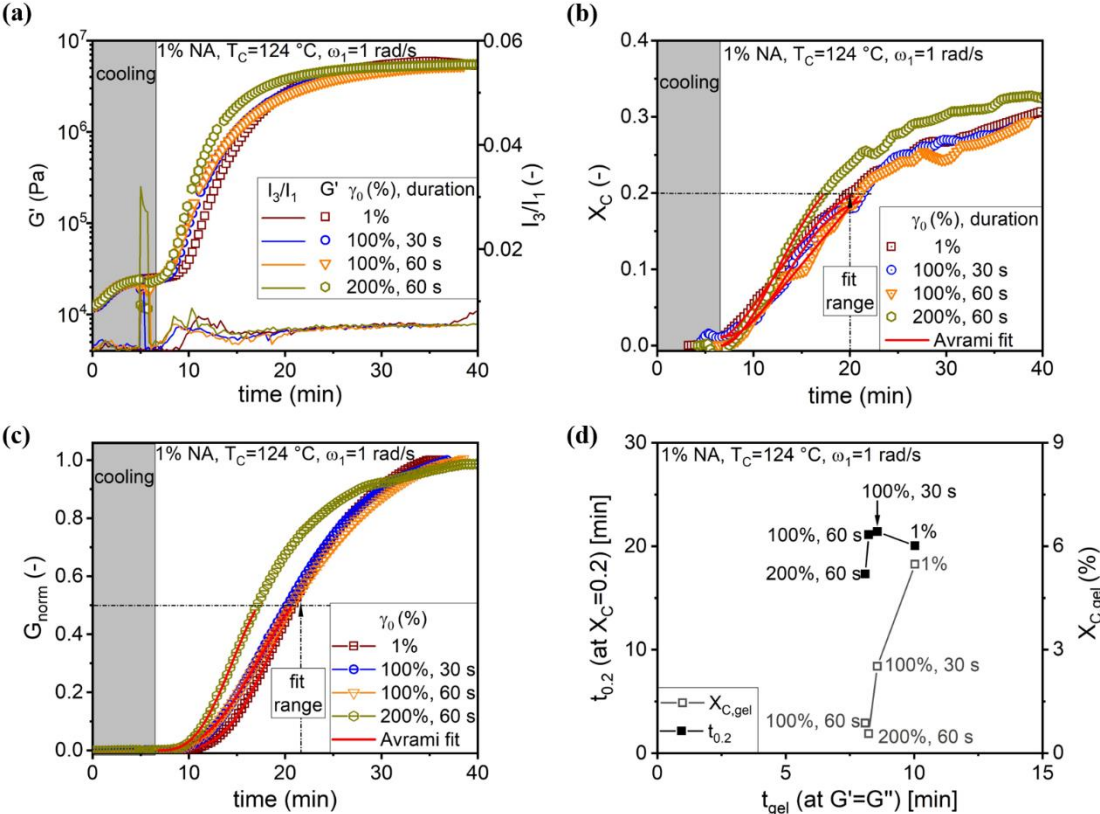


**Figure 6.31:** (a) The  $G'$  with the  $I_{3/1}$ , (b) the  $X_C$  evolution, and also (c) the  $G'_{norm}$  as a function of time for strain-induced crystallization. The Avrami model was fitted to  $X_C$  curves up to  $X_C = 0.2$  and up to half of the  $G'_{norm}$  curves. (e) Direct correlation of the time of crystallization  $t_{0.2}$  at  $X_C = 0.2$  and the crystallinity at gel point  $X_{C, gel}$  as a function of the  $t_{gel}$  for strain induced crystallization of 1% NA sample.

Applied high deformation at 5<sup>th</sup> minute caused to a peak in  $I_{3/1}$ . Meanwhile, a drop in the  $G'$  and in the  $X_C$  were observed at the moment of the exerted  $\gamma_0 = 200\%$  for 60 s. This may be an indication of the destroyed crystal growth and/or flowing the sample out from the gap between the geometries. The extracted kinetic parameters as a result of fitting the

Avrami model to the  $X_C$  and the  $G'_{\text{norm}}$  are presented in Table 6.5. In case of the applied  $\gamma_0 = 100\%$  during 60 s while the extracted  $K_{\text{NMR}}$  value showed a slower crystallization factor of  $\sim 2.5$ , the value of  $K_{\text{Rheo}}$  was almost the same value with the quiescent crystallization result. However, the extracted  $K_{\text{NMR}} = K_{\text{Rheo}}$  values for  $\gamma_0 = 200\%$  for 60 s experiment represented an acceleration of crystallization by a factor of  $\sim 1.3$ . While the dimensionality  $n_{\text{Rheo}}$  showed a maximum of 3.7 for quiescent condition, the  $n_{\text{Rheo}}$  was minimum as 2.6 for  $\gamma_0 = 100\%$  during 60 s condition. The minimum value for  $n_{\text{NMR}}$  was 1.3 for also  $\gamma_0 = 100\%$  for 60 s condition. Resulting minimum  $n$  values indicated the decreased dimensionally and rod shape crystal growth under heterogeneous crystallization by exerted  $\gamma_0 = 100\%$  during 60 s. The rest of the  $n_{\text{NMR}}$  values were around 2 which indicated disc shape crystal growth under heterogeneous crystallization.

**Table 6.5:** Kinetic parameters for strain-induced experiments.

Experiment	$K_{\text{NMR}}$	$n_{\text{NMR}}$	$K_{\text{Rheo}}$	$n_{\text{Rheo}}$
Condition	(1/min)	(-)	(1/min)	(-)
$\gamma_0 = 1\%$ (quiescent)	0.096	1.9	0.078	3.7
$\gamma_0 = 100\%$ for 30 s	0.092	2.3	0.082	2.9
$\gamma_0 = 100\%$ for 60 s	0.037	1.3	0.076	2.6
$\gamma_0 = 200\%$ for 60 s	0.118	1.8	0.112	3.0

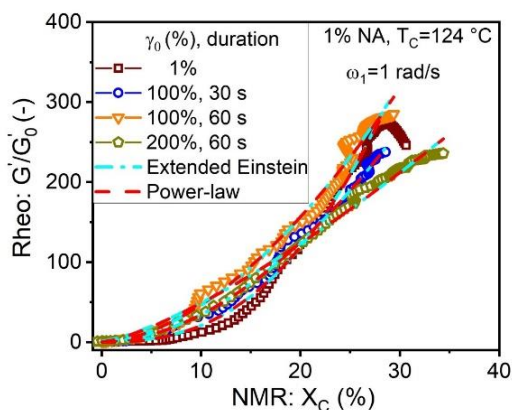


**Figure 6.32:** Correlation between the  $\frac{G'}{G'_0}$  and the  $X_C$  of 1% NA sample at  $T_C = 124\text{ }^\circ\text{C}$  for strain-induced crystallization. The used models for modeling: extended Einstein and power-law models.

Early-stage of the crystallization under large strain amplitude can be evaluated by the correlation of  $t_{0.2}$  and  $X_{\text{C,gel}}$  with  $t_{\text{gel}}$  as seen in Figure 6.31d. A drastic decrease in the

$X_{C, \text{gel}}$  was observed by increased the  $\gamma_0$  and its duration. This could be related to the induced crystals by applied large  $\gamma_0$  such as extended crystals or oriented crystals. While only the  $t_{\text{gel}}$  was decreased by almost 2 min for conducted  $\gamma_0 = 100\%$  during 30 s or 60 s experiments, the applied  $\gamma_0 = 200\%$  for 60 s experiment caused a reduction in both  $t_{\text{gel}}$  and  $t_{0.2}$  as  $\sim 2$  and  $\sim 3$  min respectively. While faster gelation suggested the enhanced nucleation, the accelerated crystal growth was exhibited by reduced  $t_{0.2}$ .

For further analysis, the correlation between the  $\frac{G'}{G'_0}$  and the  $X_C$  for the strain-induced experiment is shown in Figure 6.32. The extracted fitting parameters from these curves are given in Table 6.6. The exponents  $C'$  and  $p$  values were almost the same, and they were in a similar trend with decreasing values for applied larger strain amplitude with longer duration. The  $D'$  and  $\psi$  and were also close to each other and the smallest values were identified for the applied  $\gamma_0 = 200\%$  for 60 s.

**Table 6.6:** Extracted fit results from the fitted models in Figure 6.33.

Fitted models		Extended Einstein (Equation 6.2)		Power-law $\frac{G'}{G'_0} = \psi X_C^p$	
Experiment Conditions		$D'$	$C'$	$p$	$\psi$
NA amount (wt%)	$\gamma_0$ (%), duration				
1	1%	7383	2.57	2.52	6873
	100%, 30 s	2555	1.88	1.86	2501
	100%, 60 s	2747	1.78	1.74	2590
	200%, 60 s	1063	1.33	1.33	1057

### 6.4.3 Long-term applied high deformation effect on HDPE/NA blends

This section focuses on the effects of applied large strain amplitudes during isothermal crystallization. The strain-induced crystallization of commercial neat HDPE and nucleated HDPE samples (HDPE/NA) was investigated by RheoNMR measurements. Pogodina *et al.* (1999) reported that the imposed large strain in the crystal growth stage was more quickened the gelation compared to the applied strain in the nucleation stage.

The experimental protocol was the same as illustrated in Figure 5.5. Monitored dynamic moduli of the samples during isothermal crystallization for varying  $\gamma_0$  are displayed in Figure 6.33. Simultaneously monitored the  $X_C$  development of the samples as a function of time for strain-induced crystallization are depicted in Figure 6.34.

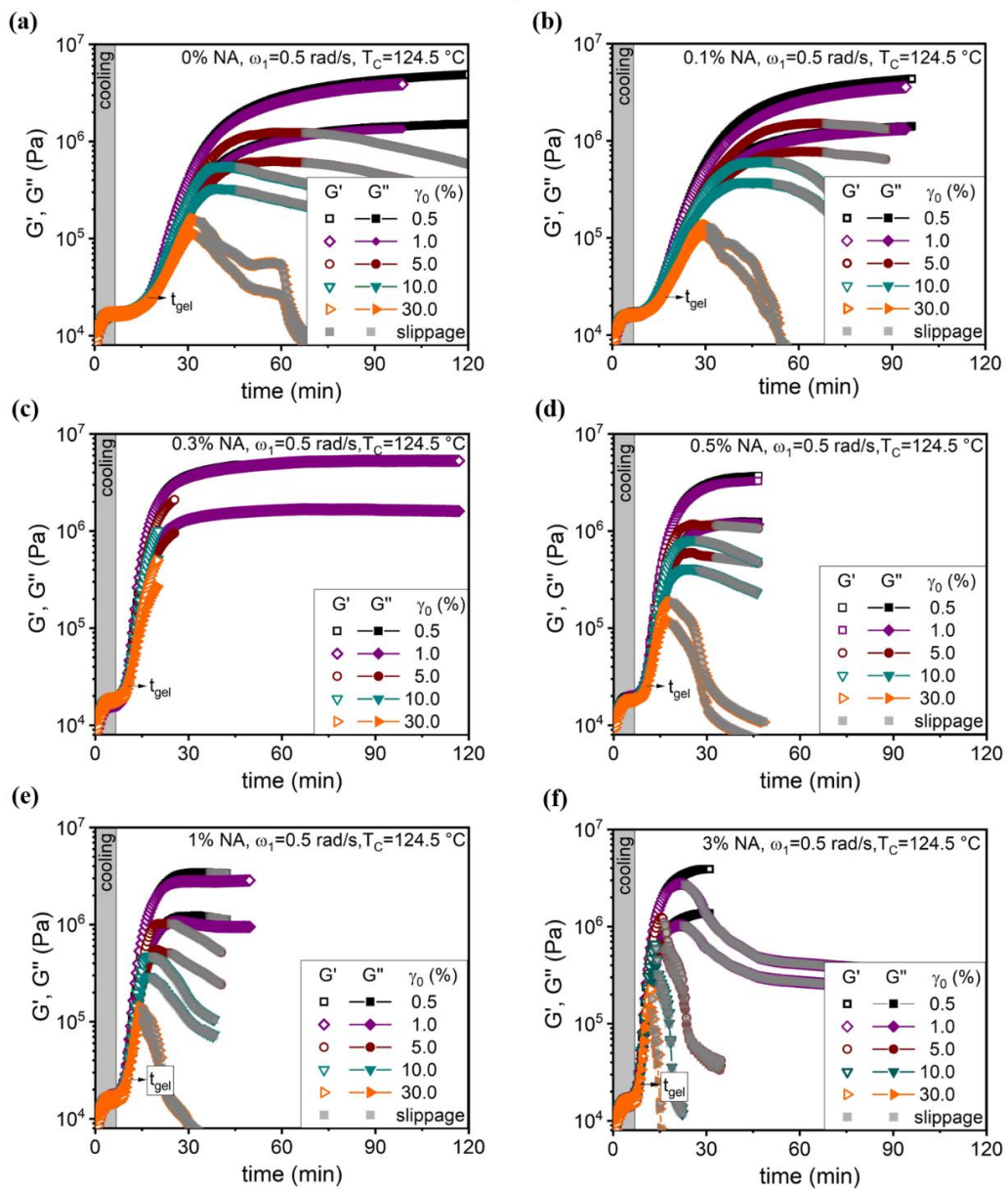


**Figure 6.33:** The  $G'$  and  $G''$  evolution as a function of time for strain-induced crystallization of (a) 0% NA (neat HDPE) and HDPE/NA blend samples as (b) 0.1% NA, (c) 0.3% NA, (d) 0.5% NA, (e) 1% NA, and (f) 3% NA. The slippage is indicated with a grey color.

A sharp decrease in the moduli was observed when the moduli reached its maximum value  $G'_{\infty}$ . This was because of the slippage due to the shrinkage of the crystallized

sample. The slippage was indicated with grey color in the Figure 6.33. In the case of the crystallized sample could not slip, the rheometer was overloaded. Thus, the experiment was stopped automatically. This was the case for sample 0.3% NA. The achieved  $G'_{\infty}$  value decreased by increasing  $\gamma_0$  for all samples. Although the moduli reached the  $G'_{\infty}$ , the continues rise in the  $X_C$  indicated the evolving crystallization.

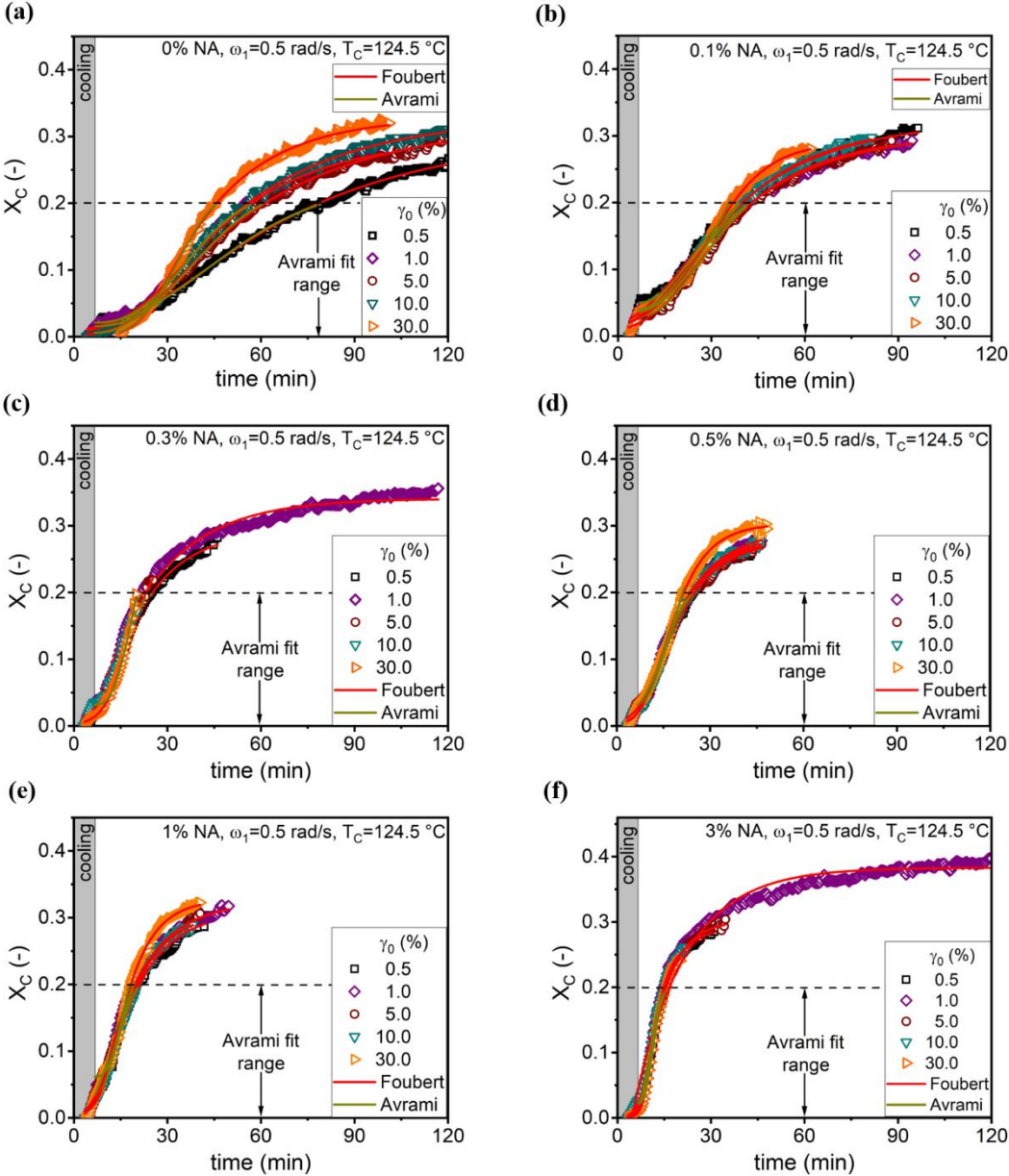


**Figure 6.34:** The  $X_C$  development as a function of time for strain-induced crystallization (a) 0% NA, (b) 0.1% NA, (c) 0.3% NA, (d) 0.5% NA, (e) 1% NA, and (f) 3% NA.

The neat HDPE (0% NA) sample crystallized during cooling for applied  $\gamma_0 \leq 10\%$ , and the  $X_C = \sim 0.22$  was observed in approximately 50 min. In the case of applied  $\gamma_0 = 30\%$ , crystallization of 0% NA sample started after cooling, but, the  $X_C = \sim 0.20$  was achieved in around 40 min due to accelerated crystallization. Additionally, the  $X_C$  data of the exerted  $\gamma_0 = 0.5\%$  experiment of 0% NA sample (see Figure 6.34a) exhibited slower crystallization compared to the result of the applied  $\gamma_0 = 1\%$  experiment.

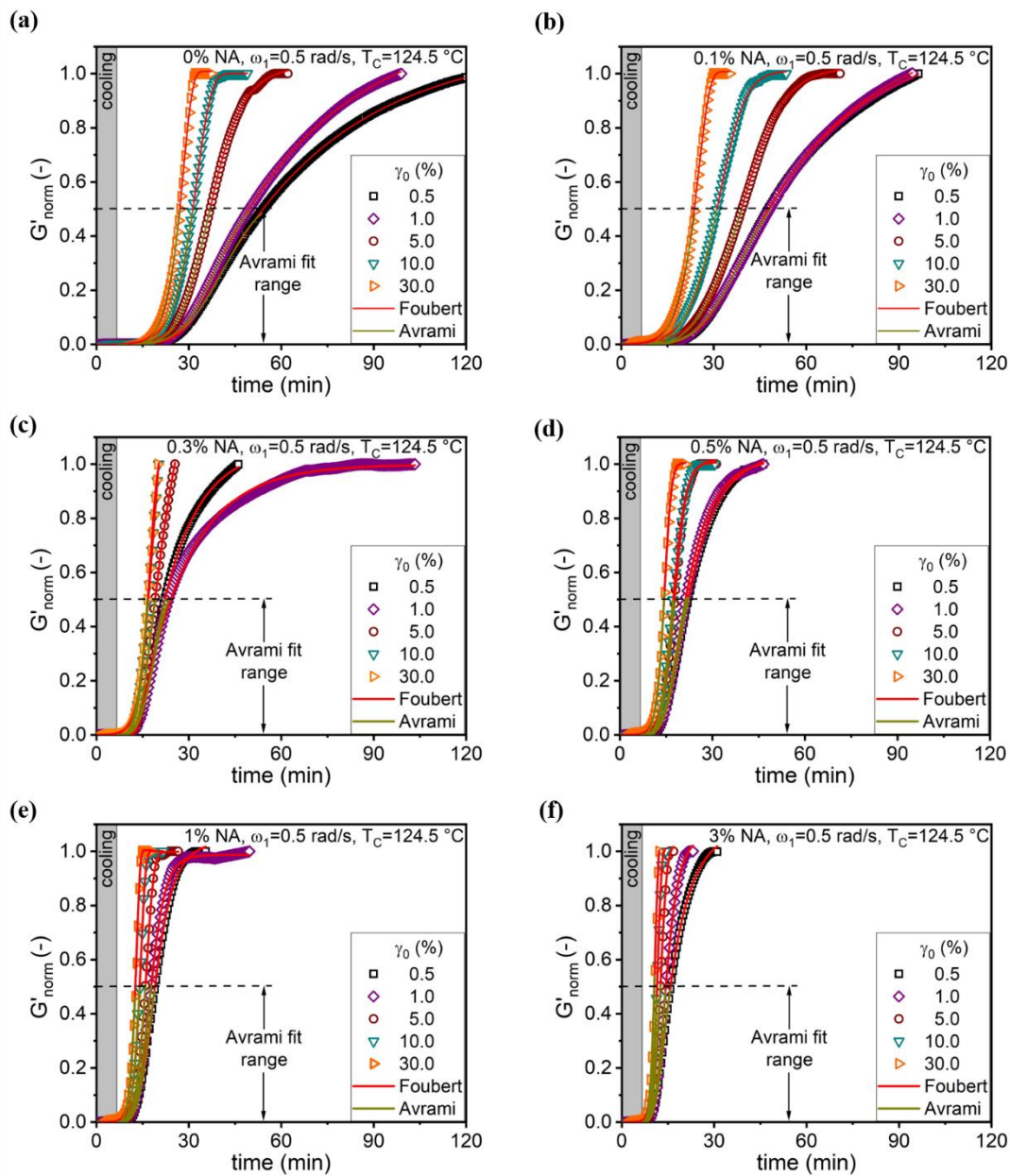


**Figure 6.35:** The  $G'_{norm}$  development as a function of time for strain-induced crystallization (a) 0% NA and HDPE/NA blend samples as (b) 0.1% NA, (c) 0.3% NA, (d) 0.5% NA, (e) 1% NA, and (f) 3% NA.

There was no difference in the dynamic moduli curves of 0% NA sample for both experimental conditions. Other samples, HDPE/NA blends, started crystallization during cooling for all conditions, and the exerted  $\gamma_0 = 0.5\%$  was not slower the crystallization compared to the crystallization of the applied  $\gamma_0 = 1\%$  condition.

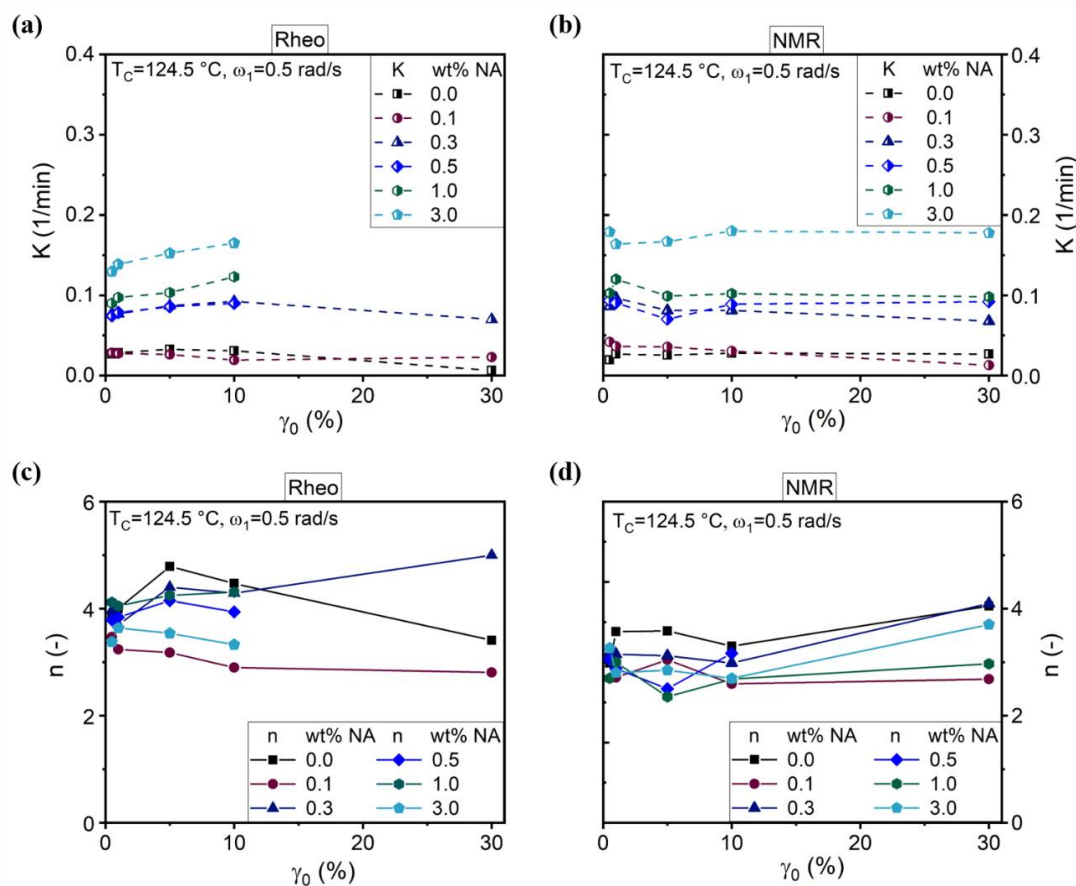


**Figure 6.36:** Avrami rate ( $K$ ) parameters for neat HDPE and HDPE/NA blends from the data of (a) Rheo ( $K_{\text{Rheo}}$ ) and (b) NMR part ( $K_{\text{NMR}}$ ). The deduced Avrami exponent  $n$  from the data of (a) the Rheo part ( $n_{\text{Rheo}}$ ), and (b) NMR part ( $n_{\text{NMR}}$ ), of RheoNMR method.

The detailed kinetic analysis was done by Avrami and Foubert fit to the  $X_C$  and the  $G'_{\text{norm}}$  curves. The  $G'_{\text{norm}}$  curves are displayed in Figure 6.35. The deduced fit parameters are shown in Figure 6.36. If the parameter was extracted from NMR, it is called “NMR” as a subindex for simplification. The exponent  $n_{\text{NMR}}$  and  $n_{\text{Rheo}}$  values were between 3 and 4 as seen in Figure 6.36c-d. This reflected the heterogeneous nucleation mechanism with possible spherical crystal growth. The extracted  $K_{\text{Rheo}}$  value increased by 30% by applying  $\gamma_0 = 10\%$  for nucleated samples with wt% of NA  $\geq 0.3$ . Except for this, the calculated  $K_{\text{Rheo}}$  and  $K_{\text{NMR}}$  values indicated almost no change in the rate of crystallization

by applied larger strain amplitude. An approximately  $\pm 10\%$  error for extracted parameters were taken into account depending on the number of data points, the induction time and the overall noise level. The rate  $K_{\text{Rheo}}$  and the  $n_{\text{Rheo}}$  values for applied  $\gamma_0 = 30\%$  experiment was not calculated due to the less data point for fast crystallized samples.

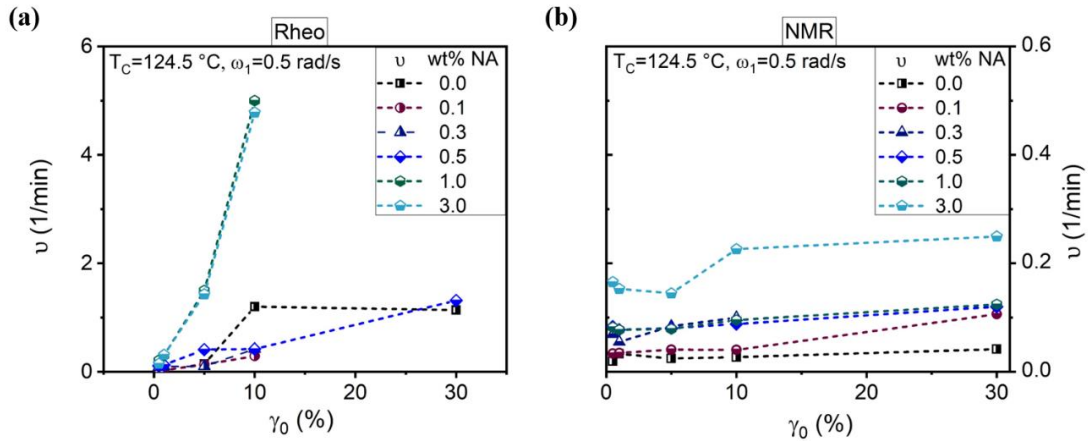


**Figure 6.37:** Foubert model rate ( $v$ ) parameter by fitting complete crystallization curves of neat HDPE and HDPE/NA blends from the data of (a) Rheo part ( $v_{\text{Rheo}}$ ) and (b) NMR part ( $v_{\text{NMR}}$ ) of the RheoNMR.

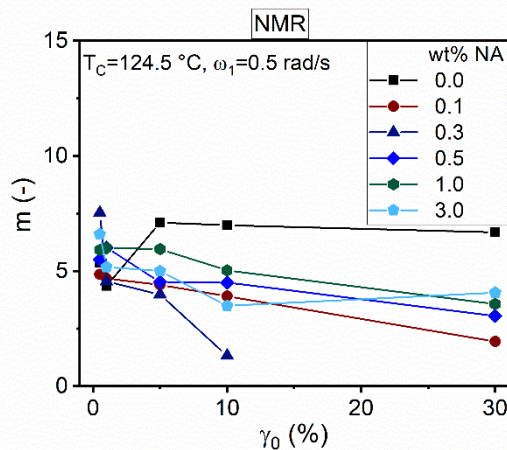


**Figure 6.38:** Foubert exponent ( $m_{\text{NMR}}$ ) for neat HDPE and HDPE/NA blends from the data of the NMR part of the RheoNMR.

Besides, the Foubert model was used to determine the complete crystallization rate  $v$  by fitted complete crystallization curve. The extracted  $v_{\text{NMR}}$  values as depicted in Figure 6.37b were in a similar range and trend with the  $K_{\text{NMR}}$  parameter (see Figure 6.36b). The Foubert model could not describe well the crystallization process in the  $G'_{\text{norm}}$  curves. Thus, the difference between the deduced  $v_{\text{Rheo}}$  the  $v_{\text{NMR}}$  values were high. The Foubert

exponent value  $m$  showed a decreasing tendency for nucleated samples by applied larger strain amplitude.

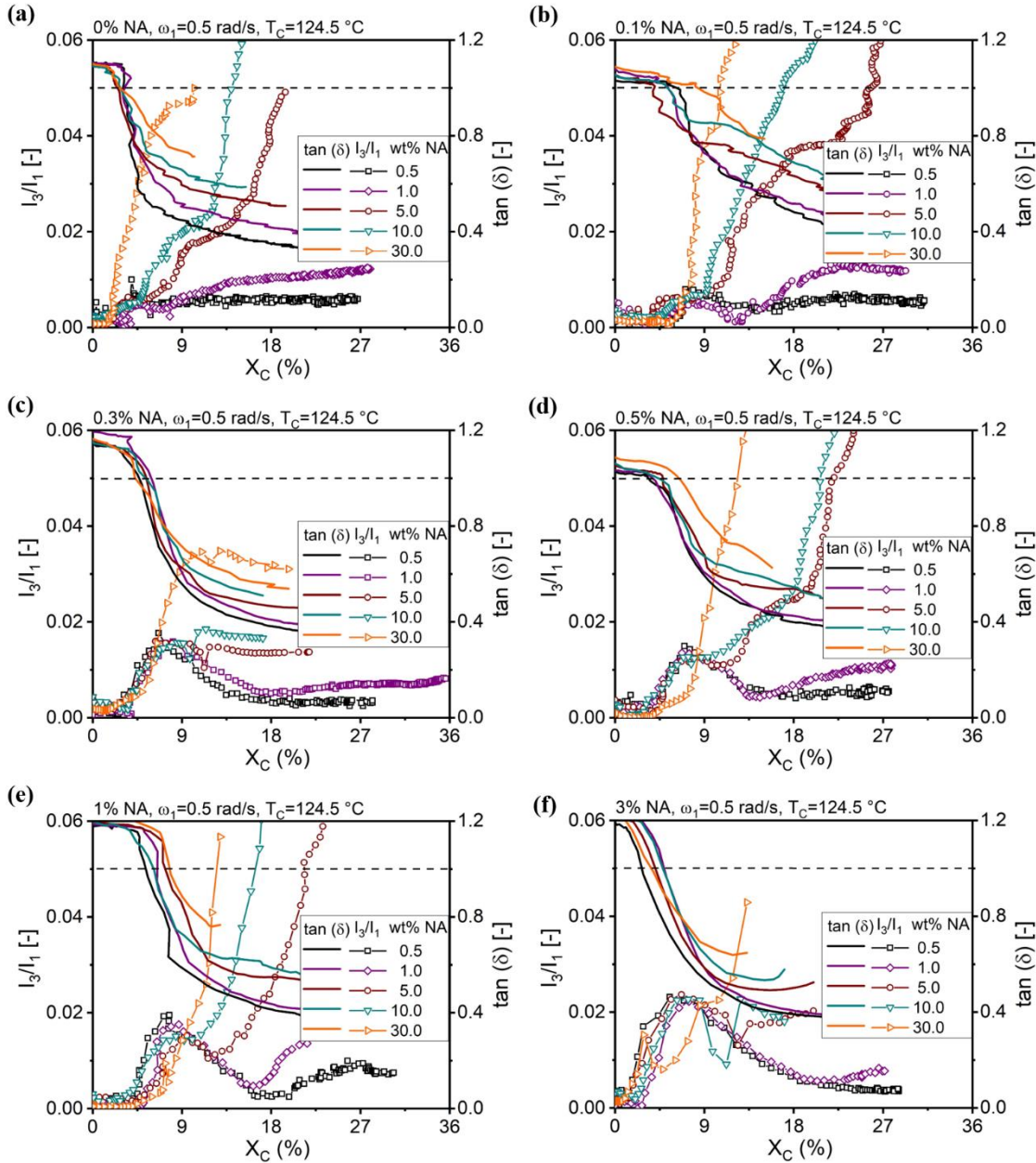


**Figure 6.39:** The  $I_{3/1}$  change as a function of the  $X_C$  for strain-induced crystallization (a) 0% NA, (b) 0.1% NA, (c) 0.3% NA, (d) 0.5% NA, (e) 1% NA, and (f) 3% NA.

The  $I_{3/1}$  as a function of the  $X_C$  under applied varying  $\gamma_0$  are illustrated in Figure 6.39. In section 6.3.3, the  $I_{3/1}$  showed a sensitivity for the NA content and temperature. The  $I_{3/1}$  was also responsive towards to the applied varying  $\gamma_0$ . The slippage for applied  $\gamma_0 \geq 5\%$

experiments led to a further rise in the  $I_{3/1}$ . The sensitivity of  $I_{3/1}$  for the failure in the experiment at applied high strain amplitudes were also observed by Dötsch *et al.* (2003).

Moreover, directly correlated  $t_{0.2}$  and  $t_{gel}$  values showed a clear picture of the influence of applied strain amplitude on  $t_{0.2}$  and  $t_{gel}$  values for the samples as seen in Figure 6.40a. In Section 6.3.3, a linear correlation between the  $t_{0.2}$  and  $t_{gel}$  was observed towards to varying  $T_C$  within a slope range of  $\sim 5.5$  to  $\sim 2.5$ , which was dependent on the NA content in the sample. In the strain-induced crystallization experiments, while  $t_{gel}$  delayed, the  $t_{0.2}$  was found shorter by exerted larger  $\gamma_0$ . When the  $t_{gel}$  was 20% longer, the  $t_{0.2}$  was 43% shorter as a result of the applied  $\gamma_0 = 30\%$  for the 0% NA sample. Increasing NA content to 1 wt% and more decreased the effect of the applied strain, and thus, the  $t_{0.2}$  and  $t_{gel}$  were almost stable by used  $\gamma_0$  range. Additionally, the impact of applied varying  $\gamma_0$  on the  $X_{C,gel}$  and the  $t_{gel}$  correlation can be seen in Figure 6.40b. While the  $t_{gel}$  delayed  $\sim 4$  minutes, the  $X_{C,gel}$  showed a 20% decrease for the 0% NA sample with applied maximum deformation compared to the quiescent condition. The observed delay in the  $t_{gel}$  was 10 min for the 0.1% NA sample, and the  $X_{C,gel}$  increased 2% with increment  $\Delta\gamma_0 = 30\%$ . Furthermore, increasing in NA content in HDPE to 3 wt% decreased the delay in  $t_{gel}$  to less than a minute and caused almost no change in the  $X_{C,gel}$ .

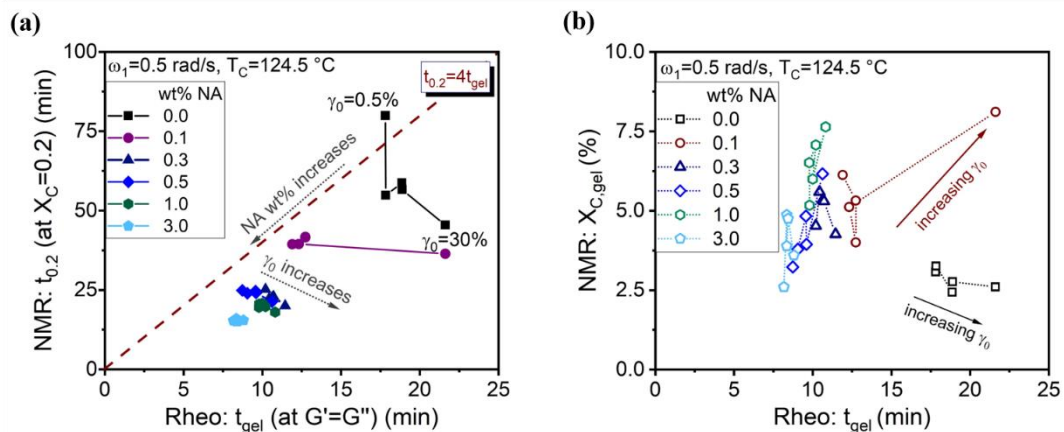


**Figure 6.40:** Direct correlation of (a) the time of crystallization  $t_{0.2}$  at  $X_C = 0.2$  with  $t_{gel}$  and (b) the relationship between the  $X_{C,gel}$  and  $t_{gel}$  for strain-induced crystallization of HDPE/NA blend samples.

Figure 6.41 shows the different perspective of crystallization dynamic with a relationship between the  $\frac{G'}{G_0}$  and the  $X_C$  at  $T_C = 124.5$  °C for 0% NA and 3% NA samples. Modeling of the correlation was done by using Einstein, extended Einstein, power-law, Batchelor-Green models up to  $X_C = 20\%$ . Extracted fit parameters can be seen in Table 6.7. Resulting  $C'$  and  $p$  values were close to each other within a decreasing trend by operated  $\gamma_0 > 1\%$  conditions for both samples. Additionally, both  $D'$  and  $\psi$  parameters increased a factor of  $\sim 1.7$  with the increased  $\gamma_0$  to 1%. Then, these values decreased to less than half of their quiescent condition value within an increment  $\gamma_0 = 30\%$  for both parameters.

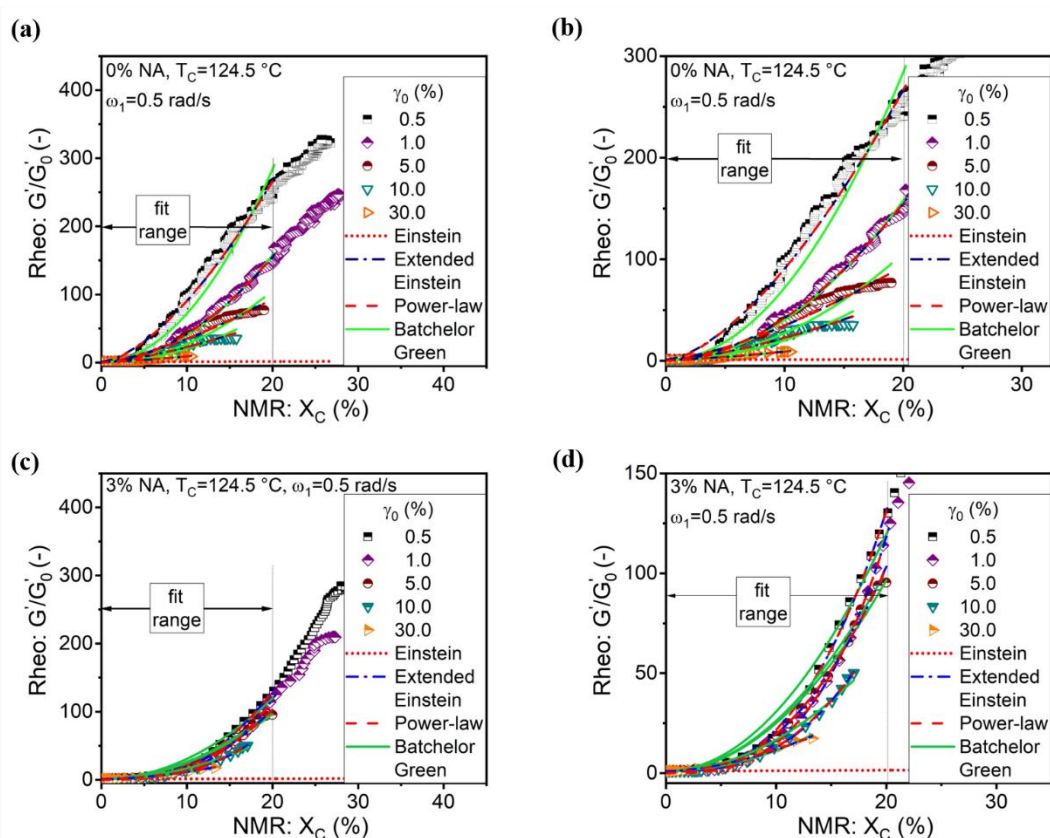


**Figure 6.41:** Correlation between the  $\frac{G'}{G_0}$  and the  $X_C$  at  $T_C = 124.5$  °C with modeling by using Einstein, extended Einstein, power-law, Batchelor-Green models up to  $X_C = 20\%$  (a) for 0% NA sample and (b) a closer look to Figure 6.40a (c) for 3% NA, (d) a closer look to Figure 6.40c.

The Batchelor-Green model was also fitted up to  $X_C = 20\%$ . This fit was not as good as with extended Einstein and power-law models. The deduced  $k_H$  parameter decreasing with increasing deformation for both samples. Moreover, the transition from the Einstein model was delayed from  $X_C = 2.5\%$  to  $X_C = 8\%$  with applied  $\gamma_0 = 30\%$  for the sample

0% NA. This delay was from  $X_C = 3\%$  to  $X_C = 6\%$  for the sample 3% NA under the exerted largest deformation.

**Table 6.7:** Results of the fitted models in Figure 6.41.

Fitted models		Extended Einstein (Equation 6.2)		Batchelor-Green $\frac{G'}{G'_0} = 1 + 2.5X_C + k_H\phi^2$	Power-law $\frac{G'}{G'_0} = \psi X_C^p$	
Experiment	Conditions	$D'$	$C'$	$k_H$	$p$	$\psi$
NA amount (wt%)	$\gamma_0$ (%)					
3	0.5	9240	2.65	2952	2.59	8473
	1	16435	3.07	2495	2.97	13994
	5	5387	2.46	2374	2.39	4833
	10	6066	2.72	1550	2.53	4396
	30	595	1.75	1016	1.45	339
0	0.5	3311	1.57	7063	1.55	3252
	1	3344	1.91	3907	1.88	3224
	5	964	1.46	2605	1.42	913
	10	689	1.50	1904	1.42	597
	30	261	1.20	845	1.15	127

## 6.5 Microstructure, crystallinity and morphology analyses

### *Microstructure analyses*

The microstructure is studied by XRD analysis. The XRD examines the degree of crystallinity, unit cell, and crystallite (domain) size. The XRD patterns of neat HDPE and HDPE/NA samples were recorded using a solid sample, which had the same thermal and shear history via the RheoNMR crystallization experiment. A Bruker AXS D8-Advance diffractometer in  $\theta$ - $\theta$  geometry equipped with a PSD Lynxeye® and Cu  $K\alpha_{1,2}$ -radiation with  $\lambda = 0.15418$  nm at 40 kV and 40 mA were used in the XRD measurements. The diffractograms were recorded over an angular range of 10 - 50°  $2\theta$  with a step of 0.02°  $2\theta$  and a total counting time of 1056 seconds per step owing to the position sensitive detector

(PSD) which consists of 192 single detectors, thus, per step takes 5.5 s. The disk shape samples were partially wrapped with an aluminum (Al)-foil and the Al (111) and (200) peaks were used a correction standard (PDF file (catalog number) 04-0787) to account for the shift in  $^{\circ} 2\theta$  to avoid any errors due to the slightly curved shape of samples. The resulting XRD patterns are displayed in Figure 6.42. The Scherrer equation with the integral breadth was used for the calculation of the domain size as a function of the NA content and crystallization conditions. The integral-breadth Scherrer constant ( $k$ ) was taken as 0.89 for cubic crystallites (Langford and Wilson 1978). The domain size values were also identified by the data evaluation program DIFFRAC-EVA 4.2 with Bruker AXS. Subsequently, these values were corrected for the instrumental contribution of the line width as the linewidth =  $0.009^{\circ}$  at  $21^{\circ} 2\theta$ . The correction-function was established earlier with the help of  $\text{LaB}_6$  a line width standard provided by NIST (NIST SRM 660c).

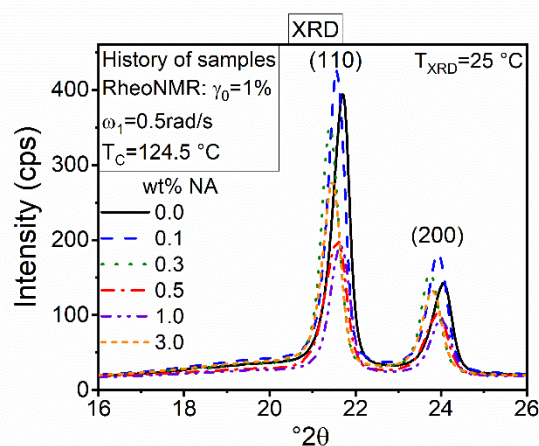


**Figure 6.42:** The XRD patterns of neat HDPE (0% NA) and HDPE/NA samples. Samples were crystallized isothermally at constant  $\omega_1 = 0.5 \text{ rad/s}$ ,  $T_c = 124.5 \text{ }^{\circ}\text{C}$  under applied  $\gamma_0 = 1\%$  and  $\gamma_0 = 30\%$  condition via RheoNMR. The peaks indicated an orthorhombic crystal structure (see Figure 3.2) for all samples.

The XRD profiles of samples started with the amorphous halo, and then, the peaks gradually intensified, which was indicative of crystal structures and the unit cell type. The observed strongest visible two distinct reflection peaks for all samples in Figure 6.42 indicated (110) and (200) planes related with orthorhombic unit cell crystal structure known as the most stable structure for PE (Piorkowska and Rutledge 2013; Schmacke 2010; Gedde and Mattozzi 2004; Wunderlich 2003). The two distinct reflection peaks of (110) and (200) planes were used to calculate the domain size as displayed in Figure 6.43

for the samples as a function of NA content and applied varying  $\gamma_0$  during crystallization.

Increasing NA content in the HDPE sample up to 1 wt% led to smaller domain sizes for both planes compared to the neat HDPE for both crystallization conditions. It has been known that nanoscale NA particles provide high surface area, increase in nucleation, and the smaller domain size (Seven *et al.* 2016). This enhancement in crystallization depends on the NA content in the sample because an increase in NA amount above a threshold value could cause agglomeration of NA due to poor dispersion in polymer melt (Seven *et al.* 2016). Briefly, the domain size decreases with increasing NA content, however, further increased NA amount, which could be above the threshold value, in the polymer sample could cause agglomeration.

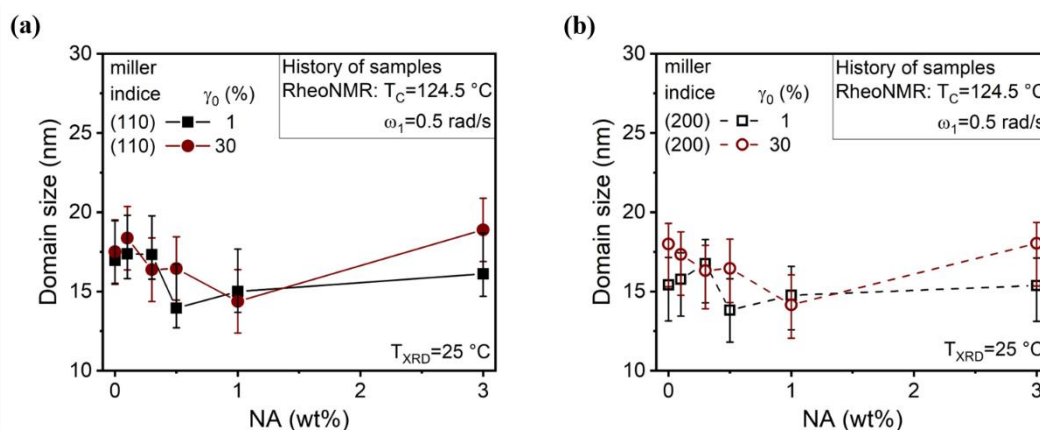


**Figure 6.43:** The calculated domain size from seen two peaks in Figure 6.42a for (a) (110), and (b) (200) planes as a function of NA content (wt%) from the reflection peaks of HDPE/NA samples. Samples were crystallized isothermally at constant  $\omega_1 = 0.5 \text{ rad/s}$ ,  $T_C = 124.5 \text{ }^\circ\text{C}$  under applied  $\gamma_0 = 1\%$  and  $\gamma_0 = 30\%$  conditions via RheoNMR.

Additionally, it has been reported by Weidenthaler (2011) that a decreased crystallite size could also cause agglomeration of small crystals. These agglomerated smaller crystallites can be determined as domain size from XRD reflections (Weidenthaler 2011). This information may explain the reason for the observed decrease in the domain size with increasing NA content up to 1 wt%. Furthermore, an increase in NA content to 3 wt% showed an increase in domain size which could be either related to the agglomeration of smaller crystals or agglomerated NA which did not effectively decrease in the crystallite size. However, this increase in domain size was not significant under considered  $\pm 10\%$  error. Scardi *et al.* (2004) reported that the polycrystalline materials show polydisperse

systems constituting of variable size and shape in crystals. Therefore, the precise calculation and evaluation of domain size are difficult.

### **Crystallinity analyses by XRD, DSC and NMR methods**

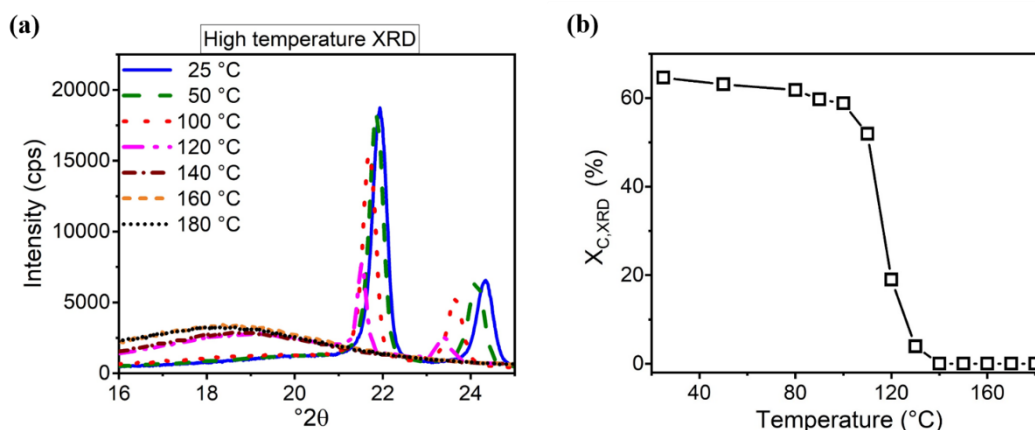


**Figure 6.44:** (a) The XRD pattern of neat HDPE sample at increasing temperature, and (b) the calculated crystallinity  $X_{C,XRD}$  (%) from the XRD pattern in Figure 6.44a.

High-temperature XRD measurement of neat HDPE was conducted by using an HTK1200N high-temperature oven chamber from Anton-Paar (Anton-Paar GmbH, Graz, Austria). The sample was placed in a ceramic holder ( $\alpha$ - $\text{Al}_2\text{O}_3$ ) at ambient temperature (25 °C), and heated up to 180 °C with a heating rate of 10 °C/min. The XRD pattern was taken at every 10 °C in the temperature range 80-180 °C. The temperature calibration was done by using the thermal expansion of BN (boron nitride) after the method of Pease (1952). The diffraction peak position was recorded as the detector angle within a range of 15-65°  $2\theta$  by the step size of 0.0130°  $2\theta$ , and the measurement time was 50 seconds per step. The recorded XRD patterns by varying temperatures are displayed in Figure 6.44a. Changes in intensity of (110) peak from 21.9° to 22.5° with an increased temperature from 25 to 120 °C indicated the loosening of PE chains due to the temperature of pre-melting (Ancharova *et al.* 2016). With the continuous increase in temperature, the diffraction peaks turned to the amorphous halo. Calculation of the crystallinity was described in Chapter 4.4 (see Figure 4.16). A decreasing crystallinity trend was deduced as displayed in Figure 6.44b from the X-ray diffractograms in Figure 6.44. The decrease in  $X_C$  was rather slow until the softening of the material in the temperature range between room temperature up to 100 °C. The reduction in  $X_C$  accelerated in the temperature range

100 °C and 140 °C, and then, the  $X_C$  showed a decaying trend to zero with resulting in a fully amorphous molten sample.

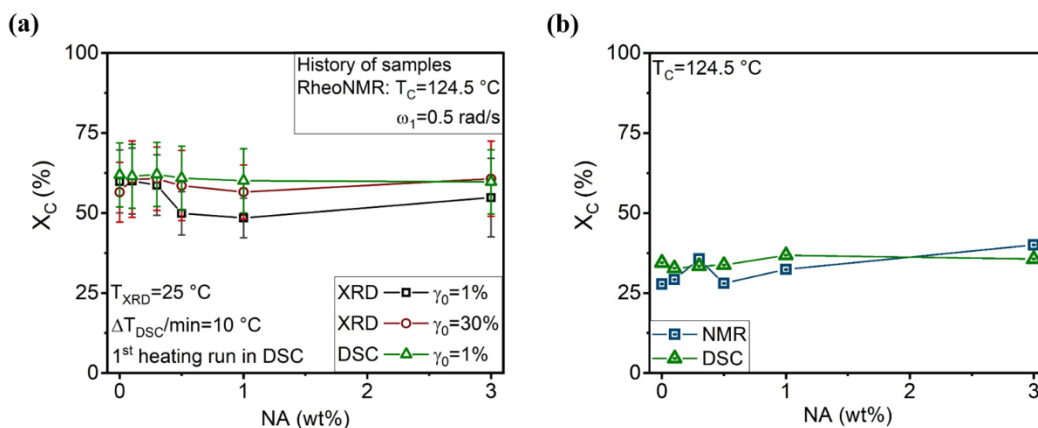


**Figure 6.45:** (a) The calculated crystallinity ( $X_C$ ) from XRD patterns of nucleated and neat HDPE samples as a function of NA content. All samples had a history of RheoNMR experiment at  $\omega_1 = 0.5\text{ rad/s}$ ,  $T_C = 124.5\text{ }^\circ\text{C}$  with applied  $\gamma_0 = 1\%$  and  $\gamma_0 = 30\%$ . Corresponding  $X_C$  results from XRD were compared with DSC analyses on the same samples. (b) The  $X_C$  of HDPE/NA samples under quiescent crystallization as a function of NA content at  $T_C = 124.5\text{ }^\circ\text{C}$  determined by the NMR part of the RheoNMR and the DSC method.

Additionally, the degree of crystallinity values depending on NA content and crystallization condition were obtained by the X-ray diffractograms (see Figure 6.42), and results were compared with the  $X_C$  values determined by DSC. The corresponding  $X_C$  values as a function of NA content are demonstrated in Figure 6.45a. Within  $\pm 10\%$  error for the calculated  $X_C$  values from the XRD curves may result from the estimated non-symmetric Gaussian shape amorphous halo fit with a selected baseline and integrated area range. The crystallinity  $X_C$  showed a  $\sim 15\%$  decrease within 1 wt% increment in the NA content in the HDPE sample under quiescent crystallization. The increment in NA content under strain-induced crystallization did not show a significant change in the  $X_C$  of HDPE/NA samples. Comparison of the the  $X_C$  results via DSC method showed a close estimation with the  $X_C$  values determined by the XRD method. Additionally, determined  $X_C$  values from DSC and NMR part of the RheoNMR are displayed in Figure 6.45b for neat HDPE and HDPE/NA samples at  $124.5\text{ }^\circ\text{C}$  under isothermal quiescent crystallization within a good agreement for both methods with estimated  $\pm 10\%$  error. The difference between the designated  $X_C$  values via DSC method at  $124.5\text{ }^\circ\text{C}$  and  $\sim 25\text{ }^\circ\text{C}$  after quiescent

isothermal crystallization showed a continued secondary crystallization by a temperature drop.

### ***Morphology analyses***

The visual representation of the neat HDPE and nucleated HDPE can be seen through polarized optical microscopy (POM) images in Figure 6.46 and Figure 6.47 respectively. Both samples were placed in between thin two glass slides on the heated stage and the temperature changed from 180 °C to ambient temperature. Then, the POM images were taken with an optical polarizer at the ambient temperature.

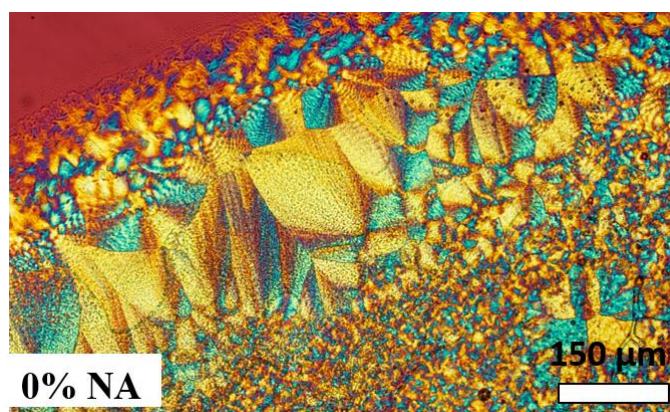


**Figure 6.46:** Polarized optical microscopy (POM) micrograph of banded spherulites of 0% NA (neat HDPE) sample.

Radially symmetric polymer spherulites are composed of lamellae, and they are known as birefringent entities (Auriemma *et al.* 2017). A characteristic extinction pattern with a four-fold symmetry (Maltese cross) can be seen in the POM images of neat and nucleated HDPE samples in Figure 6.46 and 6.47. Without NA content for sample 0% NA, the impinging spherulites with a size smaller than  $\sim 150 \mu\text{m}$  were seen. Additionally, a particular type of spherulite known as banded or ringed spherulite was observed in Figure 6.46. These ringed spherulites composed of the twisting lamella which occurred during crystal growth in bulk crystallization of HDPE. Moreover, in Figure 6.47 the observed size and number of spherulites showed a clear impact of the 1wt% NA content in HDPE with significantly smaller average spherulite size and a remarkably enhanced nucleation density. A more detailed understanding of the influenced morphology by applied large oscillatory shear under isothermal crystallization condition was investigated using scanning electron microscopy (SEM). Crystallized neat HDPE and HDPE/NA blends

were taken after RheoNMR experiments, and then, etching procedure was applied on the samples for preparation to SEM analysis as described in Chapter 6.2. The morphologies after etching were revealed the microstructure of neat HDPE (0% NA), crystallized at 124.5 °C under the quiescent condition, as seen in Figure 6.48. Randomly distributed loose lamellae were observed for 0% NA in Figure 6.48. Additionally, some flat-lying lamellae, and also the elastically bent C-shaped lamellae structures were found for 0% NA. The thicknesses of the lamellae were approximately 25 nm with almost  $\sim 1$   $\mu$ m length.

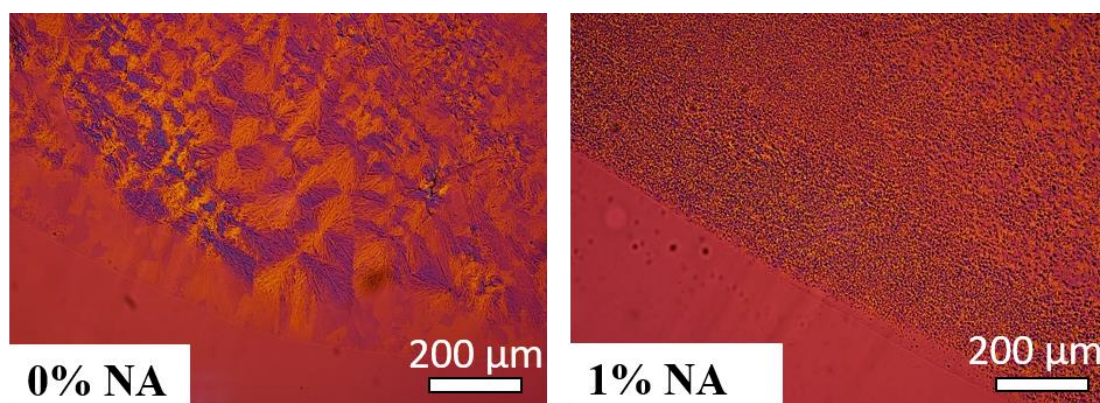


**Figure 6.47:** Polarized optical microscopy (POM) images of 0% NA (neat HDPE) and 1% NA crystallized simultaneously under the same thermal condition by using hot stage which was cooled down from 180 °C to room temperature.

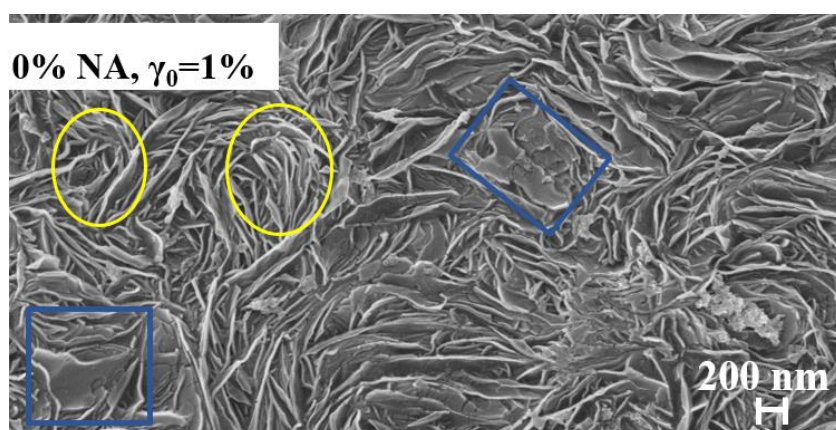


**Figure 6.48:** SEM micrograph of neat HDPE (0% NA) crystallized under the quiescent condition at 124.5 °C via RheoNMR. Blue square shows the flat-lying lamellae, and the yellow circle indicates the elastically bent C-shaped lamella.

Additionally, SEM micrographs of HDPE/NA samples, which were taken after RheoNMR experiment at constant  $\omega_1 = 0.5$  rad/s,  $T_C = 124.5$  °C for applied  $\gamma_0 = 1\%$ , and  $\gamma_0 = 30\%$  conditions, are displayed in Figure 6.49.

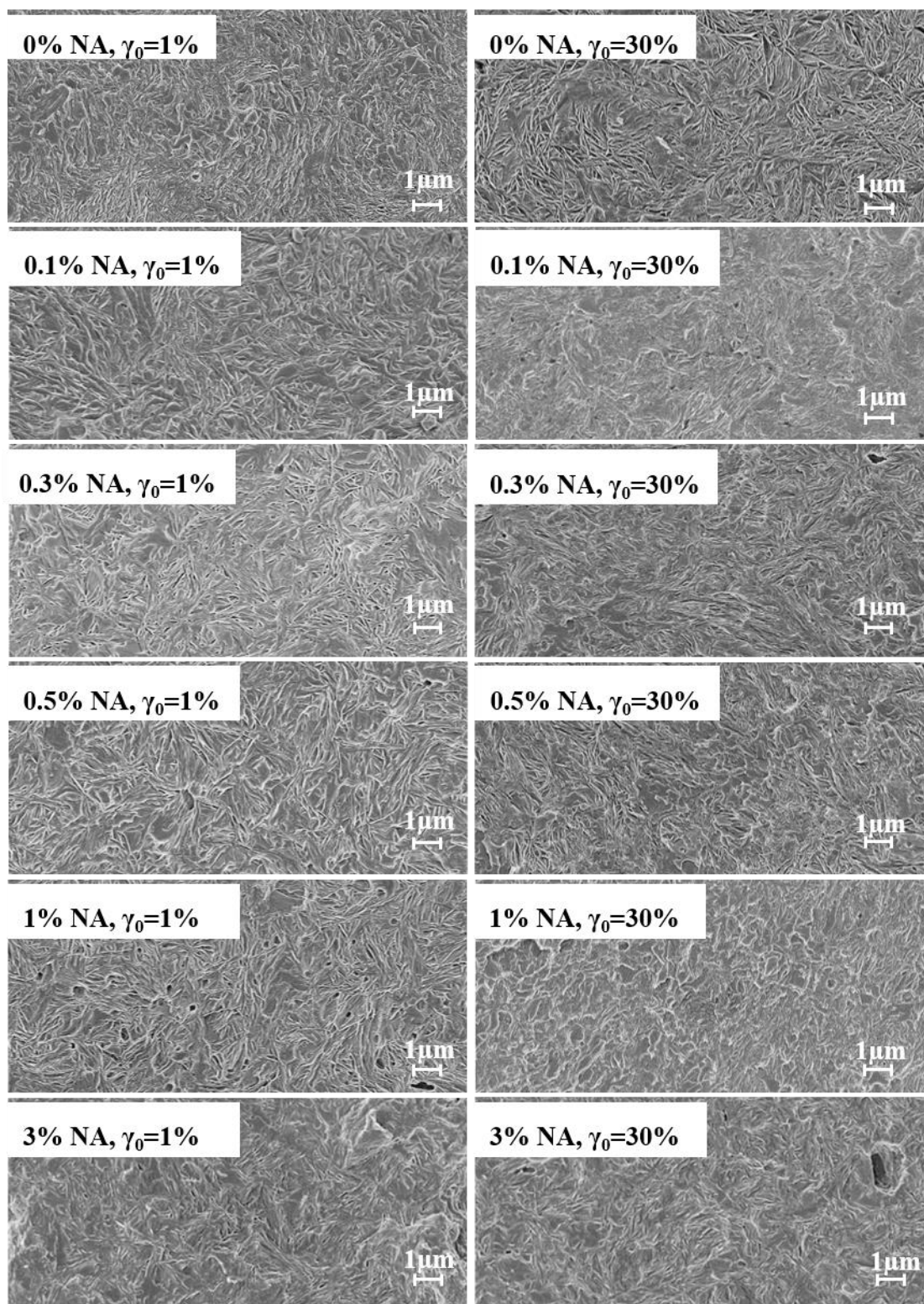


**Figure 6.49:** SEM images of etched neat HDPE and HDPE/NA samples were taken after RheoNMR isothermal crystallization experiment at  $\gamma_0 = 1\%$  and separately  $\gamma_0 = 30\%$  with constant  $\omega_1 = 0.5 \text{ rad/s}$ ,  $T_C = 124.5 \text{ }^\circ\text{C}$ .

A randomly oriented lamellae structure was achieved for all samples under the quiescent crystallization condition. However, partially oriented lamellae were observed for neat HDPE and HDPE/NA samples for exerted  $\gamma_0 = 30\%$ . The lamellae width decreased to almost half in HDPE/NA samples for strain-induced crystallization. It is known that increasing orientation leads to a decrease in the separation between lamellae (Peacock 2000). The observed closely packed partially oriented thinner lamellar structure for applied  $\gamma_0 = 30\%$  condition may be the reason for the slightly higher  $X_C$  values determined via XRD for HDPE/NA blends compared to the observed  $X_C$  value of quiescently crystallized samples (see in Figure 6.45). Additionally, the observed oriented lamellar structures under applied  $\gamma_0 = 30\%$  in SEM images indicated the enhanced crystallization which was agreed with information displayed in Figure 6.40 as the observed shorter time in  $t_{0.2}$  under strain-induced crystallization for all samples. The enhancement was not suggested in the nucleation stage, because the delay was observed in  $t_{gel}$ . In the SEM images, all samples showed lamellar stacks with some flat-lying lamellae. The presence of some round holes was observed for especially for 1% NA. These holes could be the etch pits of a more susceptible part of thin lamellae.

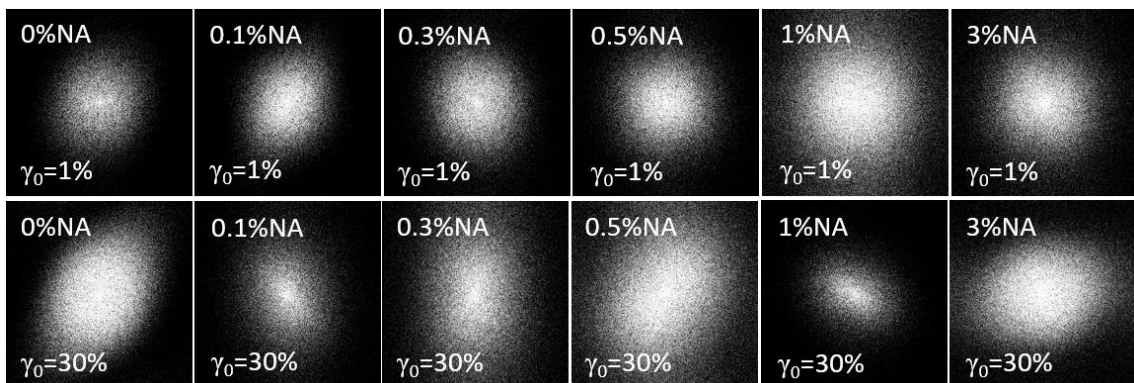


**Figure 6.50:** Corresponding fast Fourier transforms (FFTs) of the SEM images shown in Figure 6.49.

Further analysis of lamellae orientation was investigated by using fast Fourier transforms (FFT) based on the conversion of the SEM image into frequency spacing, using ImageJ software. The resulting FFT images are demonstrated in Figure 6.50. Corresponding FFTs consisted of distribution of grayscale pixels in a pattern that reflects the presence of lamellar alignment in SEM micrographs. The FFT of 0% NA sample could be representative of a randomly aligned lamellar structure. Except for the 0.1% NA sample,

all samples for quiescent crystallization condition ( $\gamma_0 = 1\%$ ) showed a symmetrical circular shape FFT image which indicated that randomly aligned lamellar structure. In contrast to all quiescently crystallized samples, the FFT image of quiescently crystallized 0.1% NA sample containing elliptical distribution demonstrated an orientation of lamellar structures. All samples crystallized under strain-induced crystallization represented elliptical distribution and this indicated an orientation of lamellar in a different direction. FFT images reflected the existing orientation of lamellar much clearly. However, the numerical designation was needed to investigate the direction of the orientation. An assignation of the numerical value for lamella alignment can be generated by placing a circular projection on the FFT image with processed oval profile plug-in (authored by William O'Connell) of ImageJ software (NIH, <http://rsb.info.nih.gov/ij>). A radial summation of the pixel intensities from  $0^\circ$  to  $360^\circ$  with  $1^\circ$  increment was conducted, and then corresponding data was plotted as a function of the degree. This protocol is described in Figure 6.51.

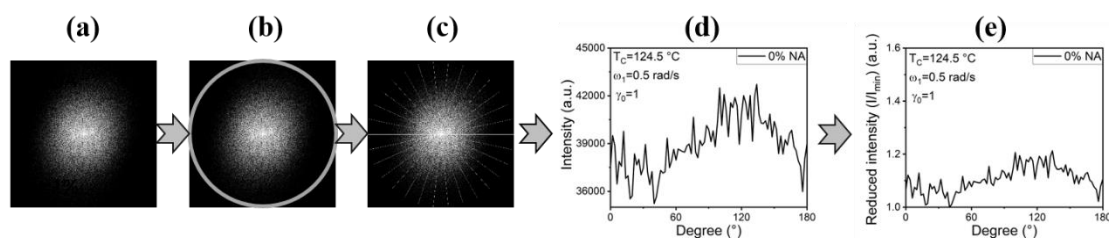


**Figure 6.51:** Schematic description of the structure alignment analysis on the FFT image by using ImageJ software (NIH, <http://rsb.info.nih.gov/ij>) oval profile plug-in, authored by William O'Connell. (a) Fast Fourier transform of the SEM images of HDPE sample, (b) chosen oval profile for analysis, (c) circular projection on the FFT output image, (d) conducting a radial summation of the pixel intensities ( $I$ ) for each degree between  $0^\circ$  and  $180^\circ$ , and (e) Normalized intensity as a function of the degree.

The intensity ( $I$ ) value was divided by the minimum value ( $I_{\text{minimum}}$ ), and resulted in reduced-intensity with arbitrary units was plotted in a degree between  $1^\circ$  and  $180^\circ$  due to the symmetric horizontal axis of the FFT (see Figure 6.50). A graphical depiction in Figure 6.52 shows the comparison of the amount of lamellar alignment for all samples under quiescent and strain-induced crystallization, generated by using FFT images in Figure 6.50. The lamellar alignment is reflected by the height and the overall shape of the peak in Figure 6.52. The quiescently crystallized sample 0.1% NA showed a lamellar orientation dominantly around  $100^\circ$  determined directly from the peak position.

However, no certain direction was observed for other quiescently crystallized samples. In the strain-induced crystallization case, peaks of the sample were higher compared to the observed peaks in Figure 6.52a. While the 0% NA and 0.5% NA oriented dominantly at  $120^\circ$ , maximum of the peak was found for 0.3% NA, 0.1% NA, 1% NA and 3% NA mainly around  $80^\circ$ ,  $70^\circ$ ,  $25^\circ$  and  $170^\circ$  respectively. Regarding the peak maximum value of each sample in between two crystallization conditions, the maximum difference was observed for sample 0.3% NA and 1% NA. The lowest difference in the peak maximum was achieved for sample 0.1% NA.

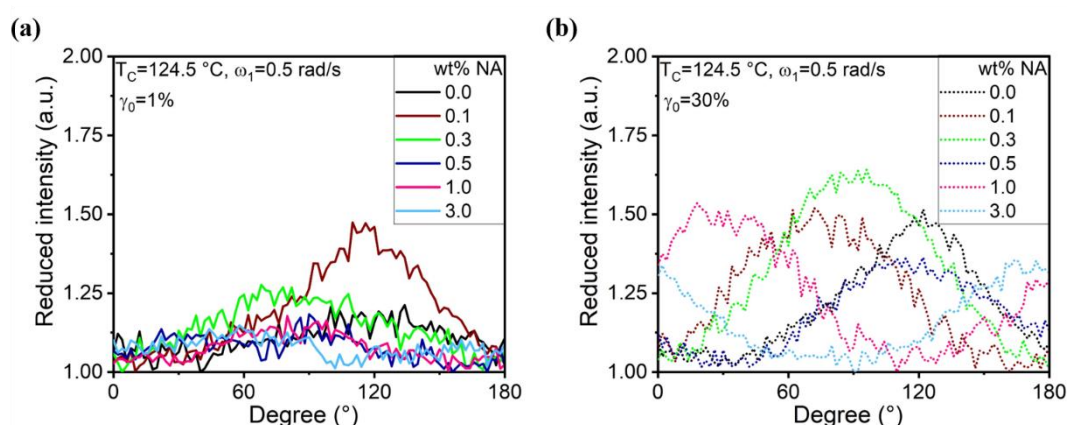


**Figure 6.52:** Analysis of structure alignment using ImageJ software oval profile plug-in (authored by William O’Connell) on FFT images for a graphical depiction of Figure 6.49 samples which were taken after RheoNMR experiment at constant  $\omega_1 = 0.5\text{ rad/s}$ ,  $T_C = 124.5^\circ\text{C}$  for (a) quiescent ( $\gamma_0 = 1\%$ ) and (b) strain-induced ( $\gamma_0 = 30\%$ ) crystallization conditions.

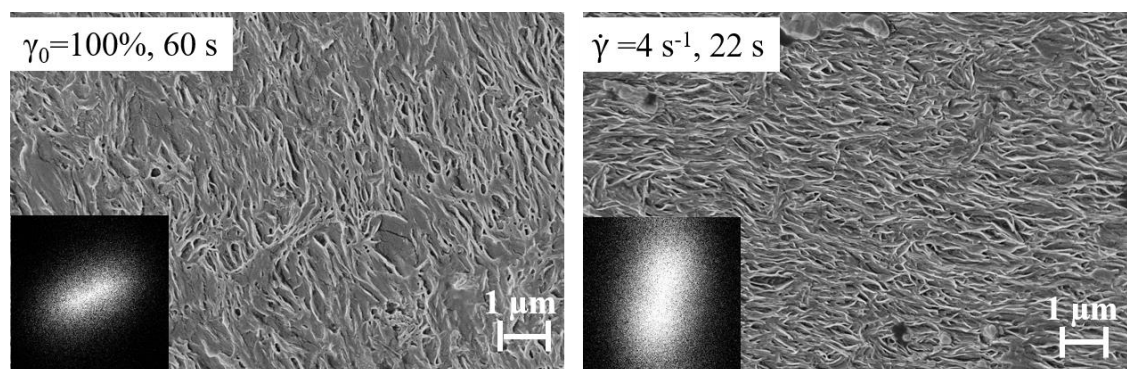


**Figure 6.53:** SEM micrographs of the etched 1% NA sample which crystallized under constant  $\omega_1 = 0.5\text{ rad/s}$ ,  $T_C = 124^\circ\text{C}$  (a) for applied short term large strain amplitude as  $\gamma_0 = 100\%$  during 60 s, and (b) for applied steady shear with a shear rate  $\dot{\gamma} = 4\text{ s}^{-1}$  during 22 s. The steady shear was applied at the beginning of the experiment. The short term large strain amplitude was applied at the 5<sup>th</sup> min of the experiment (see Chapter 6.4.2) Corresponding FFTs are displayed at the down left corner on the SEM images.

Morphological evolution is displayed as SEM images in Figure 6.53 for the 1% NA sample crystallized at  $\omega_1 = 0.5$  rad/s,  $T_C = 124.5$  °C for applied short term large strain amplitude as  $\gamma_0 = 100\%$  during 60 s at the 5<sup>th</sup> min of the experiment. This micrograph can be compared with the SEM image of the same sample (see Figure 6.53) crystallized at  $\omega_1 = 0.5$  rad/s,  $T_C = 124.5$  °C with applied shear rate  $\dot{\gamma} = 4$  s<sup>-1</sup> during 22 s at the beginning of the cooling. It was observed that crystal morphology mainly consisted of oriented parallel lamellar stacks for both crystallization conditions due to the applied large deformation or steady shear. The lamellar alignment was reflected also in FFT images with elliptical distribution in grayscale pixels. These oriented parallel lamellar stacks are known as the kebab part of the shish-kebab crystal structure (Wang *et al.* 2013). The application of weak shear was responsible for the non-existence of shish structures. The lamellae thickness was similar for both samples (25 nm or less). The length of the lamellae was  $\sim 1$   $\mu\text{m}$  for applied steady shear samples, and it was about 2  $\mu\text{m}$  for applied  $\gamma_0 = 100\%$ , 60 s sample. Tilted structures were seen for both samples as a small number compared to the density of oriented lamellar. The bending degree angle was about 90° for conducted large strain amplitude  $\gamma_0 = 100\%$ , 60 s sample, but this tilted to a degree of angle around 40° for conducted steady shear with a shear rate  $\dot{\gamma} = 4$  s<sup>-1</sup>, 22 s sample. A major difference between the melt orientation and the orientation during crystallization is that the motion of polymer chains is limited due to the increasing viscosity by a temperature drop during crystallization. Polymer chains are oriented in the non-crystalline region and remained like that when the large oscillatory shear is applied during crystallization. However, orientation is much easier in the melt under applied flow, and thus, lamellae are well aligned.

Figure 6.54 shows the SEM image of the quiescently crystallized PE-1 sample at 125 °C. Bundles of lamellae (sheaves) were observed for sample PE-1. The generation of a multitude of lamellar bundles is known as because of the high nucleation density that causes insufficient place for the spherulites to mature (Peacock 2000).

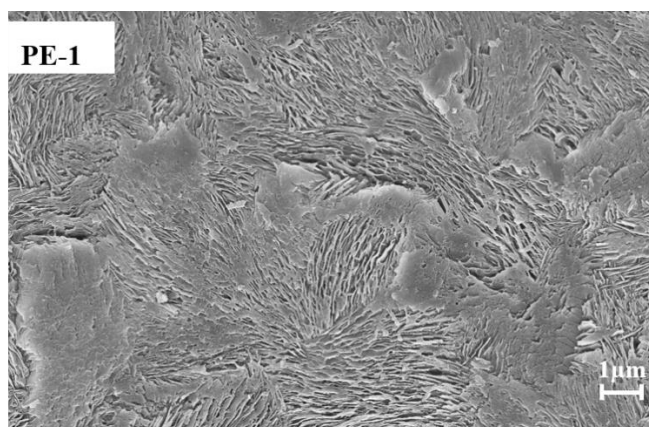


**Figure 6.54:** The SEM image of the PE-1 (see Chapter 6.3.2) quiescently crystallized.

## 6.6 Concluding remarks

In this chapter, isothermal crystallization of neat and nucleated HDPE samples was investigated by using the RheoNMR technique under quiescent and applied flow conditions such as varying shear rate ( $\dot{\gamma}$ ) or strain amplitudes ( $\gamma_0$ ) with their changing duration. The rheological quantities dynamic moduli ( $G'$  and  $G''$ ) and the relative third harmonic ( $I_{3/1}$ ) were determined by a rheometer during crystallization. Meanwhile developing crystallinity ( $X_C$ ) was examined by using the molecular mobility of protons monitored via low-field NMR using the CPMG pulse sequence (see Chapter 5). This simultaneous measurement by RheoNMR enables the direct correlation between dynamic moduli and crystallinity development of samples even for  $\Delta T_C = 0.5$  °C under the same thermal and shear history conditions. Directly correlated the  $\frac{G'}{G'_0}$  and the  $X_C$  were well explained by the power-law and the extended Einstein models up to  $X_C = \sim 20\%$ . The calculated parameters of the models were observed for the exponents  $C'$  and  $p$  in the range 1 to 3, and for  $D'$  and  $\psi$  in between  $\sim 130$  and  $\sim 16500$  depending on NA content in the sample,  $T_C$  and applied deformation.

A more important correlation was the quantities  $t_{0.2}$  and  $t_{gel}$  which clarified the influence of NA content,  $T_C$  and applied strain amplitude on the crystallization of HDPE/NA blends. Under quiescent isothermal crystallization condition, a linear relationship was observed in this time correlation towards  $T_C$  with a decreasing tendency in slope by increased NA content. A decreased in  $\Delta T_C = 0.5$  °C led to almost half of  $t_{0.2}$  and  $t_{gel}$ , and added 3 wt%

NA in HDPE was decreased the  $t_{gel}$  to half and the  $t_{0.2}$  to almost one third at constant  $T_C$ . For the strain-induced crystallization condition, the increasing strain amplitude ( $\gamma_0$ ) up to 30% application during crystallization delayed the  $t_{gel}$ , but it shortened the  $t_{0.2}$ . This suggested a dominantly induced the crystal growth stage, and thus, enhanced the crystallization. Increased NA content above 0.1 wt% in the HDPE sample reduced the effects of strain-induced crystallization, and thus, the reduction in  $t_{0.2}$  and the delay in  $t_{gel}$  was rather small compared to the observed values for sample 0.1% NA and 0% NA. Besides, applied short term  $\gamma_0 = 200\%$ , 60 s at the 5<sup>th</sup> min of the experiment accelerated crystallization. The achieved shorter  $t_{gel}$  and  $t_{0.2}$  as  $\sim 2$  and  $\sim 3$  min respectively indicated an enhanced nucleation and crystal growth stage. Furthermore, the conducted steady shear e.g.  $\dot{\gamma} = 2 \text{ s}^{-1}$ , 11 s at the beginning of the experiment promoted the nucleation stage and showed similar effect with a 1 °C drop in  $T_C$ . Additionally, an imposed shear rate  $\dot{\gamma} = 2 \text{ s}^{-1}$ , 11 s at 2 min of the experiment possibly induced not only nucleation but also crystal growth, thereby caused slightly lower  $t_{gel}$  and  $t_{0.1}$  than the achieved values for applied  $\dot{\gamma} = 16 \text{ s}^{-1}$ , 11 s experiment. The  $X_{C,gel}$  was always below 8%.

Moreover, the nonlinearity was determined with the observed peak maximum of  $I_{3/1}$  at around the  $t_{gel}$ . The observed peak maximum of  $I_{3/1}$  as a function of  $t_{gel}$  correlation showed an exponential decay like change by decreasing NA content in HDPE and/or the  $T_C$ . Conversely, the applied large oscillatory shear e.g.,  $\gamma_0 = 30\%$  led to an increase of the peak maximum of  $I_{3/1}$  compared to the applied small oscillatory shear i.e.,  $\gamma_0 = 1\%$  condition.

In this chapter, low-field NMR part of the RheoNMR, XRD, DSC methods were used to investigate the  $X_C$  by measuring molecular dynamics, unit cell order, enthalpy changes respectively. An orthorhombic unit cell structure was determined by XRD analyses for neat HDPE and HDPE/NA blends. The determined  $X_C$  values from XRD, DSC techniques as a function of NA content were close to each other within  $\pm 10\%$  errors as  $X_C = \sim 62\%$  measured at 25 °C. Compared DSC and NMR  $X_C$  results at 124 °C were found  $\sim 37\%$  and equivalent. This difference in  $X_C$  depending on measurement temperature revealed the ongoing secondary crystallization by decreased temperature. Equivalent results from the

different methods have verified the accuracy of this newly developed RheoNMR technique.

The POM image provided visual representation. A banded or ringed type spherulite was observed for neat HDPE. The addition of NA (1 wt%) led to a significantly smaller average spherulite size and a remarkably increased number of nucleation. Additionally, the morphology of samples was investigated by using SEM. The neat HDPE showed randomly distributed loose lamellae with some flat-lying lamellae, and also the elastically bent C-shaped lamellae structures. On the one hand, the closely packed slightly oriented thinner lamellar structure was revealed for HDPE/NA blend samples under strain-induced crystallization conditions. On the other hand, the oriented parallel lamellar stacks were observed for a 1% NA sample under the applied large deformation or steady shear conditions. Then, the SEM images converted to FFT images to investigate lamellar alignment. Lamellae orientation were observed with elliptical distribution in grayscale pixels for the samples crystallized under strain-induced and applied steady shear crystallization conditions. The oval profile plug-in of ImageJ software was provided the numerical value for lamella alignment. While the lamellar of 0% NA and 0.5% NA aligned mainly around 120 °, the maximum of the intensity peak was achieved for 0.3% NA, 0.1% NA, 1% NA and 3% NA around 80°, 70°, 25° and 170° respectively for strain-induced crystallization condition.

## 7 Fat Crystallization Kinetics-Coconut Oil

Popularities of crop oil is increasing to improve the efficiency of the recycling process and to reduce the amount of waste. The high costs of petroleum-based products are also a reason to recycle waste. Coconut oil is one of the most used commercially available crop oil. Coconut oil has a wide range use as raw material for the production of soaps, detergents, a body oil, as hard butter, vegetable fat ice-cream, coffee whiteners (Young 1983). It is also used as a food product, cosmetics, pharmaceutical preparation characteristics (Chaleepa, *et al.* 2010). Philippines, Malaysia, and Indonesia are the world's largest coconut oil producers The unrefined coconut oil contains 90% of several types of saturated fatty acids and triglycerides (Chaleepa *et al.* 2010). Coconut oil is solid at ambient temperature. Therefore, it can be called fat. It has a scarp melting curve because of its triglycerides content (Young 1983). The melting point ( $T_m$ ) of the coconut oil can be influenced by hydrogenation itself and the contamination during the hydrogenation process (Young 1983). Additional to the hydrogenation process the fat properties such as the firmness, texture, and stability at certain temperatures are particularly related to the melting characteristics, the crystal habit of the fat and their polymorphism. These properties can be modified by interesterification and fractionation processes (Moran and Rajan 1994). For instance, the dry fractionation process is one of the three well-established fractionation processes. This environmentally friendly and cost-effective physical fractionation process consists of a partial, or fractional, melt crystallization of the oil without using chemical additives (Ulrich 2004). The success of this process lies in a controlled crystallization condition to preserve the selectivity of crystallization to produce fat with specific characteristics. The crystallization behavior of fat is strongly influenced by the crystallization conditions such as the temperature and the deformation during industrial operation (Kellens *et al.* 1990). Thus, the comprehensive knowledge of crystallization characteristics under-identified crystallization condition is required to achieve specific physical fat properties. This knowledge must be combined with the understanding of the flow properties of the oil such as viscosity during industrial processes. The flow properties of the oil are not only related to the solid fat concentration but also are strongly affected by the interactions between the crystal entities such as

network or gelled phases (Moran and Rajan 1994). The type of microstructures, relation in between them and processing conditions effects resulting in macroscopic properties. Structure hierarchy within a fat network and their effects on macroscopic properties are described as in Figure 7.1. The essential effects of microstructures on macroscopic properties were introduced by DeMan and Beers even in 1987. A prediction of the macroscopic properties is possible by rheological quantities that has immense importance to optimize processing conditions and maintain the quality of the fat. The macroscopic rheological properties such as spreadability and texture depend on mechanical strength of the fat crystal network which can be determined by the sensory attributes such as mouthfeel (De Graef *et al.* 2008).

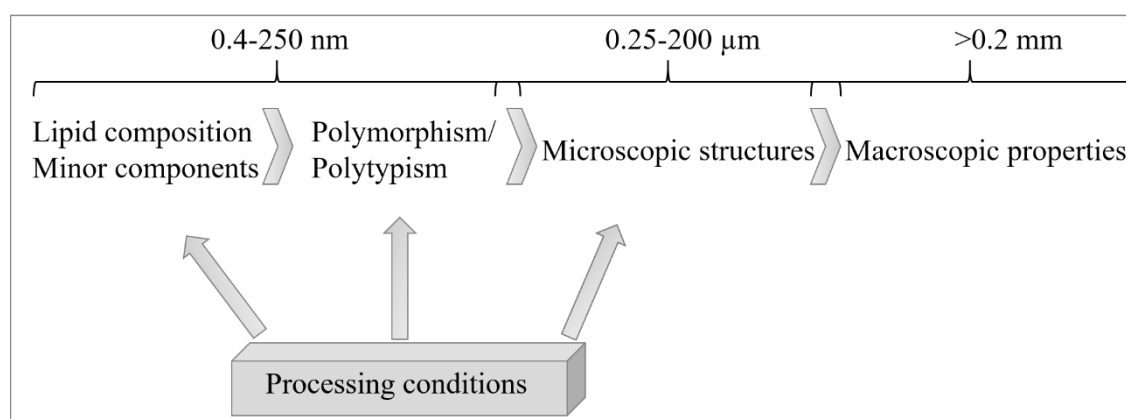


**Figure 7.1:** Schematic representation of structural levels in fat crystal network and their influence on macroscopic properties. The schema was developed by Marangoni and Narine (1999, 2002; Marangoni 2005). Polymorphism: the existence of more than one crystalline form or structural arrangement. Polytypism: a special kind of polymorphism occurs in the number and the manner of stacking layers in the crystal unit cell.

Therefore, a deeper understanding of thermal profiles and crystallization behaviors of fat systems is essential to control processing conditions to reach desired product characteristics (Chaleepa *et al.* 2010). Crystallization kinetic experiments must be conducted by sufficiently sensitive experimental techniques to be able to detect nucleation and crystal growth during crystallization. The well-known commonly practiced crystallization kinetics methods for fat are NMR, DSC, rheology and light-scattering techniques (Cerqueira *et al.* 2004). The newly developed unique low-field RheoNMR setup simultaneously monitors the full rheological shear behavior and

crystallinity. Additionally, this technique allows for correlating macroscopic material properties and microscopic molecular dynamics.

To demonstrate the capabilities of this new low-field RheoNMR technique, coconut oil was chosen as a model substance for a fat crystallization kinetic study. Although coconut oil is extensively used in several applications from food to industrial purposes, the kinetic study of coconut oil crystallization has rarely been published. As well as less publication about the crystallization kinetic on coconut oil, its low cost and easy accessibility makes it favorable for this study. The commercially available brand called Palmin as a coconut fat margarine was used in this study. The thermal profile analysis of the coconut oil product was studied by DSC (TA Q200, TA Instruments, New Castle, DE, USA) under the N<sub>2</sub> atmosphere with a heating and cool rate of 10 °C/min. First, the heating run was carried out from ambient temperature to 50 °C, and the sample was kept 2 min at 50 °C to clean the thermal history. Then, the sample was cooled down to -50 and immediately after the temperature was raised to 50 °C. The resulting peak from the melting curve from the second heating run was used to calculate the  $T_m$  as ~ 25 °C within ± 0.2 °C error. Chaleepa *et al.* (2010) observed the same  $T_m$  value for coconut oil and they extrapolated the  $T_m^0$  as ~ 27 °C.

The primary fat crystals aggregate via van der Waals interactions (De Graef *et al.* 2008; DeMan and Beers 1987). Aggregation of fat crystals starts at a low degree of volume crystallinity and forms voluminous aggregates (De Graef *et al.* 2008). The voluminous aggregates cause solid bridges between aggregated crystals, known as sintering (De Graef *et al.* 2008). Continuous fat crystal agglomeration forms a three-dimensional network (De Graef *et al.* 2008). A lot of factors affect the fat crystal growth rate such as viscosity, the conformation of the molecules, surface defects, existence impurities, shear rates, etc. (Kloed 1998).

## **7.1 Isothermal crystallization of coconut fat via RheoNMR**

The isothermal crystallization experiments of coconut fat samples were conducted via RheoNMR with using ceramic 13 mm cone-plate geometry (see Figure 5.3). The solid coconut fat was molten at 50 °C in a glass beaker, which was on the temperature

adjustable heater plate. Then, approximately a 15 ml liquid sample was loaded with the help of a syringe on the bottom plate geometry. Next, the NMR part of the technique was assembled. The temperature of the sample was heated up to 50 °C and waited until it was liquid again. The upper plate geometry was then lowered slowly until the sample filled the gap between the upper and the bottom geometries. The temperature of the sample was kept at 50 °C for 15 min to obtain an isotropic melt sample. Then, the sample was cooled to the crystallization temperature  $T_C$  as fast as possible. Cooling took approximately 200 seconds. The oil sample was kept at  $T_C$  until its fully crystalline. The temperature-dependent experiments of coconut fat are shown in Figure 7.2.

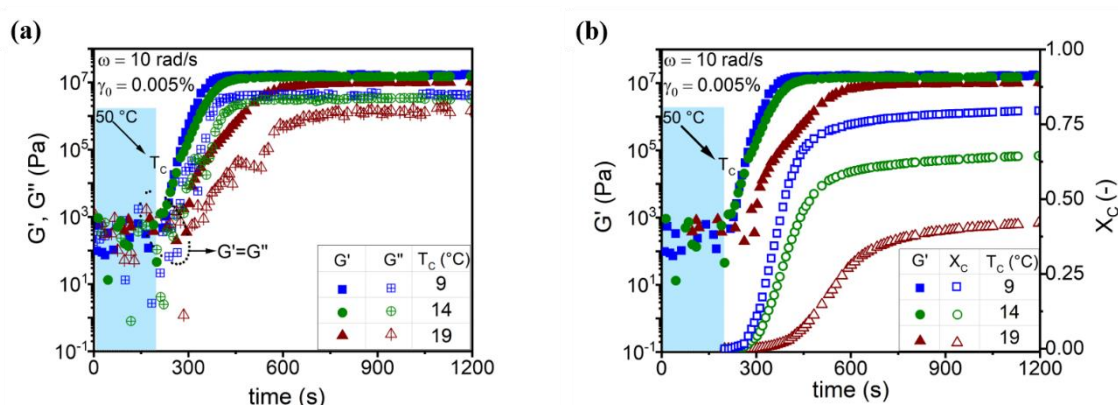


**Figure 7.2:** Isothermal crystallization profiles of coconut fat at  $\omega_1 = 10$  rad/s for varying  $T_C$  with applied  $\gamma_0 = 0.005\%$ . (a) The time evolution of  $G'(\omega_1)$  and  $G''(\omega_1)$  from the Rheo part and (b)  $G'(\omega_1)$  and simultaneously monitored the  $X_C$  via the NMR part of the RheoNMR as a function of time.

The low deformation amplitude was applied to make sure that the applied deformation amplitude does not disturb the crystal network. Figure 7.2a shows the occurred the gelation ( $G' = G''$ ) at a solid fat fraction of less than 0.01. The storage moduli ( $G'$ ) became greater in the value than loss modulus ( $G''$ ) with increasing crystallinity ( $X_C$ ) as following the crystallization principle. Although the moduli reached the final maximum stable value ( $G'_\infty$ ), the crystallization continued for another 100 s to achieve the final solid fat fraction (SFC) ( $X_C^\infty$ ) due to comprised of developing secondary crystallization (see Figure 7.2b). The  $X_C^\infty$  was observed as 80% at  $T_C = 9$  °C. The increased  $T_C$  from 9 to 19 °C reduced the  $X_C^\infty$  to almost its half. Presumably, the increasing  $T_C$  led to bigger spherulites in which had a more amorphous phase.

The various deformation amplitude was imposed during the solidification of the coconut fat as depicted in Figure 7.3 for investigation of strain-induced crystallization.

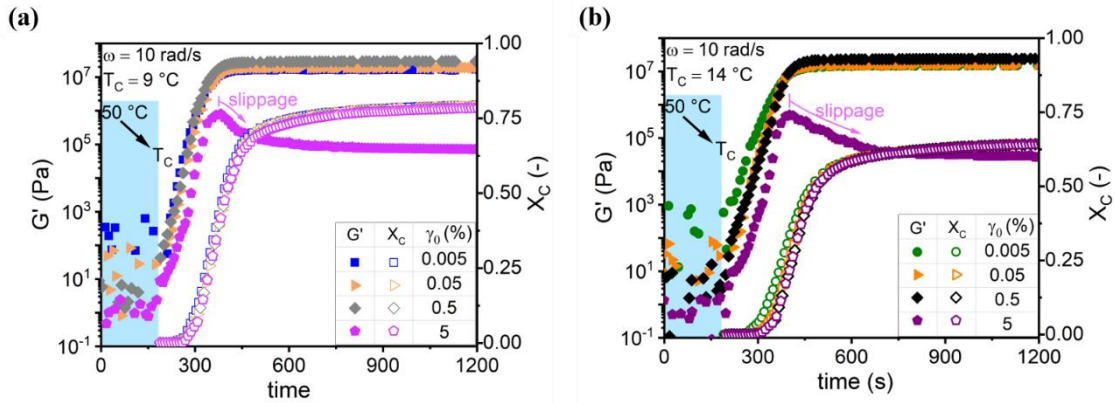


**Figure 7.3:** Simultaneously monitored the  $G'$  and the  $X_C$  from isothermal crystallization of coconut fat under imposed various  $\gamma_0$  with the  $\omega_1 = 10 \text{ rad/s}$  (a) at the  $T_C = 9 \text{ }^\circ\text{C}$ , and (b) at the  $T_C = 14 \text{ }^\circ\text{C}$ .

No significant effect was found on the macroscopic material properties ( $G'$ ) with subjected strain amplitude  $\gamma_0 \leq 0.5\%$  at  $T_C = 9 \text{ }^\circ\text{C}$ . While the imposed various deformation caused almost no difference in the  $X_C$  development at  $T_C = 9 \text{ }^\circ\text{C}$ , delaying crystallization was observed with increased deformation at  $T_C = 14 \text{ }^\circ\text{C}$ . The increased  $\gamma_0$  from 0.005% to 5% at  $T_C = 14 \text{ }^\circ\text{C}$  caused a significant decrease in  $G'$  by a factor of 100 and led to slippage or fracture when the sample was fully crystalline. The slippage or fracture occurred also under the applied  $\gamma_0 = 5\%$  at  $T_C = 9 \text{ }^\circ\text{C}$  when the sample was fully crystalline. Although the  $X_C^\infty$  was not influenced by applied varied  $\gamma_0$  for both  $T_C$ , the observed delay in the  $X_C$  development at  $14 \text{ }^\circ\text{C}$  and reduced moduli by increased  $\gamma_0$  indicated a possible change in the microstructure. This may be in a good agreement with the study of Marangoni and Narine (2002) that the macroscopic mechanical properties of oils are directly linked with the microstructure of the crystal network rather than the final crystallinity. Additionally, Shi *et al.* (2005) reported that the differences in size, shape, and polymorphs of crystal structures could cause different textural properties for oil products.

### 7.1.1 Kinetic analysis of isothermal coconut fat crystallization

The coconut fat crystallization kinetic was analyzed by using Avrami, modified Gompertz and Foubert models to extract important parameters regarding the crystallization rate and

crystallization mechanism. The commonly used Avrami model was explained in Chapter 3.2.3. The modified Gompertz model has been also used to describe the crystallization kinetics of fats (Kloek *et al.* 2000; Foubert *et al.* 2003). The modified Gompertz model is often used to represent bacteria growth in biology (Zwietering *et al.* 1990; Foubert *et al.* 2003; Tjørve and Tjørve 2017). The modified Gompertz equation is described as:

$$\frac{X_C(t)}{X_C^\infty} = \exp \left\{ -\exp \left[ \frac{\mu * e}{X_C^\infty} * (\lambda - t) + 1 \right] \right\} \quad (7.1)$$

where  $\mu$  (1/s) is the maximum increase rate in the crystallization given by the slope of the exponential increase in the crystallization curve, and  $\lambda$  (s) is a measure for the induction time with the time  $t$  and  $e$  equals  $\exp(1)$ .

A relatively newly developed Foubert model has been used to characterize isothermal fat crystallization kinetics (Foubert *et al.* 2002; Foubert *et al.* 2003; Rigolle *et al.* 2015). This model expresses the crystallization process with a combination of a first-order forward reaction and a reverse reaction of order  $m$  (-) under the isothermal condition as following,

$$\frac{X_C(t)}{X_C^\infty} = \left[ 1 - \left[ 1 + ((1 - x)^{1-m} - 1) \times e^{-(1-m) \times v \times (t - t_{\text{indx}})} \right]^{\frac{1}{1-m}} \right] \quad (7.2)$$

In Equation 7.2, the  $t_{\text{indx}}$  (s) is an induction time, needed to obtain  $x$  (%) amount of the crystallinity, and the  $v$  (1/s) is the rate constant. The parameter  $x$  was fixed to 0.01 (Rigolle *et al.* 2015) for all experiments to reduce the variable parameters from four to three to get more precise fit results. In Foubert model, parameter  $m$  is linked with the induction time  $t_{\text{indx}}$ ,  $v$  and the degree of curve asymmetry. For instance, the  $m$  value of a perfectly symmetric crystallization curve is equal to 2. In the case of  $m > 2$  the crystallization is faster at the beginning and relatively slower at the end stage of the crystallization process, and the difference between the beginning and the end-stage of the crystallization is larger for larger  $m$  values.

The relative crystallinities ( $X_C / X_C^\infty$ ) were plotted as a function of time for varying  $T_C$ , and all models were fitted to the crystallization curves as depicted in Figure 7.4a-c. The quality of fit of all models is similarly good based on the coefficient of determination (CoD) or  $R^2$  value. The CoD has a higher value up to 1 as an indicator of a better fit. All models fit the results with  $\text{CoD} > 0.995$ . While the Avrami model describes dominantly

primary crystallization part, the modified Gompertz and Foubert model fits the complete crystallization process well. The deduced kinetic parameters of the Avrami, modified Gompertz and Foubert models are displayed in Figure 7.5a-f.

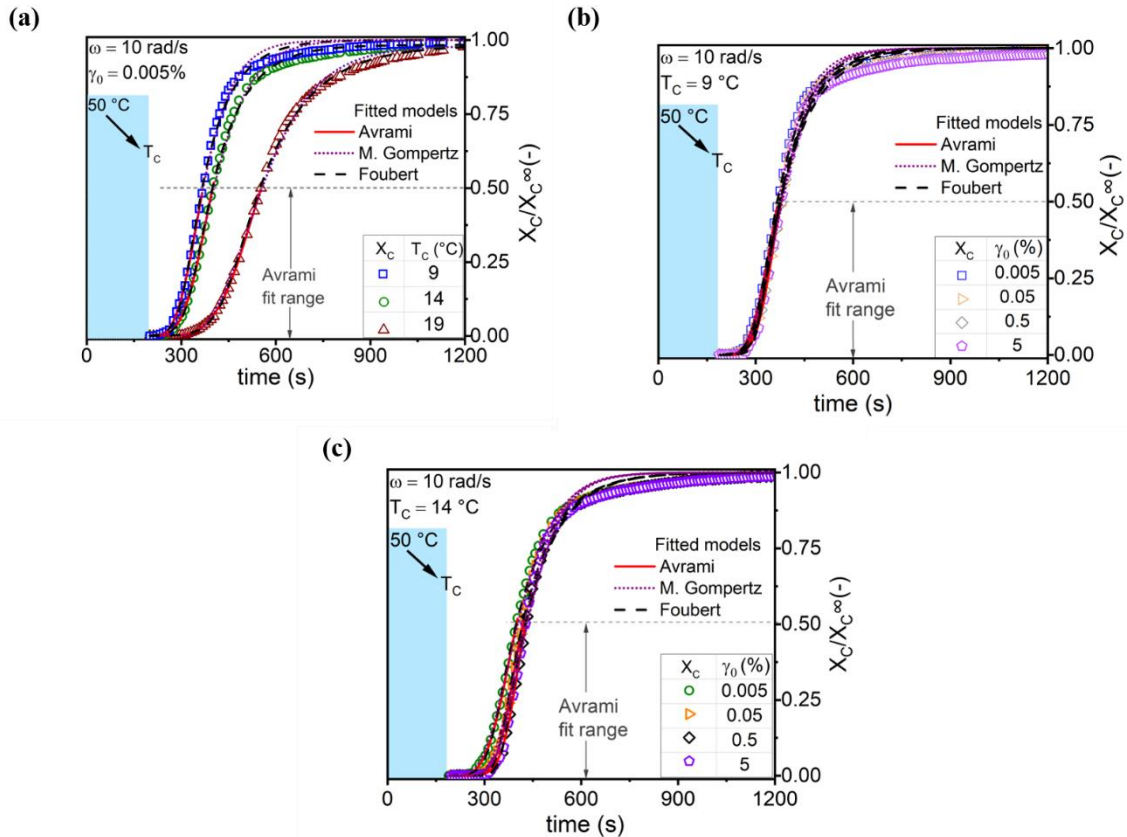


**Figure 7.4:** Visual comparison of fitted models the Avrami, modified Gompertz and Foubert to the relative crystallinity  $X_C / X_C^\infty$  curves as a function of time during isothermal crystallization of coconut fat at  $\omega_1 = 10 \text{ rad/s}$ . (a) Temperature dependent experiments at a constant  $\gamma_0 = 0.005\%$ . Strain-induced crystallization (b) at the  $T_C = 9 \text{ }^\circ\text{C}$  and (c) at the  $T_C = 14 \text{ }^\circ\text{C}$ . Avrami model (see Equation 3.47) was fitted up to  $X_C / X_C^\infty = 0.50$  and shown as red line. The modified Gompertz and Foubert models can be seen as purple dot lines and black dash lines respectively.

The extracted induction time parameters  $\lambda$  and  $t_{\text{indx}}$  were close. While the calculated  $\lambda$  increased 110 s, the  $t_{\text{indx}}$  raised 118 s with a 10 °C increment in  $T_C$ . Meanwhile, the rate values  $K$ ,  $\mu$ , and  $\nu$  decreased by approximately 50% due to the slower crystallization at higher  $T_C$ . Additionally, the  $\lambda$  and  $t_{\text{indx}}$  values increased by imposed largest  $\gamma_0$  as 10 s at  $T_C = 9 \text{ }^\circ\text{C}$  and 35 s at  $T_C = 14 \text{ }^\circ\text{C}$  compared the values for the applied smallest  $\gamma_0$  experiment. The  $K$  value showed a 10% decrease at  $T_C = 14 \text{ }^\circ\text{C}$  for applied largest  $\gamma_0$ . This result was consistent with the observed delaying curves for the increased

deformation in Figure 7.4c. The change in the overall crystallization rate was designated with  $v$  and  $\mu$  values, and they were not significant, less than 5%, by varying range of  $\gamma_0$ .

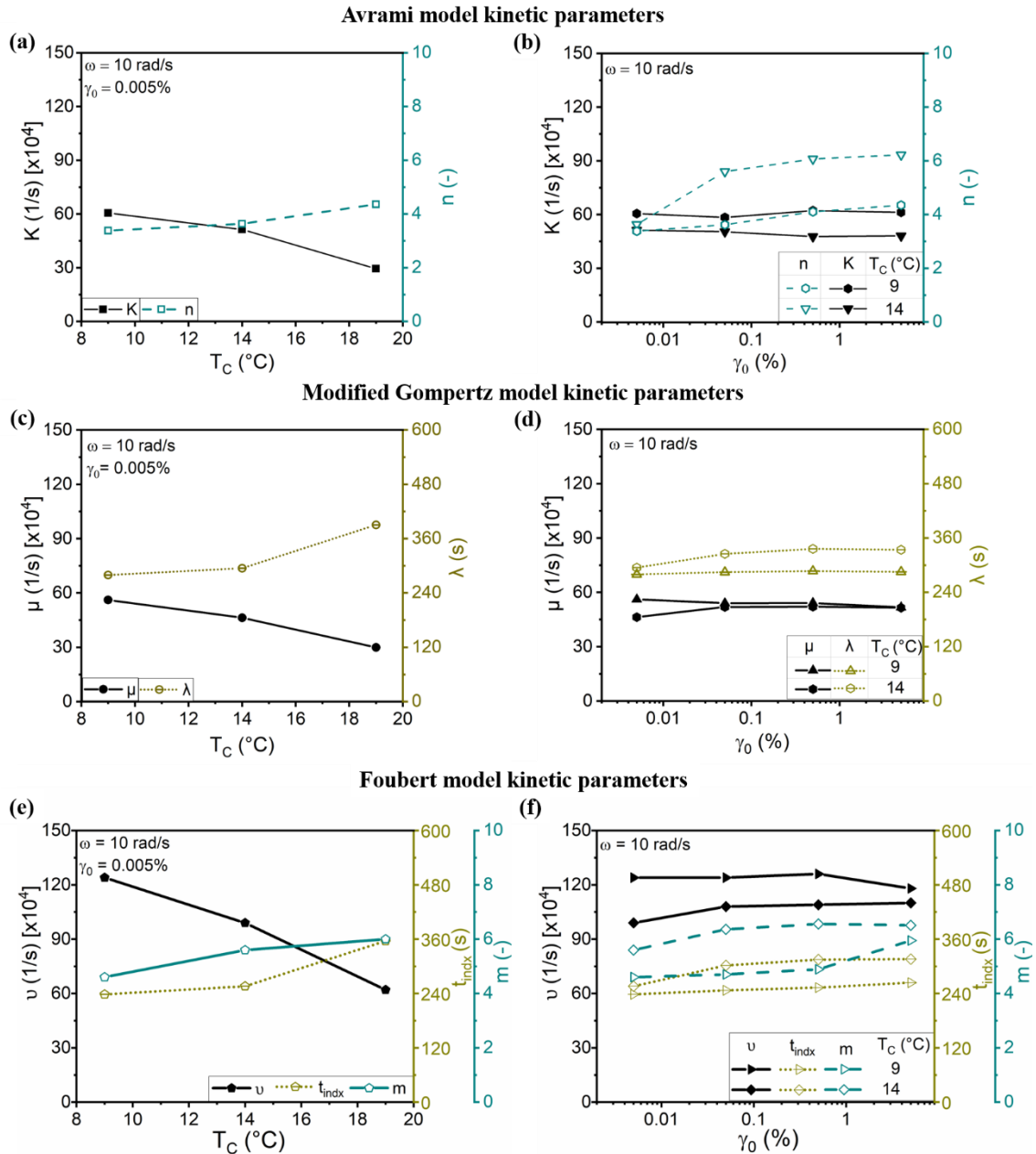


**Figure 7.5:** Kinetic parameters (a), (c) and (e) for the temperature-dependent experiments; and (b), (d) and (f) for the strain-induced crystallization experiment with varying  $\gamma_0$ . Parameters-  $n$ : Avrami exponent,  $K$ : Avrami rate constant,  $\mu$ : modified Gompertz the maximum increase rate parameter,  $v$ : Foubert rate constant,  $\lambda$ : modified Gompertz induction time,  $t_{indx}$ : Foubert model induction time.

Bulk fat nucleation is known as predominantly heterogeneous and the most practical situations due to the low degree of cooling rate and the dispersion of impurities (Campbell

*et al.* 2004). The heterogeneous nucleation results in a noninteger value of  $n$  (Marangoni 2005). Within this framework, the coconut fat system in this study was crystallized under heterogeneous nucleation, and the dimensionality  $n$  value increased by a 1 within  $\Delta T_C = 10$  °C increment. Besides, the calculated  $m$  was increased by 1.5 and reached 6 with increased 10 °C. According to the study of Foubert *et al.* (2002), the typical parameter range for the  $m$  of cocoa butter at 20 °C is in between 3 and 6. Furthermore, Rigolle *et al.* (2015) fixed the  $m$  to 6.5 for crystallized cocoa butter and 5.5 for the crystallized milk fat for chocolate at 20 °C. In case of strain-induced crystallization, it is known as the contact surface of the crystals increases by applied deformation (Bremer 1992). The increased contact surface could cause a crystal impingement, and increase  $n$  values. This may be the reason for the increased  $n$  value with the applied  $\gamma_0 = 5\%$  from 3.4 to 4.4 at the  $T_C = 9$  °C and from 3.6 to 6.2 for  $T_C = 14$  °C (see Figure 7.5b). This  $n > 4$  values indicated the complexity of crystallization mechanism with multi-dimensional growth and different morphology of coconut fat. The interaction of fat crystals with each other in the network has been already known as having a very complex nature (DeMan and Beers 1987). Presumably, the fat crystal particles become more stretched and bent at higher  $T_C$  under conducted larger deformation (Kloed 1998). While the destruction of the small crystals at the early stage of crystallization decelerates the crystallization, later on the stretched fat crystal network could increase the contact surface by applied large deformation. Thus, a slight reduction in  $K$  value with the larger  $n > 4$  values was observed due to the more complicated growing geometries or rearrangement of the fat crystals under applied large deformation. The conducted largest  $\gamma_0 = 5\%$  increased the  $m$  value factor of  $\sim 1.2$  compared to the calculated value for  $\gamma_0 = 0.005\%$  for both  $T_C$ . This could support the idea of more complex crystal growth mechanism.

As a result, although the Avrami model is far the most used model for kinetic analyses of the crystallization process, the modified Gompertz and Foubert model fitted to data as good as Avrami fit. A benefit of the modified Gompert and Foubert models is that its induction time parameters are calculated straightforwardly. However, the theoretical basis for the modified Gompert and Foubert models is rather weak for a description of the crystallization process. While the Avrami model could far better find application for describing the first half the crystallization process (dominantly primary crystallization),

the modified Gompert and Foubert models would be useful for evaluation of the overall crystallization rate and the induction time.

### 7.1.2 Analyses of the fractal dimension

The fat crystal network is composed of packed fractal flocs throughout the sample. The analysis of fractal geometry is important for understanding the link between the microstructure of fat crystal network and macroscopic rheological properties of the network. The fractal dimension is a measure of the relationship between the mass of a cluster and its size (Shi *et al.* 2005). It also quantifies the order of packing clusters in the fat crystal network (Narine and Marangoni 1999). According to Narine and Marangoni (1999), the fractal dimension is strongly influenced by mass and heat transfer which are governed by processing conditions, i. e., temperature history. With RheoNMR method crystallization processing conditions are identical for simultaneous measurement by NMR and rheometer. Thus, the direct correlation of  $G'$  as a function of the  $X_C$  evaluated based on the weak-link regime for colloidal dispersion. Above the gelation threshold, the gel network consists of closely packed fractal flocs (Shih *et al.* 1990). The links regimes between flocs are divided into two as a strong and weak-link (Shih *et al.* 1990; Narine and Marangoni 1999). In the strong-link regime, the particle concentration is low, and individual floc is large. Each floc behaves as a weak spring (Shih *et al.* 1990). However, in the weak-link regime, particle concentration is high with very small and stiff fractal flocs (Shih *et al.* 1990; Bremer 1992). Thus, the  $G'$  exhibit a power-law increasing behavior with increasing SFC (Bremer *et al.* 1989; Bremer *et al.* 1992; Shih *et al.* 1990, Marangoni and Narine 2002) by,

$$G' = \psi X_C(t)^p \quad (7.3)$$

$$\ln(G') = \ln(\psi) + p \ln(X_C(t)) \quad (7.4)$$

where  $\psi$  is a constant independent of  $X_C$ , but it depends on the polymorphic nature such as particular lipid or triglyceride composition of the fat crystal network, and  $p$  is a chemical length exponent depends on the fractal dimension  $D$  of the network in the following manner  $p = 1/(3 - D)$  in the weak-link regime for a three-dimensional

system. The linear slope ( $p$ ) of  $\ln(G')$  and  $\ln(\frac{X_C(t)}{X_C^\infty})$  correlation can be used to calculate the  $D$ . The plots of  $\ln(G')$  and  $\ln(\frac{X_C(t)}{X_C^\infty})$  can be seen in Figure 7.6.

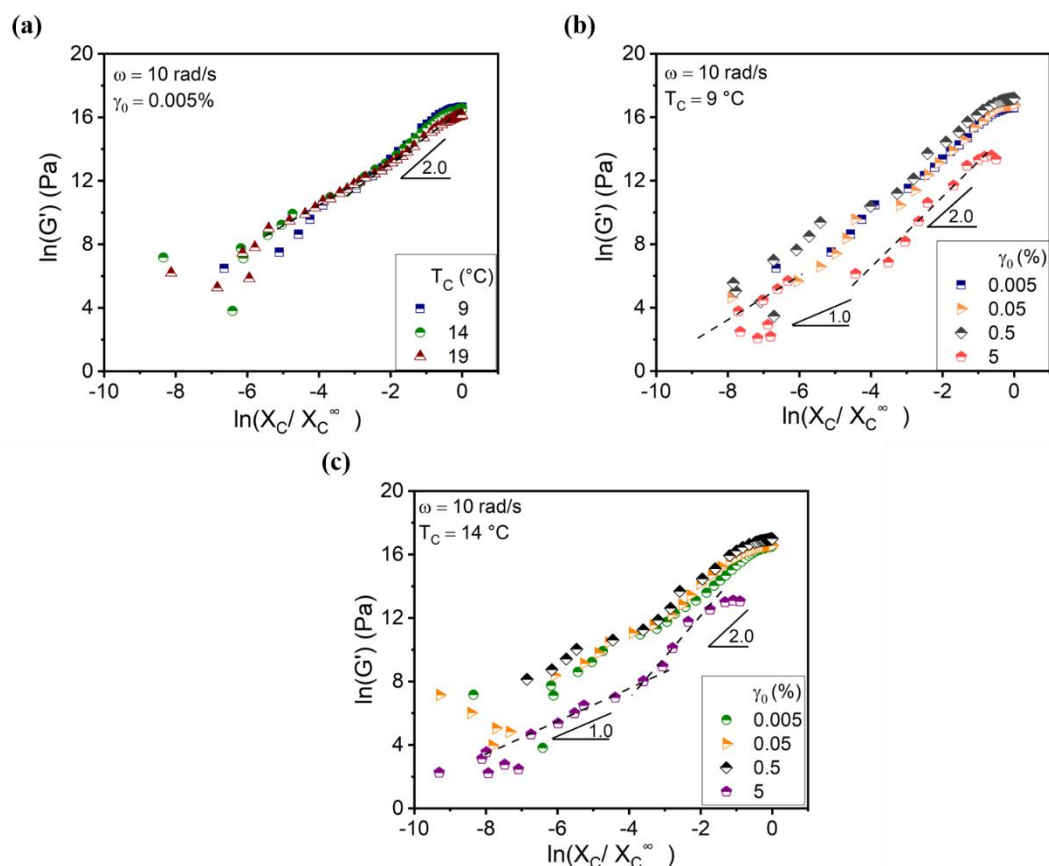


**Figure 7.6:** Correlation between  $\ln(G')$  and  $\ln(\frac{X_C(t)}{X_C^\infty})$  (a) for varying the  $T_C$  at constant  $\omega = 10$  rad/s and  $\gamma_0 = 0.005\%$ , and strain induced crystallization with varying  $\gamma_0$  at (b)  $T_C = 9$  °C and (c)  $T_C = 14$  °C. Linear fit with a dashed line represented to describe the change in slope in the initial and growth stage of crystallization.

Different slopes from different stages of crystallization experiments were observed. The first stage of the plots showed  $p$  values lower than 1.5 at  $T_C = 14$  °C for rising  $\gamma_0$ . A low fraction of fat solid was presented at this stage and thus called as an initial stage. However, the  $p$  values were found larger than 1.5 at  $T_C = 14$  °C for the second stage. At this stage, the fractal network was developed. Therefore, this stage was called a growth stage. After this stage, a plateau was observed and indicated no further change in the fractal dimension. Determined  $D$  values from the plots in Figure 7.6 are displayed in Figure 7.7. The resulting  $D$  value was stable at the growth stage by changing  $T_C$ . However, it was a

factor of 1.2 higher with a decrease in  $\Delta T_C = 10\text{ }^\circ\text{C}$ . According to Narine and Marangoni (1999) sample has instantaneous nucleation at a lower temperature, and thus, nucleation sites dissipate the heat effectively throughout the network. Therefore, these systems with a rapid nucleation stage have a higher fractal dimension.

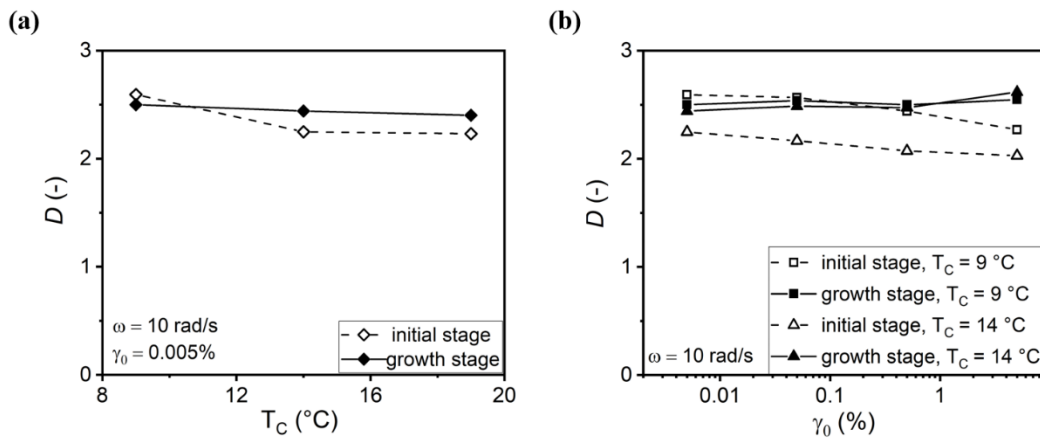


**Figure 7.7:** Fractal dimension ( $D$ ) of the crystallization of coconut fat (a) for varying  $T_C$  experiments, and (b) for conducted varying  $\gamma_0$  at  $T_C = 9\text{ }^\circ\text{C}$  and  $T_C = 14\text{ }^\circ\text{C}$ .

The  $D$  value gradually decreased up to a factor of 1.1 at the initial stage with the presence of the larger  $\gamma_0$  under both  $T_C$  conditions. The thermal and shear histories did not change for conducted coconut fat crystallization experiments, and thus, results indicated that the applied deformation affected the nucleation process and caused a decrease in the  $D$  value. This may be because of the constrained heat and mass transfer due to the deformed nuclei in the sample by applying higher  $\gamma_0$ . Lower  $D$  values were also indicators a measure of disordered packing of the microstructural elements within the network (Narine and Marangoni 1999) compared to higher  $D$  valued experiments. Nevertheless, the  $D$  value did not alter by increasing  $\gamma_0$  at the growth stage in the crystallization process. But, even so, the application of the largest  $\gamma_0$  also caused a lower  $G'$  modulus during the crystallization process independent to chosen  $T_C$  as demonstrated by Figure 7.6b-c.

The correlation between the  $G'$  and  $X_C$  can be analyzed by using the suspension theories due to the similarities between suspension and fat crystal networks. The mass fraction of solid  $X_C$  was found equivalent to the volume fraction of solid  $\varphi_c$  determined by Equation 3.48 with the used crystalline density of coconut oil  $\rho_{c,\text{coconut oil}} = 0.925\text{ g/cm}^3$  at  $15\text{ }^\circ\text{C}$ , and the amorphous density of it at  $40\text{ }^\circ\text{C}$  as  $\rho_{a,\text{coconut oil}} = 0.907\text{ g/cm}^3$  (Sulaiman *et al.*

2013; Charrondiere *et al.* 2012). The Einstein equation (see Table 8.3) describes very dilute suspension systems for non-deformable rigid particles with a coefficient of 2.5 as hard-spheres in the  $X_C < 10\%$ . Another model for dilute suspensions known as Batchelor-Green (see Table 8.3) was developed for rigid particles with a similar first coefficient with Einstein equation as 2.5 and second coefficient  $k_H$ . Furthermore, Röntzsch *et al.* 2019 developed the extended Einstein with a combination of the Einstein model and the power-law model. The formulation extended Einstein model for this study is:

$$G' = 1 + 2.5X_C + D'X_C^{C'} \quad (7.5)$$

where  $D'$  is the dynamic range of  $G'$ ,  $C'$  is related to the coordination of growing crystals.

Figure 7.8 shows the modeling of a correlation of the  $G'$  and the  $\frac{X_C(t)}{X_C^\infty}$  for temperature series of coconut fat by isothermal crystallization. The used models did not describe the complete crystallization curves. However, the model fits up to 50% of the  $\frac{X_C(t)}{X_C^\infty}$  was achieved with  $\text{CoD} \geq 0.90$  as displayed in Figure 7.8b. The applied  $\gamma_0$  dependence series with fitted models up to 50% of the  $\frac{X_C(t)}{X_C^\infty}$  is shown in Figure 7.9. The Einstein model described the crystallization system of coconut fat up to 6% of relative crystallinity.

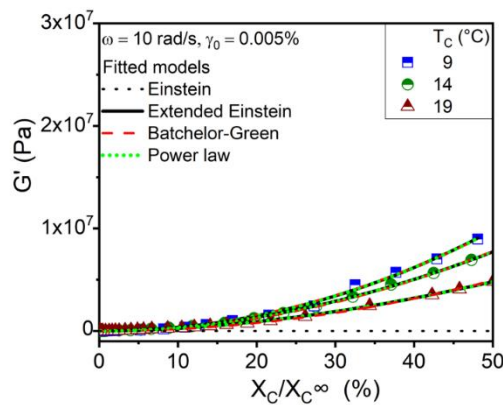


**Figure 7.8:** Correlation of the  $G'$  and the  $\frac{X_C(t)}{X_C^\infty}$  for temperature dependent experiments with fitted suspension models up to 50% of the  $\frac{X_C(t)}{X_C^\infty}$  as represented lines: black dot line for Einstein model, black line for extended Einstein, red dash line for Batchelor-Green, green short dot line for power-law models.

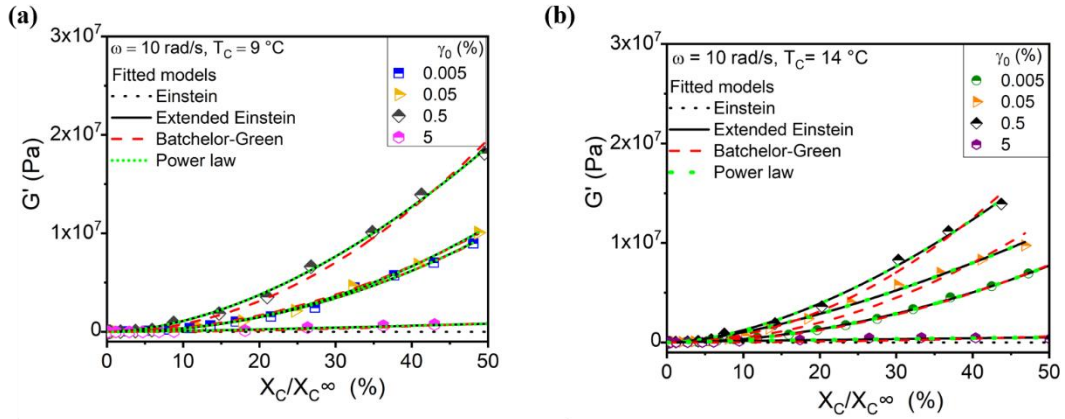


**Figure 7.9:** Correlation of the  $G'$  with the  $\frac{X_C(t)}{X_C^\infty}$  for varying  $\gamma_0$  at (a)  $T_C = 9^\circ\text{C}$ , and (b)  $T_C = 14^\circ\text{C}$ . with fitted suspension models up to 50% of the  $\frac{X_C(t)}{X_C^\infty}$  as represented lines: black dot line for Einstein model, black line for extended Einstein, red dash line for Batchelor-Green, green short dot line for power-law models.

**Table 7.1:** Calculated model parameters by fitting data up to 50% of the  $\frac{X_C(t)}{X_C^\infty}$ .

Fitted models		Extended Einstein		Batchelor-Green	Power law		
Experiment Conditions	$T_C$	$\gamma_0$					
			$D' [x10^{-6}]$	$C'$	$k_H [x10^{-6}]$	$p$	$\psi [x10^{-6}]$
	9	0.005	41	2.06	39	2.06	41
	9	0.05	46	2.11	42	2.11	46
	9	0.5	64	1.76	78	1.76	64
	9	5	2.1	1.33	3.5	1.33	2.1
	14	0.005	29	1.92	31	1.92	29
	14	0.05	30	1.47	50	1.48	30
	14	0.5	56	1.66	78	1.66	56
	14	5	0.9	0.75	2.4	0.75	0.9
	9	0.005	41	2.06	39	2.06	41
	14	0.005	29	1.92	31	1.92	29
	19	0.005	17	1.82	20	1.82	17

The deduced parameters for the fitted models are given in Table 7.1. The trend of the  $k_H$  was identical with the trend of  $D' = \psi$  values. A decreasing trend was observed for all parameter by increasing  $T_C$ . The maximum of the  $D' = \psi = 64$  and the  $k_H = 78$  values were observed with the application of  $\gamma_0 = 0.5\%$  at  $9\text{ }^\circ\text{C}$ . The maximum in the exponents was seen as 2.11 for applied  $\gamma_0 = 0.05\%$  at  $9\text{ }^\circ\text{C}$  experiment. Additionally, the minimum of the values was found as  $D' = \psi = 0.9$ , the  $k_H = 2.4$  and  $C' = p = 0.75$  for applied maximum deformation at  $14\text{ }^\circ\text{C}$ . The use of the simple power-law model was found effective compare to the other slightly complex models.

## 7.2 Concluding remarks

The Rheo-NMR was found useful for characterizing the crystallization kinetics of the coconut fat. Accelerated crystallization observed with a reduction in  $T_C$ . Applied largest deformation  $\gamma_0 = 5\%$  did not significantly affect the overall crystallization rate, but the slight deceleration was observed by the  $K$  parameter and also in the NMR result. The calculated  $m = 6$  value at  $19\text{ }^\circ\text{C}$  was found as a typical value for the fat under the quiescent crystallization. The application of larger  $\gamma_0$  caused distinct effects on the exponents  $n$  and  $m$  which designated possibly more stretched and bent fat crystal structure. A delay was observed with increasing  $T_C$  and  $\gamma_0$  with extracted induction time parameters. While the  $D$  was 2.5 and stable at the growth stage independent from varying  $T_C$  and  $\gamma_0$ . A decreasing trend was observed in the  $D$  for increasing  $T_C$  and  $\gamma_0$  at the initial stage of crystallization. This indicated a possible increase in the disordered packing of the microstructural elements within the network. Lastly, the power-law model was found effective for modeling of a correlation of the  $G'$  and the  $\frac{X_C(t)}{X_C^\infty}$  up to 50% of the  $\frac{X_C(t)}{X_C^\infty}$ .

The RheoNMR method can now benefit from a new perspective by a simultaneous measurement under identical thermal and shear conditions. This method opens up the possibility to learn required deformation or shear to apply intentionally in commercial processing for preparing the fat product with targeted physical properties. The resulting rheological properties such as viscosity under flow-crystallization conditions could be used for a possible interpretation of the sensorial properties.

## 8 Rheological Properties of Cellulose/LDPE Composites Combined with Sustainable Plant-Based Compatibiliser

The following chapter describes the sample preparation and rheological results on Cellulose/LDPE composites reinforced with sustainable plant-based compatibilizer. Most of the sample preparations and DSC analyses were done by Philip B. V. Scholten (Center for Education and Research on Macromolecules (CERM), CESAM Research Unit, University of Liege, Department of Chemistry, Liege, Belgium). On the other hand, the investigation of the rheological properties of PE composites by adopting classical models on the relative absolute complex viscosity  $|\eta^*(\omega)|$  as a function of mass filler fraction data were the scope of this Ph.D. study to predict further rheological properties of the aforementioned composite materials. The theoretical background for the presented chapter and its subsections is based on published literature: Scholten, Özen *et al.* (2020).

### 8.1 Introduction

One of the most attractive reinforcing fillers is cellulose particularly for polyolefins e.g. PE to increase the material strength. Indeed, the main advantage of the cellulose material is its remarkable nature by the virtue of its biodegradability, non-toxicity, extremely high strength, low cost and lightweight (Miao and Hamad 2013; Abdul Khalil *et al.* 2012; Dufresne 2017; Kontturi *et al.* 2018). The acylation of cellulose with fatty acids (Freire *et al.* 2008) and the epoxidized plant oils as compatibilizers (Oliveira De Castro *et al.* 2015) has been used effectively to improve the material properties of PE. However, one of the major problems encountered in the cellulose PE composite material is the hydrophilic structure of cellulose which makes it difficult to disperse in hydrophobic PE. The latter occurs mainly due to low interfacial compatibility, moisture intake and inter-fiber aggregation. Several different ways have been proposed to overcome these problems such as the use of grafting agents (Yano *et al.* 2018; Sakakibara *et al.* 2017; Kaynak *et al.* 2018; Wohlhauser *et al.* 2018), and reactive extrusion (Oliveira De Castro *et al.* 2015; Pracella *et al.* 2010) to the functionalization of one or both components (Abdul Khalil *et al.* 2012; Faruk *et al.* 2012; Singh and Palsule 2014; Prasad *et al.* 2016; Alidadi-Shamsabadi *et al.* 2015; Li *et al.* 2007).

Nevertheless, within this study, starch and amylose based renewable compatibilizer (see Figure 8.1) were employed for the formulation of cellulose-reinforced LDPE composites.

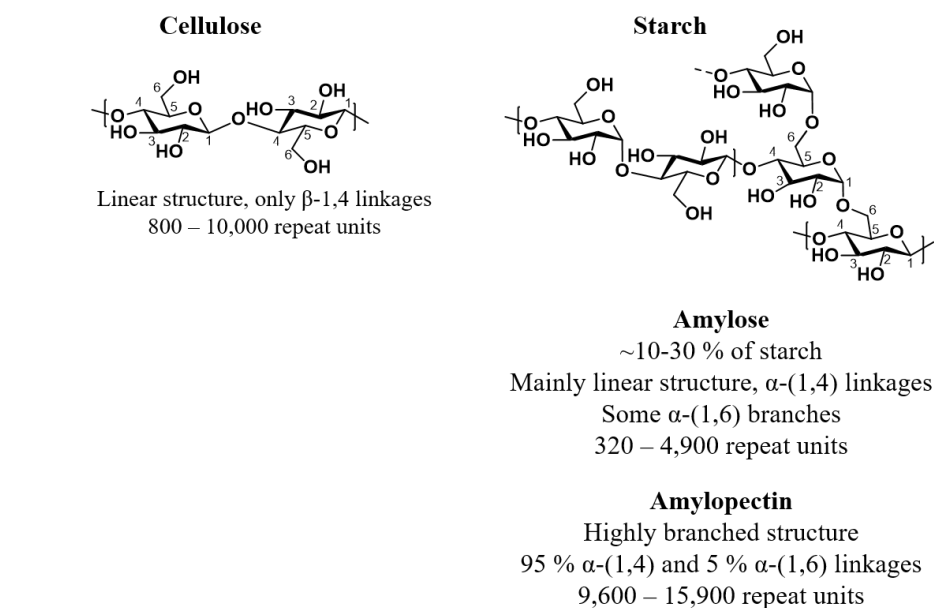


**Figure 8.1:** Structures of cellulose and starch.

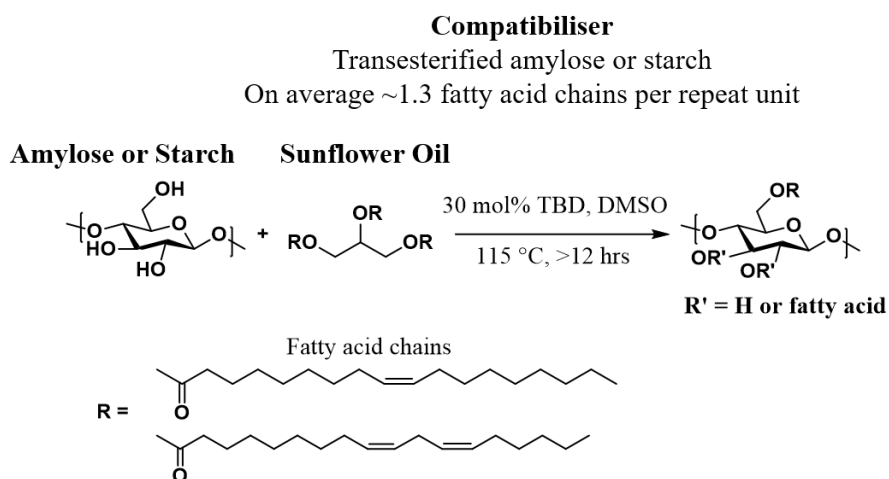


**Figure 8.2:** The synthesis of starch and amylose based compatibilizer with using sunflower oil (Söyler and Meier 2016). The synthesis was done by Philip Scholten.

These compatibilizers were synthesized using sunflower oil as depicted in Figure 8.2 by adopting the procedure reported by Söyler *et al.* 2016. The synthesized compatibilizers fuse both the hydrophilicity of a glucose repeat unit and the hydrophobicity of a fatty acid chain in their structure, which makes them suitable material to interact not only with both cellulose but also with LDPE. Subsequently, the compatibilizers and cellulose were

mixed by twin-screw extrusion, and ensuing extruded composites were analyzed by oscillatory rheometer for investigating the material flow properties.

## 8.2 Samples and their preparation

### *Samples*

A commercial-grade of the LDPE was used as a pure polymer matrix which was supplied by INEOS Polymers & Olefins Europe. The characteristics of LDPE as following: density:  $920 \text{ kg.m}^{-3}$ ; melt index MI2.16:  $8.5 \text{ g} / 10 \text{ min}$ ; number and weight average molecular weight respectively as  $M_n = 17.3 \text{ kg.mol}^{-1}$ ,  $M_w = 126 \text{ kg.mol}^{-1}$ . The melting temperature ( $T_m$ ):  $107 \text{ }^\circ\text{C}$ ; mass crystallinity: 44% was found by DSC analysis. The cellulose pulp was extracted from European beechwood (*Fagus sylvatica L.*) with using acetic acid followed by hydrogen peroxide (30 %w/w in  $\text{H}_2\text{O}$ , Aldrich) bleaching. Cellulose characterization is provided in the appendix as Figure A.1. The transesterified amylose derivative or starch was prepared accordingly to the procedure by Söyler *et al.* (2016) using high oleic sunflower oil (provided by Cargill) and starch purchased in a local supermarket. Cellulose, starch, and amylose (Aldrich) were dried at  $100 \text{ }^\circ\text{C}$  in a vacuum oven overnight before use. 1,5,7-Triazabicyclo[4.4.0]dec-5-ene (TBD; 98%, Aldrich) and dimethyl sulfoxide (DMSO; anhydrous, >99.9 %, Aldrich) were used as received.

### *Sample Preparation*

A series of wt% LDPE composites (see Table 7.1) were prepared by melt-mixed in lab-scale co-rotating twin-screw extruder, the Minilab (Thermo Scientific Haake, Germany) to ensure uniform dispersion. The cellulose, modified amylose, and modified starch were cut into small pieces, premixed with LDPE. Then, the mentioned mixture was inserted into 5 g twin-screw extruder at  $180 \text{ }^\circ\text{C}$  and 30 rpm. The rpm was increased to 80 after the sample insertion. The pure LDPE was also extruded under the same conditions to obtain identical thermal and shear history with composites samples. Subsequently, the samples were press-molded under vacuum at  $120 \text{ }^\circ\text{C}$  and 20 bar for 10 min in a Weber laboratory press to make 1 mm thick disks with a diameter of 25 mm in diameter. The cooled disk shape samples were analyzed by rheology. Before the rheological analysis the  $T_m$  values of the samples were determined by using the DSC Q100 instrument from TA with using

an aluminum pan. The 5 mg of sample was analyzed in the following temperature procedure as cooling to 0 °C, heating to 140 °C, cooling to -90 °C and heating to 200 °C with a heating/cooling rate of 10 °C/min, respectively. The last heating cycle was used for the determination of the  $T_m$  and results are provided in the appendix as Figure A2.

**Table 8.1:** *Composition of the composites in wt % of a total of 5 g of sample.*

<b>Sample code</b>	<b>LDPE (wt%)</b>	<b>Cellulose (wt%)</b>	<b>Compatibiliser (mA, A, mS or S)</b>
L100 C0mA/mS0	100	0	0
L85 C10mA/mS5	85	10	5
L80 C10mA/mS10	80	10	10
L75 C1mA/mS15	75	10	15
L90 C0mA/mS10	90	0	10
L90 C10mA/mS0	90	10	0
L80 C10A/S10	80	10	10
L90 C0A/S10	90	0	10
L45 C45mA/mS10	45	45	10
L55 C45mA/mS0	55	45	0

L: low-density poly(ethylene); C: cellulose mA: modified amylose; mS: modified starch; A: amylose; S: starch.

### 8.3 Melt shear rheology analysis of composites

The melt rheological properties of composites were investigated to understand materials suitability for processing, thermal stability, and critically the state of filler dispersion in the matrix. An ARES G2 strain-controlled rotational rheometer from TA Instruments was used for the analysis. All measurements were done with 25mm diameter parallel plate geometries under an N<sub>2</sub> atmosphere. Oscillatory shear measurements were conducted to monitor the  $G'(\omega_1, \gamma_0, T, t)$  (elastic contribution), and during measurements, the  $\omega_1$ ,  $\gamma_0$ ,  $T$ , and  $t$  were varied independently. The strain-dependent behavior was tested by dynamic strain sweep measurement of all samples at 150 °C to characterize the linear and nonlinear viscoelastic regions as seen in Figure 8.3. The linear viscoelastic region was observed up to  $\gamma_0 = 10\%$  for samples, except for the highest content of cellulose (C45mA/mS10) for

which it was attained until  $\gamma_0 = 4\%$ . The decrease in the linear viscoelastic region with increasing total filler fraction in the polymer matrix indicated a formation of a network-like structure above the percolation threshold concentration (Ahirwal *et al.* 2014). Sample with maximum filler quantity (C45mA/mS10) showed the highest  $G'$  and shortest linear viscoelastic region compare to the all other samples.

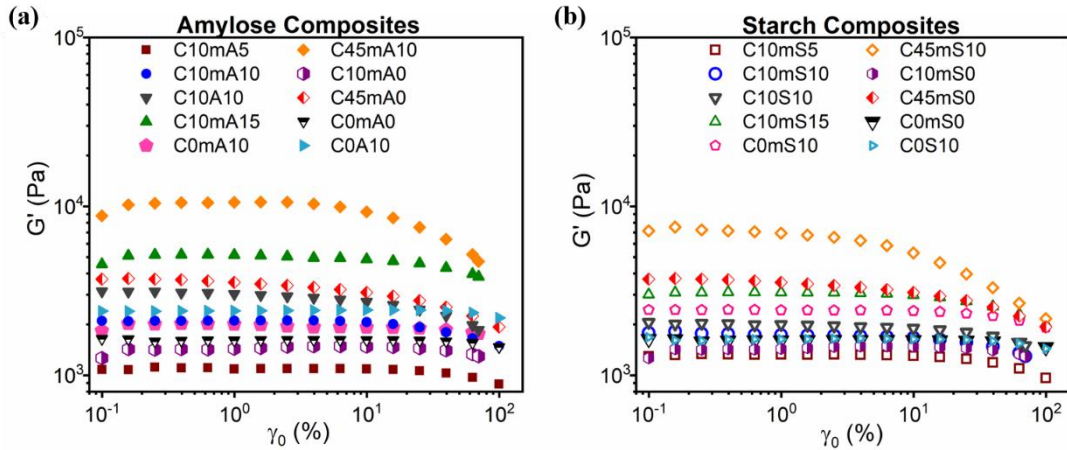


**Figure 8.3:** The  $G'$  as a function of the  $\gamma_0$  at 150 °C and  $\omega_1 = 1$  rad/s for the neat LDPE and the composite materials with cellulose (C), (a) modified and non-modified amylose (A) compatibilizer and (b) modified and non-modified starch (S) compatibilizer.

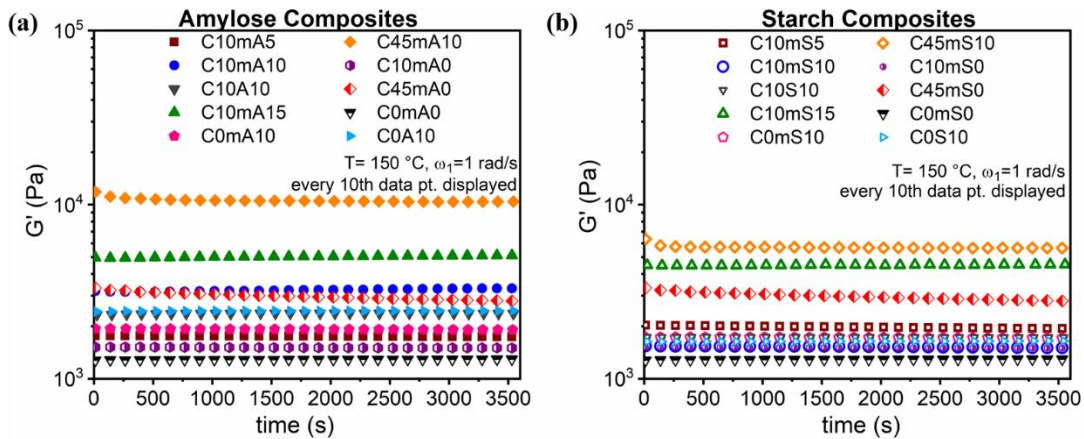


**Figure 8.4:** Time dependency of the  $G'$  at 150 °C with  $\omega_1 = 1$  rad/s in the linear viscoelastic regime for the neat LDPE and the composite samples.

Subsequently, the thermal stability of samples was analyzed at 150 and 170 °C with the  $\omega_1 = 1$  rad/s in the linear viscoelastic regime during one hour as demonstrated in Figure 8.4 and Figure 8.5. A stable  $G'$  was observed for samples in both temperatures, apart from samples with 45 wt% cellulose (C45mA10/S10 and C45mA0/S0). The stability of

modulus indicated the absence of degradation. The observed decrease in  $G'$  was  $\sim 10\%$  for C45mA10 and C45mS10 respectively, and above 15% for C45mA0/S0 at both temperature ranges. A possible reason for the modulus drop could be the loss of residual water in the cellulose fibers at that temperatures during the time.

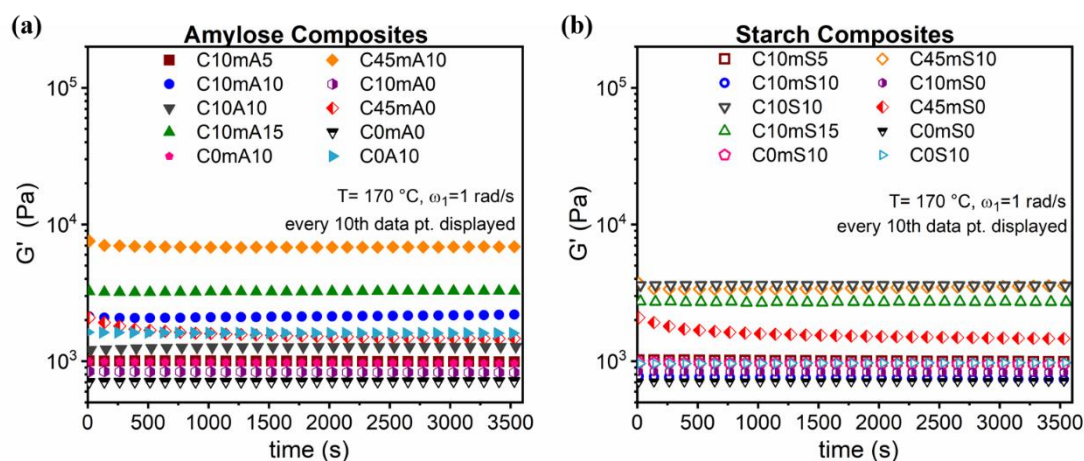


**Figure 8.5:** Time dependency of the  $G'$  at  $170\text{ }^{\circ}\text{C}$  with  $\omega_1 = 1\text{ rad/s}$  in the linear viscoelastic regime for the neat LDPE and the composite samples.

Next, frequency-dependent tests were conducted in the linear viscoelastic regime between  $120$  and  $160\text{ }^{\circ}\text{C}$ . The  $G'$  was monitored as a function of the  $\omega_1$  at reference temperature ( $T_{ref} = 150\text{ }^{\circ}\text{C}$ ) via the TTS principle. The appearance of a plateau of the  $G'(\omega_1)$  is an indication of exceeding the percolation threshold. Cellulose fibers form an interconnected network through a space-filling dispersion of the fibers within the matrix at above the percolation threshold, and hence the material properties are improved to higher strength with stress transfer from the matrix to the filler. In Figure 8.6 the frequency-dependent measurements show no difference between 10 wt% cellulose added LDPE sample (C10mA0, C10mA mS0) and neat LDPE, the latter called C0mA0 or C0mS0, which could be due to agglomeration of the cellulose. Therefore, the addition of compatibilizer was found necessary to disrupt these cellulose clusters and result in better dispersion. Modified starch (10 wt%) included a sample (C0mS10) changed the  $G'$  slightly, as a 25% increase at high ( $\omega_1 \geq 10\text{ rad/s}$ ) and 90% increase at low frequencies ( $\omega_1 \leq 1\text{ rad/s}$ ) (see Figure 8.6). However, sample (C0S10) with 10 wt% non-modified starch content showed a 10% decrease at high frequencies and a 60% increase at low frequencies. These differences in  $G'$  are very minor when they are compared with the neat LDPE sample.

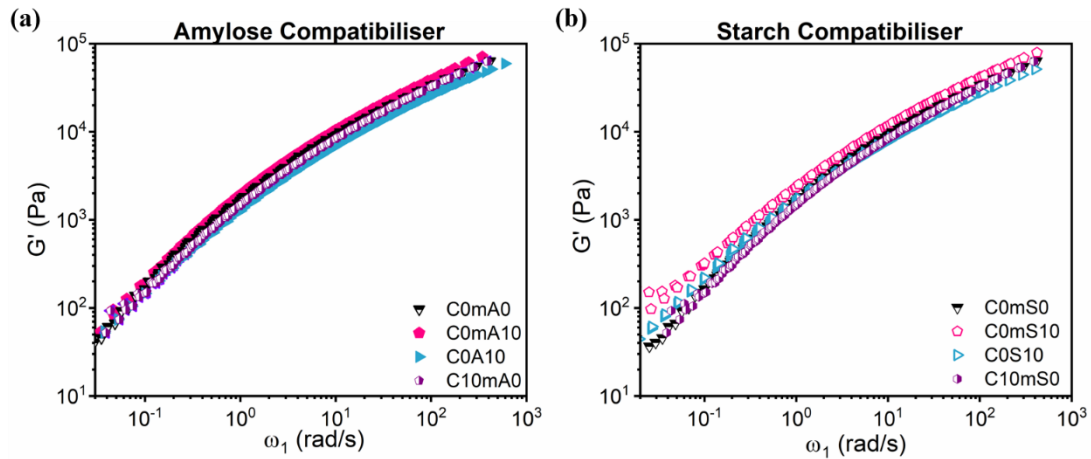


**Figure 8.6:** The  $G'$  as a function of the  $\omega_1$  at  $T_{ref} = 150\text{ }^\circ\text{C}$  was plotted via TTS for neat LDPE and LDPE composites containing 10 wt% cellulose (C10mA/S0) or composites with 10 wt% of (a) modified amylose (mA) or non-modified amylose (A), and (b) modified starch (mS) or non-modified starch (S).

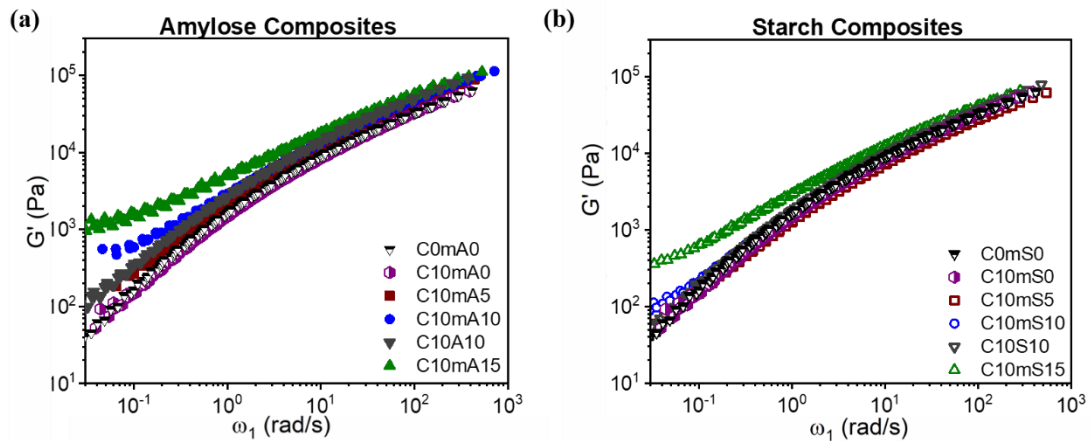


**Figure 8.7:** The  $G'$  as a function of the  $\omega_1$  at  $T_{ref} = 150\text{ }^\circ\text{C}$  was plotted via TTS for neat LDPE and LDPE composites containing 10 wt% cellulose (C) with 5-15 wt% of (a) modified amylose (mA), and (b) modified starch (mS).

Thus, the filler amount was increased as 5, 10 and 15 wt% compatibilizer and added into the sample which contains 10 wt% cellulose and LDPE to facilitate the investigation of feasible improvement in the  $G'$ . The increment in  $G'$  was observed for higher compatibilizer content (brown 5 wt%, blue 10 wt%, and green 15 wt%) as shown in Figure 8.7. This increase in  $G'$  was roughly 200% higher for C10mA15 and 30% higher for C10mS15 compared to the neat LDPE (C0mA0 or C0mS0) at high frequencies ( $\omega_1 \geq 10\text{ rad/s}$ ). The higher the filler content raised the volume fraction of the dispersed phase due to the intrinsic rigidity of fillers, and hence caused an increment in the  $G'$ . The plateau

appeared at the  $\omega_1 \leq 1$  rad/s for C10mA10, C10mA15 and C10mS15 (blue and green symbols in Figure 8.7). The observed plateau indicated the formation of a “network like” structure (Kontopoulou 2012) with an improved interfacial adhesion with the hydrophobic matrix. This was a direct reflection of the addition of the amphiphilic compatibilizers, which can provide interfacial interactions between the two materials. The observed increment in the  $G'$  at  $\omega_1 = 0.05$  rad/s of samples C10mA15 was two times higher than the increment in the  $G'$  of the sample C10mS15 and constituted an 18-fold increase compared to the neat LDPE.

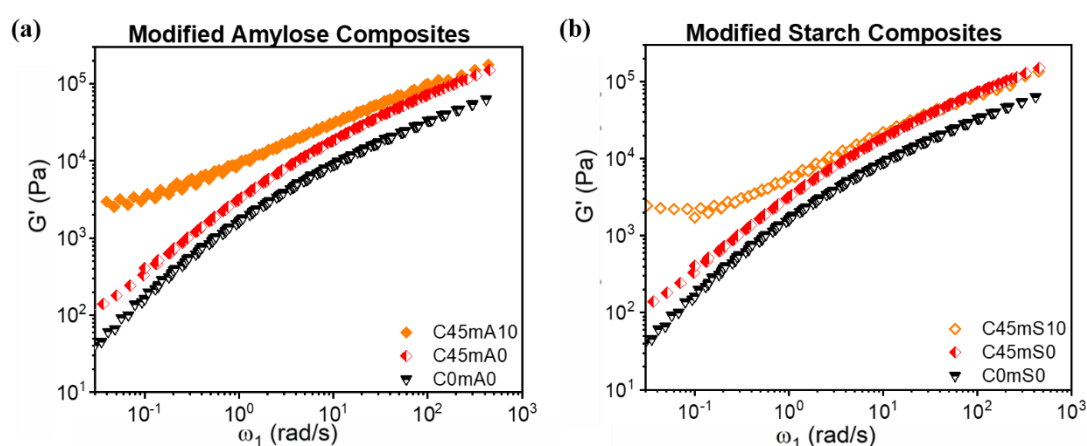


**Figure 8.8:** The  $G'(\omega_1)$  as a function of the  $\omega_1$  at  $T_{ref} = 150$  °C via TTS for neat LDPE and LDPE composites containing 45 wt% cellulose (C) and 10 wt% of (a) modified amylose (mA), and (b) modified starch (mS).

Furthermore, the cellulose content was increased to 45 wt% and monitored the  $G'(\omega_1)$  results are shown in Figure 8.8. Although a 2-fold increase in  $G'(\omega_1)$  was observed for the C45mA0/mS0 sample, no plateau was observed (red symbols in Figure 8.8). The addition of 10 wt% compatibilizer into cellulose (45 wt%)-LDPE composites raised the  $G'$  49 times and 38 times respectively for C45mA10 and C45mS10 at  $\omega_1 = 0.04$  rad/s, and a pronounced plateau at the  $\omega_1 \leq 1$  was observed. The latter indicated that the addition of compatibilizer to the composite (C45mA/mS10) effectively improved the dispersion of the cellulose compared to a simple mixture of cellulose and LDPE (C45mA/mS10), which caused an increase in  $G'$  of the samples.

Moreover, the flow activation energies  $E_a$  of the samples were calculated by using the obtained master curves via TTS at  $T_{ref} = 150$  °C with the shift factor ( $a_T$ ) as  $a_T =$

$\exp \left[ \frac{E_a}{R} \left( \frac{1}{T} - \frac{1}{T_{ref}} \right) \right]$ . The Arrhenius equation was fit to the  $a_T$  as a function of  $T$  plots of samples to calculate the  $E_a$  in the range of between 120 °C to 160 °C. A chain segment needs energy for self-diffusion in the bulk which is called as a flow activation energy  $E_a$  (Hassanabadi *et al.* 2014; Feng *et al.* 2011). The  $E_a = 49.8$  kJ/mol was calculated for the neat LDPE. While the lower  $E_a$  signifies the temperature dependence of the change of rheological parameter (e.g. melt viscosity) is low, the temperature sensitivity is higher for the samples with the higher  $E_a$  (Mohanty and Nayak 2007; Kalaprasad *et al.* 2003). The composites named as C10mA15, C45mA10 and C45mS10 showed the highest  $E_a$  as 80, 103.7, and 97.5 kJ/mol respectively. That was expected since the fibers restrain the molecular mobility due to network-like structure, and hence the alignment of fibers became harder in the flow direction especially for lower temperatures. However, some samples showed a decrease in the  $E_a$  values with increasing filler fraction. This could be related to the reduced interfacial tension between hydrophilic fiber and hydrophobic LDPE (Mohanty and Nayak 2007). For instance, sample C45 mA/mS0 with  $E_a = 50.7$  kJ/mol showed lower value than the  $E_a = 69$  kJ/mol of C10 mA/mS0. Materials with low  $E_a$  are stable in the temperature change.

The broad range of models has been developed and used for estimating the dependence of polymer composite viscosity on the particle concentration in the polymer matrix. (Willett 1994; Willenbacher and Georgieva 2013; Zhou *et al.* 2001; Cwalina *et al.* 2016) The details of these models are listed in Table 8.2. These models have been generally used for spherical particles. However, many industrial suspension samples include non-spherical particles such as fibers, disks, etc. The addition of more than one type filler into polymer results in practically insuperable problem with measuring the aspect ratios of micrometer size particles, hence taking into account in the model systems (DeArmitt and Hancock 2003). Furthermore, the soft repulsive and attractive interactions between the fillers and with also the polymer have also influenced the rheological properties of the material (Bergenholtz *et al.* 2002). In this study, cellulose and compatibilizers were fulfilling the function of the fibers. The suspension models were fitted to the relative absolute complex viscosity  $\frac{|\eta^*|}{|\eta^*|_0}$  data with increasing mass concentration on cellulose and/or compatibilizer as displayed in Figure 8.9

**Table 8.2:** Suspension models for absolute viscosity as a function of filler concentration.

Model	Equation	Description
<b>Einstein (1906, 1911)</b>	$\frac{ \eta^* }{ \eta^* _0} = 1 + k_E \phi$	Very dilute suspension model for the non-deformable rigid particles, coefficient $k_E = 2.5$ for hard-spheres for $\phi < 0.10$
<b>Batchelor-Green (1972)</b>	$\frac{ \eta^* }{ \eta^* _0} = 1 + k_E \phi + k_H \phi^2$	Dilute suspension model for rigid particles, coefficient $k_H = 5.2$ for hard-spheres and increases the value to 6.0 for Brownian motion between particles
<b>Mooney (1951)</b>	$\frac{ \eta^* }{ \eta^* _0} = \exp[2.5\phi(1 - k_M \phi)^{-1}]$	Concentrated suspension model of rigid interacting spheres, $1.35 < k_M < 1.91$ for monodisperse suspension dense packing and polydisperse suspensions $k_M < 0.75$ . (Zhou <i>et al.</i> 2001)
<b>Krieger-Dougherty (1959)</b>	$\frac{ \eta^* }{ \eta^* _0} = \left[1 - \frac{\phi}{\phi_{\max}}\right]^{-2.5\phi_{\max}}$	Concentrated suspension model, $\phi_{\max} = 0.64$ for hard-spheres
<b>Modified Eilers (Cwalina <i>et al.</i> 2016)</b>	$\frac{ \eta^* }{ \eta^* _0} = \left[1 + 1.5\phi\left(1 - \frac{\phi}{\phi_{\max}}\right)^{-1}\right]^n$	Concentrated suspension model, $\phi_{\max}$ and $n$ is the adjustable fitting parameters
<b>Quemada (1977)</b>	$\frac{ \eta^* }{ \eta^* _0} = \left[1 - \frac{\phi}{\phi_{\max}}\right]^{-2}$	Concentrated suspension model for rigid particles

$|\eta^*|$ : absolute complex viscosity of the suspension,  $|\eta^*|_0$ : absolute complex viscosity of the suspending fluid,  $\phi_{\max}$ : maximum packing fraction which depends on the particle shape and particle size distribution,  $k$ : coefficient.

The absolute complex viscosity ( $|\eta^*|$ ) was calculated by using the  $G'(\omega)$  and  $G''(\omega)$  with relation as  $|\eta^*| = [(G'(\omega)/\omega)^2 + (G''(\omega)/\omega)^2]^{1/2}$ . Determined  $|\eta^*|$  divided by the absolute complex viscosity value of neat LDPE  $|\eta^*|_0$ . The suspension models were fitted to the correlation between the  $\frac{|\eta^*|}{|\eta^*|_0}$  and the total filler weight fraction ( $\phi$ ) as displayed in

Figure 8.9. Then, the resulting fitting parameters were compared with previously reported values.

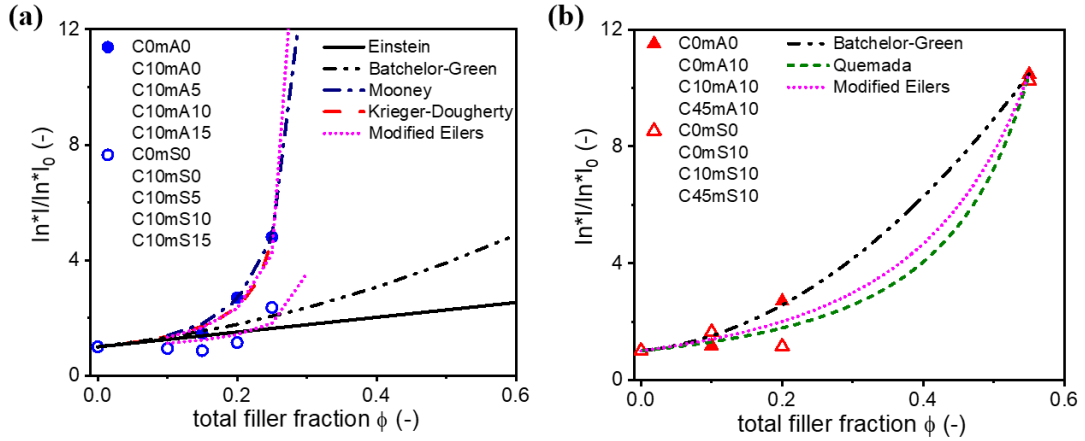


**Figure 8.9:** The  $\frac{|\eta^*|}{|\eta^*|_0}$  at  $\omega_1 = 0.05$  rad/s as a function of the  $\phi$  correlated to see the impact of (a) containing 10 wt% cellulose with addition of varying modified amylose (mA) (blue close circle) or modified starch (mS) (blue open circle); (b) added varying cellulose (C) concentration to containing 10 wt% mA (red close triangle) or 10 wt% mS (red open triangle) samples. While scatters represent the data, lines indicate the suspension models: Einstein, Batchelor-Green, Mooney, Krieger-Dougherty, Modified Eilers, Quemada models.

While the sample C10mA15 showed 5 times larger value in the  $\frac{|\eta^*|}{|\eta^*|_0}$  value and the sample C10mS15 showed an increase only 2 times in the  $\frac{|\eta^*|}{|\eta^*|_0}$  value compare to the  $\frac{|\eta^*|}{|\eta^*|_0}$  value of neat sample C0mS0. The Einstein and Batchelor-Green models were proposed for very diluted suspensions. The addition of modified amylose created a more complex suspension system. Therefore, the correlation of the  $\frac{|\eta^*|}{|\eta^*|_0}$  with increasing modified amylose amount behavior could be described by the Mooney, Krieger-Dougherty, Modified Eilers models (see Figure 8.9a). Resulting in maximum packing fraction was  $\phi_{\max} = \sim 0.30 \pm 0.03$ . It was quite low compared to the reported  $\phi_{\max}$  values for different filler shape e.g.,  $\phi_{\max, \text{cylinder}} = 0.74$ ,  $\phi_{\max, \text{cubes}} = 0.78$ , and  $\phi_{\max, \text{sphere}} = 0.64$  (Li *et al.* 2010; Cwalina *et al.* 2016). The calculated modified Eilers's exponent values were  $n = 1.44 \pm 0.36$  for amylose samples and  $n = 0.8 \pm 0.20$  for starch. This  $n$  values were also below the suggested  $n = 2 \pm 0.02$  value for cubic dense packing objects by Cwalina *et al.* (2016). The derived  $k_M = 2.4 \pm 0.5$  was lower than the reported value as  $k_M = 1.33$  and the  $\phi_{\max} = 0.61$  for starch-poly(hydroxyl ester ether) composite by Zhou *et al.*

(2001). Besides, the  $\frac{|\eta^*|}{|\eta^*|_0}$  changes for the more concentrated cellulose composites with set modified starch/amylose content (10 wt%) are displayed in Figure 8.9b. The  $k_H$  was calculated as  $26.8 \pm 0.7$  which was close to the reported  $k_H = 23.7 \pm 3$  for cubic particle suspensions as  $\phi_{\text{cubes}} = 0.15$  by Cwalina *et al.* in (2016). The fiber shape of the fillers with higher concentration could cause an increase of the  $k_H$  value, which may be anticipated due to highly attractive distribution forces. The calculated  $\phi_{\text{max}}$  was in a range as  $0.80 \leq \phi_{\text{max}} \leq 0.95 \pm 0.4$ , and the exponent was  $n = 2.2 \pm 0.2$ .

#### 8.4 Concluding remarks

The preparation of LDPE composites using bulk cellulose fibers was shown to be possible using plant-oil and starch-based compatibilizers synthesized sustainably. A clear improvement in the cellulose dispersion within the polymer matrix was observed by using the shear rheology method. Modified amylose showed a higher capacity to compatibilize cellulose compare to modified starch within the LDPE matrix. A plateau in the  $G'$  at low frequencies ( $\omega_1 \leq 1$  rad/s) was observed at both 10 and 15 wt% compatibilizer loading with 10 wt% cellulose (C10mA10-15). Additionally, the classical suspension models were used to evaluate the filler mass fraction effects on relative absolute complex viscosity  $\left(\frac{|\eta^*|}{|\eta^*|_0}\right)$ . Results of the samples including a higher concentration of modified amylose i.e., C10mA10 and C10mA15 can be described by Mooney, Batchelor-Green, modified Eilers models. This study highlights the promise of the renewable compatibilizers for the preparation of reinforced poly(olefin) matrices using bulk cellulose fillers.

## 9 Rheological Behavior of Renewable Based Long Chain Spaced Polyether Derivatives

The following chapter describes the sample preparation and rheological results on renewable-based polyethers derivatives. The synthesis of the samples and the analytical characterization, except the rheology tests, were performed by Dr. Patrick-Kurt Dannecker with the partial assistance of Nehir Kavak from the group of Prof. Dr. Michael A. R. Meier (Institute of Organic Chemistry (IOC), Materialwissenschaftliches Zentrum (MZE), Karlsruhe Institute of Technology (KIT), Karlsruhe, Germany). I would like to thank Dr. Hatice Mutlu (Institute of Biological Interfaces (IBG), KIT, Karlsruhe, Germany) for scientific discussions.

### 9.1 Introduction

Polyethers, either aliphatic or aromatic, are used in various important applications due to their alterable material properties. Polyethers find application in many areas such as automotive, construction, furniture, cosmetic industries, and more importantly in biomedical applications. Moreover, renewable-based polyethers, particularly the long-chain aliphatic ones, are of great interest, not only in science but also in the industry because of depleting fossil resources and the relevant environmental problems. Nowadays, it is feasible to synthesize polyethers in various ways from renewable sources. For instance, the synthesis of polyether polyols, derived from vegetable oils, is possible with the combination of cationic polymerization of epoxidized methyl oleate (EMO) and the reduction of carboxylate groups to hydroxyl moieties (Lligadas *et al.* 2007). Besides, understanding the rheological properties of the renewable-based polyethers is important, because it allows defining the best material for a specified application and processing technique. Therefore, in this study, the melt properties of the synthesized renewable-based long-chain spaced aliphatic polyether derivatives were analyzed via shear rheology, explicitly to investigate the material properties, along with the processability of the material. Furthermore, a defined HDPE model system with a low molecular weight was synthesized by ring-opening metathesis polymerization (ROMP) of cyclooctene. The results of the long-chain spaced aliphatic polyether derivatives were compared with the

synthesized PE samples, a commercial HDPE, and previously reported polyether derivatives to facilitate the prediction of possible industrial application areas.

## 9.2 Sample synthesis

To obtain long-chain spaced aliphatic polyether derivatives from  $\omega$ -unsaturated fatty acid methyl esters, first, a two-step procedure was applied involving a transesterification and catalytic reduction obtaining  $\alpha,\omega$ -diene monomers. The following polymerizations were carried out using acyclic diene metathesis (ADMET) or Thiol-ene polymerizations. It is relevant to note that the thiol-ene polymerization can be employed with total atom economy and rapid kinetics, and without expensive toxic metal-based catalysts. Indeed, in the literature, two ways of initiation for thiol-ene polymerizations are differentiated: thermal and UV-initiation (Türünç and Meier 2011). Due to the long aliphatic chain, the solubility of the formed polymers is very low in common organic solvents at ambient temperature, and thus the reaction has to be performed at elevated temperatures in high-boiling organic solvents to provide a homogeneous reaction mixture. Consequently, the thermal initiation method was used to synthesize the respective polymer. The detail of the synthesis was reported by Dannecker *et al.* 2018 as follows: the respective  $\alpha,\omega$ -diene diether (1.00 mmol, 1.00 eq.),  $\alpha,\omega$ -dithiol (1.00 mmol, 1.00 equivalent (eq.)) and azobisisobutyronitrile (AIBN) (0.025 mmol, 0.025 eq.), which was used as the thermal initiator, were dissolved in methyl-tetrahydrofuran (methyl-THF) (1 mL). The mixture was heated to 80 °C for 5 hours in a microwave reactor under continuous and severe stirring. The polymer was attained after precipitation of the hot reaction mixture in methanol. The schematic representation of the thiol-ene polymer (P1) is depicted in Figure 9.1. For the oxidation of the P1, sample P1 (1.00 mmol, 1.00 eq.) was dispersed in THF. In to this dispersion, an aqueous hydrogen peroxide solution (30% H<sub>2</sub>O<sub>2</sub> in H<sub>2</sub>O, 10.0 mmol, 5 eq. /sulfur atom) was added. The resulting heterogeneous mixture was heated up to 90 °C, and refluxed around 12 hours. Finally, the mixture was precipitated in a mixture of methanol: water (7:3) at room temperature. The oxidization of the thiol-ene polymer and the resulting oxidized thiol-ene sample (P1-O) is demonstrated in Figure 9.2. The  $M_w$  of both samples P1 and P1-O, which were analyzed via gel permeation chromatography (GPC) in THF, have both  $M_w = 24.5$  kg/mol ( $M_w / M_n = D = 2.58$ ).

The thermal properties of the prepared polymers were studied by a Mettler Toledo DSC stare system, operating under an N<sub>2</sub> atmosphere using about 5 mg of the respective polymer for the analysis. The  $T_m$  were recorded on the second heating scan by using the following method: cooling to -50 °C, heating from -50 °C to 200 °C at 10 °C/min, cooling from 200 °C to -50 °C at 10 °C/min and heating from -50 °C to 200 °C at 10 °C/min. DSC experiments were done by Patrick Dannecker. While the  $T_m$  of sample P1 was found via DSC measurement at 75 °C. Likewise, the  $T_m$  for P1-O was observed at 105 °C.

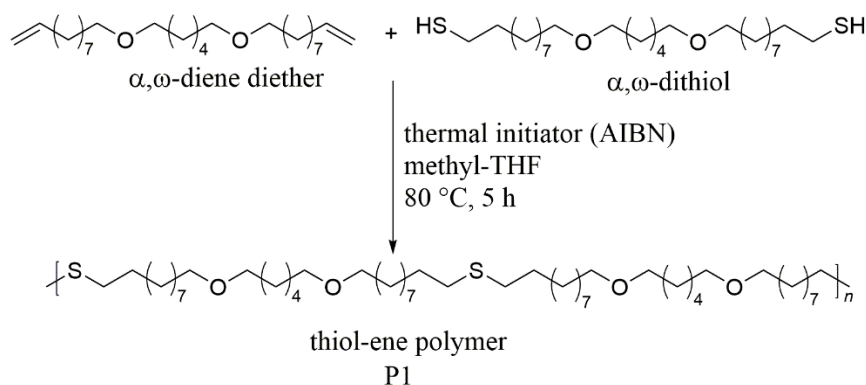


**Figure 9.1:** The schematic representation for the synthesis of the thiol-ene polymer (P1).

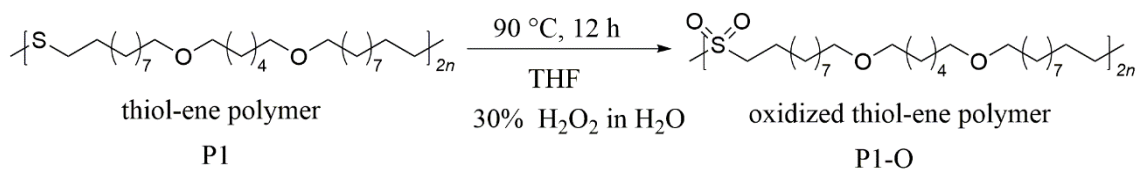


**Figure 9.2:** The schematic representation of the thiol-ene polymer (P1) and oxidized thiol-ene polymer (P1-O), respectively. To simplify the structure of the respective polymer P1 (see Figure 9.1), it was shown above as subscript “2n”.

The complementary, alternative polymer was synthesized by using acyclic diene metathesis (ADMET) polymerization (Mutlu *et al.* 2011). To aid the reader, ADMET has been considered to be a unique and efficient polycondensation strategy for the construction of polymers with precise control over the primary structure. Particularly, as compared to polymers of a similar composition that are synthesized with a lack of precise control on the sequence,  $M_w$  and  $D$  via conventional step-growth polymerization. The details of the ADMET polymerization conditions were reported by Dannecker *et al.* 2018, as following: *p*-benzoquinone (3.24 mg, 0.03 mmol, 0.06 eq.) and the  $\alpha,\omega$ -diene diether (0.5 mmol, 1.00 eq.) were dissolved in 0.2 mL dry polarclean (2.5 mol/L). The catalyst

Hoveyda-Grubbs (HG-II) (6.28 mg, 0.02 mmol, 0.02 eq.) was added at 85 °C. The pressure was reduced from atmospheric pressure to 40 mbar within 10 min. The reaction was quenched with ethyl vinyl ether, and the reaction mixture was precipitated in methanol, cooled with dry ice after 6 h. Then, the respective ADMET polymer (P2) (1.00 mmol, 1.00 eq.) was dispersed in toluene (12 mL) in an autoclave. Shvo's Catalyst (0.01 mmol, 0.01 eq./double bond) was added, and the mixture was stirred at 100 °C and 40 bar H<sub>2</sub> pressure overnight (~12 hours). After cooling to 50 °C, the mixture was precipitated in methanol (100 mL) cooled with dry ice. The resulting hydrogenated ADMET polymer (P2-H) was filtered off. The organic structures of the ADMET polymer (P2) and hydrogenated ADMET polymer (P2-H) are shown in Figure 9.3. The  $M_w$  of P2 and P2-H was found 29.5 kg/mol ( $D = 2.57$ ). The  $T_m$  of P2 was analyzed as 50 °C. Additionally, the  $T_m$  of the hydrogenated sample P2-H was obtained at 80 °C.

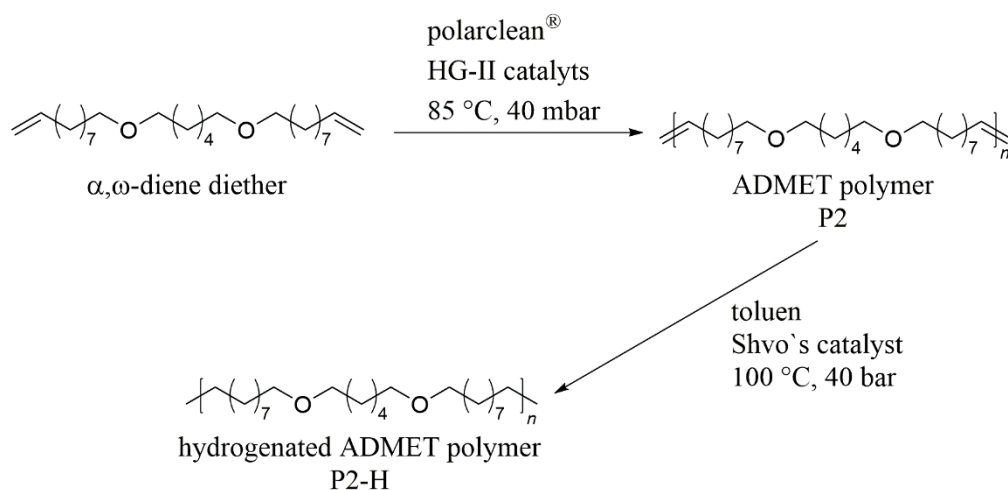


**Figure 9.3:** The schematic representation of the ADMET polymer (P2) and the hydrogenated ADMET derivative (P2-H).

Alternatively, HDPE samples P3 and P4 were synthesized via ring-opening metathesis polymerization (ROMP) as seen in Figure 9.4. (*cis*)-Cyclooctene (11.8 mL, 10.0 g, 907 mmol, 1.00 eq.) was dissolved in 30 mL CH<sub>2</sub>Cl<sub>2</sub> and depending on the targeted  $M_w$  different amounts of (*trans*)-oct-2-ene (P3: 56  $\mu$ L, 42 mg, 382 mmol, 0.005 eq.; and P4: 112  $\mu$ L, 84 mg, 764 mmol, 0.01 eq.) were added to the mixture. After the addition of the Grubbs Catalyst 1<sup>st</sup> Generation (75 mg, 0.091 mmol, 0.001 eq.) the mixture was stirred for an additional 1 h under inert gas. The reaction was quenched with 2 mL ethyl vinyl ether and precipitated in methanol; thus the polymer was attained as grey powder in 85 –

90% yield. Afterward, the ROMP polymer derivatives were hydrogenated to obtain the targeted HDPE samples P3 and P4 as displayed in Figure 9.5. Polycyclooctene (7.00 g, 62.4 mmol, calculated with respect to one repeating unit, 1.00 eq.) and Shvo's catalyst (34.0 mg, 0.031 mmol, 0.0005 eq.) were dissolved in 100 mL toluene in an autoclave, and 40 bar of H<sub>2</sub> pressure was applied. The mixture was heated to 110 °C and stirred for 24 h. The grey suspension was precipitated in methanol and a white powder was isolated via filtration (> 90% yield). Indeed, the Shvo's catalyst provides a particularly high activity (Conley *et al.* 2010), hence minimizing the catalyst loading, and facilitating easy purification. In general, homogeneous catalysts are superior in this type of transformation, as heterogeneous catalysts would be difficult to remove from insoluble HDPE, obtained after the hydrogenation process. Typically, the hydrogenation reactions are performed for approximately 24 hours to ensure a quantitative conversion. Due to the insolubility of the substrate, the conversion of the reaction was determined by infrared spectroscopy (IR spectroscopy) (see appendix in Figure A3).

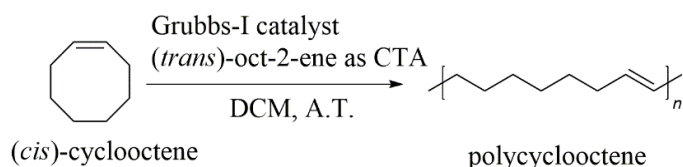


**Figure 9.4:** General reaction scheme for the ROMP of (cis)-cyclooctene. \*CTA: chain transfer agent; A.T.: ambient temperature; DCM: dichloromethane.

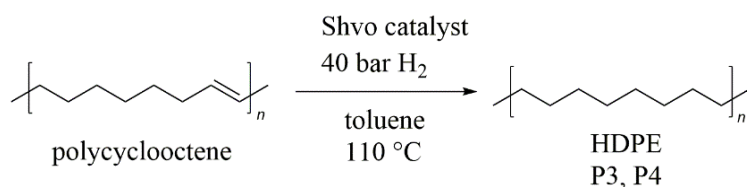


**Figure 9.5:** Hydrogenation of ROMP polymer, i.e. polycyclooctene, to obtain HDPE samples P3 and P4.

The details of the samples are listed in Table 9.1 regarding sample type/mimic, and their characteristics.

**Table 9.1:** Sample name, sample type/mimic, sample code and their characteristics as  $M_w$ ,  $\bar{D}$  and  $T_m$ .

Sample name	Polymer type/ mimic	Sample code	$M_w^a$ [kg/mol]	$\bar{D}$	$T_m^b$ [°C]
Thiol-ene	Polythioether derivate	P1	24.5	2.58	75
Oxidized-thiol-ene	Polysulfone derivative	P1-O	24.5	2.58	105
ADMET	ADMET derivative	P2	29.5	2.57	50
Hydrogenated- ADMET	Polyether derivative	P2-H	29.5	2.57	80
HDPE	HDPE	P3	71.6	1.57	128
HDPE	HDPE	P4	100.3	1.52	127
HDPE	HDPE	P5	182	11	131

<sup>a</sup>The  $M_w$  of samples were analyzed via GPC in THF. <sup>b</sup>The  $T_m$  polymers were obtained via DSC measurement by using a 10 °C/min cooling and heating rate. The 2<sup>nd</sup> heating run of DSC measurement was used to calculate  $T_m$ . The schematic representation of the P1 synthesis can be seen in Figure 9.1, and the oxidization protocol of the P1 sample and the resulting P1-O polymer is demonstrated in Figure 9.2. The schematic representation of the P2 and P2-H are depicted in Figure 9.3. The schematic representation of the P3 and P4 synthesis are displayed in Figure 9.4 and Figure 9.5,

### 9.3 Melt rheology analysis

The processability of the material was investigated by oscillatory shear measurements using an ARES-G2 strain-controlled rotational rheometer from TA. The concentric cylinder (Couette geometry), which has a 20 mm diameter cup and 18.6 mm Bob, was used particularly for low viscous samples 30 °C above their  $T_m$  ( $T_m+30$  °C). The parallel plate geometers with a 25 mm diameter were used for the analyses of HDPE polymers. All measurements were conducted under an N<sub>2</sub> atmosphere to prevent thermal degradation as much as possible. Strain-dependent measurements were performed to distinguish the linear and nonlinear viscoelastic regions at  $T_m+30$  °C with  $\omega_1 = 30$  rad/s. The storage modulus  $G'(\gamma_0)$  of P2 and P2-H remained constant up to  $\gamma_0 = 50\%$  as seen in Figure 9.6. The linear viscoelastic region broadened for P1 and P1-O, up to  $\gamma_0 = 1000\%$

and 500%, respectively. The overall behavior was dominated on the  $G''(\gamma_0)$  viscous modulus. Sample P2 and P2-H showed a factor of  $\sim 8$  higher  $G''(\gamma_0)$  due to higher  $M_w$  compared to P1 and P1-O at  $T_m + 30$  °C. Subsequently, the time-dependent experiments were exerted during an hour for all samples to investigate the thermal stability at 150 °C. The results of the time-dependent experiments are displayed in Figure 9.7. Samples were found to be thermally stable under the processing applications up to 150 °C, except the sample P1-O. Critically, P1-O showed a 10% decrease in the  $G''(t)$  by the time, which could indicate possible degradation due to the chain scission of the polymer. The result of sample P2-H showed 400 times lower in  $G''(t)$  value than the result of the PEO sample ( $M_w = 100$  kg/mol with  $D = 6.9$ ) in the study of Ferretti *et al.* (2005) due to low  $M_w$  of P2-H (29.5 kg/mol).

Frequency-dependent measurements were conducted in the linear viscoelastic region. Reference temperature ( $T_{ref} = T_m + 30$  °C) was chosen as 30 °C above the  $T_m$  to obtain isotropic melt polymer. The linear master curves of  $G'(\omega_1)$  and  $G''(\omega_1)$  at the  $T_{ref}$  were constructed via the TTS principle by using the frequency-dependent tests in the temperature range between  $T_m + 10$  °C to  $T_m + 45$  °C. The master curves of the samples are shown in Figure 9.8. All samples exhibited a dominantly viscous behavior ( $G'' > G'$ ) for this frequency range.

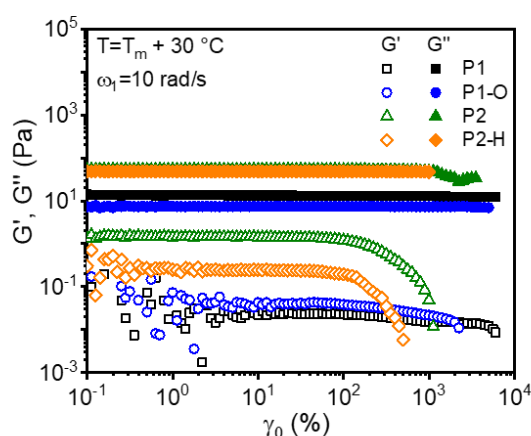


**Figure 9.6:** Strain amplitude ( $\gamma_0$ ) dependency tests for the thiol-ene (P1) polymer, oxidized thiol-ene polymer (P1-O), the ADMET polymer (P2), and the hydrogenated ADMET polymer (P2-H) at  $T_m + 30$  °C,  $\omega_1 = 10$  rad/s.

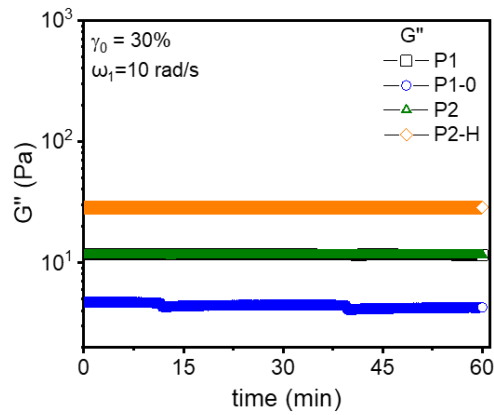


**Figure 9.7:** Time-dependent tests for the thiol-ene (P1) polymer, oxidized thiol-ene polymer (P1-O), the ADMET polymer (P2), and the hydrogenated ADMET polymer (P2-H) at 150 °C with  $\gamma_0 = 30\%$ ,  $\omega_1 = 10$  rad/s.

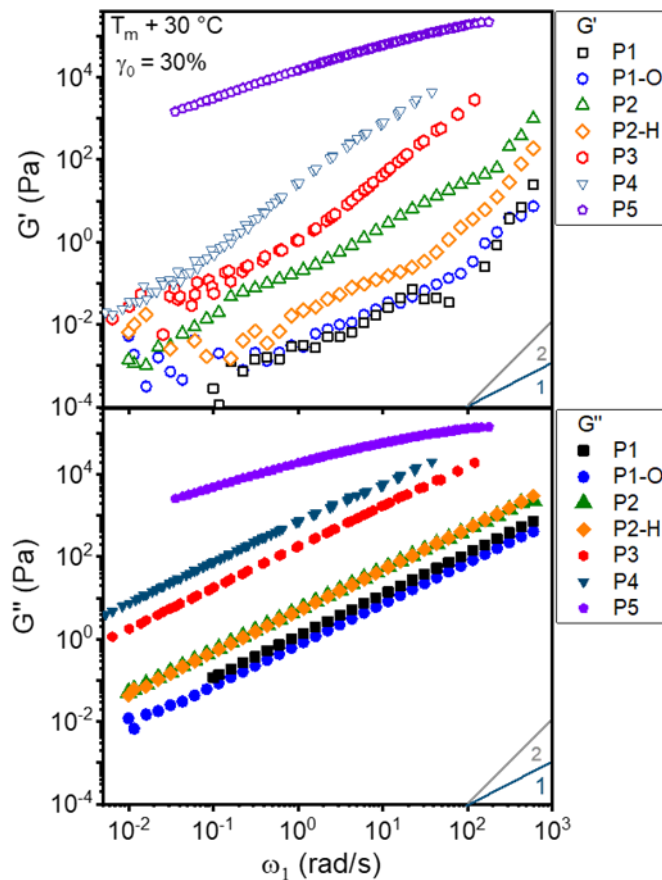


**Figure 9.8:** Frequency-dependent measurements for the thiol-ene (P1) polymer, oxidized thiol-ene polymer (P1-O), the ADMET polymer (P2), hydrogenated ADMET polymer (P2-H), HDPE samples P3, P4, and P5 at  $T_m + 30$  °C,  $\gamma_0 = 30\%$ .

The transition from liquid-like behavior to solid-like behavior ( $G' > G''$ ) could not be detected due to the low  $M_w$ , and insufficient entanglement in the polymer melt of P1, P1-O, P2, and P2-H, respectively. As it was aforementioned in section 4.1.2, a homopolymer with narrow dispersity exhibits characteristic relation  $G' \propto \omega_1^2, G'' \propto \omega_1^1$  in the flow region. In this study, all samples followed the relation in  $G'' \propto \omega_1^1$ . The  $G''$  is a measure of energy dissipation, through as a modulus it is either hardness or stiffness of a material. The  $G''$  values of P2 and P2-H samples were 5 times higher than the value of  $G''$  of the samples P1 and P1-O. The high  $G''$  of samples P2, P2-H indicated longer relaxation times of these polymers, and therefore less stiff/hard material properties. Although the  $G''$  was monitored larger than the  $G'$  at all frequencies, the interval between them was the most reduced for sample P2. The latter indicated that the viscous property was reduced in favor of elastic property. A deviation from  $G'$  at high frequency  $\omega_1 > 5$  for samples orderly P1, P2-H, P1-O, P3, P2 as following  $G' \propto \omega_{1,P1}^{2.5} > \omega_{1,P2-H}^{2.1} > \omega_{1,P1-O}^{1.8} > \omega_{1,P3}^{1.7} > \omega_{1,P2}^{1.6} > \omega_{1,P4}^{1.5} > \omega_{1,P5}^{0.5}$  respectively. Increasing  $M_w$  and  $\mathcal{D}$  caused a decrease in the slope of  $G'$ . It can be seen in Figure 9.8 that sample P2 showed higher  $G'$ , and hence, it was found to be more elastic than P1, P1-O, and P2-H. Nevertheless, P2 was not as elastic as sample P3, P4, P5, which could be a result of low  $M_w$ . Here, the study of Sungsanit (2011) can fetch an alternative point of view to the current study. Sungsanit reported that the 20 wt% addition of low  $M_w$  polyethylene glycol (PEG) as 1 kg/mol into linear poly(lactic acid) L-PLA ( $M_w = 155$  kg/mol) showed a decrease in  $G'$  at 1 rad/s from 20 Pa to 0.2 Pa and a decrease in  $G''$  from 600 Pa to 100 Pa. The latter was explained by the addition of PEG into L-PLA, particularly by the decreased energy dissipation. They also observed an 84% reduction in zero shear viscosity ( $\eta_0$ ) as a result of the improved mobility of the polymer chains within the blend. This result could support the idea that renewable-based synthesized polymers P1, P1-O, P2, P2-H may find possible material application as a blend.

Moreover, the  $\eta_0$  was measured under the shear rate from 1 to 100  $s^{-1}$ , and a reverse experiment from 100 to 1  $s^{-1}$  was conducted to investigate the reproducibility. The average value of the  $\eta_0$  was calculated. The  $\eta_0$  results are listed in Table 9.2. The lowest  $\eta_0$  was observed for P1-O. The calculated  $\eta_0$  values were the same for P2 and P2-H.

Indeed, the viscosity has a strong relation with  $M_w$  and entanglement. Therefore, sample P2, P4 showed higher  $\eta_0$ . The maximum entanglement belongs to P5, and thus it showed the highest value in  $\eta_0$ .

Furthermore, the activation energy of the flow ( $E_a$ ) is of interest for polymers related to the temperature sensitivity of the material properties. The  $E_a$  of the samples were determined via using TTS with the  $a_T$ . The calculated  $E_a$  values for ether samples and PE samples are presented in Table 8.2. The higher  $E_a$  indicates the more temperature dependency of flow properties, which is not preferred. The  $E_a$  was calculated for P2 to be 21.1 kJ/mol and for P2-H as 23.2 kJ/mol. For the synthesized linear PE derivatives P3, P4 and the commercial P5, the calculated  $E_a$  values were 24.3, 26.3, and 33.5 kJ/mol respectively. These  $E_a$  values represent less temperature sensitivity and similar mobility of the samples. However, sample P1 showed the maximum in  $E_a = 73.2$  kJ/mol and the  $E_a$  was achieved as 55.5 kJ/mol for sample P1-O. Thus, sample P1 and P1-O showed more temperature sensitivity.

**Table 9.2:** Sample code, and their respective  $\eta_0$  and  $E_a$  values.

Sample code	Zero shear viscosity $\eta_0$	Activation energy $E_a$
	at $T_m + 30$ [Pa.s]	[kJ/mol]
P1	1.4	73.2
P1-O	0.7	55.5
P2	5.6	21.7
P2-H	5.6	23.2
P3	129	24.3
P4	466	26.9
P5	63435	33.5

## 9.4 Concluding remarks

This study aimed to investigate the melt properties of the novel and renewable, long-chain spaced aliphatic polyether derivative samples. Melt elastic and viscous modulus were in discussion of processibility and possibility in the future for the replacement with HDPE,

PEO or PEG samples. The rheological characterization showed that oxidation did not cause any difference in the melt mechanical properties. The  $G'$  and the  $G''$  modulus interval was the narrowest for the sample P2, due to the low viscous properties in favor of the elastic properties. Samples P1, P1-O, P2, and P2-H can not compete in elasticity in comparison with commercial HDPE (P5). This is because of novel synthesized samples P1, P1-O, P2, P2-H have low  $M_w$ , and hence low viscosity. Nevertheless, samples P2 and P2-H showed similar temperature sensitivity with P5 and also similar mobility indicated by the low  $E_a$ . Additionally, samples P2 and P2-H with low  $M_w$  could be useful material as an impact modifier for some polymers, due to their inherent biodegradability, low  $E_a$ . Sungsanit (2011) reported that the addition of 20 wt% PEG into PLA resulted in 9 °C increase in the crystallization temperature  $T_C$ , 3 times enhanced crystallinity with a significant decrease in the moduli  $G'$ ,  $G''$  and  $\eta_0$  as the result of improved mobility of polymer chains in the blend. In summary, one can conclude that the melt properties of the polymers were largely dependent on each utilized polymerization approach (i.e. thiol-ene or ADMET), which as a result delivered unique polymer structures. Critically, these structures are not accessible by any other conventional methodologies.

## 10 General Conclusion and Future Work

The scope of this thesis was to investigate the effects of the HPN-20E nucleating agent (NA) amount in HDPE on the crystallization mechanism under controlled processing conditions such as the temperature, steady shear, applied large strain amplitude by using the RheoNMR method. Additionally, isothermal coconut fat crystallization under quiescent and strain-induced conditions was also investigated via RheoNMR. Moreover, the processability of the cellulose/LDPE composites reinforced with sustainable plant-based compatibilizer and the newly synthesized renewable-based polyethers were investigated by using the shear rheology method.

The unique RheoNMR provides valuable information on the effects of processing conditions and also the impact of the additive incorporation on the material properties. While the rheometer monitors the full rheological shear characterization during the crystallization, the evolution of the crystallinity ( $X_C$ ) is determined by detecting the molecular mobility of the protons with the low-field NMR via using the CPMG pulse sequence. Simultaneous measurements enable a direct correlation between dynamic moduli and crystallinity development for high-temperature resolution, i.e.,  $\Delta T_C = 0.5$  °C with identical thermal and shear history conditions. The isothermal crystallization of neat HDPE and HDPE/NA blends was investigated for different  $T_C$  under quiescent conditions. Additionally, the effect applied steady shear or large strain amplitudes variations were also studied. Determined crystallinity and the normalized storage modulus evolution as a function of time was plotted. Then, the Avrami and Foubert models were used to a kinetic analysis by fitting them to the data. The Avrami equation is a well-known theory and widely used to determine primary crystallization behavior and kinetic analysis of crystallization (Piorkowska and Rutledge 2013). The Avrami rate  $K$  values, which were derived from fitted Rheo and NMR data, were close to each other. When the Avrami exponent  $n$  derived from Rheo data, and NMR result, it was shown as  $n_{\text{Rheo}}$ ,  $n_{\text{NMR}}$  respectively. The calculated  $n_{\text{Rheo}}$  was approximately 1 value larger than the  $n_{\text{NMR}}$  as following:  $n_{\text{Rheo}} = n_{\text{NMR}} + \sim 1$ . This deviation can be attributed to the sensitivity scales of the methods. While the sensitivity of NMR relaxation is in local motion as microscopic (0.2-2 nm) scale, this scale is much larger ( $\approx 1$  mm) in rheological

measurement. Additionally, the isothermal crystallization experiments on the HDPE/NA blends were conducted via the DSC method for the same  $T_C$  and a similar cooling rate. Resulting relative crystallinity data was fitted by the Avrami model. The calculated rate parameters from DSC, NMR, and Rheo data showed that the crystallization was accelerated by decreasing  $T_C$  and increasing NA content in the HDPE sample. For further analysis, the activation energy of crystallization  $E_C$  values for the primary crystallization was calculated by using the Avrami rate  $K$  value. While the extracted  $E_C$  values from DSC data stayed relatively constant at -1000 kJ/mol, the extracted  $E_C$  values from Rheo and NMR data increased 2 times and reached to -750 kJ/mol for increased NA content up to 3 wt%. This may be an indication that crystallization dependency towards the  $T_C$  was higher for decreasing NA content in the HDPE samples and the neat HDPE sample. Additionally, the Foubert model was used for the crystallization kinetic analysis of the HDPE/NA blend. The Foubert model has been used to describe the fat crystallization process (Foubert *et al.* 2002). To the best of my knowledge, the Foubert model was the first time used to characterize the polymer crystallization kinetics. Although the missing physical explanation of the Foubert model parameters, rate value  $v$  well described the complete crystallization curves of HDPE/NA samples especially under the quiescent condition in the case of crystallization curves reaches their maximum stable values.

The direct correlation between the reduced storage modulus  $\frac{G'}{G'_0}$  and  $X_C$  was described well with power-law and extended Einstein model, up to  $X_C = \sim 20\%$ . The exponents  $C' = p$  were in the range of 1-3, and the  $D' = \psi$  values were calculated to be in the range of  $\sim 130$ -16500 depending on NA content in the sample,  $T_C$ , and applied deformation.

A more clear picture of the crystallization process analysis under the varying condition for HDPE/NA samples was designated by correlations of between quantities  $t_{0.2}$  and  $t_{gel}$  values. A linear relationship between  $t_{0.2}$  and  $t_{gel}$  was achieved as  $t_{0.2} = 4 t_{gel}$  for used  $T_C$  range (123-124.5 °C) of neat HDPE under quiescent crystallization. While a 0.5 °C decreased in  $\Delta T_C$  caused an almost 50% decrease in  $t_{0.2}$  and  $t_{gel}$ , the addition of 3 wt% NA in HDPE decreased the  $t_{gel}$  to half and the  $t_{0.2}$  to almost one-third of the  $t_{0.2}$  and  $t_{gel}$  values of the neat HDPE sample. Besides NA addition, accelerated crystallization for neat HDPE sample was achieved with observed shortened  $t_{gel}$  and the  $t_{0.1}$  under either the

exerted low steady shear ( $\dot{\gamma} = 2 \text{ s}^{-1}$ , 11 s) at the beginning of the experiment or a 1 °C decrease in the  $T_C$ . A similar impact was observed for applied short term large strain amplitude ( $\gamma_0 = 200\%$ , 60 s) at the 5<sup>th</sup> min of the experiment with achieved shorter  $t_{\text{gel}}$  and  $t_{0.2}$  as  $\sim 2$  and  $\sim 3$  min respectively. This result indicated both enhanced nucleation and crystal growth stage. Conversely, a delay in  $t_{\text{gel}}$  was observed for imposed large strain amplitude ( $\gamma_0 = 30\%$ ) during the complete crystallization process. In the meantime, this effect shortened the  $t_{0.2}$ . This can be interpreted that, applied  $\gamma_0 = 30\%$  influenced the nucleation stage negatively by possibly destroying nuclei via deformation. However, it effectively enhanced the growth stage of the crystallization by oriented crystal structure on the crystal growth stage. Moreover, when the NA content  $> 0.1 \text{ wt}\%$  in the HDPE sample, the reduction in  $t_{0.2}$  and the delay in  $t_{\text{gel}}$  was rather small compared to the observed  $t_{\text{gel}}$  and  $t_{0.2}$  values for the samples 0.1% NA and 0% NA. This behavior showed that when the NA content in HDPE is above 0.1 wt%, the impact of strain-induced crystallization on the  $t_{\text{gel}}$  and  $t_{0.2}$  values were minimal.

The further direct correlation between the observed peak maximum of  $I_{3/1}$  at around the gel point and the  $t_{\text{gel}}$  was demonstrated a nonlinearity change in the sample response to crystallization condition and NA addition. This relationship was revealed that an exponential decay like change was achieved with reduced NA content in the HDPE sample and with decreased  $T_C$ . The  $I_{3/1}$  was also responsive towards to the applied varying  $\gamma_0$  and the failure in the experiment at applied high strain amplitudes. Samples were taken from the RheoNMR instrument at the end of quiescent crystallization and applied long-term  $\gamma_0 = 30\%$  crystallization condition for XRD and DSC analyses. Detected  $X_C$  values at 25 °C via XRD and DSC techniques were acquired equivalent to each other as  $X_C = \sim 62\%$  underestimated  $\pm 10\%$  errors. Monitored  $X_C$  values via NMR was approximate  $\sim 37\%$ , and it was almost equal to the  $X_C$  value which was determined by the DSC method under quiescent crystallization at 124.5°C. Thus, these equivalent results confirmed the accuracy of this newly developed RheoNMR technique. Additionally, the difference in  $\Delta X_C = \sim 25\%$  determined by DSC at 124.5 °C and later at 25 °C showed the continuing secondary crystallization effect. The XRD analysis showed the orthorhombic unit cell structure for all HDPE/NA samples. Moreover, morphology

analysis via SEM images revealed the closely packed slightly oriented thinner lamellar structure for all HDPE/NA samples under applied  $\gamma_0 = 30\%$  during crystallization. Besides, the oriented parallel lamellar stacks were observed for the short term applied large deformation or steady shear conditions. For an assignment of the numerical value for lamella alignment, the oval profile plug-in (authored by William O'Connell) of ImageJ software (NIH, <http://rsb.info.nih.gov/ij>) proceeded on the generated FFT image from SEM images.

Within this Ph.D. work, the isothermal crystallization of coconut fat under applied a range of strain amplitude (0.005-5%) was also investigated via RheoNMR. Most published articles about the analysis of crystallization kinetics of oils use conventional techniques such as DSC,  $^1\text{H-NMR}$  under quiescent crystallization conditions. The study of the deformation effect is interesting since a lot of processing techniques apply shear forces in the fat processing industry e.g., the dry fractionation process. The RheoNMR method provides a prediction of varying processing condition effects on the mechanical properties of fat systems and allows further tailoring to optimize the product for specific applications. The temperature-dependent quiescent crystallization and strain-induced crystallization kinetics of coconut fat were examined by the Avrami, modified Gompertz and Foubert models. The calculated rate parameters indicated slower crystallization with increasing  $T_C$ . Applied larger strain amplitude did not significantly influence the overall crystallization rate parameters, however, the primary crystallization rate ( $K$ ) showed 10% slower crystallization at  $T_C = 14\text{ }^\circ\text{C}$  for applied largest  $\gamma_0$ . This finding was further supported by the derived induction time values which increased when the largest strain amplitude  $\gamma_0 = 5\%$  was applied. Additionally, the exponents of the models demonstrated the possible changes in the dimensionally of fat crystals. The correlation between  $G'$  and  $\frac{x_C(t)}{x_C^\infty}$  was used to determine fractal dimensions  $D = 2.5$  for the used  $T_C$  range. A slight decrease was achieved for the  $D$  at the initial stage of crystallization with increasing  $T_C$  and  $\gamma_0$ , and hence lower  $D$  implied the possible disordered packing of the microstructural elements within the network. Additionally, the extended Einstein, Batchelor-Green, and the power-law model was used to describe crystallization behavior by fitting the direct correlation of  $G'$  with  $\frac{x_C(t)}{x_C^\infty}$  up to 50% of the relative crystallinity. As a result, the

exponents  $C' = p$  were found in the range  $\sim 0.8$  to  $\sim 2.1$ ; and the  $D' = \psi$  were found in between  $\sim 9 \times 10^6$  and  $\sim 64 \times 10^6$ .

Melt shear rheology was used to characterize the dispersion of the cellulose and plant-oil based compatibilizers within the LDPE matrix. Time-dependent experiment was conducted at 150 °C to determine the thermal stability of the  $G'(t)$  modulus of the PE composite samples. Only the composites with 45% cellulose content (C45mA10/S10 and C45mA0/S0) showed a  $\sim 10$  to 15 % decrease in the  $G'$  which was predicted with the loss of residual water in the cellulose fibers. The frequency-dependent measurements on the all-composite samples revealed the cellulose compatibilized with the modified amylose showed a better adhesion of the fibers with the LDPE matrix compared to the modified starch within the cellulose-LDPE dispersion. The  $\frac{|\eta^*|}{|\eta^*|_0}$  at constant frequency was plotted as a function of total filler weight fraction  $\phi$ . This correlation behavior was described with the classical suspension models. Samples with a high amount of amylose filler content behaviors were followed the Mooney, Batchelor-Green, modified Eilers models with a good fit. The renewable compatibilizers for the preparation of reinforced poly(olefin) matrices using bulk cellulose fillers were found promising.

Another focus of the present work was the melt rheological properties of the novel and renewable, long-chain spaced aliphatic polyether samples. While the oxidation step for the synthesis of P1-O did not lead to any difference in the melt mechanical properties, the hydrogenation process showed a significant impact on the melt properties of P2. The novel synthesized samples P1, P1-O, P2, P2-H have low  $M_w$ , and thus low viscosity. Therefore, results showed that P1, P1-O, P2, and P2-H can not replace commercial HDPE (P5). However, it can be concluded that the melt properties of the polymers were largely dependent on the polymerization approach, i.e., if it is either thiol-ene or ADMET based type polymerization. Additionally, the obtained less sensitivity towards to the temperature with the low  $E_a$  for samples P2 and P2-H could make them possible material as an impact modifier for some polymers, mainly due to their inherent biodegradability.

The development of the RheoNMR setup assisted designing a smaller magnet for the RheoNMR method which is also built by Karl-Friedrich Ratzsch. The newly constructed

smaller magnet design has better usability own to its lightweight and sensitivity compared to the old magnet. The old magnet was the only magnet used in this study, and it was introduced in Chapter 5.

As a final remark, RheoNMR can be an advance experimental technique to gain more information on the rheological evolution corresponding to the continuing crystallization process. The further investigations could be on cooling rate effects on the time of gelation and the half time of the crystallization of semi-crystalline polymer precisely the same thermal and shear history. Moreover, analyzing empirical crystallization data by using classical suspension models or by developing semi-empirical equations for kinetic analysis is important to develop the simulation programs for solidification processes. While the kinetic analysis of the crystallization of any semi-crystalline bulk sample can be done by using both the Rheo and the NMR data of the RheoNMR, the NMR part provides additional information as a final degree of the crystallinity under control crystallization conditions. This could make the RheoNMR method useful for valuable quality control analysis i.e., in the food industry using different qualities of fat since confectionery products contain a significant amount of fat. The RheoNMR could also establish consistency in the mechanical properties of fat networks being produced, i.e., margarine products. RheoNMR method opens up the possibility to learn required deformation or shear for intentional application to the commercial processing which allows a better controlling physical property of the fat product. Thus, sensorial properties can be better interpreted. For instance, clean-melting sensation during consumption of confectionery products is provided by small fat crystals which can be obtained by the rapid crystallization process. The provided correlation between  $\ln(G')$  and  $\ln(\frac{X_C(t)}{X_C^\infty})$  for varying flow-induced crystallization conditions by using RheoNMR ensures valuable information related to the fractal dimension which could be used for the prediction on the sensorial properties by comparison with the values of other products. Therefore, further investigation with RheoNMR could be studying a steady shear which is a practical procedure in industrial processes, effects on crystallization kinetic, final crystallinity and mechanical properties.

## A Appendix

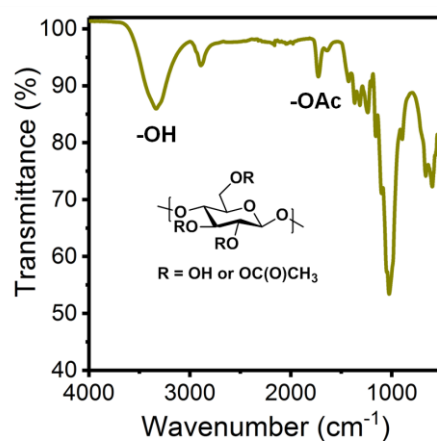


**Figure A1:** FT-IR spectrum of cellulose obtained by the acetic acid extraction of wood chips clearly showing absorption in the carbonyl region as a result of acetylation during extraction.

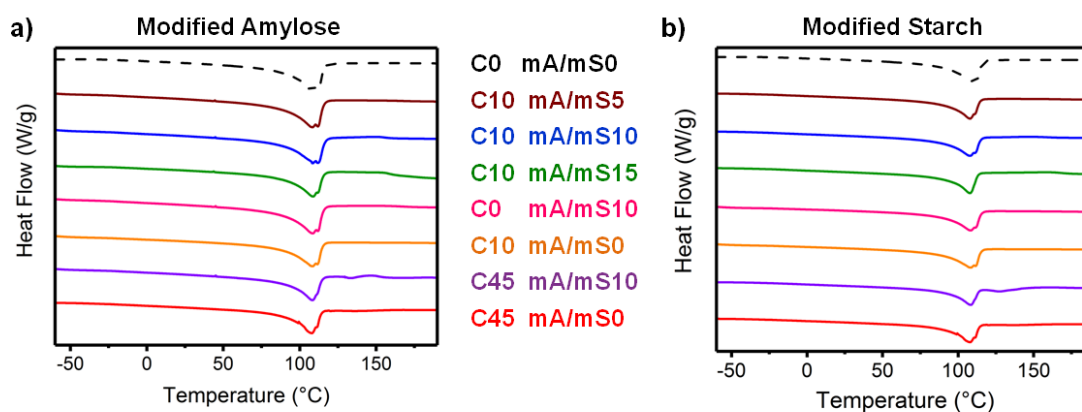


**Figure A2:** DSC results of samples containing (a) modified amylose and (b) modified starch compatibilizer and their respective reference samples.

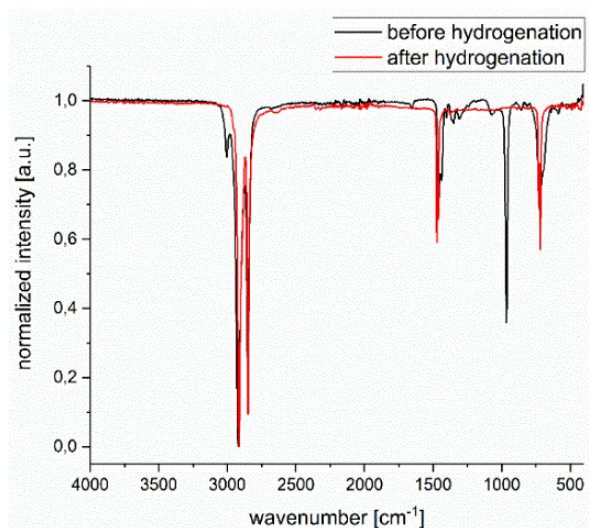


**Figure A3:** IR-Spectrum of polycyclooctene before and after hydrogenation.

The displayed Infrared spectra (IR) in Figure A3 were recorded on a Bruker Alpha-p instrument in a frequency range from 3998 to 374 cm<sup>-1</sup> applying KBr and ATR technology. All for double bonds particular vibrations cannot be observed after hydrogenation, the trans C-H<sub>oop</sub> vibration at 965 cm<sup>-1</sup> and  $\nu$ -CH at 3005 cm<sup>-1</sup>, suggesting full conversion of the double bond.

## List of Figures

- Figure 2.1:** The worldwide plastic-type demand in 2015. PE: polyethylene, PP: polypropylene, PVC: polyvinyl chloride, PET: polyethylene terephthalate, PS: polystyrene, PUR: polyurethane, PA: polyacrylate. Data was taken from the Plastic Europe Report (2016).....8
- Figure 2.2:** The growth of polyethylene chains via free radical polymerization (Peacock 2000).....9
- Figure 2.3:** The (a) intermolecular and (b) intramolecular radical transfer during the free radical polymerization of ethylene used for LDPE production (Peacock 2000)..... 10
- Figure 2.4:** Illustration of the chemical structure of low-density polyethylene (LDPE).  
..... 10
- Figure 2.5:** Illustration of the chemical structure of high-density polyethylene (HDPE).  
..... 12
- Figure 2.6:** Illustration of the chemical structure of a linear low-density polyethylene (LLDPE)..... 13
- Figure 3.1:** A simple illustration of the three-phase morphology in solid polyethylene and tie chains, loops, and cilia in the non-crystalline phases of polyethylene (Peacock 2000). A specification is given for high-density polyethylene (HDPE) as a thickness range of approximately 80-200 Å with several micrometers lateral dimension for crystallites and the range of non-crystalline phase approximately 50-300 Å (Peacock 2000). ..... 14
- Figure 3.2:** Polyethylene orthorhombic crystal (a) orthogonal view and (b) a view along the c axis (Peacock 2000)..... 16
- Figure 3.3:** Simple illustration of two central concepts: (a) fringed micelle model (Keller 1968), (b) a lozenge-shaped single crystal with perfect (regular) chain folding (Gedde and Hedenqvist 2019)..... 16
- Figure 3.4:** Multi-scale crystalline structures for polyethylene. Chain folded lamellae stack is constituted by packed crystals as a plate shape. Spherulites are formed as results of the lamellae splays, bends, and branches (Hiemenz and Lodge 2007). Shish kebab morphology consists of extended chains called shish, which act as nuclei and lamellae

called kebab part grow on shish. Shish kebab morphology can be generated by conducted elongation flow during crystallization. .... 17

**Figure 3.5:** Equilibrium cuboid shape of crystal with three different surfaces ( $i = 1, 2, 3$ ) with specific surface free energies  $\sigma_i$  (Gedde 1995) ..... 19

**Figure 3.6:** Illustration of a lamellae growth with thickness as  $L_c^*$  and width as  $L_p$  based on (a) the Lauritzen-Hoffman (LH) theory. The LH theory describes the crystal growth with a growth rate radially  $G$ , lateral spreading rate  $g$ , and nucleation rate  $i$  by attachment of a single stem has a thickness  $b$  and a width  $a$ . (b) Schematic a lamellae growth instantaneously with varying lengths based on the Sadler-Gilmer (SG) theory. Figures are replotted from references: Piorkowska and Rutledge (2013) and Bower (2002). ..... 25

**Figure 3.7:** (a) Illustration of crystal growth with formation nuclei (attached and detached stems) on the preexisting surface (secondary nucleation) and the chart shows the free energy change with formed nuclei (stems) amount. The  $A_0$  is the required free energy for the generation of the first stem. The next steps in the crystal growths with the detachment and attachment of the stem have a lower free energy barrier. (b) Schematic representation of three regimes in LH theory. The growth rate of the complete crystal (lamella) is determined by using the lateral growth rate  $g$  and the surface nucleation rate  $i$  as a function of  $\Delta T$ . These three regimes can be identified with a different slope as  $K_{g(I)} = K_{g(III)} = 2K_{g(II)}$  from the plot of  $(\log G)/G_0$  according to as  $1/(T_C \Delta T)$ . Figures are replotted from reference: Gedde 1995. .... 27

**Figure 3.8:** Multistage crystal growth model (Strobl 2006; Strobl 2009, 2000). The polymer chains are formed into a thin layer called a mesomorphic layer. The thickening of the mesomorphic layer spontaneously causes the solidification and generates the granular crystal structure. The stabilization occurs with the merging of granular crystal blocks to reduce the excess energy of the folded surface. Figure is replotted from references: Strobl 2000; 2006; 2009. .... 28

**Figure 3.9:** (a) The linear dependencies in between temperature and the inverse crystal thickness for crystallization and melting line in a multi-stage crystallization model. Here, the equilibrium crystallization temperature  $T_C^0$  is higher than the equilibrium melting temperature  $T_m^0$ , and this difference shows existence of a transient mesomorphic phase. (b) Relationship between the temperature ( $T$ ) and the inverse of the number of structural units in stem ( $1/n$ ) in multi-stage crystallization model in which labels are as following: (a) amorphous melt, mesomorphic ( $m$ ), native crystals ( $c_n$ ), and stable crystals ( $c_s$ ) for multistage crystallization model. The three lines indicate the limits as following: melting line ( $T_{ac_s}^\infty = T_m^0$ ), the crystallization line ( $T_{mc}^\infty = T_C^0$ ), the mesomorphic structure line

( $T_{am}^{\infty} = T_{zg}$ ). For instance, of isothermal crystallization, the route is numbered starting from one and end at number three and direction showed with a grey color arrow lines. The charts are replotted from references: Strobl 2006; 2009.....29

**Figure 3.10:** Snapshots illustrating the circular crystal growth in case of heterogeneous nucleation to describe the fundamental idea of the Avrami model (Gedde and Hedenqvist 2019).....31

**Figure 3.11:** General curve of crystallization rate as a function of temperature (Gedde 1995).....33

**Figure 3.12:** (a) Structure of calcium salt part of the HPN-20E (cis-1,2-cyclohexanedicarboxylic acid) nucleating agent (NA). (b) SEM images of commercially available power like HPN-20E material.....39

**Figure 4.1:** Two-plate model for the shear experiment. Material is located between two plates in a distance  $h$ . The upper plate with the area  $A$  is moved by the force  $F$  over a distance  $x$ .....40

**Figure 4.2:** Schematic illustration of (a) parallel-plate, (b) cone-plate and (c) Couette geometry in a strain-control rheometer. The motor is located at the bottom and applies defined deformation to the sample (the black part in between geometries) via the lower geometry. The torque transducer measures the resulting mechanical response and it is connected to the upper geometry.....41

**Figure 4.3:** (a) Hooke`s spring for ideal elastic materials and (b) dash-pot for ideal viscous materials at a constant temperature. A sinusoidal deformation is applied with a rotational movement at a constant angular frequency. ....42

**Figure 4.4:** (a) Kelvin-Voigt model for elastic solids with some viscous part. (b) Maxwell model for viscous liquids with some elastic part. ....43

**Figure 4.5:** A strain dependency test of a predominantly elastic material ( $G' > G''$ ). In the linear viscoelastic regime, moduli are independent of applied strain. After the critical strain  $\gamma_0$ , the module  $G$  is dependent to applied strain  $\gamma_0$ , and this regime is called as the non-linear viscoelastic regime.....46

**Figure 4.6:** Master curve, designated via TTS, shows the frequency dependency of the storage ( $G'$ ), loss modulus ( $G''$ ), complex viscosity  $|\eta^*|$  and  $\tan\delta$  (linear polystyrene with  $M_w = 105$  kg/mol,  $T_{ref} = 160$  °C). ....48

**Figure 4.7:** (a) Interaction between a spinning nucleus and an external magnetic field  $\vec{B}_0$  and precession of nuclear magnetic moments  $\mu$ . The axis set shows xyz-planes (Keeler 2010). (b) The energy splitting as a function an external magnetic field  $\vec{B}_0$  for nucleus with the magnetic nuclear spin quantum number  $\hat{I}_z = \frac{1}{2}$  (Keeler 2010). This interaction is called Zeeman interaction. .... 53

**Figure 4.8:** Illustration of (a) a rapidly dephasing signal as a result of short  $T_2^*$ . Fourier transform (FT) of this spectrum gives a broad frequency-domain signal. (b) The dephasing speed is slower than the example in Figure 4.8a due to longer  $T_2^*$  and hence, result in a narrower frequency-domain peak. (c) The slowly dephasing signal with long  $T_2^*$  and sharp frequency-domain signal. .... 57

**Figure 4.9:** (a) Representation of a  $90^\circ$  pulse and the resulting free induction decay (FID). (b) The Hahn echo is depicted for measuring the  $T_2^*$  relaxation via variation of  $\tau$ . .... 60

**Figure 4.10:** (a) Illustration of Carr-Purcell-Meiboom-Gill (CPMG) pulse sequence that is used to derive the full  $T_2^*$  relaxation in shorter experimental time compare to Hahn echo. (b) The magic-sandwich echo (MSE) pulse sequence is represented. That provides fast refocusing on decaying signals for solid materials. .... 60

**Figure 4.11:** (a) The inverse recovery pulse sequences and (b) the saturation recovery sequence for measuring the longitudinal relaxation. .... 62

**Figure 4.12:** Illustration plots of signal intensity as a function of delay time  $\tau$  (a) for the inverse recovery pulse sequences and (b) for the saturation recovery sequence for measuring the longitudinal relaxation. .... 62

**Figure 4.13:** A typical DSC thermogram of an HDPE sample shows the heat flow rate as a function of the temperature to determine the  $T_C$ , the  $T_m$  of HDPE. The enthalpy of fusion is calculated by the integration of the melting peak, and it is used to calculate the crystallinity of the HDPE sample. The heat of fusion of the 100% perfect crystalline PE is  $H_{f,100} = 293 \text{ J/g}$  (Wunderlich 1990). .... 64

**Figure 4.14:** (a) DSC thermogram of an isothermal crystallization experiment of HDPE with 1 wt% NA content (1.0% NA) at  $T_C = 123 \text{ }^\circ\text{C}$  (circle sign) after cooling from  $180 \text{ }^\circ\text{C}$  with a cooling rate of  $17 \text{ }^\circ\text{C/min}$ . The red-colored dotted line is the extrapolated line of the crystallization beginning. The solid line is the baseline of the peak. The crossover point of the baseline and red-colored dotted line indicates the crystallization induction time  $t_i$ . This approach was used by Choupin *et al.* 2017. (b) The relative mass crystallinity

as a function of time at  $T_C = 123$  °C for sample called 1.0% NA. The Avrami model (see Equation 3.47) is fitted up to half of the final crystallinity. ....64

**Figure 4.15:** Schematic representation of the diffraction of incident X-rays by regularly spaced atomic planes (Weidenthaler 2011).....65

**Figure 4.16:** (a) The XRD patterns of the HDPE sample at 25 and 180 °C. The two distinct reflection peaks (blue line) indicate (110) and (200) planes related to the orthorhombic crystal structure of PE at 25 °C. The broad peak (dash black line) shows the fully molten structure of PE. (b) The XRD diffractogram of the HDPE sample at 25 °C and the calculation of the  $X_C$  (%) by the proportion of the integrated total area ( $I_T$ ) and the integrated amorphous area ( $I_A$ ), which is the area below (dash black line) broad peak. ....66

**Figure 5.1:** Schematic overview of used Halbach magnet with the NMR probe of the RheoNMR setup and the rheometry counterparts. Adapted from Ratzsch *et al.* (2017).70

**Figure 5.2 :** (a) Drawing and the photo of the machinable ceramic cone geometry for rheometer which has 13 mm diameter and 86.50 mm length. It has holes for fast thermal stabilization. (b) Illustration of the probe coil (length 21 mm  $N = 7$  turn) is in a glass tube with an inner diameter of 17.2 mm. Adapted from Ratzsch *et al.* (2017).....70

**Figure 5.3:** (a) Photo of the lower geometry, that is surrounded by a heating coil. Nitrogen gas is blown from the bottom holes. The thermocouple measures the temperature of the sample chamber. (b) Dewar is used to insulating the magnet to avoid frequency drifts due to changes in the temperature of the magnet. ....71

**Figure 5.4:** (a) Illustration and (b) a photograph of the RheoNMR setup taken from Ratzsch *et al.* 2017. The BVT unit is the temperature controller. ....71

**Figure 5.5:** Schematic illustration of the general temperature protocol that is applied for all RheoNMR and DSC isothermal crystallization experiments. The melt temperature  $T_{iso-melt}$  was chosen as 180 °C in order to remove the thermal and shear memory. Cooling was divided into two regions as cooling and critical cooling. A similar temperature protocol was also used by Mursalin *et al.* (2016) for fat crystallization. ....73

**Figure 5.6:** (a) The  $I_{CPMG}$  echoes as a function of  $t_{NMR}$ , (b) the back extrapolated intensity  $I_{CPMG}$  values at  $t_{NMR} = 0$  ms as a function of  $t_{exp}$  and (c) the time evolution of  $X_C$  for an isothermal crystallization of HDPE at  $T_C = 124$  °C. ....74

<b>Figure 5.7:</b> Illustrated inside view of RheoNMR setup from the top shows that (a) the pieces with inner diameter and distance in between pieces and (b) the measured temperature gradient in the sample chamber which causes temperature inhomogeneity across sample volume. ....	76
<b>Figure 5.8:</b> The designed and plotted vortex creator by Karl-Friedrich Ratzsch. Dimensions are in mm size. ....	76
<b>Figure 5.9:</b> Photograph of the special upper geometry with the connected thermocouple. ....	77
<b>Figure 5.10:</b> The recorded temperature change as a function of time during cooling (a) with and without temperature ramp ( $\Delta T/\Delta t$ ) which were set to the BVT unit. (b) The cooling trend for reassembled setup to $T_C = 124$ °C under a 50 °C/min temperature ramp (blue circle sign), and compared with further cooling test $T_C = 122$ °C under a 50 °C/min temperature ramp (dark square sign). This difference in the cooling trend was due to the different thermocouple positions (see Figure 5.12). ....	79
<b>Figure 5.11:</b> Photograph of the BVT connected thermocouple which was changed by put vortex creator on the heating resistor. ....	80
<b>Figure 5.12:</b> The designed fixed thermocouple to outer to the glass tube which holds the probe coil. The design and the plot of it were done by Karl-Friedrich Ratzsch. ....	80
<b>Figure 5.13:</b> The temperature change during the time in the BVT unit and the thermometer. The BVT thermocouple was positioned at the outer part of the glass tube which holds probe coils (see Figure 5.12). The thermocouple of the thermometer was placed inside of the special upper geometry as touching the sample from the center. Cooling was divided into two regions with rates of cooling = 17 °C/min and critical cooling = ~4 °C/min. ....	80
<b>Figure 5.14:</b> (a) Consecutively repeated two RheoNMR experiments with an HDPE sample which contents 0.1 wt% NA (0.1% NA) and then, the setup sample was taken out from the top of the setup without disassembling all setup. The experiment was repeated under the same conditions such as $T_C = 122$ °C, $\omega_1 = 1$ rad/s, $\gamma_0 = 1\%$ with loaded fresh sample (0.1% NA). (b) Repeated experiment results in Figure 5.14a displayed with an error bar and ultimately certainty was calculated as ~90% for the RheoNMR method at the time of gelation $t_{gel}$ ( $G' = G''$ ) for moduli and $X_{gel}$ , and also at the final value of the moduli $G'_\infty$ and crystallinity $X_C^\infty$ under no disassembled setup conditions. ....	82

**Figure 6.1:** Simultaneous measurement of low-field RheoNMR data on the isothermal crystallization of 0% NA (neat HDPE) sample. (a) The dynamic moduli ( $G'$  and  $G''$ ), and (b) crystallinity ( $X_C$ ) evolution as a function of time at different crystallization temperatures  $T_C$ . .....88

**Figure 6.2:** (a) The time zero  $t_0$ , the time of the beginning of the crystallization, results of in Avrami model as a variable parameter. (b) Chosen  $t_0$  effects on calculated Avrami rate parameter  $K$  and the exponent  $n$ . The resulting  $t_0$  for  $T_C = 124.5$  °C was a negative value that was obviously a defect. Equivalent fit parameters were determined for  $t_0$  to 400 and 450 seconds. The needed time to reach  $T_C$  was 400 seconds in our study regarding  $T_C$  range. ....90

**Figure 6.3:** (a) Normalized  $G'_{norm}$  determined by the Rheo part of the RheoNMR, and (b) relative crystallinity ( $X_C/X_C^\infty$ ) evolution as a function of time as monitored by the DSC during isothermal crystallization at different crystallization temperatures  $T_C$  for neat HDPE sample called 0% NA. ....90

**Figure 6.4:** Comparison of calculated the Avrami rate parameter  $K$  and the exponent  $n$  depending on the  $T_C$  based on the isothermal crystallization data collected by NMR (see Figure 6.1b) and Rheo part (see Figure 6.3a) of RheoNMR and DSC (see Figure 6.3b) for 0% NA. ....91

**Figure 6.5:** The Foubert model (see Chapter 7) applied (red line) to complete crystallization curves of 0% NA. (a) The crystallinity  $X_C$  determined by NMR part, and (b) the normalized  $G'_{norm}$  monitored via the Rheo part of the RheoNMR. (c) The relative crystallinity ( $X_C/X_C^\infty$ ) development by time were determined via DSC. (d) Quantified kinetic parameters by the Foubert model. Parameters-  $m$ : exponent and  $v$ : rate constant. ....93

**Figure 6.6:** Comparison of calculated the activation energy of crystallization  $E_C$  values from the linear regression of the Avrami rate parameter  $\ln K$  versus inverse  $T_C$  from the obtained temperature dependency results of 0% NA via Rheo and NMR part of RheoNMR and DSC methods. ....94

**Figure 6.7:** Direct correlation of the time of crystallization  $t_{0.2}$  at  $X_C = 0.2$  and the absolute crystallinity value  $X_{C, gel}$  at the crossover time  $t_{gel}$  with  $t_{gel}$  for different  $T_C$  assays of 0% NA by RheoNMR. The required time needed to reach  $T_C$  ( $t_0 = 6.7$  min) was removed for plotting Figure 6.6. ....95

<b>Figure 6.8:</b> Loss tangent $\tan(\delta)$ and relative third harmonic ( $I_3/I_1$ ), reflects nonlinearity, as a function of (a) crystallinity $X_C$ and (b) time for the different $T_C$ isothermal crystallization RheoNMR assays of 0% NA. The required time for cooling $t_0 = 6.7$ min was removed for plotting Figure 6.8b.....	95
<b>Figure 6.9:</b> (a) Correlation of dynamic moduli ( $G'$ , $G''$ ) and crystallinity $X_C$ and (b) vice versa.....	96
<b>Figure 6.10:</b> Correlation among the reduced storage modulus $\frac{G'}{G_0}$ and crystallinity $X_C$ for different $T_C$ . Suspension models describe the plot up to $X_C = 20\%$ (a) Einstein, extended Einstein (Equation 6.2), power-law, Batchelor-Green (see Table 6.2). (b) Tried other suspension models that did not describe the correlated plot: Einstein, Krieger-Dougherty, Quemada, Modified Eilers, Money (see Table 8.3).....	97
<b>Figure 6.11:</b> The results of thermogravimetric analysis (TGA) for commercial HDPE (0% NA), PE-1, and PE-2.....	99
<b>Figure 6.12:</b> (a)-(b) The dynamic moduli ( $G'$ and $G''$ ), and (e)-(f) crystallinity ( $X_C$ ) evolution as a function of time for varying $T_C$ for PE-1, PE-2. (c)-(d) Normalized $G'_{norm}$ (see Equation 6.1) during isothermal crystallization of PE-1 and PE-2. Results were monitored by RheoNMR. ....	100
<b>Figure 6.13:</b> Comparison of extracted (a) Avrami rate parameter $K$ , (b) Foubert rate parameter $\nu$ and (c) the Avrami exponent $n$ as a function of the $T_C$ based on the $X_C$ data determined by the NMR and the $G'_{norm}$ monitored by Rheo part of RheoNMR.....	101
<b>Figure 6.14:</b> (a) Direct correlation of half time of crystallization $t_{1/2}$ and $t_{gel}$ for varying $T_C$ . (b) The crystallinity value $X_{C,gel}$ at the $t_{gel}$ as a function of the $T_C$ for the RheoNMR isothermal crystallization of synthesized PE samples. ....	101
<b>Figure 6.15:</b> The dynamic moduli ( $G'$ and $G''$ ) evolution as a function of time at varying $T_C$ for (a) 0% NA (neat HDPE) and HDPE/NA blend samples as (b) 0.1% NA, (c) 0.3% NA, (d) 0.5% NA, (e) 1% NA, and (f) 3% NA. ....	103
<b>Figure 6.16:</b> The crystallinity ( $X_C$ ) evolution as a function of time at different $T_C$ for (a) 0% NA (neat HDPE) and HDPE/NA blend samples as (b) 0.1% NA, (c) 0.3% NA, (d) 0.5% NA, (e) 1% NA, and (f) 3% NA. ....	104
<b>Figure 6.17:</b> Normalized storage modulus ( $G'_{norm}$ ) evolution as a function of time at varying $T_C$ for (a) 0% NA (neat HDPE) and HDPE/NA blend samples as (b) 0.1% NA, (c) 0.3% NA, (d) 0.5% NA, (e) 1% NA, and (f) 3% NA.....	105

**Figure 6.18:** The relative crystallinity ( $X_C/X_C^\infty$ ) development as a function of time determined by the DSC measurement at varying  $T_C$  for (a) 0% HDPE (neat HDPE) and HDPE/NA blend samples as (b) 0.1% NA, (c) 0.3% NA, (d) 0.5% NA, (e) 1% NA, and (f) 3% NA..... 106

**Figure 6.19:** Rate parameters for neat HDPE and HDPE/NA blends by Avrami model from the data of (a) Rheo and (b) NMR part of RheoNMR method and additionally (c) DSC method. Calculated the overall crystallization rate parameter via the Foubert model fitting to the data of (d) Rheo and (e) NMR part of the RheoNMR and (f) DSC method. The scale of y ax in Figure 6.19d is different than others. Parameters-  $K$ : Avrami rate and  $v$ : Fobert rate constant..... 107

**Figure 6.20:** Comparison of the calculated Avrami exponent  $n$  based on (a) Rheo and (b) NMR part of RheoNMR, and (c) DSC data at varying  $T_C$  for 0%NA and HDPE/NA blends. .... 107

**Figure 6.21:** Comparison of the deduced the activation energy of crystallization ( $E_C$ ) values for the primary crystallization based on the data of Rheo, NMR and DSC method as a function of NA content in HDPE/NA blends..... 109

**Figure 6.22:** Direct correlation of the time of crystallization  $t_{0.2}$  at  $X_C = 0.2$  with  $t_{gel}$  for varying  $T_C$  in between 123 and 124.5 °C assays of RheoNMR for 0% NA and HDPE/NA blends. .... 109

**Figure 6.23:** (a) The relative intensity of third harmonic  $I_{3/1}$  change by  $X_C$  evolution of 0% NA and HDPE/NA blends. (b) The peak maximum of the  $I_{3/1}$  as a function of the  $t_{\tan(\delta)} = t_{gel}$  for varying  $T_C$  results of 0% NA and HDPE/NA blends..... 110

**Figure 6.24:** Correlation among the reduced storage modulus  $\frac{G'}{G'_0}$  and crystallinity  $X_C$  at  $T_C = 123$  °C for neat HDPE and HDPE/NA blends and fitted suspension models up to  $X_C = 20\%$  as follows: Einstein, extended Einstein (Equation 6.2), power-law, Batchelor-Green (see Table 6.2). (b) A closer look of Figure 6.23a..... 111

**Figure 6.25:** Temperature-dependent isothermal crystallization experiments of HDPE. Simultaneously monitored (a) dynamic moduli ( $G'$  and  $G''$ ) with the relative intensity of third harmonic  $I_{3/1}$  and (b) the crystallinity  $X_C$  development by time measured by RheoNMR. Kinetic analyses were done by using Avrami and Foubert model represented red and black lines, respectively..... 113

**Figure 6.26:** Applied steady shear effects on (a) the storage modulus  $G'$  with the relative intensity of third harmonic  $I_{3/1}$ , and (b) the crystallinity  $X_C$  of HDPE at  $T_C = 122$  °C. Kinetic analyses were done by using Avrami and Foubert model represented red and black lines, respectively. The named  $2\text{ s}^{-1}$ ,  $11\text{ s}^*$  steady shear experiment was applied during cooling at 2<sup>nd</sup> min of the experiment, while the rest of the steady shear was applied at the beginning of the experiment. .... 114

**Figure 6.27:** (a) Applied steady shear effect on the normalized storage modulus  $G'_{\text{norm}}$  at  $122$  °C. The named  $2\text{ s}^{-1}$ ,  $11\text{ s}^*$  steady shear experiment was applied during cooling at 2<sup>nd</sup> min of the experiment, while the rest of the steady shear was applied at the beginning of the experiment. (b) The temperature-dependent results of the  $G'_{\text{norm}}$ . .... 114

**Figure 6.28:** Fit parameters by using the Avrami and Foubert model to the  $G'_{\text{norm}}$  data determined by rheometer (Rheo) and the  $X_C$  data monitored via NMR (a) rate parameters  $K$  and  $\nu$ , (b) Avrami exponent  $n$  for applied steady shear; and (c) rate parameters  $K$  and  $\nu$ , (d) Avrami exponent  $n$  for varying  $T_C$  measurements. .... 115

**Figure 6.29:** (a) The relationship between the time of crystallization  $t_{0.1}$  at  $X_C = 0.1$  and  $t_{\text{gel}}$  for varying  $T_C$  and applied steady shear at the constant  $T_C$  assays. (b) The peak maximum of the  $I_{3/1}$  as a function of  $t_{\text{tan}(\delta)} = t_{\text{gel}}$  for varying  $T_C$  and applied steady shear at the constant  $T_C$  experiments. .... 116

**Figure 6.30:** Correlation between the  $\frac{G'}{G'_0}$  and the  $X_C$  with modelling by using the suspension models up to  $X_C = 10\%$ : extended Einstein (Equation 6.2) and power-law (see Table 6.4) (a) for steady shear experiments at  $T_C = 122$  °C, and (b) for temperature-dependent experiments of HDPE. .... 116

**Figure 6.31:** (a) The  $G'$  with the  $I_{3/1}$ , (b) the  $X_C$  evolution, and also (c) the  $G'_{\text{norm}}$  as a function of time for strain-induced crystallization. The Avrami model was fitted to  $X_C$  curves up to  $X_C = 0.2$  and up to half of the  $G'_{\text{norm}}$  curves. (e) Direct correlation of the time of crystallization  $t_{0.2}$  at  $X_C = 0.2$  and the crystallinity at gel point  $X_{C,\text{gel}}$  as a function of the  $t_{\text{gel}}$  for strain induced crystallization of 1% NA sample. .... 118

**Figure 6.32:** Correlation between the  $\frac{G'}{G'_0}$  and the  $X_C$  of 1% NA sample at  $T_C = 124$  °C for strain-induced crystallization. The used models for modeling: extended Einstein and power-law models. .... 119

**Figure 6.33:** The  $G'$  and  $G''$  evolution as a function of time for strain-induced crystallization of (a) 0% NA (neat HDPE) and HDPE/NA blend samples as (b) 0.1% NA,

(c) 0.3% NA, (d) 0.5% NA, (e) 1% NA, and (f) 3% NA. The slippage was indicated with a grey color..... 121

**Figure 6.34:** The  $X_C$  development as a function of time for strain-induced crystallization (a) 0% NA, (b) 0.1% NA, (c) 0.3% NA, (d) 0.5% NA, (e) 1% NA, and (f) 3% NA... 122

**Figure 6.35:** The  $G'_{norm}$  development as a function of time for strain-induced crystallization (a) 0% NA and HDPE/NA blend samples as (b) 0.1% NA, (c) 0.3% NA, (d) 0.5% NA, (e) 1% NA, and (f) 3% NA..... 123

**Figure 6.36:** Avrami rate ( $K$ ) parameters for neat HDPE and HDPE/NA blends from the data of (a) Rheo ( $K_{Rheo}$ ) and (b) NMR part ( $K_{NMR}$ ). The deduced Avrami exponent  $n$  from the data of (a) the Rheo part ( $n_{Rheo}$ ), and (b) NMR part ( $n_{NMR}$ ), of RheoNMR method. .... 124

**Figure 6.37:** Foubert model rate ( $v$ ) parameter by fitting complete crystallization curves of neat HDPE and HDPE/NA blends from the data of (a) Rheo part ( $v_{Rheo}$ ) and (b) NMR part ( $v_{NMR}$ ) of the RheoNMR. .... 125

**Figure 6.38:** Foubert exponent ( $m_{NMR}$ ) for neat HDPE and HDPE/NA blends from the data of the NMR part of the RheoNMR..... 125

**Figure 6.39:** The  $I_{3/1}$  change as a function of the  $X_C$  for strain-induced crystallization (a) 0% NA, (b) 0.1% NA, (c) 0.3% NA, (d) 0.5% NA, (e) 1% NA, and (f) 3% NA. .... 126

**Figure 6.40:** Direct correlation of (a) the time of crystallization  $t_{0.2}$  at  $X_C = 0.2$  with  $t_{gel}$  and (b) the relationship between the  $X_{C,gel}$  and  $t_{gel}$  for strain-induced crystallization of HDPE/NA blend samples..... 127

**Figure 6.41:** Correlation between the  $\frac{G'}{G'_0}$  and the  $X_C$  at  $T_C = 124.5$  °C with modeling by using Einstein, extended Einstein, power-law, Batchelor-Green models up to  $X_C = 20\%$  (a) for 0% NA sample and (b) a closer look to Figure 6.40a (c) for 3% NA, (d) a closer look to Figure 6.40c. .... 128

**Figure 6.42:** The XRD patterns of neat HDPE (0% NA) and HDPE/NA samples. Samples were crystallized isothermally at constant  $\omega_1 = 0.5$  rad/s,  $T_C = 124.5$  °C under applied  $\gamma_0 = 1\%$  and  $\gamma_0 = 30\%$  condition via RheoNMR. The peaks indicated an orthorhombic crystal structure (see Figure 3.2) for all samples..... 130

**Figure 6.43:** The calculated domain size from seen two peaks in Figure 6.42a for (a) (110), and (b) (200) planes as a function of NA content (wt%) from the reflection peaks of HDPE/NA samples. Samples were crystallized isothermally at constant  $\omega_1 = 0.5$  rad/s,  $T_C = 124.5$  °C under applied  $\gamma_0 = 1\%$  and  $\gamma_0 = 30\%$  conditions via RheoNMR. .... 131

**Figure 6.44:** (a) The XRD pattern of neat HDPE sample at increasing temperature, and (b) the calculated crystallinity  $X_{C,XRD}$  (%) from the XRD pattern in Figure 6.44a. .... 132

**Figure 6.45:** (a) The calculated crystallinity ( $X_C$ ) from XRD patterns of nucleated and neat HDPE samples as a function of NA content. All samples had a history of RheoNMR experiment at  $\omega_1 = 0.5$  rad/s,  $T_C = 124.5$  °C with applied  $\gamma_0 = 1\%$  and  $\gamma_0 = 30\%$ . Corresponding  $X_C$  results from XRD were compared with DSC analyses on the same samples. (b) The  $X_C$  of HDPE/NA samples under quiescent crystallization as a function of NA content at  $T_C = 124.5$  °C determined by the NMR part of the RheoNMR and the DSC method..... 133

**Figure 6.46:** Polarized optical microscopy (POM) micrograph of banded spherulites of 0% NA (neat HDPE) sample. .... 134

**Figure 6.47:** Polarized optical microscopy (POM) images of 0% NA (neat HDPE) and 1% NA crystallized simultaneously under the same thermal condition by using hot stage which was cooled down from 180 °C to room temperature. .... 135

**Figure 6.48:** SEM micrograph of neat HDPE (0% NA) crystallized under the quiescent condition at 124.5 °C via RheoNMR. Blue square shows the flat-lying lamellae, and the yellow circle indicates the elastically bent C-shaped lamella..... 135

**Figure 6.49:** SEM images of etched neat HDPE and HDPE/NA samples were taken after RheoNMR isothermal crystallization experiment at  $\gamma_0 = 1\%$  and separately  $\gamma_0 = 30\%$  with constant  $\omega_1 = 0.5$  rad/s,  $T_C = 124.5$  °C..... 136

**Figure 6.50:** Corresponding fast Fourier transforms (FFTs) of the SEM images shown in Figure 6.49. .... 137

**Figure 6.51:** Schematic description of the structure alignment analysis on the FFT image by using ImageJ software (NIH, <http://rsb.info.nih.gov/ij>) oval profile plug-in, authored by William O’Connell. (a) Fast Fourier transform of the SEM images of HDPE sample, (b) chosen oval profile for analysis, (c) circular projection on the FFT output image, (d) conducting a radial summation of the pixel intensities ( $I$ ) for each degree between 0° and 180°, and (e) Normalized intensity as a function of the degree..... 138

**Figure 6.52:** Analysis of structure alignment using ImageJ software oval profile plug-in (authored by William O’Connell) on FFT images for a graphical depiction of Figure 6.49 samples which were taken after RheoNMR experiment at constant  $\omega_1 = 0.5$  rad/s,  $T_C = 124.5$  °C for (a) quiescent ( $\gamma_0 = 1\%$ ) and (b) strain-induced ( $\gamma_0 = 30\%$ ) crystallization conditions..... 139

**Figure 6.53:** SEM micrographs of the etched 1% NA sample which crystallized under constant  $\omega_1 = 0.5$  rad/s,  $T_C = 124$  °C (a) for applied short term large strain amplitude as  $\gamma_0 = 100\%$  during 60 s, and (b) for applied steady shear with a shear rate  $\dot{\gamma} = 4$  s<sup>-1</sup> during 22 s. The steady shear was applied at the beginning of the experiment. The short term large strain amplitude was applied at the 5<sup>th</sup> min of the experiment (see Chapter 6.4.2) Corresponding FFTs are displayed at the down left corner on the SEM images..... 139

**Figure 6.54:** The SEM image of the PE-1 (see Chapter 6.3.2) quiescently crystallized. .... 141

**Figure 7.1:** Schematic representation of structural levels in fat crystal network and their influence on macroscopic properties. The schema was developed by Marangoni and Narine (1999, 2002; Marangoni 2005). Polymorphism: the existence of more than one crystalline form or structural arrangement. Polytypism: a special kind of polymorphism occurs in the number and the manner of stacking layers in the crystal unit cell..... 145

**Figure 7.2:** Isothermal crystallization profiles of coconut fat at  $\omega_1 = 10$  rad/s for varying  $T_C$  with applied  $\gamma_0 = 0.005\%$ . (a) The time evolution of  $G'(\omega_1)$  and  $G''(\omega_1)$  from the Rheo part and (b)  $G'(\omega_1)$  and simultaneously monitored the  $X_C$  via the NMR part of the RheoNMR as a function of time. .... 147

**Figure 7.3:** Simultaneously monitored the  $G'$  and the  $X_C$  from isothermal crystallization of coconut fat under imposed various  $\gamma_0$  with the  $\omega_1 = 10$  rad/s (a) at the  $T_C = 9$  °C, and (b) at the  $T_C = 14$  °C. .... 148

**Figure 7.4:** Visual comparison of fitted models the Avrami, modified Gompertz and Foubert to the relative crystallinity  $X_C / X_C^\infty$  curves as a function of time during isothermal crystallization of coconut fat at  $\omega_1 = 10$  rad/s. (a) Temperature dependent experiments at a constant  $\gamma_0 = 0.005\%$ . Strain-induced crystallization (b) at the  $T_C = 9$  °C and (c) at the  $T_C = 14$  °C. Avrami model (see Equation 3.47) was fitted up to  $X_C / X_C^\infty = 0.50$  and shown as red line. The modified Gompertz and Foubert models can be seen as purple dot lines and black dash lines respectively. .... 150

**Figure 7.5:** Kinetic parameters (a), (c) and (e) for the temperature-dependent experiments; and (b), (d) and (f) for the strain-induced crystallization experiment with

varying  $\gamma_0$ . Parameters-  $n$ : Avrami exponent,  $K$ : Avrami rate constant,  $\mu$ : modified Gompertz the maximum increase rate parameter,  $v$ : Foubert rate constant,  $\lambda$ : modified Gompertz induction time,  $t_{\text{indx}}$ : Foubert model induction time..... 151

**Figure 7.6:** Correlation between  $\ln(G')$  and  $\ln(\frac{X_C(t)}{X_C^\infty})$  (a) for varying the  $T_C$  at constant  $\omega = 10$  rad/s and  $\gamma_0 = 0.005\%$ , and strain induced crystallization with varying  $\gamma_0$  at (b)  $T_C = 9$  °C and (c)  $T_C = 14$  °C. Linear fit with a dashed line represented to describe the change in slope in the initial and growth stage of crystallization. .... 154

**Figure 7.7:** Fractal dimension ( $D$ ) of the crystallization of coconut fat (a) for varying  $T_C$  experiments, and (b) for conducted varying  $\gamma_0$  at  $T_C = 9$  °C and  $T_C = 14$  °C. .... 155

**Figure 7.8:** Correlation of the  $G'$  and the  $\frac{X_C(t)}{X_C^\infty}$  for temperature dependent experiments with fitted suspension models up to 50% of the  $\frac{X_C(t)}{X_C^\infty}$  as represented lines: black dot line for Einstein model, black line for extended Einstein, red dash line for Batchelor-Green, green short dot line for power-law models. .... 156

**Figure 7.9:** Correlation of the  $G'$  with the  $\frac{X_C(t)}{X_C^\infty}$  for varying  $\gamma_0$  at (a)  $T_C = 9$  °C, and (b)  $T_C = 14$  °C. with fitted suspension models up to 50% of the  $\frac{X_C(t)}{X_C^\infty}$  as represented lines: black dot line for Einstein model, black line for extended Einstein, red dash line for Batchelor-Green, green short dot line for power-law models. .... 157

**Figure 8.1:** Structures of cellulose and starch..... 160

**Figure 8.2:** The synthesis of starch and amylose based compatibilizer with using sunflower oil (Söyler and Meier 2016). The synthesis was done by Philip Scholten. . 160

**Figure 8.3:** The  $G'$  as a function of the  $\gamma_0$  at 150 °C and  $\omega_1 = 1$  rad/s for the neat LDPE and the composite materials with cellulose (C), (a) modified and non-modified amylose (A) compatibilizer and (b) modified and non-modified starch (S) compatibilizer..... 163

**Figure 8.4:** Time dependency of the  $G'$  at 150 °C with  $\omega_1 = 1$  rad/s in the linear viscoelastic regime for the neat LDPE and the composite samples..... 163

**Figure 8.5:** Time dependency of the  $G'$  at 170 °C with  $\omega_1 = 1$  rad/s in the linear viscoelastic regime for the neat LDPE and the composite samples..... 164

**Figure 8.6:** The  $G'$  as a function of the  $\omega_1$  at  $T_{ref} = 150$  °C was plotted via TTS for neat LDPE and LDPE composites containing 10 wt% cellulose (C10mA/S0) or composites with 10 wt% of (a) modified amylose (mA) or non-modified amylose (A), and (b) modified starch (mS) or non-modified starch (S). ..... 165

**Figure 8.7:** The  $G'$  as a function of the  $\omega_1$  at  $T_{ref} = 150$  °C was plotted via TTS for neat LDPE and LDPE composites containing 10 wt% cellulose (C) with 5-15 wt% of (a) modified amylose (mA), and (b) modified starch (mS). ..... 165

**Figure 8.8:** The  $G'(\omega_1)$  as a function of the  $\omega_1$  at  $T_{ref} = 150$  °C via TTS for neat LDPE and LDPE composites containing 45 wt% cellulose (C) and 10 wt% of (a) modified amylose (mA), and (b) modified starch (mS)..... 166

**Figure 8.9:** The  $\frac{|\eta^*|}{|\eta^*|_0}$  at  $\omega_1 = 0.05$  rad/s as a function of the  $\phi$  correlated to see the impact of (a) containing 10 wt% cellulose with addition of varying modified amylose (mA) (blue close circle) or modified starch (mS) (blue open circle); (b) added varying cellulose (C) concentration to containing 10 wt% mA (red close triangle) or 10 wt% mS (red open triangle) samples. While scatters represent the data, lines indicate the suspension models: Einstein, Batchelor-Green, Mooney, Krieger-Dougherty, Modified Eilers, Quemada models. .... 169

**Figure 9.1:** The schematic representation for the synthesis of the thiol-ene polymer (P1). ..... 173

**Figure 9.2:** The schematic representation of the thiol-ene polymer (P1) and oxidized thiol-ene polymer (P1-O), respectively. To simplify the structure of the respective polymer P1 (see Figure 9.1), it was shown above as subscript “ $_{2n}$ ”..... 173

**Figure 9.3:** The schematic representation of the ADMET polymer (P2) and the hydrogenated ADMET derivative (P2-H). ..... 174

**Figure 9.4:** General reaction scheme for the ROMP of (*cis*)-cyclooctene. \*CTA: chain transfer agent; A.T.: ambient temperature; DCM: dichloromethane. .... 175

**Figure 9.5:** Hydrogenation of ROMP polymer, i.e. polycyclooctene, to obtain HDPE samples P3 and P4. .... 175

**Figure 9.6:** Strain amplitude ( $\gamma_0$ ) dependency tests for the thiol-ene (P1) polymer, oxidized thiol-ene polymer (P1-O), the ADMET polymer (P2), and the hydrogenated ADMET polymer (P2-H) at  $T_m + 30$  °C,  $\omega_1 = 10$  rad/s. .... 177

**Figure 9.7:** Time-dependent tests for the thiol-ene (P1) polymer, oxidized thiol-ene polymer (P1-O), the ADMET polymer (P2), and the hydrogenated ADMET polymer (P2-H) at 150 °C with  $\gamma_0 = 30\%$ ,  $\omega_1 = 10$  rad/s. .... 178

**Figure 9.8:** Frequency-dependent measurements for the thiol-ene (P1) polymer, oxidized thiol-ene polymer (P1-O), the ADMET polymer (P2), hydrogenated ADMET polymer (P2-H), HDPE samples P3, P4, and P5 at  $T_m + 30$  °C,  $\gamma_0 = 30\%$  ..... 178

## List of Tables

<b>Table 2.1:</b> The most common types of initiators (Peacock 2000).....	9
<b>Table 2.2:</b> Properties of different types of polyethylene (Peacock 2000). ....	13
<b>Table 3.1:</b> The relation between n and nucleation mode/crystal growth shape (Sperling 2006).....	33
<b>Table 4.1:</b> The NMR properties of some nuclei (Bovey and Mirau 1996). ....	52
<b>Table 5.1:</b> Thermocouple temperatures of the BVT controller of RheoNMR and thermometer in the center of upper geometry under constant gas flow and gas pressure. ....	77
<b>Table 6.1:</b> Preparation conditions for the HDPE with NA.....	86
<b>Table 6.2:</b> Results of the fitted models in Figure 6.10a.....	97
<b>Table 6.3:</b> Results of the fitted models in Figure 6.24a.....	111
<b>Table 6.4:</b> Extracted fit results from the fitted models in Figure 6.30. ....	117
<b>Table 6.5:</b> Kinetic parameters for strain-induced experiments. ....	119
<b>Table 6.6:</b> Extracted fit results from the fitted models in Figure 6.33. ....	120
<b>Table 6.7:</b> Results of the fitted models in Figure 6.41. ....	129
<b>Table 7.1:</b> Calculated model parameters by fitting data up to 50% of the $\frac{X_C(t)}{X_C^\infty}$ .....	157
<b>Table 8.1:</b> Composition of the composites in wt % of a total of 5 g of sample .....	162
<b>Table 8.2:</b> Suspension models for absolute viscosity as a function of filler concentration. ....	168
<b>Table 9.1:</b> Sample code and their characteristics as $M_w$ , $D$ and $T_m$ . ....	176
<b>Table 9.2:</b> Sample code, and their respective $\eta_0$ and $E_a$ values. ....	180

## References

- Abdul Khalil, H. P. S., Bhat, A. H. and Ireana Yusra, A. F. (2012), Green composites from sustainable cellulose nanofibrils: A review. *Carbohydrate Polymers* **87**:963-979.
- Ahirwal, D., Palza, H., Schlatter, G. and Wilhelm, M. (2014), New way to characterize the percolation threshold of polyethylene and carbon nanotube polymer composites using Fourier transform (FT) rheology. *Korea-Australia Rheology Journal* **26**(3):319-326.
- Alfonso, G. C. and Ziabicki, A. (1995), Memory effects in isothermal crystallization II. Isotactic polypropylene. *Colloid Polymer Science* **273**:317-323.
- Alidadi-Shamsabadi, M., Behzad, T., Bagheri, R. and Nari-Nasrabadi, B. (2015), Preparation and characterization of low-density polyethylene thermoplastic starch composites reinforced by cellulose nanofibers. *Polymer Composites* **36**(12):2309–16.
- Alvarez, V. A. and Perez, C. J. (2013), Gamma irradiated LDPE in presence of oxygen. Part I. Non-isothermal crystallization. *Thermochimica Acta* **570**:64-73.
- Ancharova, U. V., Mikhailenko, M. A., Sharafutdinov, M. R., Tolochko, B. P., Nazmov, V. P., Korobeynikov, M. V. and Bryazgin, A. A. (2016), Structure investigations of radiation-modified polymers polyethylene and polymethylmethacrylate. *Physics Procedia* **84**:360-365.
- Androsch, R., Di Lorenzo, M. L., Schick, C. and Wunderlich, B. (2010), Mesophases in polyethylene, polypropylene, and poly(1-Butene). *Polymer* **51**(21):4639–62.
- Auriemma, F., Alfonso, G. C. and De Rosa, C. (2017), *Polymer crystallization II, from chain microstructure to processing*. Springer.
- Avrami, M. (1939), Kinetics of phase change. I general theory, *Journal of Chemical Physics* **7**(12):1103-1112.
- Avrami, M. (1940), Kinetics of phase change. II transformation—time relations for random distribution of nuclei. *Journal of Chemical Physics* **8**(2):212-224.
- Banks, W., and Sharples, A. (1963), The AVRAMI equation in polymer crystallization. *Macromolecular Chemistry and Physics* **59**(1):233-236.
- Bashir, Z., Odell, J. A. and Keller, A. (1986), Stiff and strong polyethylene with shish kebab morphology by continuous melt extrusion. *Journal of Material Science* **21**:3993-4002.
- Batchelor, G. K., and Green, J. T. (1972) The determination of the bulk stress in a suspension of spherical particles to order  $c^2$ . *Journal of Fluid Mechanics* **56**(3):401–427.

- Beck, H. N. (1967), Heterogeneous nucleating agents for polypropylene crystallization, *Journal of Applied Polymer Science*, **11**:673-685.
- Bergenholtz, J., Brady, J. F. and Vicic, M. (2002), The non-Newtonian rheology of dilute colloidal suspensions. *Journal of Fluid Mechanics*, **456**:239-275.
- Binsbergen, F. L. (1977), Natural and artificial heterogeneous nucleation in polymer crystallization. *Journal of Polymer Science: Polymer Symposia* **59**(1):11-29.
- Blaine, R. L. (2008), Isothermal crystallization using the Q series™ DSC and liquid nitrogen cooling system. *TA Application Notes*.
- Bloch, F. (1946), Nuclear induction. *Physical Review* **70**:460-473.
- Bloch, F., Hansen, W. W. and Packard, M. (1946), The nuclear induction experiment. *Physical Review* **70**:474-485.
- Bloembergen, N., Purcell, E. M. and Pound, R. V. (1948), Relaxation effects in nuclear magnetic resonance absorption. *Physical Review* **73**(7):679-712.
- Bovey, F. A., and Mirau, P. A. (1996) *NMR of polymers*. Academic Press.
- Bower, D. I. (2002). *An introduction to polymer physics*. Cambridge University Press.
- Bremer, L. G. B. (1992), *Fractal aggregation in relation to formation and properties of particle gels*. (Doctoral dissertation). Retrieved from <https://edepot.wur.nl/201301>
- Bremer, L. G. B., van Vliet, T. and Walstra, P. (1989), Theoretical and experimental study of the fractal nature of the structure of casein gels. *Journal of the Chemical Society, Faraday Transactions 1: Physical Chemistry in Condensed Phases* **85**(10):3359-72.
- Bridges, B. J., Charlesby, A. and Folland, R. (1979), Pulsed NMR Studies of the crystallization kinetics of polyethylene from the melt and solution. *Proceedings of the Royal Society of London A* **367**:343-351.
- Brox, T. I., Douglass, B., Galvosas, P. and Brown, J. R. (2016), Observations of the influence of Taylor-Couette geometry on the onset of shear-banding in surfactant wormlike micelles. *Journal of Rheology* **60**(5):973-982.
- Bunn, C. W. (1939), The crystal structures of the long chain normal paraffin hydrocarbons. The “shape” of the >CH<sub>2</sub> group. *Transactions of the Faraday Society* **35**:482-491.
- Callaghan, P. T. (2007), Rheo-NMR. *Modern Magnetic Resonance Part 1: Applications in chemistry, biological and marine Sciences*, Edited by G. A. Web, Springer, pp. 379-384.

- Callaghan, P. T. (2002), Rheo-NMR: A new window on the rheology of complex fluids. *Encyclopedia of nuclear magnetic resonance, Advances in NMR* Vol. **9**, Edited by D. M. Grant and R. K. Harris, John Wiley and Sons, Hoboken, pp. 737–750.
- Campbell, S. D., Goff, H. D. and Rousseau, D. (2004), Modeling the nucleation and crystallization kinetics of a palm stearin/canola oil blend and lard in bulk and emulsified form. *Journal of the American Oil Chemists' Society* **81**(3):213–219.
- Canet, D., Levy, G. C. and Peat, I. R. (1975), Time saving in  $^{13}\text{C}$  spin-lattice relaxation measurements by inversion-recovery. *Journal of Magnetic Resonance* **18**(1):199–204.
- Carr, H. Y. and Purcell, E. M. (1954), Effects of diffusion on free precession in nuclear magnetic resonance experiments. *Physical Review* **94**(3):630–38.
- Cerdeira, M., Candal, R. J. and Herrera, M. L. (2004), Analytical techniques for nucleation studies in lipids: advantages and disadvantages. *Journal of Food Science* **69**(9):185-191.
- Chaleepa, K., Szepes, A. and Ulrich, J. (2010), Effect of additives on isothermal crystallization kinetics and physical characteristics of coconut Oil. *Chemistry and Physics of Lipids* **163**:390–396.
- Charrondiere, U. R., Haytowitz, D. and Stadlmayr, B. (2012), FAO/INFOODS Density Database Version 2.0 (2012). *Food and Agriculture Organization of the United Nations (FAO)* pp. 1–21.
- Choupin, T., Fayolle, B., Régnier, G., Paris, C., Cinquin, J. and Brulé, B. (2017), Isothermal crystallization kinetic modeling of poly(etherketoneketone) (PEKK) copolymer. *Polymer* **111**:73–82.
- Conley, B. L., Pennington-boggio, M. K., Boz, E. and Williams, T. J. (2010), Discovery, applications, and catalytic mechanisms of Shvo's catalyst. *Chemical Reviews* **110**:2294–2312.
- Coppola, S., Acierno, S., Grizzuti, N. and Vlassopoulos, D. (2006), Viscoelastic behavior of semicrystalline thermoplastic polymers during the early stages of crystallization. *Macromolecules* **39**(4):1507–1514.
- Cwalina, C. D., Harrison, K. J. and Wagner, N. J. (2016), Rheology of cubic particles suspended in a newtonian fluid. *Soft Matter* **12**:4654–4665.
- Czies, M. A., Abbasi, M., Heck, M., Arens, L. and Wilhelm, M. (2016), Effect of molecular weight, polydispersity, and monomer of linear homopolymer melts on the intrinsic mechanical nonlinearity  $^3Q_0(\omega)$  in MAOS. *Macromolecules* **49**:3566-3579.
- Dannecker, P. -K., Biermann, U., Sink, A., Bloesser, F. R., Metzger, J. O. and Meier, M. A. R. (2018), Fatty acid-derived aliphatic long chain polyethers by a combination of

- catalytic ester reduction and ADMET or Thiol-Ene polymerization. *Macromolecular Chemistry and Physics* **220**(4):1–17.
- Dealy, J. M. and Larson, R. G. (2006), *Structure and rheology of molten polymers: from structure to flow behavior and back again*, Hanser.
- DeArmitt, C., and Hancock, M. (2003), Filled thermoplastics. *Particulate-filled polymer composites second edition, in Technology*, Edited by R.N. Rother, Rapra technology, pp. 357-424.
- De Graef, V., Goderis, B., Puyvelde, P. V., Foubert, I. and Dewettinck, K. (2008), Development of a rheological method to characterize palm oil crystallizing under shear, *European Journal of Lipid Science and Technology* **110**:521–29.
- DeMan, J. M. and Beers, A. M. (1987), Fat crystal networks: structure and rheological properties. *Journal of Texture Studies* **18**(4):303–318.
- Dötsch, T., Pollard, M. and Wilhelm, M. (2003), Kinetics of isothermal crystallization in isotactic polypropylene monitored with rheology and Fourier-transform rheology. *Journal of Physics Condensed Matter* **15**(11):923-931.
- Dotson, D. L. (2007), A novel nucleating agent for polyethylene. *Proceedings of the TAPPI PLACE Conference 2007*.
- Dufresne, A. (2017), Cellulose nanomaterial reinforced polymer nanocomposites. *Current Opinion in Colloid and Interface Science* **29**:1–8.
- Eder, G., Janeschitz-Kriegl, H. and Leidauer, S. (1990), Crystallization processes in quiescent and moving polymer melts under heat transfer conditions. *Progress in Polymer Science* **15**:629–714.
- Eder, G. and Janeschitz-Kriegl, H. (1988), Theory of shear-induced crystallization of polymer melts. *Colloid and Polymer Science* **266**(12):1087–1094.
- Eder, G., Janeschitz-Kriegl, H. and Leidauer, S. (1992), Influence of flow on the crystallization kinetics of polymers, *Progress in Colloid and Polymer Science* **87**:129–131.
- Einstein, A. (1906), Eine Neue Bestimmung der Moleküldimension. *Annalen Der Physik* **324**(2):289–306.
- Einstein, A. (1911), Berichtigung Zu Meiner Arbeit: Eine Neue Bestimmung Der Molekül-Dimension. *Annalen Der Physik* **339**(3):591–592.
- Faruk, O., Bledzki, A. K., Fink, H.-P. and Sain, M. (2012), Biocomposites reinforced with natural fibers: 2000-2010. *Progress in Polymer Science* **37**(11):1552–1596.

- Fechete, R., Demco, D. E. and Blümich, B. (2003), Chain orientation and slow dynamics in elastomers by mixed magic-Hahn echo decays. *Journal of Chemical Physics* **118**(5):2411–2421.
- Feng, Y.-H., Zhang, D.-W., Qu, J.-P., He, H.-Z. and Xu, B.-P. (2011), Rheological properties of sisal fiber/poly(butylene succinate) composites. *Polymer Testing* **30**:124–130.
- Ferretti, A., Carreau, P. J. and Gerard, P. (2005), Rheological and mechanical properties of PEO/block copolymer blends. *Polymer Engineering and Science* **45**(10):1385–1394.
- Ferry, J. D. (1980), *Viscoelastic properties of polymers third edition*, Wiley.
- Fetters, L. J., Lohse, D. J., Richter, D., Witten, T. A. and Zirkel, A. (1994), Connection between Polymer Molecular Weight, Density, Chain Dimensions, and Melt Viscoelastic Properties, *Macromolecules* **27**(17):4639–4647.
- Fisher, J. C., Hollomon, J. H. and Turnbull, D. (1948), Nucleation. *Journal of Applied Physics* **19**:775–784.
- Flory, P. J. (1947), Thermodynamics of crystallization in high polymers. I. crystallization induced by stretching. *Journal of Chemical Physics* **15**(6):397–408.
- Foubert, I., Dewettinck, K. and Vanrolleghem, P. A. (2003), Modelling of the Crystallization Kinetics of Fats. *Trends in Food Science and Technology* **14**(3):79–92.
- Foubert, I., Vanrolleghem, P. A., Vanhoutte, B. and Dewettinck, K. (2002), Dynamic mathematical model of the crystallization kinetics of fats. *Food Research International* **35**:945–956.
- Freeman, R. and Hill, H. D. W. (1971), Fourier transform study of NMR spin-lattice relaxation by “progressive saturation”. *Journal of Chemical Physics* **54**(8):3367–3377.
- Freire, C. S. R., Silvestre, A. J. D., Neto, C. P., Gandini, A., Martin, L. and Mondragon, I. (2008), Composites based on acylated cellulose fibers and low-density polyethylene: effect of the fiber content, degree of substitution and fatty acid chain length on final properties. *Composites Science and Technology* **68**(15–16):3358–3364.
- Frenkel, J. (1946), *Kinetic theory of liquids*, Oxford.
- Fuschillo, N., Rhian, E. and Sauer, J. A. (1957), Nuclear magnetic resonance and crystallinity in polyethylene. *Journal of Polymer Science* **25**(110):381–384.
- Gedde, U. W. (1995), *Polymer physics*, Chapman and Hall.
- Gedde, U. W. (1999), *Polymer physics*, Springer.
- Gedde, U. W. and Mattozzi, A. (2004), Polyethylene morphology. *Advances in Polymer Science* **169**:29–73.

- Gedde, U. W. and Hedenqvist, M. S. (2019), *Fundamental polymer science second edition*, Springer.
- Gelfer, M. Y. and Winter, H. H. (1999), Effect of branch distribution on rheology of LLDPE during early stages of crystallization. *Macromolecules* **32**:8974-8981.
- Goodwin, J. W. and Hughes, R. W. (2000), *Rheology for chemists an introduction*, The Royal Society of Chemistry.
- Gullion, T., Baker, D. B. and Concardi, M. S. (1990), New, compensated Carr-Purcell sequences. *Journal of Magnetic Resonance* **89**:479–84.
- Hafner, S., Demco, D. E. and Kimmich, R. (1996), Magic echoes and NMR imaging of solids. *Solid State Nuclear Magnetic Resonance* **6**:275–293.
- Hahn, E. L. (1950), Spin Echoes. *Physical Review* **80**(4):580-594.
- Hardy, E. H., Mertens, D., Hochstein, B. and Nirschl, H. (2006), Compact NMR-based capillary rheometer. *Proceedings of the 5th International Symposium on Food Rheology and Structure* p. 94–97.
- Haris, R. K. (1986), Nuclear Magnetic Resonance Spectroscopy. *Magnetic resonance in chemistry*, Longman Scientific and Technical.
- Hassanabadi, H. M., Wilhelm, M. and Rodrigue, D. (2014), A rheological criterion to determine the percolation threshold in polymer nano-composites. *Rheologica Acta* **53**:869–882.
- Herold, H., Hardy, E. H., Ranft, M., Wassmer, K. H. and Nestle, N. (2013), Online rheo-TD NMR for analysing batch polymerisation processes. *Microporous and Mesoporous Materials* **178**:74–78.
- Hiemenz, P. C. and Lodge, T. P. (2007), *Polymer chemistry second edition*, CRC Press.
- Hill, M. J. and Keller, A. (1969), Direct evidence for distinctive, stress-induced nucleus crystals in the crystallization of oriented polymer melts. *Journal of Macromolecular Science, Part B* **3**(1):153–169.
- Hoffman, K., Huber, G. and Mäder, D. (2001), Nucleating and clarifying agents for polyolefins. *Macromolecular Symposia* **176**:83–91.
- Huang, J.-W., Wen, Y.-L., Kang, C.-C., Tseng, W.-J. and Yeh, M.-Y. (2008), Nonisothermal crystallization of high density polyethylene and nanoscale calcium carbonate composites. *Polymer Engineering and Science* **48**:1268–78.
- Huo, H., Jiang, S., An, L. and Feng, J. (2004), Influence of shear on crystallization behavior of the  $\beta$  phase in isotactic polypropylene with  $\beta$ -nucleating agent. *Macromolecules* **37**:2478–2483.

- Hyun, K., Wilhelm, M., Klein, C. O., Cho, K. S., Nam, J. G., Ahn, K. H., Lee, S. J., Ewoldt, R. H. and McKinley, G. H. (2011), A review of nonlinear oscillatory shear tests: analysis and application of large amplitude oscillatory shear (LAOS). *Progress in Polymer Science* **36**:1697–1753.
- Janeschitz-Kriegl, H. (1992), Polymer solidification by crystallization under heat transfer and flow conditions. *Progress in Colloid and Polymer Science* **87**:117–127.
- Janeschitz-Kriegl, H. and Eder, G. (2007), Shear induced crystallization, a relaxation phenomenon in polymer melts: a re-collection. *Journal of Macromolecular Science, Part B: Physics* **46**:591-601.
- Janeschitz-Kriegl, H., Ratajski, E. and Wippel, H. (1999), The physics of athermal nuclei in polymer crystallization. *Colloid and Polymer Science* **277**:217–226.
- Jerschow, P., and Janeschitz-Kriegl, H. (1997), The role of long molecules and nucleating agents in shear induced crystallization of isotactic polypropylenes. *International Polymer Processing* **12**(1):72–77.
- Jiang, H., Zhang, X. and Qiao, J. (2012), Different influences of nucleating agents on crystallization behavior of polyethylene and polypropylene. *Science China Chemistry* **55**(6):1140-1147.
- Kalaprasad, G., Mathew, G., Pavithran, C. and Thomas, S. (2003), Melt rheological behavior of intimately mixed short sisal–glass hybrid fiber-reinforced low-density polyethylene composites. I. Untreated fibers. *Journal of Applied Polymer Science* **89**:432-442.
- Kawai, T., Matsumoto, T., Kato, M. and Maeda, H. (1968), Crystallization of polyethylene in steady-state flow. *Polymere* **222**(1):1–10.
- Kaynak, B., Spoerk, M., Shirole, A., Ziegler, W. and Sapkota, J. (2018), Polypropylene/cellulose composites for material extrusion additive manufacturing. *Macromolecular Materials and Engineering* **303**(5):1–8.
- Keeler, J. (2010), *Understanding NMR spectroscopy second edition*, Wiley.
- Kellens, M., Meeussen, W. And Reynaers, H. (1990), Crystallization and phase transition studies of tripalmitin. *Chemistry and Physics of Lipids* **55**:163–78.
- Keller, A. (1957), A note on single crystals in polymers: evidence for a folded chain configuration. *Philosophical Magazine: A Journal of Theoretical Experimental and Applied Physics* **2**:1171–1175.
- Keller, A. (1968), Polymer crystals. *Reports on Progress in Physics* **31**:624-699.
- Keller, A., Hikosaka, M., Rastogi, S., Toda, A., Barham, P. J. and Goldbeck-Wood, G. (1994), An approach to the formation and growth of new phases with application to

polymer crystallization: effect of finite size, metastability, and Ostwald's rule of stages. *Journal of Materials Science* **29**(10):2579–2604.

Keller, A. and Mackley, M. R. (1974), Chain orientation and crystallization. *Pure and Applied Chemistry*, **39**(1–2):195–224.

Khanam, P. N. and AlMaadeed, M. A. A. (2015), Processing and characterization of polyethylene-based composites. *Advanced Manufacturing: Polymer and Composites Science* **1**:63–79.

Khanna, Y. P. (1993), Rheological mechanism and overview of nucleated crystallization kinetics. *Macromolecules* **26**:3639–3643.

Kloed, W. (1998), *Mechanical properties of fats in relation to their crystallization* (Doctoral dissertation). Retrieved from <https://library.wur.nl/WebQuery/wurpubs>

Kloek, W., Pieter, W. and van Vliet, T. (2000), Crystallization kinetics of fully hydrogenated palm oil in sunflower oil mixtures. *Journal of the American Oil Chemists' Society* **77**(4):389-398.

Kontopoulou, M. (2012), *Applied polymer rheology: polymeric fluids with industrial applications*. Edited by M. Kontopoulou, John Wiley and Sons.

Kontturi, E., Laaksonen, P., Linder, M. B., Nonappa, Gröschel, A. H., Rojas, O. J. and Ikkala, O. (2018), Advanced materials through assembly of nanocelluloses. *Advanced Materials* **30**:1-39.

Kosher, E. and Fulchiron, R. (2002), Influence of shear on polypropylene crystallization Kinetics. *Polymer* **43**:6931–6942.

Kricheldorf, H. R., Oskar, N. and Swift, G. (2005) *Handbook of polymer synthesis*, Marcel Dekker.

Krieger, I. M. and Dougherty, T. J. (1959), A mechanism for non-newtonian flow in suspensions of rigid spheres. *Transactions of the Society of Rheology* **3**:137–152.

Kristiansen, P. E., Hansen, E. W. and Pedersen, B. (1999), Phase distribution during isothermal crystallization of polyethylene probed by solid-state proton NMR free induction decay. *Journal of Physical Chemistry B* **103**:3552–3558.

Kristiansen, P. E., Hansen, E. W. and Pedersen, B. (2001), Isothermal crystallization of polyethylene monitored by in situ NMR and analyzed within the 'Avrami' model framework. *Polymer* **42**:1969–1980.

Kumaraswamy, G. (2005), Crystallization of polymers from stressed melts. *Journal of Macromolecular Science-Part C: Polymer Reviews* **45**(4):375–397.

- Kurtz, S. M. (2004), *The UHMWPE handbook ultra-high molecular weight polyethylene in total joint replacement*, Elsevier.
- Lagasse, R. R. and Maxwell, B. (1976), An experimental study of the kinetics of polymer crystallization during shear flow. *Polymer Engineering and Science* **16**(3):186–199.
- Lamberti, G., Peters, G. W. M. and Titomanlio, G. (2007), Crystallinity and linear rheological properties of polymers. *International Polymer Processing, the journal of the Polymer Processing Society* **3**:303-310.
- Langford, J. I. and Wilson, A. J. C. (1978), Scherrer after sixty years: a survey and some new results in the determination of crystallite size. *Journal of Applied Crystallography* **11**:102–113.
- Lauritzen, J. I. and Hoffman, J. D. (1960), Theory of formation of polymer crystals with folded chains in dilute solution. *Journal of research of the National Bureau of Standards. Physics and chemistry* **64**(1):73-102.
- Lee, S.-H., Wang, S. and Teramoto, Y. (2008), Isothermal crystallization behavior of hybrid biocomposite consisting of regenerated cellulose fiber, clay, and poly(lactic acid). *Journal of Applied Polymer Science* **116**: 2658-2667.
- Li, S. X., Zhao, J., Lu, P. and Xie, Y. (2010), Maximum packing densities of basic 3D objects. *Chinese Science Bulletin* **55**(2):114–119.
- Li, X., Tabil, L. G. and Panigrahi, S. (2007), Chemical treatments of natural fiber for use in natural fiber-reinforced composites: a review. *Journal of Polymers and the Environment* **15**(1):25–33.
- Lligadas, G., Ronda, J. C., Galià, M. and Cádiz, V. (2007), Poly(ether urethane) networks from renewable resources as candidate biomaterials: synthesis and characterization. *Biomacromolecules* **8**:686–92.
- Lorenzo, A. T., Arnal, M. L., Albuérne, J. and Müller, A. J. (2007), DSC isothermal polymer crystallization kinetics measurements and the use of the Avrami Equation to fit the data: guidelines to avoid common problems. *Polymer Testing* **26**:222-231.
- Luft, G., Kämpf, R. and Seidl, H. (1982), Synthesis conditions and structure of low density polyethylene I. short and long chain branching. *Macromolecular Materials and Engineering* **108**(1):203-217.
- Mackley, M. R. (1975), Shish kebabs an experimental preparation. *Colloid and Polymer Science* **253**(3):261–263.
- Mackley, M. R., Frank, F. C. and Keller, A. (1975), Flow induced crystallization of polyethylene melts. *Journal of Materials Science* **10**:1501–1509.
- Macosko, C. W. (1994), *Rheology: principles, measurements, and applications*, Wiley.

- Mandelkern, L. (1985), The relation between structure and properties of crystalline polymers. *Polymer Journal* **17**(1):337-349.
- Mandelkern, L. (2004a) *Crystallization of polymers second edition volume 2 kinetics and mechanisms*, Cambridge University Press.
- Mandelkern, L. (2004b), Crystallization kinetics of homopolymers: overall crystallization: a review. *Biophysical Chemistry* **112**:109-116.
- Marangoni, A. G. (2005), *Fat Crystal Networks*, Marcel Dekker.
- Marangoni, A. G. and Narine, S. S. (2002), *Physical Properties of Lipids*, Marcel Dekker.
- Matsui, S. (1991), Solid-State NMR Imaging by Magic Sandwich Echoes. *Chemical Physics Letters* **179**(1-2):187-190.
- Maus, A., Hertlein, C. and Saalwächter, K. (2006), A robust proton NMR method to investigate hard/soft ratios, crystallinity, and component mobility in polymers. *Macromolecular Chemistry and Physics* **207**:1150-1158.
- McDonald, G. G. and Leigh, J. S. (1973), A new method for measuring longitudinal relaxation times. *Journal of Magnetic Resonance* **9**(3):358-362.
- Meiboom, S. and Gill, D. (1958), Modified spin-echo method for measuring nuclear relaxation times. *Review of Scientific Instruments* **29**(8):688-691.
- Mendoza, C. I. and Santamaría-Holek, I. (2009), The rheology of hard sphere suspensions at arbitrary volume fractions: an improved differential viscosity model. *Journal of Chemical Physics* **130**(4):1-22.
- Mercier, J. P. (1990), Nucleation in polymer crystallization: a physical or a chemical mechanism?. *Polymer Engineering and Science* **30**(5):270-278.
- Miao, C. and Hamad, W. Y. (2013), Cellulose reinforced polymer composites and nanocomposites: a critical review. *Cellulose* **20**(5):2221-2262.
- Mohanty, S. and Nayak, S. N. (2007), Rheological characterization of HDPE/sisal fiber composites. *Polymer Engineering and Science* **47**:1634-1642.
- Monasse, B. (1995), Nucleation and anisotropic crystalline growth of polyethylene under shear. *Journal of Materials Science* **30**(19):5002-5012.
- Mooney, M. (1951), The viscosity of a concentrated suspension of spherical particles. *Journal of Colloid Science* **6**(2):162-170.
- Moran, D. P. J. and Rajan, K. K. (1994), *Fats in Food Products*, Springer Science+Business Media.

- Mursalin, Hayriyadi, P., Purnomo, E. H., Andarwulan, N. and Fardiaz, D. (2016), Determination of appropriate technique on crystallization and fractionation of coconut oil. *Jurnal Teknologi dan Industri Pangan* **27**(2):193–199.
- Muthukumar, M. (2004), Nucleation in polymer crystallization. *Advances in Chemical Physics* **128**:1–64.
- Mutlu, H., de Espinosa, L. M and Meier, M. A. R. (2011), Acyclic diene metathesis: a versatile tool for the construction of defined polymer architectures. *Chemical Society Reviews*, **40**:1404.
- Nakatani, A. I., Poliks, M. D. and Samulski, E. T. (1990), NMR investigation of chain deformation in sheared polymer fluids. *Macromolecules* **23**:2686–2692.
- Narine, S. S. and Marangoni, A. G. (1999), Relating structure of fat crystal networks to mechanical properties: a review. *Food Research International* **32**:227–248.
- Natta, G. (1956), Stereospezifische Katalysen und isotaktische Polymere. *Angewandte Chemie* **68**(12):393–424.
- Odell, J. A., Grubb, D. T. and Keller, A. (1978), A new route to high modulus polyethylene by lamellar structures nucleated onto fibrous substrates with general implications for crystallization behavior. *Polymer* **19**(6):617–626.
- Okada, K., Watanabe, K., Urushihara, T., Toda, A. and Hikosaka, M. (2007), Role of epitaxy of nucleating agent (NA) in nucleation mechanism of polymers. *Polymer* **48**:401–408.
- Okui, N. (1990), Relationships between melting temperature, maximum crystallization temperature and glass transition temperature. *Polymer* **31**(1):92-94.
- Oliveira De Castro, D., Frollini, E., Ruvolo-Filho, A. and Dufresne, A. (2015), “Green polyethylene” and curauá cellulose nanocrystal based nanocomposites: effect of vegetable oils as coupling agent and processing technique. *Journal of Polymer Science, Part B: Polymer Physics* **53**:1010–1019.
- Osswald, T. A. and Rudolph, N. (2015), *Polymer rheology fundamental and applications*, Edited by C. Strohm, Hanser.
- Özen, M. B., Ratzsch, K.-F., Rätzsch, V. and Wilhelm, M. (2015), Correlating Crystallization Kinetics and Rheological Properties of Polyethylene Using a New RheoNMR Setup. *Proceedings of 4<sup>th</sup> International Polymeric Composites Symposium, Exhibition and Brokerage event (IPC)* p.308-310.
- Özen, M. B., Rätzsch, V., Ratzsch, K.-F., Guthausen, G. and Wilhelm, M. (2016), Newly developed combination of rheology and <sup>1</sup>H TD-NMR to correlate mechanical

properties with molecular dynamics in soft matter. *Annual Transactions of the Nordic Rheology Society* **24**:38–40.

Pantani, R., Coccorullo, I., Speranza, V. and Titomanlio, G. (2005), Modeling of morphology evolution in the injection molding process of thermoplastic polymers. *Progress in Polymer Science* **30**(12):1185–1222.

Pasch, H. and Malik, M. I. (2014), Crystallization-based fractionation techniques. advanced separation techniques for polyolefins. *Advanced Separation Techniques for Polyolefins* (pp. 11-68), Springer.

Patki, R. P. and Phillips, P. J. (2008), Crystallization kinetics of linear polyethylene: the maximum in crystal growth rate-temperature dependence. *European Polymer Journal* **44**:534-541.

Peacock, A. J. (2000), *Handbook of polyethylene structures, properties and applications*, Marcel Dekker.

Peacock, A. J. and Mandelkern, L. (1990), The mechanical properties of random copolymers of ethylene: force-elongation relations. *Journal of Polymer Science Part B: Polymer Physics* **28**(11):1917–1941.

Pease, R. S. (1952), An X-ray study of boron nitride. *Acta Crystallographica* **5**:356–361.

Pines, A., Rhim, W.-K. and Waugh, J. S. (1972), Homogeneous and inhomogeneous nuclear spin echoes in solids. *Journal of Magnetic Resonance* **6**:457–465.

Piorkowska, E. and Rutledge, G. C. (2013), *Handbook of polymer crystallization first edition*, John Wiley and Sons.

Pogodina, N. V. and Winter, H. H. (1998), Polypropylene Crystallization as a Physical Gelation Process. *Macromolecules* **31**:8164–8172.

Pogodina, N. V., Winter, H. and Srinivas, S. (1999), Strain effects on physical gelation of crystallizing isotactic polypropylene. *Journal of Polymer Science, Part B: Polymer Physics* **37**:3512–3519.

Pracella, M., Minhaz-Ul Haque, M. and Alvarez, V. (2010), Functionalization, compatibilization and properties of polyolefin composites with natural fibers. *Polymers* **2**:554-574.

Prasad, N., Agarwal, V. K. and Sinha, S. (2016), Banana fiber reinforced low-density polyethylene composites: effect of chemical treatment and compatibilizer addition. *Iranian Polymer Journal* **25**:229–241.

Praveen, C. H., Arthanareeswari, M., Ravikiran, A., Kamaraj, P. and Pavan, K. V. (2014), Kinetic studies on crystallization process of amorphous vilazodone hydrochloride. *International Journal of Pharmacy and Pharmaceutical Sciences* **6**(5):630-635.

- Purcell, M. E., Torrey, H. C. and Pound, R. V. (1946), Resonance absorption by nuclear magnetic moments in a solid. *Physical Review* **69**:37-38.
- Quemada, D. (1977), Rheology of concentrated disperse systems and minimum energy dissipation principle - I. Viscosity-Concentration Relationship. *Rheologica Acta* **16**:82–94.
- Rabi, I. I., Milmann, S. and Kusch, P. (1939), The molecular beam resonance method for measuring nuclear magnetic moments. *Physical Review* **55**:526–535.
- Raghavan, S. R., Chen, L. A., McDowell, C. and Khan, S. A. (1996), Rheological study of crosslinking and gelation in chlorobutyl elastomer systems. *Polymer* **37**(26):5869–5875.
- Räntzsch, V. A. (2018), *Polymer crystallization under quiescent and flow conditions : relationships between molecular dynamics , morphology , and rheology* (Doctoral dissertation). Retrieved from <https://publikationen.bibliothek.kit.edu>
- Räntzsch, V., Haas, M., Özen, M. B., Rätzsch, K.-F., Riazi, K., Kauffmann-Weiss, S., Palacios, J. K., Müller, A. J., Vittorias, I., Guthausen, G. and Wilhelm, M. (2018), Polymer crystallinity and crystallization kinetics via benchtop <sup>1</sup>H NMR relaxometry: revisited method, data analysis, and experiments on common polymers. *Polymer* **145**:162–173.
- Räntzsch, V., Özen, M. B., Rätzsch, K.-F., Stellamanns, E., Sprung, M., Guthausen, G. and Wilhelm, M. (2019), Polymer crystallization studied by hyphenated rheology techniques: Rheo-NMR, Rheo-SAXS, and Rheo-Microscopy. *Macromolecular Materials and Engineering* **304**(2):1-14.
- Räntzsch, V., Wilhelm, M. and Guthausen, G. (2015), Hyphenated low-field NMR techniques: combining NMR with NIR, GPC/SEC and Rheometry. *Magnetic Resonance in Chemistry* **54**(6):494-501.
- Rätzsch, K.-F., Friedrich, C. and Wilhelm, M. (2017), Low-field rheo-NMR: a novel combination of NMR relaxometry with high end shear rheology. *Journal of Rheology* **61**(5):905–917.
- Reiter, G. and Strobl, G. R. (2007), *Progress in Understanding of Polymer Crystallization*, Springer.
- Rhim, W.-K., Pines, A. And Waugh, J. S. (1971), Time-reversal experiments in dipolar-coupled spin systems. *Physical Review B* **3**(3):684-695.
- Rigolle, A., Gheysen, L., Depypere, F., Landuyt, A., Van Den Abeele, K. and Foubert, I. (2015), Lecithin influences cocoa butter crystallization depending on concentration and matrix. *European Journal of Lipid Science and Technology* **117**(11):1722–1732.

- Roger, C. (2014), Global demand for polyethylene to reach 99,6 million tons in 2018. *Pipeline and Gas Journal* **241**(12):52-53.
- Rosato, D. V. and Rosato D. V. (2003), *Plastics Engineered Product Design*. Elsevier.
- Sadler, D. M. (1983), Roughness of growth faces of polymer crystals: Evidence from morphology and implications for growth mechanisms and types of folding. *Polymer* **24**:1401.
- Sadler, D. M. (1987), New explanation for chain folding in polymers. *Nature* **326**:174-177.
- Sadler, D. M. and Gilmer, G. H. (1988), Selection of lamellar thickness in polymer crystal growth: a rate-theory model. *Physical Review B* **38**(8):5684–5693.
- Sakakibara, K., Moriki, Y. Yano, H. and Tsujii, Y. (2017), Strategy for the improvement of the mechanical properties of cellulose nanofiber-reinforced high-density polyethylene nanocomposites using diblock copolymer dispersants. *American Chemical Society Applied Materials and Interfaces* **9**(50):44079–44087.
- Sawyer, L. C., Grubb, D. T. and Meyers, G. F. (2008), *Polymer microscopy third edition*, Springer.
- Scardi, P., Leoni, M. and Delhez, R. (2004), Line-broadening analysis using integral breadth methods: a critical review. *Journal of Applied Crystallography* **37**(3):381–390.
- Schäler, K., Roos, M., Micke, P., Golitsyn, Y., Seidlitz, A., Thurn-Albrecht, T., Schneider, H., Hempel, G. and Saalwächter, K. (2015), Basic principles of static proton low-resolution spin diffusion NMR in nanophase-separated materials with mobility contrast. *Solid State Nuclear Magnetic Resonance* **72**:50-63.
- Schmacke, S. (2010), *Investigations of polyethylene materials by means of X-ray diffraction artificial ageing of polyethylene gas pipes* (Doctoral dissertation). Retrieved from <https://eldorado.tu-dortmund.de>
- Schmidt-Rohr, K. and Spiess, H. W. (1994), *Multidimensional Solid-State NMR and Polymers*, Academic Press.
- Scholten, P. B. V., Özen, M. B., Söyler, Z., Thomassin, J.-M., Wilhelm, M., Detrembleur, C. and Meier, M. A. R. (2020), Rheological and mechanical properties of cellulose/LDPE composites using sustainable and fully renewable compatibilisers. *Journal of Applied Polymer Science* **137**(22):48744.
- Schonhorn, H. and Ryan, F. W. (1966), Wettability of polyethylene single crystal aggregates. *Journal of Physical Chemistry* **70**(12):3811–3815.
- Schramm, G. (2000), *A practical approach to rheology and rheometry second edition*, Karlsruhe, Gebrueder HAAKE GmbH.

- Schwittay, C., Mours, M. and Winter, H. H. (1995), Rheological expression of physical gelation in polymers. *Faraday Discussions* **101**:93–104.
- Seven, K. M., Cogen, J. M. and Gilchrist, J. F. (2016), Nucleating agents for high-density polyethylene - a review. *Polymer Engineering and Science* **56**(5):541-554.
- Shaw, M. T. (2012), *Introduction to Polymer Rheology*, John Wiley and Sons.
- Sherman, L. M. (2014), *Polyolefin Additives: Pushing the Limits in Films and Molded Parts*. Retrieved from <https://www.ptonline.com/articles/polyolefin-additives-pushing-the-limits-in-films-molded-parts>
- Shi, Y., Liang, B. and Hartel, R. W. (2005), Crystal morphology, microstructure, and textural properties of model lipid systems. *Journal of the American Oil Chemists' Society* **82**(6):399-408.
- Shih, W.-H., Shih, Y. W., Kim, S.-I, Liu, J. and Aksay, I. A. (1990), Scaling behavior of the elastic properties of colloidal gels. *Physical Review A* **42**(8):4772-4779.
- Silvestre, C., Cimmino, S. and Di Pace, E. (2000), Morphology of polyolefins. *Handbook of polyolefins, second edition, revised and expanded*, Edited by C. Vasile, pp. 175–205.
- Singh, A. A. and Palsule, S. (2014), Coconut fiber reinforced chemically functionalized high-density polyethylene (CNF/CF-HDPE) composites by *Palsule* process. *Journal of Composite Materials* **48**(29):3673–3684.
- Slichter, W. P. and McCall, D. W. (1957), Note on the degree of crystallinity in polymers as found by nuclear magnetic resonance. *Journal of Polymer Science* **25**(109):230–234.
- Smith, D. E., Babcock, P. H. and Chu, S. (1999), Single-polymer dynamics in steady shear flow. *Science* **283**:1724–1727.
- Söyler, Z. and Meier, M. A. R. (2016), Catalytic transesterification of starch with plant oils: a sustainable and efficient route to fatty acid starch esters. *ChemSusChem* **10**:182–188.
- Sperling, L. H. (2006), *Introduction to physical polymer science fourth edition*, John Wiley and Sons.
- Storks, K. H. (1938), An electron diffraction examination of some linear high polymers. *Journal of the American Chemical Society* **60**(8):1753–1761.
- Strobl, G. (2000), From the melt via mesomorphic and granular crystalline layers to lamellar crystallites: a major route followed in polymer crystallization?. *European Physical Journal E* **3**(2):165–183.
- Strobl, G. (2006), Crystallization and melting of bulk polymers: New observations, conclusions and a thermodynamic scheme. *Progress in Polymer Science* **31**(4):398-442.

- Strobl, G. (2007), *The physics of polymers*, Springer.
- Strobl, G. (2009), Colloquium: laws controlling crystallization and melting in bulk polymers. *Reviews Of Modern Physics* **81**(3):1287-1300.
- Strobl, G. and Cho, T. Y. (2007), Growth kinetics of polymer crystals in bulk. *European Physical Journal E* **23**(1):55–65.
- Sturniolo, S. and Saalwächter, K. (2011), Breakdown in the efficiency factor of the mixed magic sandwich echo: a novel NMR probe for slow motions. *Chemical Physics Letters* **516**(1–3):106–110.
- Sulaiman, S., Raman, A. A. A. and Aroua, M. K. (2013), Optimization and modeling of extraction of solid coconut waste oil. *Journal of Food Engineering* **114**(2):228–234.
- Sungsanit, K. (2011), *Rheological and mechanical behaviour of poly (lactic acid)/polyethylene glycol blends* (Doctoral dissertation). Retrieved from <https://www.semanticscholar.org/paper>
- Takegoshi, K. and McDowell, C. A. (1985), A “magic echo” pulse sequence for the high-resolution NMR spectra of abundant spins in solids. *Chemical Physics Letters* **116**(2-3):100-104.
- Tanner, R. I. and Qi, F. (2005), A comparison of some models for describing polymer crystallization at low deformation rates. *Journal of Non-Newtonian Fluid Mechanics* **127**(2-3):131–141.
- Tjørve, K. M. C. and Tjørve, E. (2017), The use of Gompertz models in growth analyses, and new Gompertz-model approach: an addition to the unified-richards. *PLOS ONE* **12**(6):1-17.
- Tolinski, M. (2015), *Additives for polyolefins getting the most out of polypropylene, polyethylene and TPO second edition*, Elsevier.
- Türünc, O. and Meier, M. A. R. (2011), Thiol-Ene vs. ADMET: a complementary approach to fatty acid-based biodegradable polymers. *Green Chemistry* **13**(2):213-456.
- Ulrich, J. (2004), Is melt crystallization a green technology?. *Crystal Growth and Design* **4**(5):879–880.
- van Dam, J. E. G. (2008), Environmental benefits of natural fibre production and use. *Proceedings of the Symposium on Natural Fibres*.
- van Krevelen, D. W. and te Nijenhuis, K. (2009), *Properties of Polymers: Their Correlation with Chemical Structure; their Numerical Estimation and Prediction from Additive Group Contributions*, Elsevier.

- Vera-Sorroche, J., Kelly, A., Brown, E., Coates, P., Karnachi, N., Harkin-Jones, E., Li, K. and Deng, J. (2013), Thermal optimisation of polymer extrusion using in-process monitoring techniques. *Applied Thermal Engineering* **53**(2):405–413.
- Verdejo, R. and Mills, N. (2002), Performance of EVA foam in running shoes. *The Engineering of Sport 4*, Eds S. 4:580–7.
- Vleeshouwers, S. and Meijer, H. E. H. (1996), A rheological study of shear induced crystallization. *Rheologica Acta* **35**(5):391–399.
- Wang, L., Wang, J.-H., Yang, B., Wang, Y., Zhang, Q.-P., Yang, M.-B. and Feng, J.-M. (2013), A novel hierarchical crystalline structure of injection-molded bars of linear polymer: co-existence of bending and normal shish-kebab structure. *Colloid and Polymer Science* **291**(6):1503–1511.
- Wang, S. and Zhang, J. (2014), Non-isothermal crystallization kinetics of high density polyethylene/titanium dioxide composites via melt blending. *Journal of Thermal Analysis and Calorimetry* **115**:63–71.
- Weidenthaler, C. (2011), Pitfalls in the characterization of nanoporous and nanosized materials. *Nanoscale* **3**:792-810.
- Wilhelm, M., Maring D. and Spiess, H.-W. (1998), Fourier-transform rheology. *Rheologica Acta* **37**:399–405.
- Wilhelm, M. (2002), Fourier-transform rheology. *Macromolecular Materials and Engineering* **287**:83–105.
- Willenbacher, N. and Georgieva, K. (2013), Rheology of disperse systems. *Product Design and Engineering*, Wiley-VCH Verlag GmbH, pp. 1–57.
- Willett, J. L. (1994), Mechanical properties of LDPE/granular starch composites. *Journal of Applied Polymer Science* **54**:1685–1695.
- Williams, M. L., Landel, R. F. and Ferry, J. D. (1955), The temperature dependence of relaxation mechanisms in amorphous polymers and other glass-forming liquids. *Journal of The American Chemical Society* **77**(14):3701–3707.
- Wilson, C. W. and Pake, G. E. (1953), Nuclear magnetic resonance determination of degree of crystallinity in two polymers. *Journal of Polymer Science* **10**(5):503–505.
- Wittmann, J. C. and Lotz, B. (1981), Epitaxial crystallization of polyethylene on organic substrates: a reappraisal of the mode of action of selected nucleating agents. *Journal of Polymer Science: Polymer Physics Edition* **19**:1837–1851.

- Wohlhauser, S., Delepierre, G., Labet, M., Morandi, G., Thielemans, W., Weder, C. and Zoppe, J. O. (2018), Grafting polymers from cellulose nanocrystals: synthesis, properties, and applications. *Macromolecules* **51**:6157–6189.
- Wunderlich, B. (1990), *Thermal analysis*, Academic Press.
- Wunderlich, B. (2003), Reversible crystallization and the rigid-amorphous phase in semicrystalline macromolecules. *Progress in Polymer Science* **28**:383–450.
- Wunderlich, B. and Melillo, L. (1968), Morphology and growth of extended chain crystals of polyethylene. *Die Makromolekulare Chemie* **118**:250–264.
- Wunderlich, B. (2005), *Thermal Analysis of Polymeric Materials*, Springer.
- Wypych, G. (2016), *Handbook of Polymers 2<sup>nd</sup> Edition*, ChemTec Publishing.
- Yano, H., Omura, H., Honma, Y., Okumura, H., Sano, H. and Nakatsubo, F. (2018), Designing cellulose nanofiber surface for high density polyethylene reinforcement. *Cellulose* **25**:3351–3362.
- Yeh, G. S. Y. (1976), Strain-induced crystallization I. limiting extents of strain-induced nuclei. *Polymer Engineering and Science* **16**(3):138–144.
- Yi, P., Locker, C. R. and Rutledge G. C. (2013), Molecular dynamics simulation of homogeneous crystal nucleation in polyethylene. *Macromolecules* **46**:4723–4733.
- Young, F. V. K. (1983), Palm kernel and coconut oils: analytical characteristics, process technology and uses. *Journal of the American Oil Chemists' Society* **60**(2):374–379.
- Yu, F., Zhang, H., Liao, R., Zheng, H., Yu, W. and Zhou, C. (2009), Flow induced crystallization of long chain branched polypropylenes under weak shear flow. *European Polymer Journal* **45**:2110–2118.
- Zhou, G., Willet, J. L. and Carrier, C. J. (2001), Effect of starch content on viscosity of starch-filled poly(hydroxy ester ether) composites. *Polymer Engineering and Science* **41**(8):1365–1372.
- Ziegler, K., Holzkamp, E., Breil, H. and Martin, H. (1955), Polymerisation von äthylen und anderen olefinen. *Angewandte Chemie* **67**(16):426.
- Zuidema, H. (2000), *Flow induced crystallization of polymers: application to injection moulding* (Doctoral dissertation). Retrieved from <https://doi.org/10.6100/IR536185>
- Zuidema, H., Peters, G. W. M. and Meijer, H. E. H. (2001), Development and validation of a recoverable strain-based model for flow-induced crystallization of polymers. *Macromolecular Theory and Simulations* **10**(5):447–460.

Zwietering, M. H., Jongenburger, I., Rombouts, F. M. and Van`t Riet, K. (1990), Modeling of the bacterial growth curve. *Applied and Environmental Microbiology* **56**(6):1875-1881.